TECHNISCHE UNIVERSITÄT
ILMENAU

Pontificia Universidad Católica del Perú

Escuela de Posgrado

Dynamic and Algebraic Observer Design for Leak Detection, Size Estimation and Localization in Water Pipe Systems

Tesis para obtener el grado académico de Maestro en Ingeniería de Control y Automatización que presenta:

Julius Paul Rußmann

Asesor PUCP (PUCP):	***Prof. Dr. Carlos Gustavo Pérez Zuñiga***
Co-Asesor (TU Ilmenau):	***Prof. Dr.-Ing. Johann Reger***
Tutor responsable (TU Ilmenau):	***M. Sc. Matti Noack***

Lima, 2023

TECHNISCHE UNIVERSITÄT
ILMENAU

Master's thesis

Dynamic and Algebraic Observer Design for Leak Detection, Size Estimation and Localization in Water Pipe Systems

Submitted by:	Julius Paul Rußmann
Date of submission:	October 24, 2023
Study course:	Technical Cybernetics and Systems Theory
Matriculation number:	58789
Department:	Faculty of Computer Science and Automation
	Institute for Automation and Systems Engineering
	Control Engineering Group
Responsible professor TU Ilmenau:	Prof. Dr.-Ing. Johann Reger
Responsible professor PUCP:	Prof. Dr. Carlos Gustavo Pérez Zuñiga
Supervisor:	M. Sc. Matti Noack

Informe de similitud

Yo, Carlos Gustavo Pérez Zuñiga, docente de la Escuela de Posgrado de la Pontificia Universidad Católica del Perú, asesor de la tesis titulada Dynamic and Algebraic Observer Design for Leak Detection, Size Estimation and Localization in Water Pipe Systems, del autor Julius Paul Rußmann dejo constancia de lo siguiente:

- El mencionado documento tiene un índice de puntuación de similitud de $8\ \%$. Así lo consigna el reporte de similitud emitido por el software Turnitin el 10/08/2023.
- He revisado con detalle dicho reporte y la Tesis o Trabajo de Suficiencia Profesional, y no se advierte indicios de plagio.
- Las citas a otros autores y sus respectivas referencias cumplen con las pautas académicas.

Lugar y fecha:

Lima, 24 de octubre 2023

Apellidos y nombres del asesor: Pérez Zuñiga, Carlos Gustavo	
DNI: 41864666 ORCID: 0000-0001-5946-1395	Firma 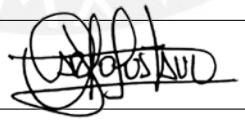

Declaration of Originality

I, Carlos Gustavo Pérez Zuñiga, professor at the Graduate School of the Pontifical Catholic University of Peru, advisor to the thesis of Julius Paul Rußmann, hereby record the following:

- The present document has a similarity score of $8\ \%$. This is stated in the similarity report issued by the Turnitin software on August 10, 2023.
- I have thoroughly reviewed that report and the thesis, and there are no signs of plagiarism.
- The citations to other authors and their respective references comply with the academic guidelines.

Place and date:
Lima, October 24, 2023

Surname and name of the advisor: Pérez Zuñiga, Carlos Gustavo	
DNI: 41864666 ORCID: 0000-0001-5946-1395	Firma 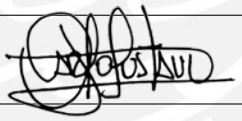

Statutory Declaration

I, Julius Paul Rußmann, hereby declare that this master thesis presented here is to the best of my knowledge and belief original and the result of my own investigations and independent authoring, unless otherwise acknowledged.
Formulations and ideas taken from external resources are declared as such.
This work has not been published and submitted, either in part or whole, for obtaining a degree at this or any other university.

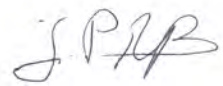

Lima, October 24, 2023 Julius Paul Rußmann

Acknowledgements

The author of this thesis, Julius Paul Rußmann, thanks the support of the project: Sistema de Detección y Localización Temprana de Derrames en Oleoductos through the contract: PE501079992-2022 of the convention: Proyectos Especiales - Modalidad: Escalamiento de Tecnologías 2022 - 01 de PROCIENCIA-CONCYTEC. The present thesis has been developed in the framework of this project.

Resumen

En esta tesis se aplican por primera vez métodos basados en modelos sin discretización espacial para detectar y localizar fugas en una planta piloto de transporte de fluidos. Basado en un modelo matemático que describe la dinámica de fluidos dentro de la tubería de agua mediante dos ecuaciones diferenciales parciales que son hiperbólicas, lineales, unidimensionales y acopladas, se deriva y diseña tanto un observador dinámico como algebraico. El diseño del observador dinámico combina un enfoque de Luenberger con una transformación de backstepping para demostrar la estabilidad asintótica del error del observador. Como consecuencia, el observador resulta en un sistema dinámico de dos sistemas diferenciales parciales hiperbólicos acoplados. Por el contrario, el diseño del observador algebraico aplica el método de las funciones de modulación para convertir el modelo matemático en problemas auxiliares que también son dados por ecuaciones diferenciales parciales. Los problemas auxiliares se pueden resolver fuera de línea, tal que para estimar el tamaño y la posición de la fuga en línea se tienen que resolver solamente ecuaciones algebraicas input-output. Se enfatiza que ambos esquemas de observación se derivan directamente del modelo matemático sin discretización espacial. Por lo tanto, esta tesis aborda la brecha de investigación con respecto a métodos de detección y localización de fugas que sean basados en un modelo matemático y que no requieren una discretización espacial del sistema.

En simulaciones comparativas, se evalúa el desempeño de ambos observadores para una tubería de agua ejemplar en diversas condiciones de operación, por ejemplo, el tamaño de la fuga, la posición de la fuga, el caudal de entrada y el ruido de medición. Se compara la precisión de los esquemas de observación, y se verifica la capacidad en tiempo real de ambos algoritmos.

Finalmente, la dinámica y el observador algebraico se utilizan para estimar el tamaño y la posición de la fuga para una planta piloto de transporte de fluidos instalada en el laboratorio de Ingeniería de Control Avanzado en la PUCP. Se revela que, al contrario de la suposición de un modelo lineal para la perdida por fricción, las pérdidas por fricción dependen cuadráticamente del caudal tal que un modelo no lineal describa con mayor exactitud la dinámica del fluido de la planta piloto. Sin embargo, se ha demostrado que para las fugas que surgen cerca de la salida de la tubería, ambos observadores estiman la posición de la fuga con desviaciones inferiores al $5\,\%$ y logran la precisión deseada. Además, se ha demostrado que una extensión del observador dinámico hacia el modelo no lineal permite localizar la fuga con desviaciones inferiores al $5\,\%$, independientemente de la posición de la fuga.

Abstract

The present work utilizes for the first time model-based late lumping leak detection methods to detect and localize leakage in a real water pipe. Based on a mathematical model that describes the fluid dynamics inside the water pipe by two coupled linear one dimensional hyperbolic partial differential equations, a dynamic and an algebraic leakage observer are designed. The dynamic observer design combines a Luenberger ansatz with a backstepping transformation to prove the asymptotic stability of the observer error and results in a dynamic system of two coupled hyperbolic partial differential systems. Contrary to that, the algebraic observer design applies the modulating function method to convert the mathematical model into offline solvable auxiliary problems and algebraic input-output equations that are resolved online to estimate the leak size and the leak position. It is emphasized that both observer schemes are derived directly from the mathematical model without spatial discretization. Thereby, this thesis addresses the research gap regarding model-based late lumping leak detection and localization techniques.

In comparative simulations, the performance of both observer schemes is evaluated for an exemplary water pipe under various operating conditions, e.g., w.r.t. the leak size, the leak position, the inlet flow rate and the measurement noise. The accuracy of the observer schemes is compared, and the real-time capability of both algorithms is verified.

Finally, the dynamic and the algebraic observer are utilized to estimate the leak size and the leak position for a pilot fluid transport plant installed in the laboratory of Advanced Control Engineering at the PUCP. It is revealed that, in opposite to the model assumption of linear friction losses, the friction losses depend quadratically on the flow rate such that a nonlinear model describes the flow dynamics of the pilot plant more exactly. However, it is shown that for leaks occurring near to the outlet of the pipe, both observers estimate the leak position with deviations of under $5\ \%$ and reach thereby the desired accuracy. Furthermore, it is demonstrated that an extension of the dynamic observer towards the nonlinear model permits localizing the leak with deviations of under $5\ \%$ regardless of its position.

Kurzfassung

Die vorliegende Arbeit verwendet erstmals räumlich undiskretisierte modellbasierte Methoden zur Erkennung und Lokalisierung von Leckagen in einer realen Wasserleitung. Basierend auf einem mathematischen Modell, das die Strömungsdynamik im Rohr durch zwei gekoppelte lineare eindimensionale hyperbolische partielle Differentialgleichungen beschreibt, werden ein dynamischer und ein algebraischer Leckagebeobachter entworfen. Der dynamische Beobachterentwirf kombiniert einen Luenberger-Ansatz mit einer Backstepping-Transformation, um die asymptotische Stabilität des Beobachterfehlers nachzuweisen und resultiert in einem dynamischen System aus zwei gekoppelten hyperbolischen partiellen Differentialgleichungen. Im Gegensatz dazu verwendet der algebraische Beobachterentwurf die Modulationsfunktionsmethode, um das mathematische Modell in offline lösbare Hilfsprobleme sowie algebraische Eingangs-Ausgangs-Gleichungen zu überführen, die online gelöst werden, um die Leckgröße und die Leckageposition zu schätzen. Es wird hervorgehoben, dass beiden Beobachter direkt aus dem mathematischen Modell ohne räumliche Diskretisierung abgeleitet sind. Die vorliegende Arbeit adressiert damit eine existierende Forschungslücke hinsichtlich modellbasierter Leckagelokalisierung.

In vergleichenden Simulationen wird die Performance beider Beobachter für eine exemplarische Wasserleitung unter unterschiedlichen Betriebsbedingungen untersucht, z. B. hinsichtlich der Leckgröße, der Leckposition, des Volumenstroms am Einlass und dem Messrauschen. Die Genauigkeit der Beobachter wird verglichen und die Echtzeitfähigkeit beider Algorithmen überprüft.

Anschließend werden der dynamische und der algebraische Beobachter verwendet, um die Leckgröße und die Leckageposition für eine Pilotanlage, die im Labor für Regelungstechnik an der PUCP installiert ist, zu schätzen. Es zeigt sich, dass die Reibungsverluste entgegen der Modellannahme quadratisch von der Strömungsgeschwindigkeit abhängen, sodass ein nichtlineares Modell die Strömungsdynamik der Pilotanlage genauer beschreibt. Es zeigt sich jedoch, dass bei Leckagen in der Nähe des Rohrauslasses beide Beobachter die Leckageposition mit Abweichungen von unter $5\ \%$ schätzen und damit die gewünschte Genauigkeit erreichen. Abschließend wird gezeigt, dass eine Erweiterung des dynamischen Beobachters hin zum nichtlinearen Modell die Lokalisierung des Lecks mit Abweichungen von weniger als $5\ \%$ unabhängig von seiner Position ermöglicht.

Contents

Acronyms iv

Symbols vi

Motivation 1

1. Introduction 3
- 1.1. State of the Art . . . 3
- 1.2. Research Objectives . . . 7
  - 1.2.1. General Objective . . . 7
  - 1.2.2. Specific Objectives . . . 8
- 1.3. Methodology . . . 9

2. System Modeling of Water Pipes 12
- 2.1. Mathematical Modeling of Fluid Dynamics in Water Pipes . . . 12
  - 2.1.1. Modeling of Friction Losses . . . 14
    - 2.1.1.1. Linear Friction Modeling . . . 15
    - 2.1.1.2. Nonlinear Friction Modeling . . . 16

3. Observer Design 18
- 3.1. State Transformation of the Pipe Model . . . 19
- 3.2. Dynamic Observer Design . . . 22
  - 3.2.1. Leak Size Estimation and State Estimation . . . 23
  - 3.2.2. Leak Localization . . . 26
- 3.3. Algebraic Observer Design with Modulating Functions . . . 28
  - 3.3.1. Modulating Function Method (MFM) . . . 30
  - 3.3.2. Leak Size Estimation by MFM . . . 32
    - 3.3.2.1. Derivation of the Algebraic Input-Output Expression and the Auxiliary Problem . . . 32
    - 3.3.2.2. Solution of the Auxiliary Problem . . . 35

3.3.3. Leak Localization by MFM . . . 37
3.3.3.1. Direct Leak Localization by MFM . . . 38
3.3.3.2. Leak Localization by MFM-based State Estimation . . . 42
Derivation of the Algebraic Input-Output Expression and the Auxiliary Problem . . . 42
Solution of the Auxiliary Problem . . . 44

4. Simulation-Based Results **47**
4.1. Generation of the Modulating Functions . . . 48
4.2. KPI-based Evaluation of the Leak Observer Results for a Simulation Plant . . . 54
4.2.1. Simulation-based Leak Observer Results under Variation of the Measurement Noise Level . . . 55
4.2.2. Simulation-based Leak Observer Results under Variation of the Leak Size . 61
4.2.3. Simulation-based Leak Observer Results under Variation of the Leak Localization and Distribution . . . 65
4.2.4. Simulation-based Leak Observer Results under Variation of the Operating Point . . . 68
4.2.5. Simulation-based Leak Observer Results under Model Uncertainty . . . 73

5. Experimental-Based Results **82**
5.1. Friction Identification of the Pilot Plant . . . 84
5.2. Validation of the Pipe Model . . . 88
5.2.1. Model Verification and Validation without Leakage . . . 89
5.2.2. Model Verification and Validation in the Leakage Case . . . 98
5.3. KPI-based Evaluation of the Leak Observer Results for the Pilot Plant . . . 107
5.3.1. Experimental-based Leak Observer Results under Variation of the Leak Size 112
5.3.2. Experimental-based Leak Observer Results under Variation of the Leak Position 115
5.3.3. Experimental-based Leak Observer Results under Variation of the Inlet Flow Rate . . . 118

6. Conclusion and Outlook **121**

7. Bibliography **125**

List of Figures **135**

List of Tables **140**

A. Appendix **143**

A.1. Leak Localization with ABSO for different Leak Distribution Functions 143

A.2. FIR Filter Realization of the Algebraic Leak Size Estimation Equation 144

A.3. Spatial Discretization of the Pipe Model 146

Acronyms

ABSO Adaptive Backstepping Observer.

EKF Extended Kalman Filter.

FIR Finite Impulse Response.

IO Input-Output.

IWSA International Water Services Association.

KF Kalman Filter.

KPI Key Performance Indicator.

LMF Left Modulating Function.

MF Modulating Function.

MFM Modulating Function Method.

MISO Multiple-Input Single-Output.

MOL Method of Lines.

NRMSE Normalized Root Mean Square Error.

ODE Ordinary Differential Equation.

OECD Organisation for Economic Co-operation and Development.

PDE Partial Differential Equation.

PID Proportional–Integral–Derivative.

PUCP Pontifica Universidad Católica del Perú.

RTTM Real-Time Transient Modeling.

SNR Signal-to-Noise Ratio.

TMF Total Modulating Function.

UKF Unscented Kalman Filter.

Symbols

α	Order of Gevrey function
A	Cross-sectional area of the pipe
$b(\tau)$	Basic variable of power series ansatz
β	Bulk modulus
$c_1(x),\ c_2(x)$	Spatially distributed parameters of transformed system
$\bar{c}_1(x),\ \bar{c}_2(x)$	Spatially mean values of $c_1(x),\ c_2(x)$
c^k	k-th coefficient of function expansion
d	Pipe diameter
$d(z)$	Leak distribution function
$\delta(z)$	Auxiliary variable describing leak distribution
$\delta(t)$	Estimated value of $\delta(z=0)$
$\Delta\chi$	Mean error of leak size estimation
Δz^*	Mean error of leak localization
ϵ	Wave velocity
ϵ_p	Pipe surface roughness
η	Parameter describing leak characteristics in momentum balance
η_v	Fluid viscosity
$\eta_1(\tau)$	Boundary condition (degree of freedom) in auxiliary problem
F	Friction factor

f_d	Darcy-Weisbach friction coefficient
φ	Modulating Function
$\hat{\varphi}_1(x,\tau),\ \hat{\varphi}_2(x,\tau)$	Modulating functions resulting from power series ansatz
$\hat{\varphi}_{1,k}(\tau),\ \hat{\varphi}_{2,k}(\tau)$	Temporal coefficients of power series ansatz for $\hat{\varphi}_1(x,\tau),\ \hat{\varphi}_2(x,\tau)$
g	Gravity acceleration
γ	Leak localization observer gain
h	Height difference between inlet and outlet of pipe
$H(z,t)$	Pressure head distributed in z and t
I_n	Modified Bessel function of the first kind of order n
$J(q(z,t))$	Friction losses in momentum balance
ℓ	Length of the pipe
L	Output injection gain for leak size estimation
$\mathcal{M}$	Modulating functional
N	Approximation order
n	Number of spatial nodes
Ω	Spatial domain
$p_1(x),\ p_2(x)$	Output injection gains
$p(z,t)$	Pressure distributed in z and t
$p_0(t)$	Inlet pressure
$\hat{p}_0(t)$	Estimated inlet pressure
p_{out}	Constant describing operating pressure point of the pipe
$p_\ell(t)$	Outlet pressure
Ψ^k	k-th function of orthonormal function basis

$q(z,t)$	Flow rate distributed in z and t
$q_0(t)$	Inlet flow rate
q_{in}	Constant describing operating flow rate point of the pipe
$q_\ell(t)$	Outlet flow rate
Re	Reynolds number
ρ	Fluid density
σ	Slope of Gevrey function
σ_p	Standard deviation of measurement noise (pressure)
σ_q	Standard deviation of measurement noise (flow rate)
σ_χ	Standard deviation of leak size estimate
σ_z	Standard deviation of leak position estimate
θ	Inclination angle of the pipe
t	Time variable
t_f	Final time of simulation
t_F	Finite time for stabilizing auxiliary problem for state estimation
$t_{conv,\chi}$	Convergence time of leak size estimate
$t_{conv,z}$	Convergence time of leak localization
t_{exec}	Runtime
τ	Time variable of modulating functions
T	Moving time horizon of modulating function
T_χ	Moving time horizon of modulating functions for leak size estimation
T_z	Moving time horizon of modulating functions for state estimation
$u(x,t)$	Distributed state of transformed system
$\hat{u}(x,t)$	Estimation of $u(x,t)$
$\tilde{u}(x,t)$	Estimation error w.r.t $u(x,t)$
$U(t)$	Boundary condition of transformed system

$v(x,t)$	Distributed state of transformed system
$\hat{v}(x,t)$	Estimation of $v(x,t)$
$\tilde{v}(x,t)$	Estimation error w.r.t $v(x,t)$
$w(x)$	Weighting function for orthonormalization of basis functions
x	Spatial variable of transformed system
χ	Leak size
$\hat{\chi}$	Estimated leak size
$\tilde{\chi}(t)$	Estimation error w.r.t χ
$Y(1,t)$	Boundary output of the transformed system
z	Spatial coordinate of pipe system
z^*	Leak position

Motivation

Pipelines form a barely visible but indispensable part of our modern societies. Without them, our daily life in heated buildings provided with running water would be inconceivable. Distributing the potable water from the source to the water treatment plant to almost every building, pipelines allow us to pursue our everyday activities, beginning from the shower in the morning, through boiling water for lunch, to falling asleep in a heated apartment. Moreover, parts of our transportation and heating systems rely heavily on the oil and gas pipelines around the planet that transport natural gas and crude oil from the resource deposit to the refineries and from the refineries to the end consumer.

From a more technical perspective, pipelines are an essential part of fluid transport infrastructure to convey gas or liquid over long distances and to connect thereby fluid sources and sinks. A total length of worldwide constructed pipelines of around 3,500,000 kilometers [1] and a continuously expanding global pipe network [2, 3] reflect the importance of pipelines in infrastructure systems. Compared to alternative transport technologies like transport by road, roadway or waterway, pipe systems show various advantages like higher transport volumes and lower transportation expenses [1].

Nevertheless, since pipelines directly affect our daily needs and operate in various parts of critical infrastructure, like e.g., heating systems, water distribution networks or fuel transport, a high level of safety and reliability is demanded. One of the major risks to deal within this context is the appearance of leaks. Mainly caused by external interferences, corrosion, construction defects, material failure and ground movement (see Figure 1) [4], leaks provoke severe multidimensional consequences and dangers for man and nature. First, the suspension of the normal operation of the pipeline and the repairing of the leak lead to additional economical costs and an abrupt interruption of the comforts of our daily life, e.g., when the supply of running water is interrupted. Moreover, and in light of a planet where water becomes an increasingly scarce and valuable resource due to the climate change, an economical and careful use that minimizes the losses is imperative to maintain our living standard. However, according to a study of the International Water Services Association (IWSA) carried out in 2001, the water losses sum up to between $8\ \%$ and $24\ \%$ in developed countries, $15 - 24\ \%$ in newly industrialized countries, and $25 - 45\ \%$ in developing countries [5]. A more recent study of the Organisation for Economic Co-operation and Development (OECD)

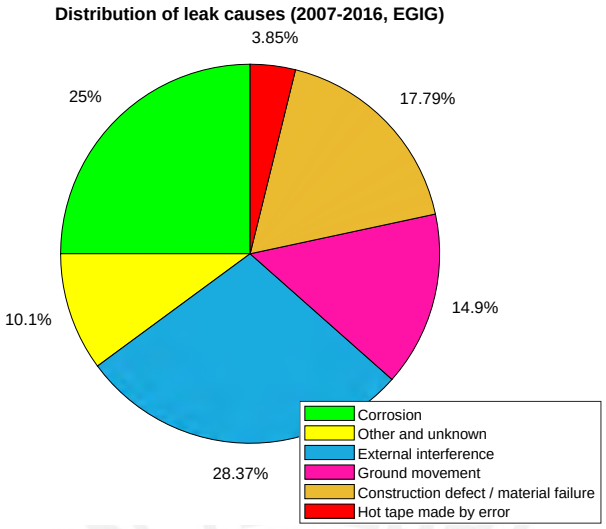

Figure 1.: Distribution of leak causes (2007-2016, EGIG) [4]

realized in 2012 that surveys 48 cities from OECD countries indicates an average water loss of 21 % including cities in Mexico with a water loss rate higher than 50 % [6]. An approach to quantify the economical costs due to leakage in water pipes concluded that the yearly water losses sum up to a value of about USD 39 billion [7]. In short, these statistics emphasize the great need of reliable and accurate leak detection and localization methods.

The main subject of this thesis is confined to the leak detection, size estimation and localization for water pipes. Nonetheless, the same issue of leak detection and localization applies w.r.t. to fossil fuels like crude oil and natural gas. Moreover, escaped fossil fuels can cause health risks (e.g., by contaminating potable water) and environmental damage up to social conflicts (see e.g., [8, 9, 10]). Consequently, there is a great need for monitoring of pipeline systems to detect the occurrence of leaks in a rapid, reliable, and accurate way. It is required not only to detect the leak, but also to estimate its size and locate its position accurately enough to ensure that the leak can be repaired rapidly and that the economic, as well as the environmental impact, is minimized.

1. Introduction

1.1. State of the Art

Due to the severe economical, ecological, and social impacts of leakage[1], the development of leak detection methods is of great research, economic and common interest, such that a wide range of leak detection and localization approaches exists. To order this wide field and obtain a better overview of the state-of-the-art approaches, the leak detection methods can be classified according to their technical nature and are categorized into three main classes as Figure 1.1 illustrates: hardware-based methods, non-technical methods, and software-based methods [12].[2]

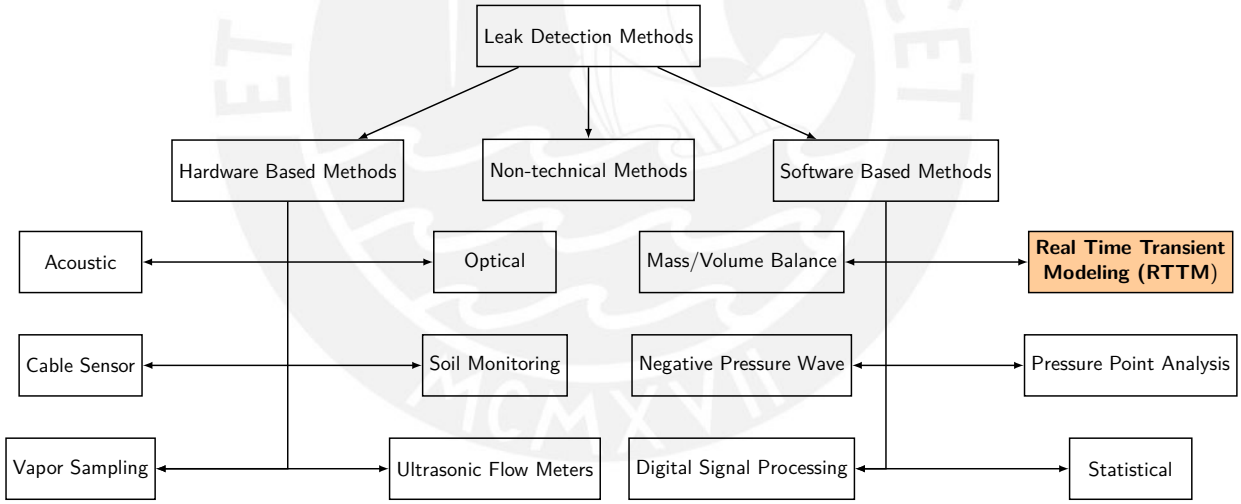

Figure 1.1.: Overview of leak detection techniques, based on [12].

Non-technical or biological methods apply e.g., trained dogs or line patrols to detect and locate leaks based on visual, olfactory, or sound observations like unusual patterns near the pipeline,

[1] Throughout this thesis, the terms leak and leakage are used as synonyms. For a differentiation between leak and leakage see e.g., [11].

[2] Some authors use the terminology externally based methods to refer to hardware-based methods and internally based methods referring to software-based methods (see e.g., [13]).

recognition of odour-intense substances or listening to specific noises evoked by fluid that escapes through the leak [14]. Although these methods guarantee the highest degree of accuracy and reliability and are still the most common leak detection and localization method [15], the accuracy and the rapidness of these methods depend strongly on the experience and sensitivity of the personnel, as well as the frequency of the inspections. Furthermore, the application of biological or non-technical methods is limited by the topographic conditions and hardly automatable.

Hardware-based methods are characterized by the implementation of local sensing devices to detect and locate directly the leak. According to the physical principles that govern the functioning of the sensing devices, several types of hardware-based methods are distinguished: acoustic, optical, cable sensor, soil monitoring, ultrasonic flow meters and vapor sampling. On the one hand, hardware-based methods can guarantee high accuracy in detecting and locating the leak since they do not depend on measured or identified pipeline parameters [15]. Nevertheless, the reliability of hardware-based methods depends strongly on the accurate and adequate installation of the sensors to ensure that a change in the pipeline integrity due to a leak can be recognized. Consequently, hardware-based methods have the drawback of high complexity of installation (especially in the case of difficult topographic conditions or underground pipelines) and high system costs [13]. Hence, their application is mainly concentrated in high-risk areas like natural reserves [13].

Software-based methods use the measurement of field sensors to internally run an implemented algorithm that constantly monitors the state of main physical pipeline parameters like the flow rate, the pressure, or the temperature. Based on the analysis of the physical states, the algorithm infers if and where a leak has occurred. A simplistic leak detection method would compare the inlet flow and the outlet flow and infer the occurrence of a leak if this difference is higher than a prescribed threshold. According to the underlying mathematical and physical approach, software-based methods can be subdivided into several categories: acoustic/negative pressure wave, pressure point analysis, statistics, digital signal processing, mass/volume balance and Real-Time Transient Modeling (RTTM) [12]. In the following, the focus will lay on the latter approach.

RTTM algorithms are model-based and require firstly the derivation of a mathematical pipe model that describes the fluid dynamics inside the pipe adequately. Mostly, physical principles like the conservation of mass and the conservation of momentum are utilized to derive a system of coupled Partial Differential Equation (PDE) that describe the temporal and spatial dependency of the physical states (e.g., flow rate, pressure, and temperature). Subsequently, an observer is designed that compares the state values measured by the field sensors and the state values simulated by the pipe model and infers based on this error signal if and where a leak has occurred.

Since the resulting PDEs represents an infinitely dimensional system, the dimension of this system must be reduced to be able to implement the resulting observers. The process of reducing the infinitely dimensional system to a finite dimensional system is called lumping and leads to two different categories of RTTM approaches, that are illustrated in Table 1.1: early lumping and late

lumping [16].

Early lumped RTTM	Late lumped RTTM
•Gradient Intersection method ([17, 18, 19]) •Kalman Filter Design ([21, 22, 23, 24, 25]) •Sliding Mode Differentiators ([28, 29])	•Luenberger type observers ([20]) •Adaptive Backstepping Observer ([26, 27])

Table 1.1.: Overview of RTTM approaches.

Early lumping approaches are characterized by the fact that the reducing of the infinite model order to a finite model order is performed before the observer is designed, i.e., the PDE system is discretized to obtain a set of Ordinary Differential Equations (ODEs) [16]. After the spatial discretization, classical approaches of observer theory for finite dimensional systems like sliding mode observers [28, 29], Luenberger type observer or Kalman Filter (KF)-type observers (e.g. Extended Kalman Filter (EKF), Unscented Kalman Filter (UKF), particle filter, ...) [21, 22, 23, 24, 25] can be applied to the resulting ODE system to detect and locate the leak.

Especially, the design of KF-type observers to estimate and locate pipe leaks is the subject of intense research during the four decades and can be regarded as a benchmark for RTTM approaches. In [25], a review of KF-based approaches for leak detection and estimation is provided. The results of different research groups are bundled and analyzed regarding the reliability, accuracy, sensitivity, and robustness of the proposed leak detection and localization schemes. Furthermore, a classification of the KF-based techniques to detect and locate leaks is proposed: (i) approaches based on a bank of KFs, (ii) approaches based on the estimation of internal pressures and flow rates and (iii) approaches based on the direct estimation of the leak parameters. This classification also represents the historical evolution of the KF-based leak detection and localization techniques. The approach based on a bank of filters was the first KF-based technique to detect and localize leaks in pipelines and was proposed in 1980 in [30]. The main idea was to discretize the pipe into n spatial segments and to design a filter for the leak case in each of the spatial segments of the pipe. Thereby, a bank of independent filters is obtained, where the n-th filter is designed to recognize a single leak in the n-th segment. To identify the leak position, a multiple-model hypothesis probability test is performed to select the filter which optimally fits the model based on the available measurement data. This approach based on a bank of estimators was revisited and further refined in [31] and combined with genetic algorithms in [32] to improve the accuracy in noisy environments. Moreover, the approach is already used for commercial leak detection algorithms like PipePetrol by the KROHNE Group [33]. However, one main drawback of the approach is that a higher accuracy not only requires a finer discretization of the pipe but also an increasing number of filters that have to be designed and implemented in real-time. To overcome this disadvantage, the approaches based on the estimation of internal pressures and flow rates were developed. The first publication in this context is [34] that

deals with the detection and localization of leaks in gas pipelines. Based on a lumped model of two PDEs that describe the gas dynamics inside the pipeline, only one KF is necessary to design to estimate the leak localization. The estimation of the physical states (flow rate and pressure) of the pipe model are used to resolve auxiliary algebraic equations (e.g., derived from head loss balances, mass balance and the estimation of fictitious leaks) for the leak localization. The accuracy of this approach can be tuned by augmenting the number of estimated internal states of the pipe model what also implies increasing computational costs. The most recently developed KF-type leak detection algorithms utilize approaches based on the direct estimation of the leak parameters. Thereby, the design and real-time implementation of multiple filters, like it is the case for approaches of type (i), or of a spatially discretized filter, like for (ii), is circumvented. Instead, a unique KF is implemented to estimate the leak localization, where the design of the KF is realized based on a spatially discretized mathematical model of the fluid dynamics that includes the leak position and leak size in form of state variables. The first publication concerning this approach is [35] where the design of a single Extended Kalman Filter (EKF) to detect and localize at maximum two leaks is proposed. This approach was refined in [36] to design an EKF to detect and localize leaks in a plastic pipeline and was validated successfully. Nowadays, the research interest focuses on the design of EKF-based leak detection and localization algorithms for complex pipeline networks that include series and branch junctions [37, 38]. Another focus lies on the transfer of the KF-based leak detection and localization techniques, that are mostly designed for water pipelines, to the case of oil or gas pipelines. Examples can be found in [39], where the design of an Unscented Kalman Filter (UKF) is proposed, and in [40], where an EKF is utilized to detect and locate leakages for a simulation pipe with characteristics similar to the first section of the North Peruvian oil pipeline.

Although the KF-type observers show an acceptable accuracy in simulation and real data-based test environments (see e.g., an accuracy of $1.36\ \%$ w.r.t. the leak localization in [21]), the early lumping approaches share several drawbacks. Firstly, since the PDE model is discretized before the observer design, physical information contained in the PDE model is lost and important conditions for the observer design like the observability of the obtained ODE system can depend on the choice of the discretization scheme and the location of the discretization points [16]. Furthermore, the stability analysis of the observer loop including the physical PDE model of the pipe and the ODE based observer becomes more complicated.

These theoretical limitations motivate the design of late lumping leak observers, which make use of the full physical information contained in the PDE model. The observer is designed based on the PDE model and represents also an infinite dimensional system, such that the discretization is performed only during the last stage, the implementation phase. Thereby, all modelled physical features of the problem are included in the observer design process [16] and a rigorous stability analysis can be performed using PDE theory for the observer loop, including the physical PDE model of the pipe and the PDE system representing the observer. In [27], such a late lumped

observer is proposed using backstepping methods to prove the asymptotic stability of the observer error in the leak size estimation and the leak localization. Throughout this thesis, one focus lies on a profound evaluation of the approach presented in [27] using simulation-based, and real data-based results. Afterwards, this approach is compared to an alternative late lumping method applying modulating functions to design an algebraic observer.

1.2. Research Objectives

Throughout this thesis, dynamic and algebraic observer algorithms are designed to detect and localize leakage in pipe systems. While dynamic observer schemes require an online simulation of the PDE model, the dynamic auxiliary problem of algebraic observers can be solved offline such that only an algebraic equation that can be implemented as a Finite Impulse Response (FIR) filter has to be solved online. It is of great interest to compare the capacity to detect and locate leaks of both observer schemes and to investigate which observer scheme performs better under various conditions regarding several important KPIs like the accuracy of leak size estimation and localization, sensitivity to leak size and measurement noise and the calculation time. It is aimed at evaluating the performance of both observers not only for a simulation plant, but also for a pilot plant installed at the Laboratory for Advanced Control Engineering at the Pontifica Universidad Católica del Perú (PUCP). Thereby, to the best of the author's knowledge, this thesis analyzes for the first time late lumped, RTTM approaches to detect and localize leaks based on real measurement data. To reach these research objectives, the following general and specific objectives, that will guide this thesis, are formulated.

1.2.1. General Objective

The main goal of this thesis is to derive, implement and validate a dynamic and an algebraic observer to detect leaks smaller than $1\ \%$ of the nominal flow rate, estimate its size and localize its position with deviations under $5\ \%$ regarding the real leak size and the total length of the pipe. Moreover, it is aimed at enabling an implementation of the two observers in real time. To this end, the main goal is subdivided into two parts.

Firstly, the Adaptive Backstepping Observer (ABSO), a dynamic observer proposed in [27], is profoundly analyzed in a simulation-based test environment to identify the limitations of the observer regarding e.g. measurement noise and model uncertainties. In particular, the model assumption of linear friction losses is investigated critically.

The application of the Modulating Function Method (MFM) [41, 42, 43] to detect and locate

pipe leaks represents the second research interest of this thesis. The goal is to develop, implement and test this algebraic observer design approach firstly in a simulation-based test environment in order to evaluate its efficiency and possible advantages or drawbacks over the ABSO. To this end, the MFM is applied to the linear PDE pipe model to derive the auxiliary problems that can be solved offline and to derive the algebraic Input-Output (IO) relation for the leak size estimation and the leak localization. Finally, the simulation-based results of both observer schemes are compared profoundly regarding important performance indicators like accuracy, sensitivity and run time of the leak detection and localization.

Furthermore, both observer designs are evaluated with data from a pilot plant installed at PUCP. The goal is to verify and validate the simulation-based results in a real data-based environment. Therefore, relevant model parameters are identified, the model is validated and the performance of both observers regarding accuracy and sensibility of the leak size estimation and localization is evaluated under different conditions (magnitude of the leak, position of the leak, nominal flow rate ,...). The objective of this part is to verify the applicability of the different observer design to real pipeline systems and to identify limits and future work to implement them in an industrial environment.

1.2.2. Specific Objectives

To achieve the general objective, the following work steps of research, development, and implementation need to be done:

- Comprehensive research on the state of the art regarding model-based leak detection and localization observer design
- Setting up a PDE model describing the physical behavior of the flow and the pressure in water pipes
- Identification of the limitations of the model, especially regarding the friction modeling
- Development, implementation, and testing of the two different model-based observer structures (dynamic and algebraic) providing accurate results w.r.t. the estimation of the leak size and the leak position in a simulation-based environment
- Development, implementation, and testing of the two different model-based observer structures (dynamic and algebraic) providing accurate results w.r.t. the estimation of the leak size and the leak position with real measurement data of the pilot plant at PUCP

- Critical evaluation of the obtained results regarding strength, drawbacks, and limitations of each observer
- Identification of future work and challenges to implement the two different model-based observer types in a real plant.

1.3. Methodology

To reach the general and specific objectives formulated in Section 1.2, a certain methodology to ensure a coherent and well-structured workflow is essential. Therefore, the methodological chronology is organized into three parts that are described subsequently. This methodology will also guide the structure of the present work.

Firstly, the theoretical background of the observer design is described in Chapter 2. Since the observers presented in this work fall into the category of RTTM approaches, i.e., model-based observer design, it is required to investigate on the

- Mathematical PDE model of the water pipe system [44, 21, 27]
- Discretization scheme for the mathematical PDE model to obtain a system of ODEs [45].

The drawn model assumptions are discussed, whereby a particular focus lies on the modeling of the friction losses.

Subsequently, the design of the dynamic and algebraic observer based on the selected pipe model is realized in Chapter 3. The first Section 3.1 of this chapter lays the groundwork for the observer design by introducing a state transformation that decouples leak size and leak position. Subsequently, the design of the dynamic observer, the ABSO is described in Section 3.2 according to the current publications [20, 27, 46]. Then, the design of the algebraic observer is thematized in Section 3.3. Since this part represents a new application of the MFM and develops for the first time an algebraic, MFM-based observer for leak detection and leak localization, several steps have to be realized. At first, it is investigated on the

- Theoretical background of the MFM and its application [47, 41, 48, 49, 50]
- Application of the MFM to estimate source terms in PDEs [42]
- Application of the MFM to estimate states of coupled PDE systems [51].

Hereinafter, the MFM is applied in Section 3.3.2 for estimating the leak size and in Section 3.3.3 for the leak localization. The latter section is divided into two parts. The first part shows that a direct leak localization is not possible and hence, a state estimation performed in Section 3.3.3.2 is required. Throughout these two sections, the challenge of solving the auxiliary problems resulting from the application of the MFM occurs. To this end, the

- Trajectory planning to solve the auxiliary problem resulting from the application of the MFM [52, 42]
- Backstepping methods to stabilize PDE systems [27, 53].

will be reviewed.

The last part of this thesis verifies and validates the presented observers for leak detection and leak localization in simulation as well as for real measurement data obtained from the pilot plant installed at PUCP. The simulation part presented in Chapter 4 is mainly performed using MATLAB/Simulink® and involves the

- Implementation of the discretized mathematical PDE model in MATLAB/Simulink®
- Implementation of the discretized ABSO in MATLAB/Simulink®
- Simulation of the discretized ABSO in MATLAB/Simulink® under different operating conditions
- Generation of the Modulating Functions (MFs) resulting from the auxiliary problems in MATLAB/Simulink®
- Introduction of KPIs to analyze the performance of both observers objectively
- Comparative analysis of the simulation-based results of both approaches.

The second part of the validation of the observer performances involves the application of the derived observer schemes to the pilot plant at PUCP in Chapter 5. The practical fundament of this part was done in previous works [54] where the operation of the pilot plant is explained using the software Studio 5000 Logix Designer® to manipulate the power of the pumps and to log the measurement data of the sensors. Based on this fundament, the first steps thematised in Section 5.1 and Section 5.2 consider the identification and validation of the utilized pipe model. To this end, the following tasks are realized

- Logging of measurement data (flow rate and pressure) under different operating conditions (leak size, leak position, nominal inlet flow)

- Identification of the system parameters in MATLAB/Simulink® based on technical specifications of the pilot plant and the measurement data
- Verification and validation of the mathematical pipe model without and with leakage.

An approach to estimate the friction factor based on flow rate and pressure measurements in steady state is presented. Furthermore, the assumption of friction losses that depend linearly on the flow rate is examined critically, and the model accuracy is compared with a nonlinear pipe model. Finally, the dynamic and algebraic observer are used in Section 5.3 to estimate the leak size and localize the leak position from the logged measurement data. Based on the KPIs introduced in the previous Chapter 4, the performance of both observers is compared regarding the accuracy, the sensitivity, and the calculation time. Limitations and drawbacks of the observers that occur in this real application environment are pointed out and topics for future work are identified. Conclusively, in Chapter 6, the main results of this thesis, as well on a theoretical level as on a more practical level, are summarized, and an outlook for future work is given. In particular, the transfer of the results that are obtained for water pipes, towards the application of the results for oil pipelines is of special interest.

In the following chapter, the first part of the theoretical background of the methodology, that involves the modeling of the pipe system, is presented.

2. System Modeling of Water Pipes

As discussed in the review of the state of the art in Section 1.1, RTTM approaches to leak detection and localization require firstly an appropriate mathematical model of the pipeline system upon which the observer is designed later on. In the context of mathematical modeling of a physical system, an appropriate model is understood as a model that "is not as exact as possible, but as exact as necessary" [55]. For the case of water pipe systems, this principle implies, that the model should represent the main fluid transient phenomena, providing a reasonable compromise between accuracy and simplicity, in particular w.r.t. the subsequent observer design. Thus, this chapter introduces the physical model, that is used subsequently for the leakage detection and localization. Furthermore, the limitations of the model are discussed, while a special focus lies on different approaches to model the effect of friction losses.

2.1. Mathematical Modeling of Fluid Dynamics in Water Pipes

A well established and widely applied approach in the literature to model the fluid dynamics in pipelines is provided by the so-called water hammer equations [56]. The derivation of these equations requires some assumptions on the fluid characteristics that are summarized as follows:

- **Assumption 1**: the pipeline is completely filled with liquid [57].
- **Assumption 2**: the cross-section area of the pipeline does not vary over the pipe length and is independent of the pressure [57].
- **Assumption 3**: an average fluid speed is used for calculations, while changes in the fluid speed distribution are neglected [57].
- **Assumption 4**: effects of heat exchange between fluid, pipe wall, fluid, and environment are not taken into account [57].
- **Assumption 5**: temperature effects are not considered, i.e., fundamental physical fluid characteristics like density, viscosity are assumed to be constant.

- **Assumption 6**: the fluid is regarded as incompressible [56].
- **Assumption 7**: the fluid flow is treated as single-phase, i.e., commixtures of different fluids or fluid phases over the pipe length are not considered.
- **Assumption 8**: one-dimensional nonsteady dynamic flow is considered, i.e., the physical states depend on time t and horizontal position z [56].

Based on these assumptions, the application of the mass and momentum balance leads to a hyperbolic PDE system of two coupled PDEs representing the water hammer equations [56][1]:

$$\Sigma_{\text{WH, nom}} : \begin{cases} \frac{\partial p}{\partial t}(z,t) &= -\frac{\beta}{A}\frac{\partial q}{\partial z}(z,t) \\ \frac{\partial q}{\partial t}(z,t) &= -\frac{A}{\rho}\frac{\partial p}{\partial z}(z,t) - A\, g\, \sin(\theta(z)) \\ & \quad -A\, J(q(z,t)) \\ q(0,t) &= q_0(t),\ p(\ell,t) = p_\ell(t). \end{cases} \tag{2.1}$$

where z represents the one-dimensional spatial coordinate $[\mathrm{m}] \in [0, \ell]$, ℓ is the length $[\mathrm{m}]$ of the pipe, t is the time $[\mathrm{s}]$, $q(z,t)$ denotes the volumetric fluid flow rate $[\frac{\mathrm{m}^3}{\mathrm{s}}]$, $p(z,t)$ is the fluid pressure $[\mathrm{Pa}]$, β is the bulk modulus $[\mathrm{Pa}]$ describing the compressibility of the fluid, A is the cross-sectional area $[\mathrm{m}^2]$ of the pipe, ρ is the density $[\frac{\mathrm{kg}}{\mathrm{m}^3}]$ of the fluid, $\theta(z)$ is the inclination angle $[\mathrm{rad}]$ of the pipe, g is the gravity acceleration $[\frac{\mathrm{m}}{\mathrm{s}^2}]$ and $J(q(z,t))$ represents the friction losses $[\frac{\mathrm{m}}{\mathrm{s}^2}]$ that depend on the flow rate and affect the fluid dynamics by causing a negative pressure gradient from the inlet to the outlet of the pipe. The boundary conditions of the system are given by the inlet flow rate $q_0(t)$ and the outlet pressure $p_\ell(t)$.

The system $\Sigma_{\text{WH,nom}}$ represents the nominal case without leakage. To include the effect of a leakage on the fluid dynamics, the following assumptions are made:

- **Assumption 9**: the total leak size $\chi[\frac{\mathrm{m}^3}{\mathrm{s}}]$ is non-negative and constant over the pipeline [46].
- **Assumption 10**: the distribution of the total leak size χ over the pipe is described by a normalized non-negative leakage distribution function $d : [0, \ell] \to \mathbb{R}_{\geq 0}, \int_0^\ell d(z)\mathrm{d}z = 1$ [46].

Especially, the assumption of a constant leakage size differs significantly from other literature (e.g. [56]) where a transient leak size depending on the nominal flow rate is assumed. Therefore, in Chapter 5 it is analyzed based on measurement data from the pilot plant if the fluid flow rate

[1] In [56], the water hammer equations are occasionally given w.r.t. the pressure head $H(z,t) = \frac{p(z,t)}{\rho g}$. Nevertheless, throughout this thesis the representation of the system in the system states pressure $p(z,t)$ and flow $q(z,t)$ is preferred due to its simpler physical interpretation.

passing through the leak reaches a constant value.

According to [46], the pipe model in the case with leakage reads finally

$$\Sigma_{\text{WH, leak}}: \begin{cases} \frac{\partial p}{\partial t}(z,t) &= -\frac{\beta}{A}\frac{\partial q}{\partial z}(z,t) - \frac{\beta}{A}\chi \\ \frac{\partial q}{\partial t}(z,t) &= -\frac{A}{\rho}\frac{\partial p}{\partial z}(z,t) - A\, g\, \sin(\theta(z)) - \frac{\eta}{A} d(z)\chi \\ & \quad -A\, J(q(z,t)) \\ q(0,t) &= q_0(t),\ p(\ell,t) = p_\ell(t) \end{cases} \tag{2.2}$$

where the effect of the leakage on the mass balance is included straightforwardly while the effect on the momentum balance requires an additional constant parameter $\eta[\frac{\mathsf{m}^3}{\mathsf{s}}]$ describing the geometrical characteristics of the leak like shape, size, and orientation [46]. In [58], it is stated that a reasonable parametrization of η is given by $\eta = c\, q_0$ where q_0 is the average flow rate through the pipe and the factor c is identified experimentally by $c \approx 0.8$ for point leakages [58]. Summarizing the modeling of the fluid dynamics in the pipe, Figure 2.1 illustrates the examined pipe system schematically, including the inlet and outlet flow rates and pressures, the geometrical parameters of the pipe, the fluid parameters, the leak characteristics and the leak position z^*.

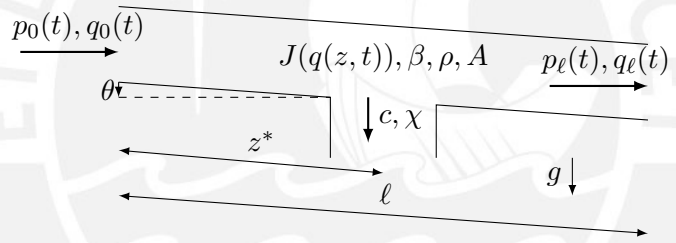

Figure 2.1.: Schematic illustration of the pipe system

To complete the modeling of the fluid dynamics within the pipe, an appropriate description of the friction losses $J(q(z,t))$ has to be found. Thus, the following Section 2.1.1 introduces two different approaches to model the friction losses.

2.1.1. Modeling of Friction Losses

The relative movement between different fluid layers as well as the friction between the fluid and the pipe wall lead to a pressure gradient from the inlet to the outlet. The form and the slope of this gradient depend strongly on the characteristics of the fluid motion (laminar or turbulent) and the pipe wall geometry (roughness, material, ...) [59]. Since the friction losses play an import role in fluid dynamics modeling, and e.g. several leakage localization approaches base on the form of the pressure drop caused by the friction losses and the leakage [19], an appropriate modeling of the

friction losses is essential. In the following, two different friction loss models are presented, a linear approach and a nonlinear approach. The system identification and parametrization of these two models will be discussed in Section 5.1 based on measurement data from the pilot plant installed at PUCP.

2.1.1.1. Linear Friction Modeling

For laminar flow or an analysis near to an operating point where the flow rate $q(z,t) \approx q_{0,\infty} = const.$ is approximately constant, the friction losses can be assumed to depend linearly on the flow rate $q_{0,\infty}$ [44] and are calculated as

$$J(q(z,t)) = \frac{F}{\rho\, A} q(z,t) \tag{2.3}$$

where F denotes the linear friction factor $[\frac{\mathsf{kg}}{\mathsf{m}^3\mathsf{s}}]$. Inserting the linear friction loss model (2.3) into the water hammer equations (2.2) leads to a coupled, linear, hyperbolic PDE system:

$$\Sigma_{\mathsf{WH_{lin},leak}} : \begin{cases} \frac{\partial p}{\partial t}(z,t) &= -\frac{\beta}{A}\frac{\partial q}{\partial z}(z,t) - \frac{\beta}{A}\chi \\ \frac{\partial q}{\partial t}(z,t) &= -\frac{A}{\rho}\frac{\partial p}{\partial z}(z,t) - A\, g\, \sin(\theta(z)) - \frac{\eta}{A} d(z)\chi \\ & \quad -\frac{F}{\rho} q(z,t) \\ q(0,t) &= q_0(t),\ p(\ell,t) = p_\ell(t) \end{cases} . \tag{2.4}$$

Remark 1. *For reasons of simplicity in the derivation of the algebraic observer, the matrix form of the linear system $\Sigma_{WH_{lin},leak}$ is introduced:*

$$\Sigma_{WH_{lin},leak} : \begin{cases} \begin{bmatrix} \dot{p}(z,t) \\ \dot{q}(z,t) \end{bmatrix} = \underbrace{\begin{bmatrix} 0 & -\frac{\beta}{A} \\ -\frac{A}{\rho} & 0 \end{bmatrix}}_{:=\Lambda} \begin{bmatrix} p'(z,t) \\ q'(z,t) \end{bmatrix} + \underbrace{\begin{bmatrix} 0 & 0 \\ 0 & -\frac{F}{\rho} \end{bmatrix}}_{:=\Sigma} \begin{bmatrix} p(z,t) \\ q(z,t) \end{bmatrix} \\ \qquad\qquad + \underbrace{\begin{bmatrix} 0 \\ -Ag\sin(\theta(z)) \end{bmatrix}}_{:=\Theta(z)} + \underbrace{\begin{bmatrix} -\frac{\beta}{A}\chi \\ -\frac{\eta}{A}\chi \end{bmatrix}}_{:=\mathcal{X}} d(z) \\ \begin{bmatrix} p(\ell,t) \\ q(0,t) \end{bmatrix} = \begin{bmatrix} p_\ell(t) \\ q_0(t) \end{bmatrix} \end{cases} \tag{2.5}$$

where the temporal derivatives are abbreviated by $\dot{p}(z,t) := \frac{\partial}{\partial t} p(z,t)$ and the spatial derivatives are denoted by $p'(z,t) := \frac{\partial}{\partial z} p(z,t)$.

Since the linear PDE model facilitates the observer design and the stability analysis of the observer structure, the main focus of this thesis lies on the leak detection and localization based on the linear pipe system (2.4). The assumption of a linear friction loss is analyzed critically in Chapter 5 using real data from a pilot plant installed at PUCP. In the following, a nonlinear friction model is introduced to compare and to validate the linear PDE model, as well as to evaluate the limitations of the linear PDE model.

2.1.1.2. Nonlinear Friction Modeling

To border a wider class of fluid flow operating conditions, nonlinear friction losses are introduced. The nonlinear friction loss model is valid for turbulent, non-steady flow and is described by [56]

$$J(q(z,t)) = f_d \frac{|q(z,t)|q(z,t)}{2\ d\ A^2} \tag{2.6}$$

where d denotes the pipe diameter [m] and f_d is the Darcy-Weisbach friction coefficient $[-]$. This friction coefficient depends on the fluid dynamics as well as the pipe wall roughness and can be calculated via the widely used Darcy-Colebrook Equation [60]:

$$\frac{1}{\sqrt{f_d}} = -2\log\left(\frac{\epsilon_p}{3.7\ d} + \frac{2.51}{Re\sqrt{f_d}}\right) \tag{2.7}$$

where ϵ_p corresponds to the pipe surface roughness $[m]$ and Re to the Reynolds number $[-]$ calculated by

$$Re = \frac{4\rho\ q}{\pi\ d\ \eta_v} \tag{2.8}$$

where q corresponds to the current flow rate $[\frac{\mathsf{m}^3}{\mathsf{s}}]$ and η_v to the dynamical viscosity $[\frac{\mathsf{kg}}{\mathsf{ms}}]$ of the fluid. Since the Equation (2.7) is implicit in f_d, an approximation is needed for observer design and implementation purposes. An accurate and common approximation in literature [61] is given by the Haaland equation [62]

$$\frac{1}{\sqrt{f_d}} = -1.8\log_{10}\left(\left(\frac{\epsilon_p}{3.7\ d}\right)^{1.11} + \frac{6.9}{Re}\right). \tag{2.9}$$

Inserting the nonlinear friction loss model (2.6) with (2.9) into the water hammer equations (2.2) leads to the highly nonlinear PDE model

$$\Sigma_{\mathsf{WH_{nl},leak}}: \begin{cases} \frac{\partial p}{\partial t}(z,t) &= -\frac{\beta}{A}\frac{\partial q}{\partial z}(z,t) - \frac{\beta}{A}\chi \\ \frac{\partial q}{\partial t}(z,t) &= -\frac{A}{\rho}\frac{\partial p}{\partial z}(z,t) \; - A\; g\; \mathsf{sin}(\theta(z)) \; - \frac{\eta}{A} d(z)\chi \\ & \quad -f_d \frac{|q(z,t)|q(z,t)}{2\; d\; A} \\ q(0,t) &= q_0(t),\; p(\ell,t) = p_\ell(t) \end{cases} \tag{2.10}$$

since the friction term $J(q(z,t))$ as well as the calculation of the friction factor f_d depend nonlinear on the flow rate $q(z,t)$. Hence, in Chapter 5 the linear and the nonlinear pipe model are validated using real data to analyze whether the nonlinear model provides a more accurate representation of the fluid dynamics what would justify the more complex structure of the friction loss calculations.

Furthermore, it is noted that non-stationary friction losses that depend on the spatial and temporal derivative of the flow rate (see e.g., [56]) are not regarded in this thesis, since former investigations in other literature concluded, that the modeling of non-stationary friction losses only leads to a more complex model without improving the results of the leak detection and localization [63]. The following Chapter 3 presents the theoretical core of this thesis, the dynamic and algebraic observer design to detect and locate leakage in water pipes based on the linear pipe model (2.4).

3. Observer Design

This chapter forms the theoretical fundament of the thesis. Two different approaches to design an observer to detect and localize leakage in pipe systems are examined: a dynamic observer scheme and an algebraic observer scheme. Both observers have the same basic structure that is illustrated in Figure 3.1.

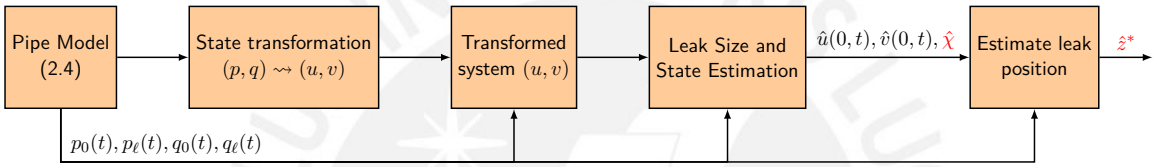

Figure 3.1.: Schematic illustration of the general structure of the proposed algebraic and dynamic leak detection and localization observers.

Despite the differences in the design of the observer schemes, both approaches share a common starting point. Since the leak size χ and the leak distribution $d(\cdot)$ appear as a product in both equations of the physical pipe model (2.4), a state transformation is sought to decouple both variables and to permit designing the estimate schemes for both variables separately. Based on this decoupling, that results in a transformed, hyperbolic PDE system with dimensionless states $u(x,t), v(x,t)$, the dynamical as well as the algebraic observer estimate first the leak size χ and the states of the transformed system. Based on this first estimation step, the leak location is estimated utilizing the estimate $\hat{\chi}$ of the leak size and the estimates of the boundary states $\hat{u}(0,t)$ and $\hat{v}(0,t)$ of the transformed system. The transformed system is completely defined by the physical parameters of the pipe model and the boundary measurements of the states of the pipe model. Thus, throughout this thesis, it is assumed that the pressure and the flow rate at the inlet and the outlet of the pipe are known and given by $p(0,t) = p_0(t),\ p(\ell,t) = p_\ell(t),\ q(0,t) = q_0(t)$ and $q(\ell,t) = q_\ell(t)$.

The dynamic observer scheme follows mainly the approach presented in [27] and results in a Luenberger-type observer whose observer gains are derived from a backstepping transformation, i.e. the estimation of the leak size and the state estimation originate from the simulation of a dynamical (PDE) system. Contrary to that, the algebraic observer is derived based on the application of the

MFM and results in an algebraic IO-relation such that the leak size and the states of the transformed system are estimated by solving algebraic equations that are implemented as an FIR filter.

The following section presents the first part of the observer design, the state transformation of the linear pipe model (2.4) to decouple the leak size χ from the leak distribution $d(\cdot)$.

3.1. State Transformation of the Pipe Model

This section presents the state transformation of the linear pipe model (2.4) to decouple the leak size χ and the leak distribution $d(\cdot)$. It is assumed, that the flow and the pressure at the inlet and the outlet of the pipe are known. The transformation results in a 2×2 hyperbolic PDE system, where the leak size χ appears in one of the boundary conditions while the leak distribution $d(\cdot)$ appears only in the state transformation. The following Theorem 3.1.1 states the main result and can be found in [27]:

Theorem 3.1.1 (State transformation of the linear pipe model (2.4))**.** *Assume that the flow and the pressure at the inlet and the outlet of the pipe are known and given by* $p(0,t) = p_0(t),\ p(\ell,t) = p_\ell(t),\ q(0,t) = q_0(t)$ *and* $q(\ell,t) = q_\ell(t)$*. Define the auxiliary variable* $\delta(\cdot)$ *by*

$$\delta(z) := \ell - z - \int_z^\ell \int_0^\eta d(\gamma) d\gamma d\eta \,. \tag{3.1}$$

Then the following invertible state transformation

$$\begin{aligned} u(x,t) = \frac{1}{2} e^{\frac{\ell F}{2\sqrt{\beta\rho}}x} \Bigg(& q(x\ell,t) - q_{in} + \delta'(x\ell)\chi + \frac{A}{\sqrt{\beta\rho}} \Bigg(p(x\ell,t) - p_{out} + \rho g \int_0^{x\ell} \sin(\theta(\gamma)) d\gamma \\ & + \frac{F}{A} q_{in} \ell x + \frac{\rho}{A^2} \eta \delta'(x\ell)\chi - \frac{F}{A}\delta(x\ell)\chi \Bigg) \Bigg) \\ v(x,t) = \frac{1}{2} e^{-\frac{\ell F}{2\sqrt{\beta\rho}}x} \Bigg(& q(x\ell,t) - q_{in} + \delta'(x\ell)\chi - \frac{A}{\sqrt{\beta\rho}} \Bigg(p(x\ell,t) - p_{out} + \rho g \int_0^{x\ell} \sin(\theta(\gamma)) d\gamma \\ & + \frac{F}{A} q_{in} \ell x + \frac{\rho}{A^2} \eta \delta'(x\ell)\chi - \frac{F}{A}\delta(x\ell)\chi \Bigg) \Bigg) \end{aligned} \tag{3.2}$$

for $x = \frac{z}{\ell} \in [0,1]$ transforms the linear pipe model (2.4) *into*

$$\Sigma_{\textit{trafo,lin}} : \begin{cases} \frac{\partial u}{\partial t}(x,t) &= -\epsilon \frac{\partial u}{\partial x}(x,t) + c_1(x)v(x,t) \\ \frac{\partial v}{\partial t}(x,t) &= \epsilon \frac{\partial v}{\partial x}(x,t) \ + c_2(x)u(x,t) \\ u(0,t) &= -v(0,t) + q_0(t) - q_{in} - \chi \\ v(1,t) &= U(t) \end{cases} \tag{3.3}$$

where the parameters of the transformed system (3.3) *are given by*

$$\begin{aligned} \epsilon &= \frac{1}{\ell}\sqrt{\frac{\beta}{\rho}} \\ c_1(x) = -\frac{1}{2}\frac{F}{\rho}e^{\frac{\ell F}{\sqrt{\beta\rho}}x}, \quad c_2(x) &= -\frac{1}{2}\frac{F}{\rho}e^{-\frac{\ell F}{\sqrt{\beta\rho}}x} \\ h &= \int_0^\ell \sin(\theta(\gamma))d\gamma \\ U(t) &= \frac{1}{2}e^{-\frac{\ell F}{2\sqrt{\beta\rho}}}\left(q_\ell(t) - q_{in} - \frac{A}{\sqrt{\beta\rho}}\left(p_\ell(t) - p_{out} + \rho g h + \frac{F\ell}{A}q_{in}\right)\right) \end{aligned}$$

and q_{in} and p_{out} are arbitrary constants that can be chosen such that the origin of the transformed system (3.3) *lies in a desired operating point. The parameter ϵ is the so-called wave or sonic velocity normalized to the length ℓ of the pipe.*

Proof. The inverse of the coordinate transformation (3.2) is given by

$$\begin{aligned} p(z,t) = \frac{\sqrt{\beta\rho}}{A}\left(e^{-\frac{F}{2\sqrt{\beta\rho}}z}u(\frac{z}{\ell},t) - e^{\frac{F}{2\sqrt{\beta\rho}}z}v(\frac{z}{\ell},t)\right) + p_{out} - \rho g\int_0^z \sin(\theta(\gamma))\mathrm{d}\gamma \\ - \frac{F}{A}q_{in}z - \frac{\rho}{A^2}\eta\delta'(z)\chi + \frac{F}{A}\delta(z)\chi \\ q(z,t) = u(\frac{z}{\ell},t)e^{-\frac{F}{2\sqrt{\beta\rho}}z} + v(\frac{z}{\ell},t)e^{\frac{F}{2\sqrt{\beta\rho}}z} + q_{in} - \delta'(z)\chi\,. \end{aligned}$$

With

$$\begin{aligned} \delta(z) &= \ell - z - \int_z^\ell \int_0^\eta d(\gamma)\mathrm{d}\gamma\mathrm{d}\eta \\ \Rightarrow \delta'(z) &= -1 + \int_0^z d(\gamma)\mathrm{d}\gamma \\ \Rightarrow \delta''(z) &= d(z) \end{aligned}$$

and by inserting the inverse coordinate transformation (3.4) into the linear pipe model (2.4) follows

$$\begin{aligned}&\frac{\partial}{\partial t}u(\frac{z}{\ell},t)e^{-\frac{F}{2\sqrt{\beta\rho}}z}-\frac{\partial}{\partial t}v(\frac{z}{\ell},t)e^{\frac{F}{2\sqrt{\beta\rho}}z}\\&=-\epsilon\frac{\partial}{\partial z}u(\frac{z}{\ell},t)e^{-\frac{F}{2\sqrt{\beta\rho}}z}+\frac{F}{2\rho}u(\frac{z}{\ell},t)e^{-\frac{F}{2\sqrt{\beta\rho}}z}-\epsilon\frac{\partial}{\partial z}v(\frac{z}{\ell},t)e^{\frac{F}{2\sqrt{\beta\rho}}z}-\frac{F}{2\rho}u(\frac{z}{\ell},t)e^{\frac{F}{2\sqrt{\beta\rho}}z}\end{aligned}\tag{3.4}$$

and

$$\begin{aligned}&\frac{\partial}{\partial t}u(\frac{z}{\ell},t)e^{-\frac{F}{2\sqrt{\beta\rho}}z}+\frac{\partial}{\partial t}v(\frac{z}{\ell},t)e^{\frac{F}{2\sqrt{\beta\rho}}z}\\&=-\epsilon\frac{\partial}{\partial z}u(\frac{z}{\ell},t)e^{-\frac{F}{2\sqrt{\beta\rho}}z}-\frac{F}{2\rho}u(\frac{z}{\ell},t)e^{-\frac{F}{2\sqrt{\beta\rho}}z}+\epsilon\frac{\partial}{\partial z}v(\frac{z}{\ell},t)e^{\frac{F}{2\sqrt{\beta\rho}}z}-\frac{F}{2\rho}u(\frac{z}{\ell},t)e^{\frac{F}{2\sqrt{\beta\rho}}z}.\end{aligned}\tag{3.5}$$

Adding of both Equations (3.4) and (3.5) leads to

$$\frac{\partial u}{\partial t}(x,t)=-\epsilon\frac{\partial u}{\partial x}(x,t)+c_1(x)v(x,t)\tag{3.6}$$

while subtracting Equation (3.4) from Equation (3.5) results in

$$\frac{\partial v}{\partial t}(x,t)=\epsilon\frac{\partial v}{\partial x}(x,t)+c_2(x)u(x,t)\,.\tag{3.7}$$

Finally, inserting the inverse transformation (3.2) into the boundary conditions of the linear pipe model (2.4) with $\delta'(0)=-1$ gives

$$\begin{aligned}u(0,t)&=-v(0,t)+q_0(t)-q_{in}-\chi\\v(1,t)&=\frac{1}{2}e^{-\frac{\ell F}{2\sqrt{\beta\rho}}}\left(q_\ell(t)-q_{in}-\frac{A}{\sqrt{\beta\rho}}\left(p_\ell(t)-p_{out}+\rho gh+\frac{F\ell}{A}q_{in}\right)\right)\\h&=\int_0^\ell\sin(\theta(\gamma))\mathsf{d}\gamma\end{aligned}$$

what completes the proof of the statement of the Theorem 3.1.1. □

Remark 2. *The transformation* (3.2) *can be understood as the composition of two transformations. Firstly, the linear pipe model* (2.4) *is diagonalized regarding the spatial derivative* $\frac{\partial}{\partial z}$*, i.e. a coordinate transformation* $\begin{bmatrix}\bar{p}(z,t)\\\bar{q}(z,t)\end{bmatrix}=V\begin{bmatrix}p(z,t)\\q(z,t)\end{bmatrix}$ *is applied such that* $V^{-1}\begin{bmatrix}0&\frac{-\beta}{A}\\-\frac{A}{\rho}&0\end{bmatrix}V$ *is diagonal. Afterwards, a second transformation is applied that removes the constant terms as well as the diagonal terms in* $V^{-1}\begin{bmatrix}0&0\\0&-\frac{F}{\rho}\end{bmatrix}$ *[26].*

Remark 3. *For reasons of simplicity in the derivation of the algebraic observer, the matrix form of the transformed system $\Sigma_{trafo,lin}$ is introduced:*

$$\Sigma_{trafo,\ lin}: \begin{cases} \begin{bmatrix} \dot{u}(x,t) \\ \dot{v}(x,t) \end{bmatrix} = \underbrace{\begin{bmatrix} -\epsilon & 0 \\ 0 & \epsilon \end{bmatrix}}_{:=\Lambda_\chi} \begin{bmatrix} u'(x,t) \\ v'(x,t) \end{bmatrix} + \underbrace{\begin{bmatrix} 0 & c_1(x) \\ c_2(x) & 0 \end{bmatrix}}_{:=\Sigma_\chi(x)} \begin{bmatrix} u(x,t) \\ v(x,t) \end{bmatrix} \\ \begin{bmatrix} u(0,t) \\ v(1,t) \end{bmatrix} = \begin{bmatrix} -v(0,t) + q_0(t) - q_{in} - \chi \\ U(t) \end{bmatrix} \end{cases} \tag{3.8}$$

where the temporal derivatives are abbreviated by $\dot{u}(x,t) := \frac{\partial}{\partial t} u(x,t)$ and the spatial derivatives are denoted by $u'(x,t) := \frac{\partial}{\partial x} u(x,t)$

The state transformation (3.2) accomplishes the decoupling of the leak size χ and the leak distribution $d(\cdot)$. Since the transformed system (3.3) is independent of the leak distribution $d(\cdot)$, the leak size χ can be estimated firstly. Thereby, the significance of the estimation of the leak size is twofold. On the one hand, the estimated leak size allows to provide a reasonable leak detection signal by comparing the estimated leak size to a threshold, that is defined e.g., by analysing the measurement noise level of the sensors. If the estimated leak size is higher than this threshold, the leak detection alarm is triggered. On the other hand, the estimation of the leak size is required to localize the leak. In the following section, the design of a dynamic observer as proposed in [27] to estimate and localize the leak is presented.

3.2. Dynamic Observer Design

This section is dedicated to the design of a dynamic observer to estimate firstly the leak size and secondly the leak localization. The design of the observer is proposed in [27] and has a Luenberger-type observer structure based on the transformed system (3.3). In contrast to KF-type approaches (see e.g. [24]), the observer design does not require a spatial discretization of the physical model (2.4) but develops the observer structure directly on the physical PDE model (2.4) and the transformed model (3.3). Moreover, the injection gains of the observer errors are not chosen heuristically but derived from a backstepping transformation of the transformed system (3.3). Thereby, the exponential stability of the observer error is proven. In the following, the main results of [27] are summarized to enable the implementation in a simulative environment and to test the performance of the dynamic observer under various operating conditions. The observer

design is performed for the linear pipe model (2.4). A still unpublished extension of the dynamic observer to the nonlinear pipe model (2.10) can be found in [64].

3.2.1. Leak Size Estimation and State Estimation

To estimate the leak size and the states of the transformed system (3.3), the following observer structure is proposed [27]:

$$\Sigma_{\text{obs},\chi}: \begin{cases} \frac{\partial \hat{u}}{\partial t}(x,t) &= -\epsilon \frac{\partial \hat{u}}{\partial x}(x,t) + c_1(x)\hat{v}(x,t) + p_1(x)\left(Y(1,t) - \hat{u}(1,t)\right) \\ \frac{\partial \hat{v}}{\partial t}(x,t) &= \epsilon \frac{\partial \hat{v}}{\partial x}(x,t) + c_2(x)\hat{u}(x,t) + p_2(x)\left(Y(1,t) - \hat{u}(1,t)\right) \\ \hat{u}(0,t) &= -\hat{v}(0,t) + q_0(t) - q_{in} - \hat{\chi}(t) \\ \hat{v}(1,t) &= U(t) \\ \dot{\hat{\chi}}(t) &= L\left(Y(1,t) - \hat{u}(1,t)\right) \end{cases} \tag{3.9}$$

where the output injection $Y(1,t)$ is calculated by the parameters of the model and the available measurements of the flow rate and the pressure at the outlet:

$$Y(1,t) = u(1,t) = \frac{1}{2} e^{\frac{lF}{2\sqrt{\beta\rho}}} \left(q_\ell(t) - q_{in} + \frac{A}{\sqrt{\beta\rho}} \left(p_\ell(t) - p_{in} + \rho g h \frac{F\ell}{A} q_{in} \right) \right). \tag{3.10}$$

The observer system (3.9) is a copy of the transformed model (3.3) with an additional injection of the output error $Y(1,t) - \hat{u}(1,t)$ where the output injection gains are given by the spatial functions $p_1 : [0,1] \to \mathbb{R},\ p_2 : [0,1] \to \mathbb{R}$ and the constant $L \in \mathbb{R}$. By introducing the observer state estimation errors $\tilde{u}(x,t) := u(x,t) - \hat{u}(x,t), \tilde{v}(x,t) := v(x,t) - \hat{v}(x,t)$ and $\tilde{\chi}(t) := \chi - \hat{\chi}(t)$ and subtracting the observer system (3.9) from the transformed system (3.3), the following observer error system is obtained:

$$\Sigma_{\text{obs},\chi}: \begin{cases} \frac{\partial \tilde{u}}{\partial t}(x,t) &= -\epsilon \frac{\partial \tilde{u}}{\partial x}(x,t) + c_1(x)\tilde{v}(x,t) + -p_1(x)\tilde{u}(1,t) \\ \frac{\partial \tilde{v}}{\partial t}(x,t) &= \epsilon \frac{\partial \tilde{v}}{\partial x}(x,t) + c_2(x)\tilde{u}(x,t) + -p_2(x)\tilde{u}(1,t) \\ \tilde{u}(0,t) &= -\tilde{v}(0,t) - \tilde{\chi}(t) \\ \tilde{v}(1,t) &= 0 \\ \dot{\tilde{\chi}}(t) &= -L\tilde{u}(1,t) \end{cases} . \tag{3.11}$$

The following two theorems summarize the stability analysis performed in [27] and indicate how the output injection gains $p_1(\cdot), p_2(\cdot)$ and L have to be chosen to guarantee asymptotic stability

of the origin of the observer error system (3.11).

Theorem 3.2.1 (Asymptotic stability of the ABSO [27])**.** *Consider the backstepping transformation [53]*

$$\begin{aligned}\tilde{u}(x,t) &= \tilde{\alpha}(x,t) - \int_x^1 P^{uu}(x,\xi)\tilde{\alpha}(\xi,t)d\xi - \int_x^1 P^{uv}(x,\xi)\tilde{\beta}(\xi,t)d\xi\tilde{v}(x,t) \\ &= \tilde{\beta}(x,t) - \int_x^1 P^{vu}(x,\xi)\tilde{\alpha}(\xi,t)d\xi - \int_x^1 P^{vv}(x,\xi)\tilde{\beta}(\xi,t)d\xi\end{aligned} \tag{3.12}$$

on the domain $\mathbb{T}_o := \{(x,\xi) : 0 \leq x \leq \xi \leq 1\}$ *where the kernels are defined as the solution of the following PDE system:*

$$\Sigma_{bs}: \begin{cases} \epsilon\frac{\partial P^{uu}}{\partial x}(x,\xi) + \epsilon\frac{\partial P^{uu}}{\partial \xi}(x,\xi) &= c_1(x)P^{vu}(x,\xi) \\ \epsilon\frac{\partial P^{uv}}{\partial x}(x,\xi) - \epsilon\frac{\partial P^{uv}}{\partial \xi}(x,\xi) &= c_1(x)P^{vv}(x,\xi) \\ \epsilon\frac{\partial P^{vu}}{\partial x}(x,\xi) - \epsilon\frac{\partial P^{vu}}{\partial \xi}(x,\xi) &= -c_2(x)P^{uu}(x,\xi) \\ \epsilon\frac{\partial P^{vv}}{\partial x}(x,\xi) + \epsilon\frac{\partial P^{vv}}{\partial \xi}(x,\xi) &= -c_2(x)P^{uv}(x,\xi) \\ P^{uu}(0,\xi) &= -P^{vu}(0,\xi) \\ P^{uv}(x,x) &= \frac{c_1(x)}{2\epsilon} \\ P^{vu}(x,x) &= -\frac{c_2(x)}{2\epsilon} \\ P^{vv}(0,\xi) &= -P^{uv}(0,\xi) \end{cases}. \tag{3.13}$$

Then, the following statements hold true:
(i) The backstepping transformation (3.12) *is invertible, has a unique solution and transforms the system*

$$\Sigma_{bs}: \begin{cases} \frac{\partial\tilde{\alpha}}{\partial t}(x,t) &= -\epsilon\frac{\partial\tilde{\alpha}}{\partial x}(x,t) + L\tilde{\alpha}(1,t) \\ \frac{\partial\tilde{\beta}}{\partial t}(x,t) &= \epsilon\frac{\partial\tilde{\beta}}{\partial x}(x,t) \\ \tilde{\alpha}(0,t) &= -\tilde{\beta}(0,t) - \tilde{X}(t) \\ \tilde{\beta}(1,t) &= 0 \\ \dot{\tilde{X}}(t) &= -L\tilde{\alpha}(1,t) \end{cases} \tag{3.14}$$

into the observer error system (3.11) *where the spatial functions* $p_1(\cdot),\ p_2(\cdot)$ *are given by*

$$p_1(x) = -L - \epsilon P^{uu}(x,1) + L\int_x^1 P^{uu}(x,\xi)d\xi p_2(x) \quad = -\epsilon P^{vu}(x,1) + L\int_x^1 P^{vu}(x,\xi)d\xi \tag{3.15}$$

(ii) Let $L < 0$. Then, the origin of (3.14) *is exponentially stable in the norm*

$$\left(\tilde{X}(t)|^2 + \int_0^1 \tilde{\alpha}(x,t)dx\right)^{\frac{1}{2}}.$$

(iii) Let $L < 0$. Then, the origin of (3.14) *is exponentially stable in the norm*

$$||(\tilde{\chi},\tilde{u},\tilde{v}||^2 := |\tilde{\chi}(t)|^2 + \int_0^1 \left(\tilde{u}^2(x,t) + \tilde{v}^2(x,t)\right) dx \tag{3.16}$$

and $\lim_{t\to\infty} \tilde{u}(0,t) = 0, \lim_{t\to\infty} \tilde{v}(0,t) = 0.$

Proof. (i) see [53].
(ii) see [27, Lemma 2, Lemma 3, Lemma 5 and Remark 4]. □

The output injection gains $p_1(\cdot), p_2(\cdot)$ are calculated analytically by solving the backstepping kernel Equations (3.13) as the following theorem indicates.

Theorem 3.2.2 (Calculation of the observer gains of the ABSO [27])**.** *Consider the observer error system* (3.11)*. Let $L < 0$ and let the output injection gains $p_1(\cdot), p_2(\cdot)$ be given by*

$$\begin{aligned}
p_1(x) &= -L - \frac{1}{2}e^{\frac{c}{\epsilon}(1-x)}\left(cI_0\left(\frac{|c|}{\epsilon}\sqrt{1-x^2}\right) - |c|\sqrt{\frac{1+x}{1-x}}I_1\left(\frac{|c|}{\epsilon}\sqrt{1-x^2}\right)\right) \\
&\quad + \frac{L}{2\epsilon}\int_x^1 e^{\frac{c}{\epsilon}(\xi-x)}\left(cI_0\left(\frac{|c|}{\epsilon}\sqrt{\xi^2-x^2}\right) - |c|\sqrt{\frac{\xi+x}{\xi-x}}I_1\left(\frac{\|c|}{\epsilon}\sqrt{\xi^2-x^2}\right)\right) d\xi \\
p_2(x) &= \frac{1}{2}e^{\frac{c}{\epsilon}(1+x)}\left(cI_0\left(\frac{|c|}{\epsilon}\sqrt{1-x^2}\right) - |c|\sqrt{\frac{1-x}{1+x}}I_1\left(\frac{|c|}{\epsilon}\sqrt{1-x^2}\right)\right) \\
&\quad - \frac{L}{2\epsilon}\int_x^1 e^{\frac{c}{\epsilon}(\xi+x)}\left(cI_0\left(\frac{|c|}{\epsilon}\sqrt{\xi^2-x^2}\right) - |c|\sqrt{\frac{\xi-x}{\xi+x}}I_1\left(\frac{|c|}{\epsilon}\sqrt{\xi^2-x^2}\right)\right) d\xi
\end{aligned} \tag{3.17}$$

where $c = c_1(0) = -\frac{F}{2\rho}$ and I_n refers to the modified Bessel function of the first kind of order n. Then the origin of the observer error system (3.11) *is exponentially stable in the norm*

$$||(\tilde{\chi},\tilde{u},\tilde{v})||^2 := |\tilde{\chi}(t)|^2 + \int_0^1 \left(\tilde{u}^2(x,t) + \tilde{v}^2(x,t)\right) dx \tag{3.18}$$

and $\lim_{t\to\infty} \tilde{u}(0,t) = 0, \lim_{t\to\infty} \tilde{v}(0,t) = 0.$

Proof. see [27, Theorem 8]. □

Consequently, the observer system (3.9) enables leak detection and leak size estimation independently of the leak location and the leak distribution. The following paragraph describes how the leak location is estimated based on the estimation of the leak size and the observer states $\hat{u}(\cdot,\cdot)$ and $\hat{v}(\cdot,\cdot)$.

3.2.2. Leak Localization

To estimate the leak location, the leak distribution function $d(\cdot)$ is not estimated directly. Instead, an observer is designed who estimates the value of the auxiliary variable $\delta(\cdot)$ defined by Equation(3.1)) in $z = 0$ by using the difference between the estimate $\hat{p}_0$ of the inlet pressure and the actual inlet pressure p_0 as error input. The following theorem states the main result:

Theorem 3.2.3 (Leak localization with ABSO [27])**.** *Consider the linear pipe model* (2.4) *with* $F > 0$ *and suppose that a leak occurs, i.e.* $\chi > 0$*. Define the leak localization observer by*

$$\Sigma_{obs,\delta}: \begin{cases} \hat{p}_0(t) & = \frac{\sqrt{\beta\rho}}{A}\left(\hat{u}(0,t) - \hat{v}(0,t)\right) + p_{out} + \frac{\rho}{A^2}\eta\hat{\chi} + \frac{F}{A}\hat{\delta}(t)\hat{\chi}(t) \\ \dot{\hat{\delta}} & = \underset{[0,\ell]}{proj}\{\gamma\left(p_0(t) - \hat{p}_0(t)\right)\} \end{cases} \tag{3.19}$$

with the leak localization observer gain $\gamma > 0$*. The projection operator* $proj(\cdot)$ *respects the physical constraint, that the leak position* z^* *has to be between* $z = 0$ *and* $z = \ell$ *and is defined by*

$$\underset{[0,\ell]}{proj}: \mathbb{R}\times\mathbb{R} \to [0,\ell], \quad \underset{[0,\ell]}{proj}(\hat{\delta}, \gamma(p_0 - \hat{p}_0)) := \begin{cases} 0, & \hat{\delta}(t) = 0 \text{ and } \gamma\left(p_0(t) - \hat{p}_0(t)\right) < 0 \\ \ell, & \hat{\delta}(t) = \ell \text{ and } \gamma\left(p_0(t) - \hat{p}_0(t)\right) > 0 \\ \gamma\left(p_0(t) - \hat{p}_0(t)\right), & \text{else} \end{cases} \tag{3.20}$$

. Then $\lim_{t\to\infty} \hat{\delta}(t) = \delta(0)$ *.*

Proof. see [27, Theorem 10]. □

Remark 4. *To improve the robustness of the leak position estimation against measurement noise and in order to be able to adjust the convergence behavior by the tuning parameter* γ*, the leak position is not estimated from resolving the first part Equation* (3.19) *directly for the unknown* $\hat{\delta}$ *by means of the known measurement inlet pressure* $p_0(t)$*, but a dynamic error feedback is utilized. This dynamic error feedback can be regarded as a simplified version of time-continuous Recursive Least Squares Algorithm (see the classical EKF [65] without dynamic part, i.e.* $\dot{x} = 0$*). In that*

sense, in the leak localization observer system (3.19) *the Kalman gain is not dynamically updated in every time step by estimating the error covariance, but the gain is chosen as a constant.*

Remark 5. *The convergence speed of the estimation of the leak position using leak localization observer system* (3.19) *depends linearly on the friction factor F, the observer gain γ and the leak size χ (see [27, Remark 11].*

However, the relationship between $\delta(z = 0)$ and the leak distribution function $d(\cdot)$ is not unique, as the definition of the auxiliary variable $\delta(\cdot)$ in Equation (3.1) reveals. Therefore, additional knowledge about the characteristics of the leak distribution is needed to estimate the leak location. The following corollary shows how the leak location can be calculated in the case of point leaks. For further leak distribution functions, the interested reader is referred to Appendix A.1.

Corollary 3.2.3.1. *(i) Consider the linear pipe model* (2.4) *with a point leak located at $z = z^* \in (0, \ell)$ of size $\chi > 0$, i.e. $d(\cdot)$ is a Dirac-Impulse located at z^*. Then, $\delta(0) = z^*$ and with Theorem 3.2.3 follows $\lim_{t\to\infty} \hat{\delta}(t) = \delta(0) = z^*$.*
(ii) Consider the linear pipe model (2.4) *with two point leaks located at $z_1 = z_1^* \in (0, \ell)$ and $z_2 = z_2^* \in (0, \ell)$ of size $\chi_1 > 0$ and $\chi_2 > 0$, respectively, i.e. $d(\cdot)$ is given by two Dirac-Impulses located at z_1^* and z_2^* with amplitude each $\frac{1}{2}$. Then,*

$$\lim_{t\to\infty} \hat{\delta}(t) = \frac{\chi_1}{\chi_1 + \chi_2} z_1^* + \frac{\chi_2}{\chi_1 + \chi_2} z_2^* . \tag{3.21}$$

Proof. see [27][Corollary 12, Corollary 13] □

Finally, Figure 3.2 summarizes illustratively the structure of the proposed dynamic ABSO and specifies thereby the general observer structure presented in Figure 3.1. The leak size and state estimation is realized by the observer system $\Sigma_{\text{obs},\chi}$. The second observer system $\Sigma_{\text{obs},\delta}$ utilizes this estimates to localize the leak. The parts that can be solved offline are marked in green, while the observer parts that have to be implemented in real-time are coloured in red. Furthermore, the design parameters L and γ are highlighted in purple. Firstly, the measurements of the inlet and outlet flow as well as the outlet pressure are required to estimate the leak size based on the leak size and state observer $\Sigma_{\text{obs},\chi}$. To this end, the observer gain $L < 0$ is a free design parameter, while the observer gains $p_1(\cdot), p_2(\cdot)$ are calculated offline directly from the physical parameters. The leak size estimate $\hat{\chi}(t)$ and the estimations $\hat{u}(x,t), \hat{v}(x,t)$ of the transformed states $u(x,t), v(x,t)$ permit the estimation of the leak localization by means of the observer system $\Sigma_{\text{obs},\delta}$. Therefore, the measurement of the inlet pressure is needed while the observer gain γ is a design parameter that has to be positive. Since the leak size estimation according to $\Sigma_{\text{obs},\chi}$ is realized in a decoupled

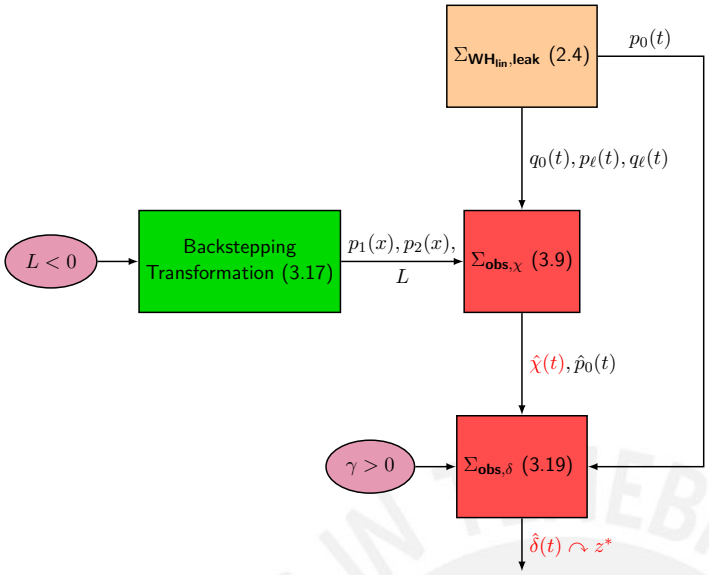

Figure 3.2.: Schematic illustration of the structure of the ABSO according to Equation (3.9) and Equation (3.19) based on the linear pipe model (2.4).

way from the leak localization $\Sigma_{\text{obs},\delta}$, the tuning of the free design parameters L and γ is done quite straightforward. Firstly, the observer gain L is tuned such that the estimation of the leak size provides an acceptable balance between accuracy of the estimation, convergence speed and robustness to measurement noise. Once the observer gain L is fixed, the remaining design parameter γ is tuned in the same way.

The proposed dynamic observer structure represented by the ABSO provides a theoretically well-founded, model-based, late lumping approach to the leak size estimation and localization problem for water pipes, including a rigorous stability proof of the observer error. However, since the ABSO is a dynamic observer, the implementation requires the online execution of the PDE system $\Sigma_{\text{obs},\chi}$. Depending on the applied discretization method and its order, this execution of the dynamic observer in real time can be linked with high computational costs. Therefore, the following Section 3.3 derives an alternative observer algorithm based on the MFM, that only needs the online solution of algebraic equations that can be implemented as an FIR filter.

3.3. Algebraic Observer Design with Modulating Functions

This section presents the design of an algebraic observer to estimate the leak size and locate the leak in pipe systems using the MFM. The MFM was firstly introduced by Shinbrot in [47] and [66] to estimate parameters of ODEs. The main idea is to convert the set of differential equations by an

integral transform with variable kernel into a set of algebraic equations that can be solved online. Thereby, the approximation of derivatives of measured signals is avoided and the robustness to measurement noise is improved. Furthermore, the kernel of the integral transform can be designed such that no knowledge about the initial conditions of the system is required. Moreover, the implementation of the estimation process by MFs can be regarded as an FIR filter that provides a non-asymptotic convergence behavior of the solution of the estimation problem. Consequently, and in contrast to typical dynamic observer approaches like Luenberger observers or KFs, the MFM is capable of providing a solution of the estimation problem in finite time.

Especially over the last two decades, the MFM became of special interest in control theory to estimate parameters, states, or source terms in ODEs over a wide range of technical applications. In [67], a broader class of nonlinear systems is considered whose parameters can be estimated by the MFM. A few years later, the MFM was applied in [68] to perform system identification on a fermentation process with time-varying parameters. An extension of the MFM to jointly estimate parameters and states of a nonlinear ODE system was presented in [41]. Based on the results of this publication, the MFM was used in [69] to identify parameters of a nonlinear MISO glass melting process and to predict the molten glass temperature to enable the adaptive correction of the parameters of a PID controller. Furthermore, in [70], the online parameter and state estimation of an air handling unit based on MFM is considered. The MFM based parameter and state estimation algorithms were implemented in real time, and the validation with experimental data showed a good match between the resulting estimates and the measured data. Recently, [71] includes the MFM to design a robust nonlinear controller for the control of liquid levels in a quadruple tank system and to provide noise-free estimations of the required state variables.

At the same time, the MFM also became more and more interest w.r.t estimation problems in PDEs. In [49], an algebraic approach based on the MFM to detect and isolate faults in a parabolic PDE is presented. Furthermore, [43] presents a state estimation via the MFM for a linear reaction diffusion PDE. This approach was extended in [51] to estimate states for a Coupled Reaction-Diffusion PDE System. Moreover, [48] and [42] presented an approach to estimate source terms in first order hyperbolic PDEs with application to the estimation of energy terms in heat transport dynamics in concentrated solar collectors. These two publications [48, 42] are of great interest for this work since the fluid dynamics according to the linear pipe model (2.4) are also described by a hyperbolic PDE where the leak appears as a source term on the right-hand side.

Before the MFM is applied to the problem of leak size estimation and localization in pipe systems, the following section reviews the basic properties of MFs.

3.3.1. Modulating Function Method (MFM)

According to the literature [41, 42], we introduce the MF as follows.

Definition 3.3.1 (Modulating Function). *A function $\varphi : [0, \ell] \times [0, T] \to \mathbb{R}^n,\ T > 0$ is called Left Modulating Function (LMF) of order $k \in \mathbb{N} :\Leftrightarrow \varphi(\cdot, \cdot)$ is sufficiently smooth and*

$$\forall i \in \{0, 1, \dots, k-1\} : \frac{\partial^i \varphi}{\partial t^i}(z, 0) = 0,\ \frac{\partial^i \varphi}{\partial t^i}(z, T) \neq 0\,. \tag{3.22}$$

Furthermore, a function $\varphi : [0, \ell] \times [0, T] \to \mathbb{R}^n,\ T > 0$ is called Total Modulating Function (TMF) of order $k \in \mathbb{N} :\Leftrightarrow \varphi(\cdot, \cdot))$ is sufficiently smooth and

$$\forall i \in \{0, 1, \dots, k-1\} : \frac{\partial^i \varphi}{\partial t^i}(z, 0) = \frac{\partial^i \varphi}{\partial t^i}(z, T) = 0\,. \tag{3.23}$$

Based on this Definition 3.3.1, the modulation functional is introduced.

Definition 3.3.2. *Let $\varphi : [0, \ell] \times [0, T] \to \mathbb{R}^n$ be an MF of order k and $h : [0, \ell] \times \mathbb{R}_{\geq 0} \to \mathbb{R}^m, m \in \{1, n\}$. Then, the modulating functional is defined as*

$$\mathcal{M}[h](t) := \int_{t-T}^{t} \int_{0}^{\ell} \varphi(z, \tau - t + T)^\top h(z, \tau) dz d\tau\,. \tag{3.24}$$

For reasons of clarity, the following abbreviation as an inner product

$$\langle \varphi, h \rangle_{\Omega, I} := \mathcal{M}[h] \tag{3.25}$$

is defined where $I := [t - T, t],\ t \geq T$ describes the moving time horizon with the receding horizon length $T > 0$ and $\Omega := [0, \ell]$ the fixed spatial domain. Furthermore, the abbreviations $\langle \varphi, h \rangle_I$ and $\langle \varphi, h \rangle_\Omega$ are introduced if the integration is realized only w.r.t. the temporal or spatial variable, respectively.

The following theorem reveals the fundamental property of TMFs.

Lemma 3.3.1 (Fundamental properties of TMFs). *Let $\varphi : [0, \ell] \times [0, T] \to \mathbb{R}$ be a TMF of order $k + 1$ and $m \in \{1, n\}$. Then,*
(i)

$$\forall h(\cdot) \in \mathcal{C}^{k+1}(\mathbb{R}, \mathbb{R}^m) : \langle \varphi, h^{(k+1)} \rangle_{\Omega, I} = (-1)^{k+1} \langle \varphi^{(k+1)}, h \rangle_{\Omega, I} \tag{3.26}$$

(ii)

$$\forall h(\cdot) \in \mathcal{C}^1([0,\ell],\mathbb{R}^m) : \langle \varphi, h' \rangle_{\Omega,I} = -\langle \varphi', h \rangle_{\Omega,I} + (\langle \varphi, h \rangle_I)|_0^\ell \tag{3.27}$$

holds, where $\varphi^{(k+1)} := \frac{\partial^{k+1}}{\partial t^{k+1}}\varphi(z,t)$ *denotes the* $(k+1)$*-th temporal derivative and* $\varphi' := \frac{\partial}{\partial z}\varphi(z,t)$ *the first spatial derivative of the TMF.*

Proof. (i) Using integration by parts iteratively and the boundary conditions (3.23) leads to

$$\begin{aligned}
\langle \varphi, h^{(k+1)} \rangle_{\Omega,I} &= \int_{t-T}^{t}\int_0^\ell \varphi(z,\tau-t+T)^\top h^{(k+1)}(z,\tau)\mathrm{d}z\mathrm{d}\tau \\
&= \sum_{i=0}^{k}(-1)^i \left(\langle \varphi^{(i)}, h^{(k-i)} \rangle_\Omega\right)\Big|_0^T + (-1)^{k+1}\langle \varphi^{(k+1)}, h \rangle_{\Omega,I} \\
&\overset{(3.23)}{=} \int_{t-T}^{t}\int_0^\ell \varphi^{(k+1)}(z,\tau-t+T)^\top h(z,\tau)\mathrm{d}z\mathrm{d}\tau \\
&=: (-1)^{k+1}\langle \varphi^{(k+1)}, h \rangle_{\Omega,I}
\end{aligned} \tag{3.28}$$

(ii) Using integration by parts results in

$$\begin{aligned}
\langle \varphi, h' \rangle_{\Omega,I} &= \int_{t-T}^{t}\int_0^\ell \varphi^\top(z,\tau-t+T)h'(z,\tau)\mathrm{d}z\mathrm{d}\tau \\
&= -\int_{t-T}^{t}\int_0^\ell \varphi'(z,\tau-t+T)h(z,\tau)^\top\mathrm{d}z\mathrm{d} + \left(\int_{t-T}^{t}\varphi'(z,\tau-t+T)^\top h(z,\tau)\mathrm{d}\tau\right)\Big|_0^\ell \\
&= -\langle \varphi', h \rangle_{\Omega,I} + (\langle \varphi, h \rangle_I)|_0^\ell
\end{aligned} \tag{3.29}$$

□

Theorem 3.3.1 shows that applying the modulating functional (3.24), time derivatives can be shifted from a measured signal $h(\cdot)$ to the known MF $\varphi(\cdot,\cdot)$. Thereby, the differentiation of a noisy signal $h(\cdot)$ can be avoided and replaced by the calculation of the known MF $\varphi(\cdot,\cdot)$. Furthermore, unknown initial and final conditions are eliminated by the boundary conditions of the MF.

The following sections of this chapter show how to apply the MFM to the leak size estimation and localization problem by employing the presented fundamental properties of MFs.

Therefore, at first, the leak size is estimated by using the MFM to transform the transformed PDE system (3.3) into an algebraic IO relation that will be called the source estimation equation. The corresponding auxiliary problem to determine the MF is derived, as well as an approach to solve the auxiliary PDE problem. Based on the estimation of the leak size, two different approaches to localize the leak position are presented. The first ansatz aims at localizing the leak directly by

applying the MFM to the linear pipe model (2.4). Similar to the case of leak size estimation, the leak distribution function $d(\cdot)$ is treated as an unknown source term on the right-hand side of the linear pipe model (2.4). The second approach does not estimate the leak position directly, but firstly estimates the states of the transformed PDE system (3.3) by applying the MFM. The MFM results again in an algebraic IO relation and an auxiliary PDE problem that has to be solved to obtain the MFs and to resolve the algebraic estimation equation regarding the states. Finally, this state estimation is inserted together with the estimated leak size into the leak localization observer system (3.19) to estimate the position of the leak.

3.3.2. Leak Size Estimation by MFM

This section deals with the estimation of the leak size by applying the MFM to the transformed system (3.3). The unknown leak size χ that appears in the first boundary condition of the transformed system (3.3) is regarded as a source term and an approach similar to [42] is followed. To this end, the following section presents the derivation of the algebraic IO expression and the auxiliary problem that result from the application of the modulating functional (3.24) to the transformed system (3.3).

3.3.2.1. Derivation of the Algebraic Input-Output Expression and the Auxiliary Problem

This section derives the algebraic IO relation between the flow rate and pressure measurements at the inlet and the outlet of the pipe and the leak size χ. Therefore, the modulating functional (3.24) is applied to the transformed system (3.3) to derive the associated auxiliary problem that has to be solved offline to generate the MFs. The main result is stated in the following Theorem 3.3.2.

Theorem 3.3.2. *Let $\Sigma_{trafo,lin}$ be given in matrix form as stated in Remark 3. Then, the estimate of the leak size is given by*

$$\hat{\chi} = \frac{1}{\langle \varphi_1(0) \rangle_I} \left(\langle \varphi_1(0), q_0 - q_{in} \rangle_I - \langle \varphi_1(1), Y \rangle_I + \langle \varphi_2(1), U \rangle_I \right) \tag{3.30}$$

where $\varphi(\cdot,\cdot) : [0,1] \times [0,T] \to \mathbb{R}^2$ is a TMF of order 1 that solves the following auxiliary problem

$$\Sigma_{aux,\chi} : \begin{cases} \dot{\varphi}(x,\tau) &= \Lambda_\chi^\top \varphi'(x,\tau) - \Sigma_\chi^\top(x)\varphi(x,\tau) \\ \varphi_1(0,\tau) &= -\varphi_2(0,\tau) \\ \varphi_1(1,\tau) &= \eta_1(\tau) \\ \varphi(x,0) &= 0,\ \varphi(x,T) = 0 \end{cases} \tag{3.31}$$

with $\int_{t-T}^{t} \varphi_1(0, \tau - t + T) d\tau \neq 0$ *where* $\eta_1 : [0, T] \to \mathbb{R}$ *represents a remaining degree of freedom in the design of the TMF.*

Proof. Applying the modulating functional (3.24) with a TMF $\varphi(\cdot, \cdot) : [0, 1] \times [0, T] \to \mathbb{R}^2$ of order 1 to the transformed system $\Sigma_{\text{trafo,lin}}$ in matrix form (as defined in Remark 3) leads to:

$$\langle \varphi, \begin{bmatrix} \dot{u} \\ \dot{v} \end{bmatrix} \rangle_{\Omega,I} = \langle \varphi, \Lambda_\chi \begin{bmatrix} u' \\ v' \end{bmatrix} \rangle_{\Omega,I} + \langle \varphi, \Sigma_\chi(x) \begin{bmatrix} u \\ v \end{bmatrix} \rangle_{\Omega,I} \; quad. \tag{3.32}$$

Employing that $\varphi(\cdot, \cdot)$ is a TMF of order 1, the left-hand side of Equation (3.32) is simplified with Theorem 3.3.1 to:

$$\langle \varphi, \begin{bmatrix} \dot{u} \\ \dot{v} \end{bmatrix} \rangle_{\Omega,I} = -\langle \dot{\varphi}, \begin{bmatrix} u \\ v \end{bmatrix} \rangle_{\Omega,I} \, . \tag{3.33}$$

To simplify the right-hand side of (3.32), integration by part is applied to the first term:

$$\begin{aligned} \langle \varphi, \Lambda_\chi \begin{bmatrix} u' \\ v' \end{bmatrix} \rangle_{\Omega,I} &= \int_{t-T}^{t} \int_0^1 \varphi(x, \tau - t + T)^\top \Lambda_\chi \begin{bmatrix} u'(x,\tau) \\ v'(x,\tau) \end{bmatrix} \mathrm{d}x\mathrm{d}\tau \\ &= -\int_{t-T}^{t} \int_0^1 \varphi'^\top(x, \tau - t + T) \Lambda_\chi \begin{bmatrix} u(x,\tau) \\ v(x,\tau) \end{bmatrix} \mathrm{d}x\mathrm{d}\tau \\ &\quad + \left(\int_{t-T}^{t} \varphi^\top(x, \tau - t + T) \Lambda_\chi \begin{bmatrix} u(x,\tau) \\ v(x,\tau) \end{bmatrix} \right) \Bigg|_0^1 \\ &= -\langle \Lambda_\chi^\top \varphi', \begin{bmatrix} u \\ v \end{bmatrix} \rangle_{\Omega,I} + \left(\langle \Lambda_\chi^\top \varphi, \begin{bmatrix} u \\ v \end{bmatrix} \rangle_I \right) \Bigg|_0^1 . \end{aligned} \tag{3.34}$$

(3.35)

Inserting Equation (3.33) and Equation (3.35) into Equation (3.32) leads to:

$$-\langle \dot{\varphi}, \begin{bmatrix} u \\ v \end{bmatrix} \rangle_{\Omega,I} = -\langle \Lambda_\chi^\top \varphi', \begin{bmatrix} u \\ v \end{bmatrix} \rangle_{\Omega,I} + \left(\langle \Lambda_\chi^\top \varphi, \begin{bmatrix} u \\ v \end{bmatrix} \rangle_I \right) \Bigg|_0^1 + \langle \Sigma_\chi^\top(x) \varphi, \begin{bmatrix} u \\ v \end{bmatrix} \rangle_{\Omega,I} \, . \tag{3.36}$$

To eliminate the unknown state variables in Equation (3.36), it is imposed that the TMF $\varphi(\cdot, \cdot)$ solves the following auxiliary PDE:

$$\dot{\varphi} = \Lambda_\chi^\top \varphi' - \Sigma_\chi(x) \varphi \, . \tag{3.37}$$

Thus, Equation (3.36) simplifies to

$$\begin{aligned} 0 &= \left(\langle \Lambda_\chi^\top \varphi, \begin{bmatrix} u \\ v \end{bmatrix} \rangle_I \right) \Bigg|_0^1 \\ &= \langle \Lambda_\chi^\top \varphi(1,t), \begin{bmatrix} u(1,t) \\ v(1,t) \end{bmatrix} \rangle_I - \langle \Lambda_\chi^\top \varphi(0,t), \begin{bmatrix} u(0,t) \\ v(0,t) \end{bmatrix} \rangle_I . \end{aligned} \tag{3.38}$$

By inserting the known boundary conditions $u(0,t) = -v(0,t) + q_0(t) - q_{in} - \chi,\ v(1,t) = U(t)$ and the known measurement $u(1,t) = Y(t)$ of the transformed system, one obtains

$$\begin{aligned} 0 = \int_{t-T}^{t} \epsilon \, &(-\varphi_1(1, \tau - t + T) Y(1, \tau - t + T) + \varphi_2(1, \tau - t + T) U(1, \tau - t + T) \\ &+ \varphi_1(0, \tau - t + T) \left(-v(0,\tau) + q_0(\tau) - q_{in} - \chi\right) - \varphi_2(0, \tau - t + T) v(0,\tau)) \, \mathrm{d}\tau . \end{aligned} \tag{3.39}$$

To eliminate the dependence on the unknown boundary state $v(0,\tau)$, the following boundary condition is imposed on the TMF to fulfill

$$\varphi_1(0,\tau) = -\varphi_2(0,\tau) . \tag{3.40}$$

Therefore, Equation (3.39) simplifies to

$$\begin{aligned} \int_{t-T}^{t} \varphi_1(0, \tau - t + T) \chi \mathrm{d}\tau = \int_{t-T}^{t} &-\varphi_1(1, \tau - t + T) Y(1, \tau - t + T) + \varphi_2(1, \tau - t + T) U(1, \tau - t + T) \\ &+ \varphi_1(0, \tau - t + T) \left(q_0(\tau) - q_{in}\right) \mathrm{d}\tau . \end{aligned} \tag{3.41}$$

Since the leak size χ is assumed to be constant (see Assumption 9 in Chapter 2) and since $\int_{t-T}^{t} \varphi_1(0, \tau - t + T) \mathrm{d}\tau \neq 0$ according to the requirements of the theorem, Equation (3.41) results in the leak size estimation equation

$$\chi = \frac{1}{\langle \varphi_1(0) \rangle_I} \left(\langle \varphi_1(0), q_0 - q_{in} \rangle_I - \langle \varphi_1(1), Y \rangle_I + \langle \varphi_2(1), U \rangle_I \right) \tag{3.42}$$

what completes the proof. □

The leak size estimation Equation (3.30) establishes an algebraic IO relation between the measurements taken from the pipe system (2.4) and the leak size χ where the TMF φ works as a filter of the measurements. This relationship can be implemented as an FIR filter, as shown in Appendix A.2.

Furthermore, the MFM basically transformed the estimation problem into a control problem, i.e. the estimation of the leak size according to Equation (3.30) requires a solution of the auxiliary

problem (3.31) such that the TMF φ is steered from the initial condition $\varphi(x,0)=0$ to the final condition $\varphi(x,T)=0$ on the time horizon $[0,T]$ avoiding the trivial solution $\varphi \equiv 0$. A solution of the auxiliary problem (3.31) is sought such that the dynamical equations, the initial and final conditions and the boundary conditions are fulfilled. To this end, the following section addresses the solution of the auxiliary problem by a power series approach.

3.3.2.2. Solution of the Auxiliary Problem

The auxiliary problem (3.31) can be regarded as a trajectory planning problem for the coupled hyperbolic PDE system (3.31) where the states have to be steered in finite time T from the origin $\varphi(x,0)=0$ to the origin $\varphi(z,T)=0$. To this end, we follow the approach presented in [72] and set the formal power series

$$\begin{aligned} \hat{\varphi}_1(x,\tau) &= \sum_{k=0}^{\infty} \varphi_{1,k}(\tau) x^k \\ \hat{\varphi}_2(x,\tau) &= \sum_{k=0}^{\infty} \varphi_{2,k}(\tau) x^k \end{aligned} \tag{3.43}$$

as an ansatz to solve the auxiliary problem (3.31). Inserting the power series approach (3.43) into the auxiliary problem (3.31) leads to

$$\begin{aligned} \sum_{k=0}^{\infty} \frac{\partial}{\partial \tau} \varphi_{1,k}(\tau) &\approx -\epsilon \sum_{k=0}^{\infty} \frac{\partial}{\partial x} \left(\varphi_{1,k}(\tau) x^k \right) - \overline{c_2(x)} \sum_{k=0}^{\infty} \varphi_{2,k}(\tau) x^k \\ &= -\epsilon \sum_{k=0}^{\infty} \varphi_{1,k+1}(\tau)(k+1) x^k - \overline{c_2(x)} \sum_{k=0}^{\infty} \varphi_{2,k}(\tau) x^k \\ \sum_{k=0}^{\infty} \frac{\partial}{\partial \tau} \varphi_{2,k}(\tau) &\approx \epsilon \sum_{k=0}^{\infty} \frac{\partial}{\partial x} \left(\varphi_{2,k}(\tau) x^k \right) - \overline{c_1(x)} \sum_{k=0}^{\infty} \varphi_{1,k}(\tau) x^k \end{aligned} \tag{3.44}$$

where we set $\overline{c_1(x)} := \int_0^1 c_1(x) \mathrm{d}x$ and $\overline{c_2(x)} := \int_0^1 c_2(x) \mathrm{d}x$ as the spatial mean value of $c_1(x)$ and $c_2(x)$.[1] Finally, the coefficient comparison in (3.44) results in the recursive formulas

$$\begin{aligned} \varphi_{1,k+1}(\tau) &= \frac{1}{\epsilon(k+1)} \left(-\frac{\partial}{\partial \tau} \varphi_{1,k}(\tau) - \overline{c_2(x)} \varphi_{2,k}(\tau) \right) \\ \varphi_{2,k+1}(\tau) &= \frac{1}{\epsilon(k+1)} \left(\frac{\partial}{\partial \tau} \varphi_{2,k}(\tau) + \overline{c_1(x)} \varphi_{1,k}(\tau) \right) \end{aligned} \tag{3.45}$$

[1] Since the denominator $\sqrt{\beta\rho}$ of $c_1(x)$ and $c_2(x)$ is in the range of 10^6, $c_1(x)$ and $c_2(x)$ do not vary strongly for pipes of a length in the range of up to $\ell \sim 10^5$ m. In the simulation case regarded in Chapter 4, the mean values $\overline{c_1(x)}$ and $\overline{c_2(x)}$ differ by maximum $6\,\%$ from the entries in $c_1(x)$ and $c_2(x)$. For a more detailed and sophisticated approach to deal with spatially varying coefficients in the trajectory planning problem, see e.g. [73, 74].

to determinate the coefficients $\varphi_{1,k}(\tau)$ and $\varphi_{2,k}(\tau)$. Furthermore, the boundary condition $\varphi_1(0,\tau) = -\varphi_2(0,\tau)$ imposes that

$$\varphi_{1,0}(\tau) = \varphi_1(0,\tau) = -\varphi_2(0,\tau) = -\varphi_{2,0}(\tau). \tag{3.46}$$

To parametrize the solution and to resolve the recursive formula (3.45), we introduce the basic variable $b : [0,T] \to \mathbb{R}$ and initialize the recursive formula by $\varphi_{1,0}(\tau) = -\varphi_{2,0}(\tau) = b(\tau)$. Since the trajectory planned by Equation (3.43) and Equation (3.45) has to realize the non-trivial set point transition from $\varphi(x,0) = 0$ to $\varphi(x,T) = 0$, the basic variable has to fulfill

$$\forall k \in \mathbb{N} : \mathrm{d}_\tau^k b(\tau) = 0\ , \tag{3.47}$$

i.e. the basic variable $b(\cdot)$ is a locally non-analytical function. Hence, we choose $b(\cdot)$ to be a so called Gevrey function of order α. The class of these Gevrey functions was firstly proposed in 1918 by Maurice Gevrey [52] and is defined as follows:

Definition 3.3.3 (Gevrey Function [72])**.** *A function $b \in \mathcal{C}^\infty([0,T],\mathbb{R})$ is called Gevrey function of order α*

$$:\Leftrightarrow \exists M, R > 0 \forall k \in \mathbb{N} : \sup_{\tau\in[0,T]} |d_\tau^k b(\tau)| \leq \frac{M}{R^k}(k!)^\alpha \tag{3.48}$$

Remark 6. *The Taylor expansion of a smooth, non-analytic function does not converge to that function. The order α of the Gevrey function can be understood as a measure of this divergence [72]. If $\alpha = 1$, the Gevrey function is analytic. For $\alpha > 1$, the Gevrey function is non-analytic and its Taylor expansion diverges, where the larger α, the "more divergent" is the Taylor expansion [72].*

Remark 7. *The scaling, integration, addition, multiplication, and composition of Gevrey functions of order $\alpha > 1$ is of order α [52].*

Remark 8. *An example of a Gevrey function is the normalized bump function which is of Gevrey order $\alpha = 1 + \frac{1}{\sigma}$. The parameter σ can be used to adjust the slope of the function, as Figure 3.3 illustrates. In the following, this bump function will be used as a basic variable for the trajectory planning problem. Thus, the requirement $\int_{t-T}^{t} \varphi_1(0,\tau - t + T)d\tau \neq 0$ of Theorem 3.3.2 is fulfilled. For alternative Gevrey functions based on the tangens hyperbolicus, and the recursive calculation of their derivatives, see e.g. [75, 76].*

$$b_\sigma(\tau) = \begin{cases} 0, & \text{if } \tau \notin (0,T) \\ \dfrac{\exp\left(-\frac{1}{((1-\frac{\tau}{T})\frac{\tau}{T})^\sigma}\right)}{\int_0^T \exp\left(-\frac{1}{((1-\frac{\tau}{T})\frac{\tau}{T})^\sigma}\right)\mathrm{d}\tau}, & \text{if } \tau \in (0,T) \end{cases} \tag{3.49}$$

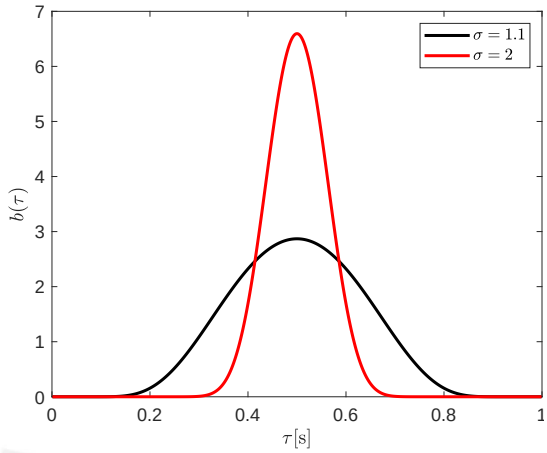

Figure 3.3.: Bump Function of Gevrey order $\alpha = 1 + 1/\sigma$ for $T = 1$ varying the slope σ.

The boundedness of the derivatives of Gevrey functions according to Equation (3.48) is essential to achieve the convergence of the formal power series ansatz (3.43) and, thereby, to solve the trajectory planning problem. Nevertheless, there was not found any analytical proof to guarantee convergence of the formal power series ansatz (3.43) in dependence on the order α of the considered Gevrey function. The utilization of proof schemes for parabolic PDEs or wave equations of second order (see e.g., [72, 77]), that apply the Cauchy-Hadamard theorem [78], has failed. Even in the case where the coupling in the recursive formula (3.45) is omitted resulting in a first order transport equation, the convergence of the power series ansatz (3.43) by utilizing the Cauchy-Hadamard theorem could not be shown. Thus, Section 4.1 deals with the simulative verification of the MFs generated by the power series ansatz (3.43).

Altogether, this section has designed the first part of the algebraic observer that serves for the estimation of the leak size. Based on this algebraic leak size estimation, the next section follows two different approaches to estimate the unknown leak position.

3.3.3. Leak Localization by MFM

This section applies the MFM to the problem of locating the leak in the pipe. Therefore, two different approaches will be presented: direct leak localization and leak localization via MFM based state estimation. The direct leak localization treats the leak distribution $d(\cdot)$ appearing on the right-hand side of the linear pipe model (2.4) as a spatial source term and performs the same steps as for the leak size estimation by deriving the auxiliary PDE problem and the source estimation equation. However, it turns out that the source estimation equation is not solvable for non-constant leak

distributions $d(\cdot)$ and, as a consequence, not useful from a practical view. Hence, an alternative way to estimate the leak localization is presented by primarily estimating the states $u(x,t)$ and $v(x,t)$ of the transformed system (3.3) and afterwards exploiting the dynamic leak localization observer (3.19) of the dynamic observer design.

3.3.3.1. Direct Leak Localization by MFM

In view of the physical pipe model (2.4), the leak distribution $d(\cdot)$ can be regarded as an unknown spatial source term. Since the leak size can be estimated independently by the algebraic observer presented in the previous Section 3.3.2, we follow the same steps as in the previous case of leak size estimation to design an algebraic observer for the unknown leak localization: (i) Derivation of the auxiliary problem by applying the MFM to the PDE system, (ii) Derivation of the source estimation equation, (iii) Resolving the source estimation equation, (iv) Solving the auxiliary problem.

The following theorem presents the resulting auxiliary problem and the source estimation equation that establishes an algebraic IO relationship between the spatial source term $d(\cdot)$ and the available measurement data at the inlet and the outlet of the pipe.

Theorem 3.3.3. *Let $\Sigma_{WH_{lin},leak}$ be given in matrix form as stated in Remark 1. Then, the algebraic IO relation to estimate the leak localization is given by*

$$\mathcal{X}^\top \langle \varphi^\top, d(z) \rangle_{\Omega,I} = -\langle \varphi, \Theta(z) \rangle_{\Omega,I} - \left(\langle \Lambda^\top \varphi, \begin{bmatrix} p \\ q \end{bmatrix} \rangle_I \right) \Big|_0^\ell \tag{3.50}$$

where $\varphi(\cdot,\cdot) : [0,\ell] \times [0,T] \to \mathbb{R}^2$ is a TMF of order 1 that solves the following auxiliary problem

$$\Sigma_{aux,d} : \begin{cases} \dot{\varphi}(z,\tau) &= \Lambda^\top \varphi'(z,\tau) - \Sigma^\top \varphi(z,\tau) \\ \varphi_1(\ell,\tau) &= \eta_1(\tau) \\ \varphi_2(0,\tau) &= \eta_2(\tau) \\ \varphi(z,0) &= 0,\ \varphi(z,T) = 0 \end{cases} \tag{3.51}$$

where the selection of the boundary condition functions $\eta_1 : [0,T] \to \mathbb{R},\ \eta_2 : [0,T] \to \mathbb{R}$ represent a remaining degree of freedom in the design of the MF.

Proof. To prove the Theorem 3.3.3, the same steps as in the proof of 3.3.2 are followed. Firstly, the modulating functional (3.24) with a TMF $\varphi(\cdot,\cdot) : [0,1] \times [0,T] \to \mathbb{R}^2$ of order 1 is applied to

the transformed system $\Sigma_{WH_{lin},leak}$ in matrix form (see Remark 1) and leads to:

$$\langle \varphi, \begin{bmatrix} \dot{p} \\ \dot{q} \end{bmatrix} \rangle_{\Omega,I} = \langle \varphi, \Lambda \begin{bmatrix} p' \\ q' \end{bmatrix} \rangle_{\Omega,I} + \langle \varphi, \Sigma \begin{bmatrix} p \\ q \end{bmatrix} \rangle_{\Omega,I} + \langle \varphi, \Theta(z) \rangle_{\Omega,I} + \langle \varphi, \mathcal{X} d(z) \rangle_{\Omega,I} \,. \tag{3.52}$$

Exploiting that $\varphi(\cdot,\cdot)$ is a TMF of order 1 and using the fundamental derivative shifting properties according to Theorem 3.3.1 leads to:

$$\begin{aligned} -\langle \dot{\varphi}, \begin{bmatrix} p \\ q \end{bmatrix} \rangle_{\Omega,I} = -\langle \Lambda^\top \varphi', \begin{bmatrix} p \\ q \end{bmatrix} \rangle_{\Omega,I} + \left(\langle \Lambda^\top \varphi, \begin{bmatrix} p \\ q \end{bmatrix} \rangle_I \right) \Big|_0^\ell + \langle \Sigma^\top \varphi, \begin{bmatrix} p \\ q \end{bmatrix} \rangle_{\Omega,I} \\ + \langle \varphi, \Theta(z) \rangle_{\Omega,I} + \langle \varphi, \mathcal{X} d(z) \rangle_{\Omega,I} \,. \end{aligned} \tag{3.53}$$

To eliminate the unknown state variables in Equation (3.53), it is imposed that the TMF $\varphi(\cdot,\cdot)$ solves the following auxiliary PDE:

$$\dot{\varphi} = \Lambda^\top \varphi' - \Sigma \varphi \,. \tag{3.54}$$

Thus, Equation (3.53) simplifies to

$$\langle \varphi, \mathcal{X} d(z) \rangle_{\Omega,I} = \left(\langle \Lambda^\top \varphi, \begin{bmatrix} p \\ q \end{bmatrix} \rangle_I \right) \Big|_0^\ell + \langle \varphi, \Theta(z) \rangle_{\Omega,I} \,. \tag{3.55}$$

In accordance with the model assumptions, the leak size χ is assumed to be constant on the time interval $[t-T, t]$. Consequently, replacing the real leak size χ in $\mathcal{X}$ by its estimate $\hat{\chi}$ given by Equation (3.30) leads to

$$\mathcal{X}^\top \langle \varphi^\top, d(z) \rangle_{\Omega,I} = - \left(\langle \Lambda^\top \varphi, \begin{bmatrix} p \\ q \end{bmatrix} \rangle_I \right) \Big|_0^\ell - \langle \varphi, \Theta(z) \rangle_{\Omega,I} \tag{3.56}$$

completing the proof. □

Since the boundary values $p_0(t),\ p_\ell(t),\ q_0(t),\ q_\ell(t)$ are assumed to be known by the measurements, Equation (3.50) represents an algebraic IO relation between the given measurement data and the unknown leak distribution, where the TMF works as a filter. However, in contrast to the case of leak size estimation, the leak distribution function cannot be assumed as a constant over the spatial domain. Consequently, a way to resolve the source estimation equation (3.50) for the leak distribution is required. To this end, we represent the leak distribution function by a function

expansion of the form

$$d(z) = \sum_{k=0}^{\infty} c^k \Psi^k(z) \approx \sum_{k=0}^{N} c^k \Psi^k(z) \tag{3.57}$$

where $\{\Psi(\cdot)\}_{k=0}^{\infty}$ is an orthogonal and normalized function basis (i.e. $\int_0^\ell \Psi^k(z)\mathrm{d}z = 1$) and $N \in \mathbb{N}$ is the approximation order. Consequently, the task consists in estimating the coefficient vector $c := \begin{bmatrix} c^0 & \dots & c^N \end{bmatrix}^\top \in \mathbb{R}^{N+1}$ of the basis representation. Therefore, it is necessary to solve N auxiliary problems of the form $\Sigma_{aux,d}$ offline. The resulting solution set of N TMFs is denoted by $\{\varphi^k(\cdot,\cdot)\}_{k=0}^{N-1}$. Inserting the basis representation (3.57) and the N TMFs into the source estimation equation (3.50) leads to N equations of the form

$$\forall k = 0, \dots, N-1 : \begin{bmatrix} \mathcal{X}^\top \langle \varphi^{k\,\top}, \Psi^0 \rangle_{\Omega,I} \\ \vdots \\ \mathcal{X}^\top \langle \varphi^{k\,\top}, \Psi^{N-1} \rangle_{\Omega,I} \end{bmatrix}^\top c = \left[-\langle \varphi^k, \Theta(z) \rangle_{\Omega,I} - \left(\langle \Lambda^\top \varphi^k, \begin{bmatrix} p \\ q \end{bmatrix} \rangle_I \right) \Big|_0^\ell \right] . \tag{3.58}$$

Furthermore, the normalization condition $\int_0^\ell d(z)\mathrm{d}z = 1$ imposes a further equation

$$\begin{bmatrix} 1 & \dots & 1 \end{bmatrix} c = 1 \tag{3.59}$$

on the coefficient vector c such that the in total $N+1$ equations can be summarized in matrix form as

$$\underbrace{\begin{bmatrix} \mathcal{X}^\top \langle \varphi^{0\,\top}, \Psi^0 \rangle_{\Omega,I} & \dots & \mathcal{X}^\top \langle \varphi^{0\,\top}, \Psi^N \rangle_{\Omega,I} \\ \vdots & \ddots & \vdots \\ \mathcal{X}^\top \langle \varphi^{N-1\,\top}, \Psi^0 \rangle_{\Omega,I} & \dots & \mathcal{X}^\top \langle \varphi^{N-1\,\top}, \Psi^N \rangle_{\Omega,I} \\ 1 & \dots & 1 \end{bmatrix}}_{:= M \in \mathbb{R}^{(N+1)\times(N+1)}} c = \underbrace{\begin{bmatrix} -\langle \varphi^0, \Theta(z) \rangle_{\Omega,I} - \left(\langle \Lambda^\top \varphi^0, \begin{bmatrix} p \\ q \end{bmatrix} \rangle_I \right) \Big|_0^\ell \\ \vdots \\ -\langle \varphi^{N-1}, \Theta(z) \rangle_{\Omega,I} - \left(\langle \Lambda^\top \varphi^{N-1}, \begin{bmatrix} p \\ q \end{bmatrix} \rangle_I \right) \Big|_0^\ell \\ 1 \end{bmatrix}}_{:= y \in \mathbb{R}^{N+1}} . \tag{3.60}$$

As a consequence, the coefficient vector c could be calculated by

$$c = M^{-1} y \, . \tag{3.61}$$

However, the following inspections of the entries of M prove analytically, that the linear regression

problem (3.60) is ill-posed and that the matrix M is singular.

Since the entries of the matrix M are given by

$$\begin{aligned}\forall i \in \{0,\dots,N-1\}\forall j \in \{0,\dots,N-1\} : M_{ij} &= \mathcal{X}^T \int_0^T \int_0^\ell \varphi^{i\,\top}(z,\tau)\Psi^j(z)\mathrm{d}z\mathrm{d}\tau \\ &= \mathcal{X}^T \int_0^\ell \left(\int_0^T \varphi^{i\,\top}(z,\tau)\mathrm{d}\tau \right) \Psi^j(z)\mathrm{d}z\,, \end{aligned} \tag{3.62}$$

an analytical expression of the temporal integral $\int_0^T \varphi(z,\tau)\mathrm{d}\tau$ of the TMF φ is sought to analyze the invertibility of M. By differentiating the temporal integral $\int_0^T \varphi(z,\tau)\mathrm{d}\tau$ w.r.t. the spatial variable z, we obtain:

$$\begin{aligned}\frac{\mathrm{d}}{\mathrm{d}z}\int_0^T \varphi(z,\tau)\mathrm{d}\tau &= \int_0^T \frac{\partial}{\partial z}\varphi(z,\tau)\mathrm{d}\tau \text{ (Leibniz integral rule)} \\ &= \int_0^T \bar{\Lambda}^{-\top}\left(\dot{\varphi}(z,\tau) + \bar{\Sigma}^\top \varphi(z,\tau)\right)\mathrm{d}\tau \text{ (see } \Sigma_{\mathrm{aux},d}) \\ &= \bar{\Lambda}^{-\top}\bar{\Sigma}^\top \int_0^T \varphi(z,\tau)\mathrm{d}\tau \text{ (since } \varphi(z,T) = \varphi(z,0) = 0) \end{aligned} \tag{3.63}$$

The last Equation (3.63) shows that the temporal integral $\int_0^T \varphi(z,\tau)\mathrm{d}\tau$ fulfills a linear ODE in space, whose solution is given by

$$\int_0^T \varphi(z,\tau)\mathrm{d}\tau = e^{\bar{\Lambda}^{-\top}\bar{\Sigma}^\top z}\int_0^T \varphi(0,\tau)\mathrm{d}\tau\,. \tag{3.64}$$

Inserting Equation (3.64) into Equation (3.62) leads to

$$\forall i \in \{0,\dots,N-1\}\forall j \in \{0,\dots,N-1\} : M_{ij} = \underbrace{\mathcal{X}^\top \int_0^\ell (e^{\bar{\Lambda}^{-\top}\bar{\Sigma}^\top z})^\top \Psi^j(z)\mathrm{d}z}_{=const.\ \forall i\in\{0,\dots,N-1\}} \cdot \int_0^T \varphi^i(0,\tau)\mathrm{d}\tau\,. \tag{3.65}$$

Equation (3.65) clearly reveals, that the remaining degrees of freedom in the auxiliary problem (3.51), i.e., the choice of the boundary conditions $\varphi_1(\ell,\tau)$ and $\varphi_2(0,\tau)$, can be factorized out in every row of M. Therefore, the rows of M are linearly dependent, and the matrix M is not invertible. Thus, the degrees of freedom in the choice of the boundary conditions of the auxiliary problem (3.51) does not permit the solvability of the source estimation equation and the leak distribution $d(\cdot)$ cannot be estimated directly by the presented approach. Hence, the following section presents an alternative approach that firstly estimates the state of the transformed system (3.3).

3.3.3.2. Leak Localization by MFM-based State Estimation

This section presents a leak localization approach by a MFM-based state estimation of the transformed system (3.3). In contrast to the previous Section 3.3.3.1, it is not aimed at estimating the entire leak distribution function $d(\cdot)$ but only the value of the auxiliary variable $\delta(\cdot)$ in $z = 0$. As already discussed in corollary 3.2.3.1, the value $\delta(z = 0)$ is equal to the leak position z^* for Dirac or rectangular shaped leak distributions. To estimate the value $\delta(z = 0)$, we evaluate the inverse state transformation (3.4) in $z = 0$

$$p_0(t) = \frac{\sqrt{\beta\rho}}{A}\left(u(0,t) - v(0,t)\right) + p_{out} + \frac{\rho}{A^2}\eta\chi + \frac{F}{A}\delta(0)\chi\,. \tag{3.66}$$

Since the boundary states $u(0,t)$ and $v(0,t)$ in Equation (3.66) are unknown, we seek to estimate the states $u(x,t)$ and $v(x,t)$ to be able to resolve Equation (3.66) for the unknown leak position $\delta(0) = z^*$. As in the case of the leak localization by the ABSO, Equation (3.66) is not resolved directly, but by the dynamic error feedback (3.19) to achieve a smoother and less noise-affected estimate of the leak position.

Derivation of the Algebraic Input-Output Expression and the Auxiliary Problem To estimate the needed states $u(x,t)$ and $v(x,t)$, we design an algebraic observer using LMFs for the transformed system (3.3). The following procedure can be regarded as a simplification of the observer design for coupled Reaction-Diffusion PDE Systems presented in [51]. In our case, we aim to estimate the states of a coupled PDE system, namely the states $u(x,t)$ and $v(x,t)$ of the coupled hyperbolic PDE system (3.3).

Firstly, we represent the states $u(x,t)$ and $v(x,t)$ by the following function expansion

$$\begin{aligned} v(x,t) &= \sum_{k=0}^{\infty} c_1^k(t)\Psi^k(x) \approx \sum_{k=0}^{N} c_1^k(t)\Psi^k(x) \\ v(x,t) &= \sum_{k=0}^{\infty} c_2^k(t)\Psi^k(x) \approx \sum_{k=0}^{N} c_2^k(t)\Psi^k(x) \end{aligned} \tag{3.67}$$

where N is the approximation order and $\{\Psi^k\}_{k=0}^{\infty}$ denotes the spatial orthonormal basis functions. The orthonormality of the basis functions is defined according to the scalar product $\langle f, g\rangle_w := \int_0^1 f(x)w(x)g(x)\mathrm{d}x$ where $w(\cdot)$ is a weighting function. In view of Equation (3.67), the goal consists in estimating the basis coefficients $c_1^k(t),\ c_2^k(t)$ of the function expansion (3.67).

Next, we apply the modulating functional (3.24) to the transformed system (3.3). The following theorem presents the resulting auxiliary problem and the algebraic IO relationship to determine the basis coefficients $c_1^k(t),\ c_2^k(t)$.

Theorem 3.3.4 (State Estimation of the transformed system by MFM). *Let $\Sigma_{trafo,lin}$ be given in matrix form as stated in Remark 3. Then, the algebraic IO relation to estimate the $m-th$ coefficients of the function expansion* (3.67) *is given by*

$$c_{1,2}^m(t) = \epsilon\left(\langle\varphi_2^m(1), U\rangle_I - \langle\varphi_1^m(1), Y\rangle_I + \langle\varphi_1^m(0), q_0 - q_{in} - \chi\rangle_I\right) \tag{3.68}$$

where $\varphi(\cdot,\cdot) : [0,\ell] \times [0,T] \to \mathbb{R}^2$ is an LMF of order 1 that solves the following auxiliary problem

$$\Sigma_{aux,u} : \begin{cases} \dot{\varphi}^m(x,\tau) &= \Lambda_\chi^\top \varphi'^m(x,\tau) - \Sigma_\chi^\top(x)\varphi^m(x,\tau) \\ \varphi(x,0) &= 0,\ \varphi(x,T) = \begin{bmatrix} w(x)\Psi^m(x) \\ 0 \end{bmatrix} \end{cases} \tag{3.69}$$

or

$$\Sigma_{aux,v} : \begin{cases} \dot{\varphi}^m(x,\tau) &= \Lambda_\chi^\top \varphi'^m(x,\tau) - \Sigma_\chi^\top(x)\varphi^m(x,\tau) \\ \varphi(x,0) &= 0,\ \varphi(x,T) = \begin{bmatrix} 0 \\ w(x)\Psi^m(x) \end{bmatrix} \end{cases} \tag{3.70}$$

, respectively.

Proof. In the following, the proof will be only shown for the estimation of the m-th coefficient of the function expansion (3.67) of the state $v(x,t)$. The proof for the state $u(x,t)$ is left to the interested reader.

Applying the modulating functional (3.24) to the transformed system (3.3) and exploiting the shifting property 3.3.1 of the modulating function $\varphi^m(\cdot,\cdot)$ regarding time and spatial derivatives results in

$$-\langle\dot{\varphi}^m, \begin{bmatrix} u \\ v \end{bmatrix}\rangle_{\Omega,I} + [\langle\varphi^m, \begin{bmatrix} u \\ v \end{bmatrix}\rangle_\Omega]_{t-T}^t = \left(\langle\Lambda_\chi^\top\varphi^m, \begin{bmatrix} u \\ v \end{bmatrix}\rangle_I\right)\Big|_0^1 - \langle\Lambda_\chi^\top\varphi'^m, \begin{bmatrix} u \\ v \end{bmatrix}\rangle_{\Omega,I} + \langle\Sigma^\top(x)\varphi^m, \begin{bmatrix} u \\ v \end{bmatrix}\rangle . \tag{3.71}$$

Since the MF $\varphi^m(\cdot,\cdot)$ fulfills the auxiliary problem $\Sigma_{\text{aux},v}$, Equation (3.71) simplifies to

$$\left(\langle\varphi^m, \begin{bmatrix} u \\ v \end{bmatrix}\rangle_\Omega\right)\Big|_{t-T}^t = \left(\langle\Lambda_\chi^\top\varphi^m, \begin{bmatrix} u \\ v \end{bmatrix}\rangle_I\right)\Big|_0^1 . \tag{3.72}$$

Imposing the initial condition $\varphi(x,0) = 0$ and the final condition $\varphi(x,T) = \begin{bmatrix} 0 \\ w(x)\Psi^m(x) \end{bmatrix}$ results

in

$$
\begin{aligned}
[\langle \varphi^m, \begin{bmatrix} u \\ v \end{bmatrix} \rangle_\Omega]_{t-T}^{t} &= \begin{bmatrix} 0 \\ \int_0^1 w(x)\Psi^m(x) \sum_{i=0}^{\infty} c^i(t)\Psi^i(x) \mathrm{d}x \end{bmatrix} \\
&= \begin{bmatrix} 0 \\ \sum_{i=0}^{\infty} c^i(t) \langle \Psi^m(x), \Psi^i(x) \rangle_w \end{bmatrix} \\
&= \begin{bmatrix} 0 \\ c^m(t) \end{bmatrix} \qquad (3.73)
\end{aligned}
$$

and introduces thereby the m-th coefficient of the function expansion (3.67) into Equation (3.72) by

$$
\begin{aligned}
\begin{bmatrix} 0 \\ c^m(t) \end{bmatrix} &= \left(\langle \varphi^m, \begin{bmatrix} u \\ v \end{bmatrix} \rangle_\Omega \right) \Big|_{t-T}^{t} \\
&= \left(\langle \Lambda_\chi^\top \varphi^m, \begin{bmatrix} u \\ v \end{bmatrix} \rangle_I \right) \Big|_{0}^{1} \\
&= \epsilon \begin{bmatrix} \int_{t-T}^{t} -\varphi_1^m(1, \tau - t + T) Y(\tau - t + T) + \varphi_1^m(0, \tau - t + T) \left(-v(0, \tau - t + T) + q_0(\tau - t + T) - q_{in} - \chi(\tau - t + T) \right) \mathrm{d}\tau \\ \int_{t-T}^{t} \varphi_2^m(1, \tau - t + T) U(\tau - t + T) - \varphi_2^m(0, \tau - t + T) v(0, \tau - t + T) \mathrm{d}\tau \end{bmatrix}.
\end{aligned}
$$

To eliminate the dependence on the unknown state $v(0,t)$, we add the boundary condition $\varphi_1^m(0,\tau) = -\varphi_2^m(0,\tau)$ and sum up both vector entries. Consequently, the m-th coefficient of the function expansion (3.67) can be estimated by the following algebraic relationship:

$$
c^m(t) = \epsilon \left(\langle \varphi_2^m(1), U \rangle_I - \langle \varphi_1^m(1), Y \rangle_I + \langle \varphi_1^m(0), q_0 - q_{in} - \chi \rangle_I \right) . \qquad (3.74)
$$

□

The following paragraph addresses the remaining task, the solution of the auxiliary problems (3.69) and (3.70).

Solution of the Auxiliary Problem The auxiliary problems (3.69) and (3.70) represent a control problem, where the state has to realize the transition from the origin $\varphi(x,0) = 0$ to the desired final condition $\varphi(x,T)$ in final time T. To bring the auxiliary problems (3.69) and (3.70) in the form considered in [53], we reverse the time t and flip the coordinates according to the following transformation for $\sigma \in [0,T]$

$$
\begin{bmatrix} \xi_1^m(x,\sigma) \\ \xi_2^m(x,\sigma) \end{bmatrix} := \begin{bmatrix} \varphi_2^m(x, T-\sigma) \\ \varphi_1^m(x, T-\sigma) \end{bmatrix}
$$

what results in the following transformed auxiliary problem

$$\Sigma_{\text{aux},\sigma}: \begin{cases} \begin{bmatrix} \dot{\xi}_1^m \\ \dot{\xi}_2^m \end{bmatrix} & = \begin{bmatrix} -\epsilon & 0 \\ 0 & \epsilon \end{bmatrix} \begin{bmatrix} \xi_1'^m \\ \xi_2'^m \end{bmatrix} + \begin{bmatrix} 0 & c_1(x) \\ c_2(x) & 0 \end{bmatrix} \begin{bmatrix} \xi_1^m \\ \xi_2^m \end{bmatrix} \\ \xi_1^m(0,\sigma) & = -\xi_2^m(0,\sigma) \\ \xi(x,0) & \neq 0,\ \xi(x,T) = 0 \\ \xi_2^m(1,\sigma) & = \eta(\sigma) \end{cases} \tag{3.75}$$

where the boundary condition $\eta(\cdot)$ represents the remaining degree of freedom to fulfill the state transition. This transformed auxiliary problem (3.75) is a stabilizing problem over the finite time horizon $[0,T]$. In [53], a backstepping based boundary control law was derived to stabilize the system in finite time that is presented in the following theorem.

Theorem 3.3.5 (Backstepping control for the auxiliary problem for state estimation)**.** *Consider the following 2×2 hyperbolic PDE system*

$$\Sigma: \begin{cases} \begin{bmatrix} \dot{\xi}_1 \\ \dot{\xi}_2 \end{bmatrix} & = \begin{bmatrix} -\epsilon & 0 \\ 0 & \epsilon \end{bmatrix} \begin{bmatrix} \xi_1' \\ \xi_2' \end{bmatrix} + \begin{bmatrix} 0 & c_1(x) \\ c_2(x) & 0 \end{bmatrix} \begin{bmatrix} \xi_1 \\ \xi_2 \end{bmatrix} \\ \xi_1(0,\sigma) & = -\xi_2(0,\sigma) \\ \xi(z,0) & = \xi_0 \\ \xi_2(1,\sigma) & = \eta(\sigma) \end{cases}$$

where $x \in [0,1]$, $c_1(\cdot) \in \mathcal{C}([0,1],\mathbb{R})$, $c_2(\cdot) \in \mathcal{C}([0,1],\mathbb{R})$, $\epsilon > 0, \xi_0 \in \mathcal{L}^2([0,1],\mathbb{R}^2)$. Then, the following control law

$$\eta(\sigma) = \int_0^1 K^{vu}(1,\zeta)\xi_1(\zeta,\sigma)d\zeta + \int_0^1 K^{vv}(1,\zeta)\xi_2(\zeta,\sigma)d\zeta \tag{3.76}$$

where the backstepping kernels K^{vu}, K^{vv} are given as the solution of (see eq. (24-31) in [53])

$$\Sigma_K: \begin{cases} \epsilon\frac{\partial K^{vu}}{\partial x} - \epsilon\frac{\partial K^{vu}}{\partial \zeta} & = c_2(\zeta)K^{vv} \\ \epsilon\frac{\partial K^{vv}}{\partial x} - \epsilon\frac{\partial K^{vv}}{\partial \zeta} & = c_1(\zeta)K^{vu} \\ K^{vu}(x,x) & = -\frac{c_2(x)}{2\epsilon} \\ K^{vv}(x,0) & = -K^{vu}(x,0) \end{cases} \tag{3.77}$$

stabilizes the system Σ in finite time $t_F = \frac{2}{\epsilon}$.

Proof. see [53, Theorem 1] □

Remark 9. *Interestingly, these backstepping kernel equations* (3.77) *were already solved analytically in [27] to calculate the observer gains of the adaptive backstepping observer (see eq. (57)-(62) in [27]).*

The combination of the state estimation obtained from the algebraic IO relation (3.68) and the leak localization observer (3.19) completes the design of the algebraic observer. Altogether, the Figure 3.4 illustrates schematically the structure of the algebraic observer and specifies thereby the general observer structure illustrated at the beginning of this chapter in Figure 3.1. The parts that can be solved offline are marked in green, while the online parts are colored in red. Furthermore, the design parameters, i.e., the lengths T_χ and T_δ of the moving time windows, the approximation order N of the function expansion (3.67) and the observer gain γ for the leak localization observer (3.19), are highlighted in purple.

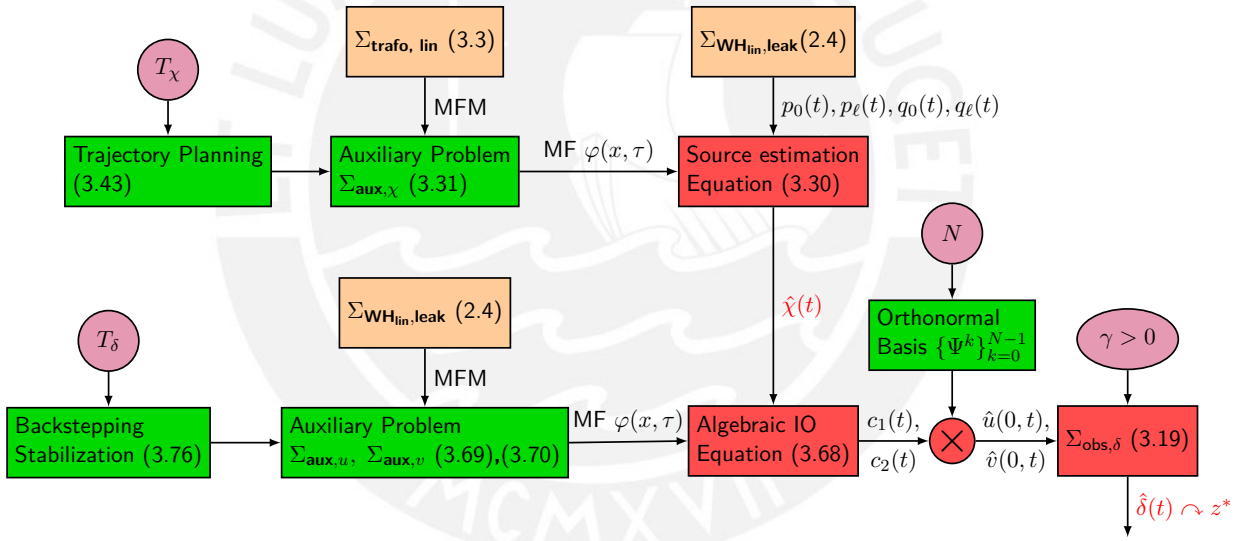

Figure 3.4.: Schematic illustration of the structure of the algebraic observer.

In conclusion, this chapter lays the theoretical fundaments of the dynamic and the algebraic observer design. The following chapter validates both observer structures in simulation for a realistic water pipe system and compares the performance to identify strengths and limitations of both observer types.

4. Simulation-Based Results

Throughout this chapter, the two observer schemes derived in Chapter 3 are implemented in MATLAB/Simulink and applied to the leak detection, size estimation and localization for an exemplary water pipeline. The performance of both observers is evaluated and compared under different simulation conditions, such as the measurement noise level, the boundary conditions, the leak size, the leak position, and the shape of the leak distribution function. Furthermore, the robustness of the leak size estimation and leak localization w.r.t. uncertainties in the modeling of the fluid friction losses is examined.

In the following sections, an exemplary pipeline according to the parametrization given in Table 4.1 will be regarded. The pipe has a length of $\ell = 20$ km and a diameter of $d = 1$ m what are reasonable values in comparison to existing, municipal and regional water pipes in Germany [79, 80, 81]. Additionally, an inclination angle of $\theta = 0.0315°$ is considered, leading to a height difference of $h = 11$ m. In the reference scenario, the boundary conditions are chosen to be constant, i.e. the inlet flow $q_0(t)$ is equal to the nominal flow and the outlet pressure is equal to the ambient pressure. Furthermore, the performance of both observer schemes for time-varying boundary conditions in the pipe model will be examined in Section 4.2.4. Finally, the density and compressibility of water are given by the literature [82]. The friction factor F is calculated for the nominal flow using the Haaland Equation (2.9) and assuming the pipe material to be steel with a pipe surface roughness of $\epsilon_p = 1.55 \cdot 10^{-4}$ m [82].

Before the performance of the leak observers can be evaluated, the first step consists in generating the required measurement data of the flow rate and the pressure at the inlet and outlet of the pipe by simulating the linear pipe model (2.4). Since the pipe is modelled as a PDE according to (2.4), a way to reduce the dimension of the infinite dimensional model is required. To this end, the Method of Lines (MOL) [45] is utilized because this technique is well-established in the literature and widely applied to simulate chemical and physical systems that are modelled by PDEs [83, 84, 85, 86, 87]. Furthermore, the MOL is simple to implement and allows the application of model order reduction schemes like the balanced truncation [88] to reduce the order of the resulting ODE system and thereby to reduce the computational costs.

The MOL introduces n spatial nodes. At these n nodes, the linear pipe model (2.4) is discretized in space by applying, e.g., first order finite differences to approximate the spatial derivatives. Con-

Parameter	Variable name	Value	Unit	
Length	ℓ	20	[km]	Pipe geometry
Diameter	d	1	[m]	
Cross-section area	A	0.7854	[m^2]	
Inclination	θ	0.0315	[°]	
Gravity	g	9.81	[$\frac{m}{s^2}$]	
Leak coefficient	c	0.8	[-]	
Friction factor	F	8.84	[$\frac{kg}{m^3 \cdot s}$]	Fluid properties
Compressibility	β	$2.1 \cdot 10^9$	[Pa]	
Density	ρ	1000	[$\frac{kg}{m^3}$]	
Inlet flow	$q_0(t)$	1	[$\frac{m^3}{s}$]	Boundary conditions
Outlet pressure	$p_\ell(t)$	$1.1 \cdot 10^5$	[Pa]	

Table 4.1.: Parametrization of the pipe model $\Sigma_{\mathsf{WH}_{\mathsf{lin}},\mathsf{leak}}$ in the reference scenario.

sequently, the spatial discretization leads to an ODE of order $2n$ that can be resolved. Since the pipe model (2.4) is linear in the states $p(\cdot,\cdot)$, $q(\cdot,\cdot)$, the ODE system resulting from the MOL is also linear, such that the MATLAB routine c2d can be used to convert the ODE to discrete time and to calculate the flow rate and pressure measurements at every time step. Following the same procedure, the infinite dynamic observer is discretized in space by employing the MOL and by implementing the resulting ODE system in MATLAB. For further regards, the interested reader is referred to appendix A.3 where the spatial discretization and derivation of the ODE system is described exemplarily for the linear pipe model (2.4).

Through the sections 4.2.1 to 4.2.5, the performance of the dynamic observer, the ABSO, and the MFM based algebraic observer is analyzed under various operating conditions of the simulation plant. The resulting KPIs are compared and the strengths and limitations of both observer schemes are evaluated. Beforehand, the following Section 4.1 discusses the generation of the required MFs that are needed to implement the algebraic observer.

4.1. Generation of the Modulating Functions

This section deals with the generation of the MFs that are required to implement the algebraic observer and calculated offline as the solutions of the auxiliary problem (3.31) for the leak size estimation and the auxiliary problems (3.69) and (3.70) for the state estimation. In this context, it is of great interest to verify that the Gevrey Function based trajectory planning approach according to the Equations (3.43) and (3.45) as well as the backstepping based control law according to Theorem 3.3.5 solve the auxiliary problems (3.31) and (3.69) as well as (3.70) accurately. Furthermore, the choice of the remaining degrees of freedom in the generation of the MFs is not that intuitive as

the tuning of the ABSO such that some remarks on the adjustment of the design parameters of the algebraic, MFM-based observer are given. To generate and adjust the MFs, the exemplary pipe is regarded as defined in the reference scenario according to Table 4.1 with a leak whose size represents $1\ \%$ of the nominal flow and that occurs after $t = 60$ s. Throughout this verification and adjustment process of the algebraic observer, measurement noise will not be considered.

First, the MFs for the leak size estimation via the algebraic IO relationship according to Equation (3.30) are generated. Therefore, the recursive formulas (3.45) are implemented to obtain the coefficients $\varphi_{1,k}(\tau)$ and $\varphi_{2,k}(\tau)$ of the power series approach (3.43). The remaining degrees of freedom are namely the choice of the Gevrey function $b(\cdot)$, the slope σ of the Gevrey function, the length T_χ of the moving time window and the truncation order N of the power series approach (3.43). In this work, the bump function $b_\sigma(\cdot)$ as defined in Remark 8 is utilized as Gevrey function. The slope is chosen as $\sigma = 2$ to simplify the calculations of the required derivatives of $b_\sigma(\cdot)$ and a truncation order of $N = 10$ is used. The adjustment of the length T_χ of the moving time window is done by comparing the solution of the auxiliary problem (3.31) obtained by the power series approach (3.43) with the solution that is obtained by discretizing the auxiliary problem (3.31) by means of the MOL.In the second case, the boundary condition $\varphi_1(1,\tau) = \eta_1(\tau)$ that is required to simulate the resulting ODE system is taken from the solution obtained by the power series approach. In Figure 4.1, the resulting MFs $\varphi_1(0),\ \varphi_1(1)$ and $\varphi_2(1)$, that are required to implement the algebraic IO relationship (3.30), are compared for $T_\chi = 130$ s and the pipe model given by the reference scenario as defined in Table 4.1. Furthermore, the temporal trajectory of the error norm $||e_\varphi(\tau)||^2 = \int_0^1 ||\varphi_{PS}(x,\tau) - \varphi_{MOL}(x,\tau)||^2 \mathrm{d}x$ between the solution $\varphi_{PS}(x,\tau)$ obtained from the power series approach (3.43) and the solution φ_{MOL} obtained by means of the MOL is displayed. As the visual coincidence of the trajectories of both solutions $\varphi_{PS}(x,\tau)$ and $\varphi_{MOL}(x,\tau)$ and the low error norm of $||e_\varphi(\tau)|| < 4 \cdot 10^{-3}$ indicate, the power series approach according to (3.43) with the temporal coefficients defined by the recursive formulas (3.45) solves the auxiliary problem (3.31) and realizes the required non-trivial set point change $\varphi(x,0) = 0 \rightsquigarrow \varphi(x,T_\chi) = 0,\ \varphi(x,\tau) \not\equiv 0$. Applying the resulting MFs $\varphi_1(0),\ \varphi_1(1)$ and $\varphi_2(1)$ to implement the algebraic IO relationship (3.30), an accurate estimate of the leak size in the noise free reference scenario is obtained with deviations under $0.28\ \%$ as Figure 4.2 illustrates. The convergence speed of the leak size estimate calculated by the algebraic observer is mainly determined by the length of the moving time horizon T_χ. The shorter the moving time window is, the faster converges the estimate. However, it is noted that for moving time windows of length smaller than $T_\chi = 130$ s, there was not found any configuration of slope σ and truncation order N such that the solution obtained from the power series approach and the solution simulated by the MOL coincide and such that an accurate result of the leak size estimation is provided.

After generating the MFs for the leak size estimation, the second part consists in calculating the MFs that are required to estimate the states of the transformed system (3.3) according to Theorem

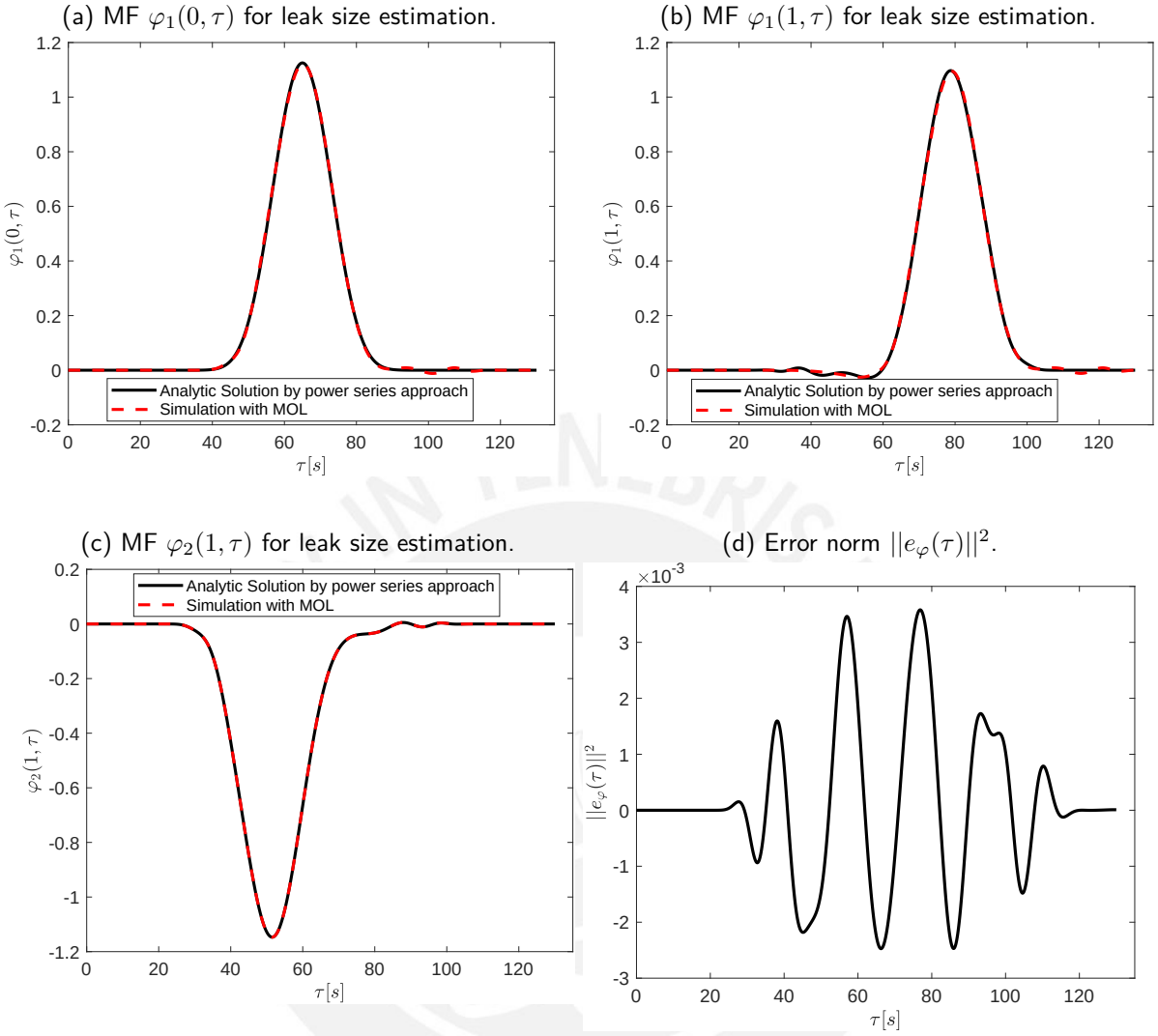

Figure 4.1.: Comparison and error norm $||e_\varphi(\tau)||^2$ of the MFs for the leak size estimation obtained by the power series approach (3.43) and the MOL-based solution for the pipe in the reference scenario according to Table 4.1.

(3.3.4). To this end, the auxiliary problems (3.69) as well as (3.70) are discretized by means of the MOL. Subsequently, the analytic solution of the backstepping kernels (3.77) is calculated and the control law presented in Theorem 3.3.5 is implemented to realize the required state transition according to Theorem 3.3.4. During this process, tuning parameters emerge at two points.

The first tuning parameters occur during the parametrization of the function expansion according to Equation (3.67) in form of the approximation order N, the choice of the orthonormal base functions $\{\Psi^k\}_{k=0}^{\infty}$ and the choice of the weighting function $w(\cdot)$. In this work, the weighting function is chosen as $w(x) = 20x^2(1-x)^2$. This function has its maximum at the centre $x = \frac{1}{2}$

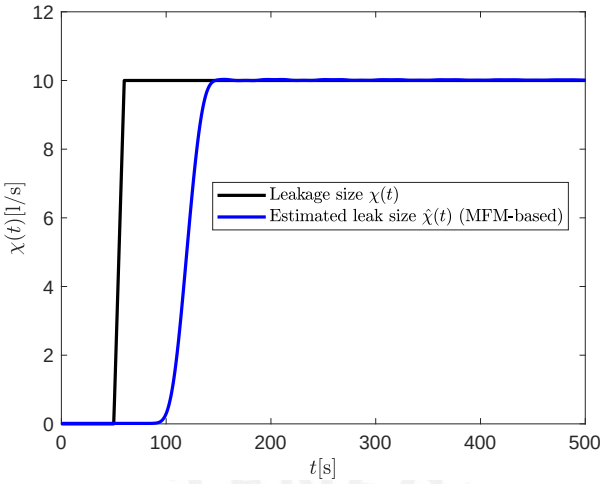

Figure 4.2.: Leak size estimation for the pipe in the noise free reference scenario defined in Table 4.1 with leakage of $1\ \%$ of the nominal flow occurring after $t = 60$ s.

and decreases symmetrically towards the boundaries $x = 0$ and $x = 1$ such that a symmetric weighting is established. A stronger weighting of one of the boundaries (e.g., $w(x) = 20x^4(1-x)^2$ or $w(x) = 20x^2(1-x)^4$) has not shown any improvement during the design process. Based on the selected weighting function, the orthonormal base functions are obtained from applying the Gram-Schmidt procedure to the canonical polynomial basis $\{x^k\}_{k=0}^{\infty}$. This choice of the orthonormal basis functions is widely applied in the MFM community [89, 43, 51]. Alternative function bases of the $\mathbb{L}^2(\mathbb{R}, \mathbb{R})$ like, e.g., a trigonometric basis, did not lead to a better performance of the leak localization in the reference scenario according to Table 4.1. The choice of an appropriate approximation order N is not straightforward and requires some testing to achieve the desired accuracy of the leak localization. In this work, an approximation order of $N = 5$ for the simulation pipe according to Table 4.1 provides a valid estimate of the leak position. The impact of higher or lower approximation orders N is discussed at the end of the section.

A further tuning parameter is given by the length T_δ of the time horizon that is considered to realize the state transition of the auxiliary problems (3.69) and (3.70). According to Theorem 3.3.5, the control law (3.76) achieves this state transition in final time $t_F = \frac{2}{\epsilon}$, i.e. the final time depends only on the system parameters ℓ, β and ρ of the pipe (remind: $\epsilon := \frac{1}{\ell}\sqrt{\frac{\beta}{\rho}}$). However, the control law (3.76) does not transfer the states of the auxiliary problems (3.69) and (3.70) exactly to the desired final state $\varphi(x, T_\delta)$ due to numerical inaccuracies, e.g., provoked by the discretization by means of the MOL, as Figure 4.3 indicates. On the other side, the leak localization is a highly sensitive problem. The estimated states $\hat{u}(0,t)$, $\hat{v}(0,t)$ are multiplied in Equation (3.66) with the factor $\frac{\sqrt{\beta\rho}}{A}$ that is in the range of 10^7 ($\beta \sim 10^9$, $\rho \sim 10^3$, $A \sim 10^{-1}$). Therefore, it is recommended to augment the time horizon T_δ such that the deviations from the desired final state

decrease. In this work, a time horizon of $T_\delta = 6 \cdot t_F = 165.6$ s leading to deviations in the range of 10^{-10}, as Figure 4.3 illustrates, is chosen for the reference scenario according to Table 4.1. Finally, the performance of the state estimation of the algebraic observer is validated, and the

(a) Error $e(x, T_\delta)$ in state transition of auxiliary problem (3.69).

(b) Error $e(x, T_\delta)$ in state transition of auxiliary problem (3.70).

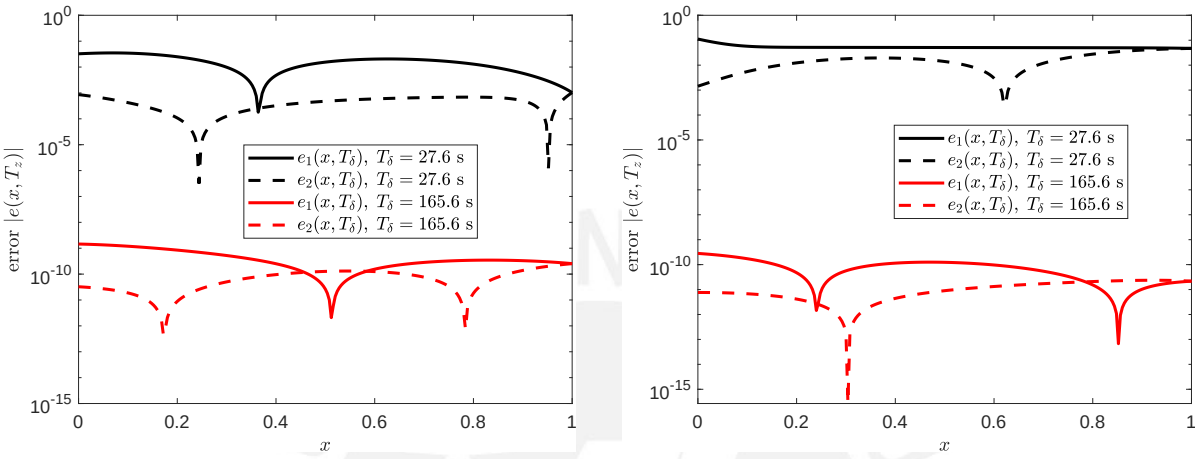

Figure 4.3.: Error $e(x, T_\delta) = \begin{bmatrix} e_1(x, T_\delta) & e_2(x, T_\delta) \end{bmatrix}^\top$ in state transition of the auxiliary problems (3.69) and (3.70) for $N = 0$, pipe parametrization according to the reference scenario in Table 4.1.

estimated states are utilized to localize the leak according to the leak localization observer system (3.19). Moreover, the influence of the approximation order N and the length T_δ of the moving time window on the accuracy of the leak localization is discussed. Therefore, the pipe is regarded in the reference scenario according to Table 4.1 with a leak of $1\ \%$ of the nominal flow that occurs after $t = 60$ s at the position $z^* = 10$ km. In Figure 4.4, the states estimated by the algebraic observer are presented at the end of the simulation time at $t = 1000$ s under variation of the length T_δ of the moving time window and the approximation order. At first glance, the algebraic observer estimates well the states of the transformed system (3.3). The estimates $\hat{u}(0, t)$ and $\hat{v}(0, t)$, that are needed to estimate the leak position according to (3.19), show deviations smaller than 10^{-3}, as the zoom indicates. However, small deviations in the estimated states are highly amplified in the leak localization observer system (3.19) by the factor $\frac{\sqrt{\beta\rho}}{A}$ that is in the range of 10^7. Consequently, the parametrization with an approximation order $N = 5$ and a moving time window of length $T_\delta = 165.6$ s is chosen to achieve the desired accuracy of the leak localization, while a shorter moving time window or a variation in the approximation order results in deviations of up to $50\ \%$ from the real leak position, as Figure 4.5 shows. Furthermore, as Figure 4.4 indicates, the states $\hat{u}(x, t)$ and $\hat{v}(x, t)$ estimated by the algebraic observer show the highest deviations near to the

(a) Estimated state $u(x, t_f)$.

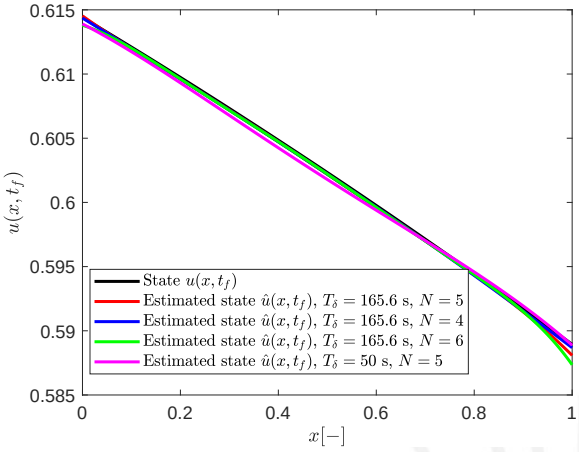

(b) Estimated state $v(x, t_f)$.

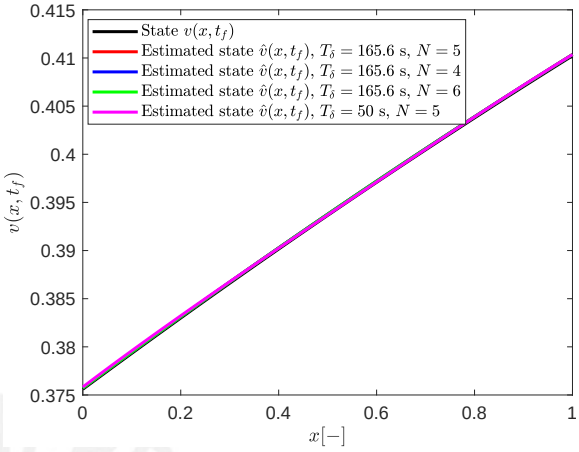

(c) Estimated state $u(x, t_f)$, Zoom at boundary $x = 0$.

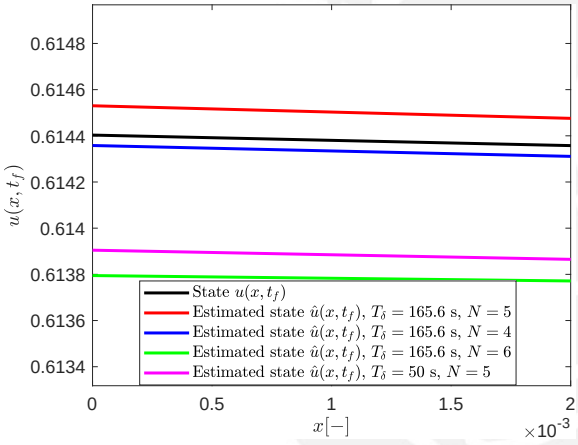

(d) Estimated state $v(x, t_f)$, Zoom at boundary $x = 0$.

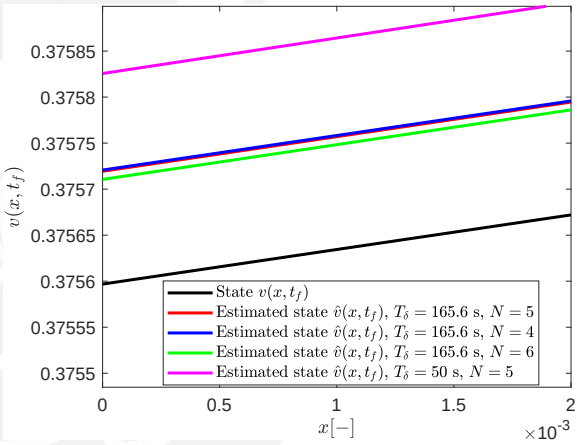

Figure 4.4.: Estimated states $u(x, t_f)$ (left) and $v(x, t_f)$ (right) at end time $t_f = 1000$ s of simulation under variation of the approximation order N and the length T_δ of the moving time window, pipe parametrization according to the reference scenario in Table 4.1 with leak of $1\ \%$ of the nominal flow occurring at $z^* = 10$ km.

boundaries $x = 0$ and $x = 1$, i.e. exactly where the state information is needed to localize the leak. This problem is well-known in the MFM community and can be explained by the orthonormal basis functions that reach their extremes at the boundaries, what increases the sensitivity to numerical errors. To improve the estimate accuracy at the boundaries and to allow thereby shorter moving time windows that lead to a faster convergence of the leak position estimate, future work could include homogenization of the transformed system (3.3). This homogenization ansatz requires the solution of (3.3) and splits it into two parts, a homogeneous solution and a particular solution.

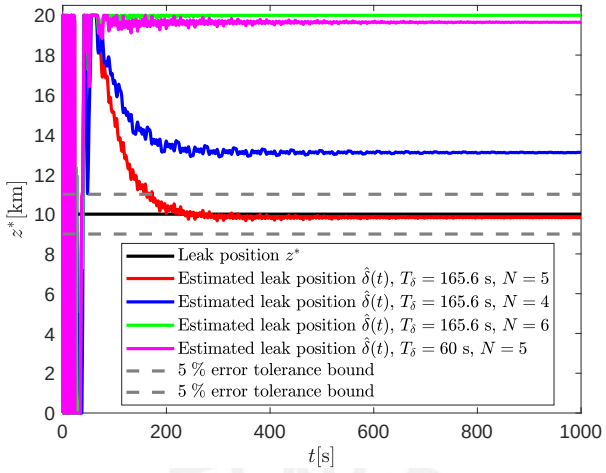

Figure 4.5.: Leak size localization for the pipe in the noise free reference scenario defined in Table 4.1 with leakage of 1 % of the nominal flow occurring after $t = 60$ s, variation of approximation order N and length T_δ of the moving time window of the algebraic observer, $\gamma = 0.2$.

Thereby, the known boundary information can be reflected better during the design of the algebraic observer [90].

In summary, this section has pointed out that the parametrization of the remaining degrees of freedom of the algebraic observer is not straightforward. The accuracy of the leak size estimation and leak localization exhibits strong sensitivity to this parametrization, such that a profound analysis has to be performed offline before the algebraic observer can be implemented. In light of this sensitivity, the following Section 4.2 validates the chosen parametrization by analyzing the accuracy of the algebraic observer, as well as of the ABSO, under various measurement and operating conditions.

4.2. KPI-based Evaluation of the Leak Observer Results for a Simulation Plant

This section presents and analyzes the performance of both observers under various measurement and operating conditions of the linear pipe model (2.4). Based on these comparative simulation studies, it is aimed at identifying advantages and limitations of both observer schemes. To evaluate the performance of both observers concisely, the following KPIs, as summarized in Table 4.2, are introduced: the mean error $\Delta\chi[\%]$ of the leak size estimation regarding the total leak size, the mean error $\Delta z^*[\%]$ of the leak localization regarding the total length of the pipeline, the standard deviations $\sigma_\chi[\frac{\text{l}}{\text{s}}]$ and $\sigma_z[\text{m}]$ of the estimated leak size and leak localization, the convergence times

$t_{\text{conv},\chi}$ and $t_{\text{conv},z}$ until the estimates are in the range of the accuracy specifications declared in Section 1.2.1 and the runtime t_{exec} of both observer schemes. The first two KPIs give indication about the accuracy of the observers, while the standard deviations $\sigma_\chi[\frac{\text{l}}{\text{s}}]$ and $\sigma_z[\text{m}]$ of the estimated leak size and leak localization serve as an indicator of the reliability of the estimates. A high standard deviation of the estimates indicates strong fluctuations, what makes a reasonable leak detection and localization more difficult for the user. Furthermore, the convergence times $t_{\text{conv},\chi}$ and $t_{\text{conv},z}$ are considered to rank how fast a leak can be detected and localized by both observer schemes. Finally, the runtime t_{exec} of both observer schemes is compared to verify the real-time capability. The indicated runtime includes the parts of the dynamic and the algebraic observer that have to be executed online according to the indications given in Figure 3.2 and Figure 3.4, i.e., the computational costs to calculate the observer gains $p_1(\cdot)$, $p_2(\cdot)$ of the ABSO or to generate the MFs of the algebraic observer are not included in the indicated runtimes.[1]

KPI	Variable name	Unit	
Mean Error (Leak size estimation)	$\Delta\chi$	$[\%]$	Accuracy
Mean Error (Leak localization)	Δz^*	$[\%]$	
Standard Deviation (Leak size estimation)	σ_χ	$[\frac{\text{l}}{\text{s}}]$	Reliability
Standard Deviation (Leak localization)	σ_z	[m]	
Convergence Time (Leak size estimation)	$t_{\text{conv},\chi}$	[s]	Rapidity
Convergence Time (Leak localization)	$t_{\text{conv},z}$	[s]	
Runtime	t_{exec}	[s]	Real-time capability

Table 4.2.: KPIs for the evaluation of the simulation-based leak size estimation and localization results.

4.2.1. Simulation-based Leak Observer Results under Variation of the Measurement Noise Level

In real technical applications, the measurements of physical variables of the system are always affected by measurement noise. Consequently, it is of great theoretical and practical interest to evaluate the performance of the leak observers when the measurements of the flow rate and the pressure are contaminated by noise. Hence, this section analyzes the performance of the dynamic and the algebraic observer regarding the KPIs defined in Chapter 4 for the case that white noise is added to the measurements of the simulation plant generated according to the explications given in the previous Section 4. To this end, three different measurement noise scenarios, as depicted in

[1] The implementation of both observer algorithms is done in MATLAB. The author does not claim to provide the runtime-optimal implementation. Hence, the indications on the runtime are rather to be understood as an upper limit of the runtime to verify the real-time capability of both observers in general.

Table 4.3 will be examined: (i) a low measurement noise level with standard deviations $\sigma_p = 100$ Pa and $\sigma_q = 10^{-5}\ \frac{\mathrm{m}^3}{s}$ of the white noise added to the flow rate and pressure measurements, (ii) a medium measurement noise level with standard deviations $\sigma_p = 250$ Pa and $\sigma_q = 10^{-4}\ \frac{\mathrm{m}^3}{s}$, and (iii) a high measurement noise level with standard deviations $\sigma_p = 400$ Pa and $\sigma_q = 2 \cdot 10^{-3}\ \frac{\mathrm{m}^3}{s}$.

	noise level		
standard deviation	low	medium	high
$\sigma_p[\mathrm{Pa}]$	100	250	400
$\sigma_q[\frac{\mathrm{m}^3}{s}]$	10^{-5}	10^{-4}	$2 \cdot 10^{-3}$

Table 4.3.: Definition of the standard deviations of the additive white Gaussian noise in the three noise scenarios.

It is pointed out that the standard deviations in the low noise scenario are in the range of the standard deviations that were observed for the sensors installed at the pilot plant at the PUCP.

Subsequently, the performance of the observers is examined in the reference scenario according to Table 4.1 for a single one-point leak that occurs after $t = 60$ s at $z^* = \frac{\ell}{2} = 10$ km and whose size $\chi = 10^{-3}\ \frac{\mathrm{m}^3}{\mathrm{s}} = 1\ \frac{\mathrm{l}}{\mathrm{s}}$ represents $1\ \%$ of the nominal flow. The noise corrupted data of the pressure and the flow rate at the inlet and the outlet is utilized without any prefiltering.

The PDE system, that realizes the leak size and state estimation part of the ABSO, is implemented via the MOL with a discretization of $n = 500$ nodes. The tunable observer gains of the ABSO were adjusted according to the tuning guidelines indicated in Section 3.2 resulting in $L = -0.3$ for the leak size estimation and $\gamma = 0.2$ for the leak localization. The algebraic, MFM-based observer uses the same leak localization gain γ while the moving time horizons of the MFs for leak detection and localization are given as derived in the previous Section 4.1 by $T_\chi = 130$ s and $T_\delta = 165.6$ s, respectively, and an approximation order of $N = 5$ is used for the function expansion (3.67). Both observers are implemented with a sampling time of 10 ms.

The results for the low noise scenario are shown in Figure 4.6. For reasons of better illustration, the leak size χ will always be displayed in $\frac{\mathrm{l}}{\mathrm{s}}$ and the leak position z^* in km. In Table 4.4 the resulting KPIs are listed. KPIs where the ABSO outperforms the algebraic observer are highlighted in bold type, and vice versa.

It is observed that both observers fulfill the desired specifications. The mean error w.r.t. the leak size is smaller than $0.13\ \%$ and smaller than $0.75\ \%$ w.r.t. the leak localization for both observers. It is noticed that the ABSO performs better regarding the accuracy of the leak size estimation while the algebraic, MFM-based observer reaches a better accuracy of the leak localization. The deviations of the estimates are in the same range for both observers and significantly less than the respective $5\ \%$ error tolerance bounds, such that a reliable estimate of the leak size and leak position is provided. Furthermore, for both observers the needed runtime is significantly smaller than the simulated time of $t_{sim} = 1000$ s such that the real-time capability of both observers is

proven. It is observed that the ABSO requires less runtime than the algebraic observer. A further visible difference in the performance of both observers can be seen in the convergence time. While the algebraic observer needs about 77.13 s and 195.41 s to reach the error bound of deviations smaller than $5\ \%$, the dynamic observer provides much faster a reliable estimation of the leak size and localization by needing only 24.45 s and 142.21 s. Consequently, the ABSO indicates faster the appearance of a leak and allows localizing the leak more rapidly.

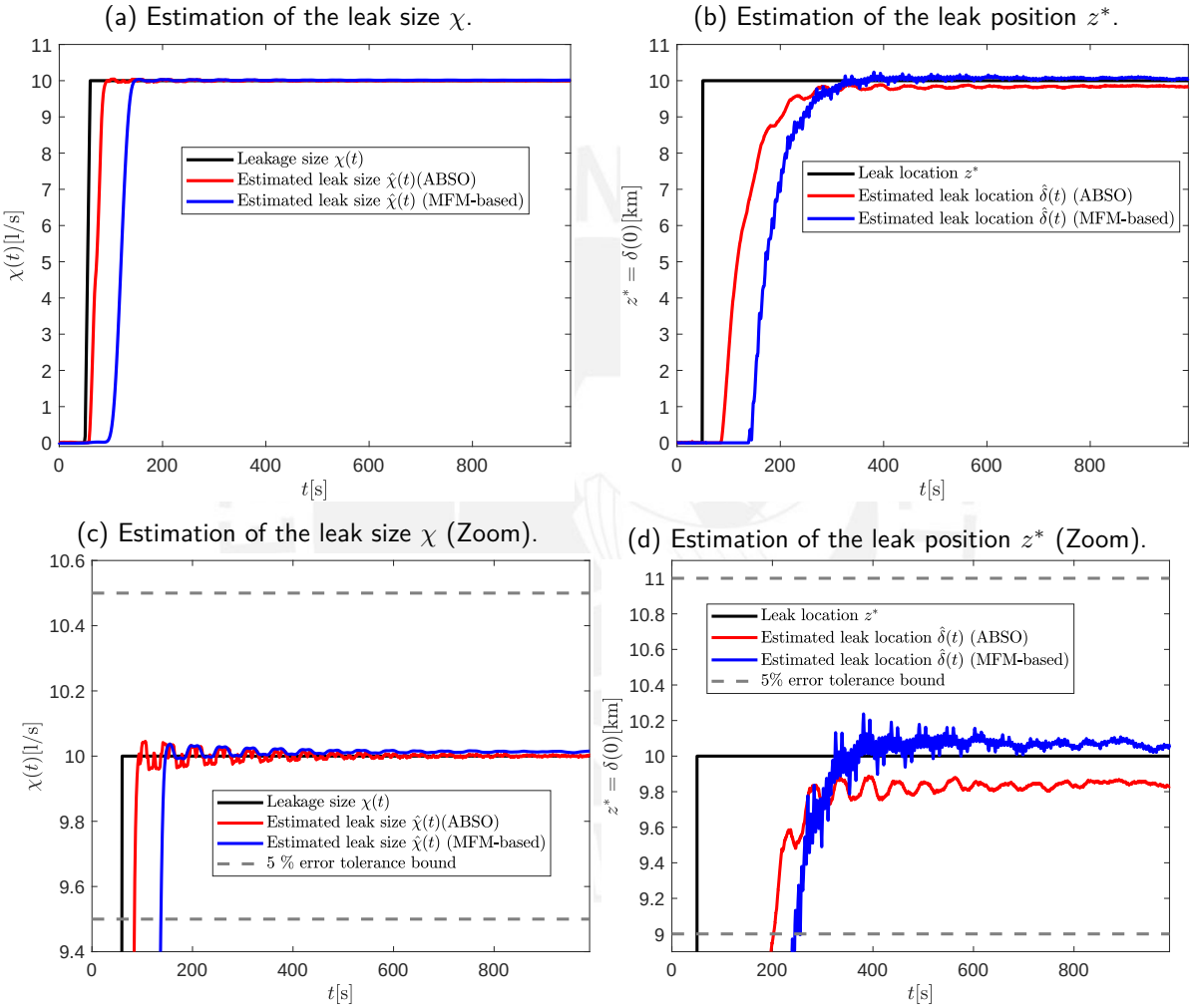

Figure 4.6.: Estimation of the leak size (left) and leak localization (right) for the simulation plant in the low noise case.

The results of the medium noise scenario, that are displayed in Figure 4.7 and Table 4.5, solidify the conclusions drawn from the low noise scenario. Both observers perform well regarding the leak size estimation and leak localization and overfulfill the predefined accuracy objectives visibly. The ABSO performs better regarding the leak size estimation with a mean error smaller than $0.003\ \%$

KPI / Observer	$\Delta\chi$[%]	Δz^*[%]	$\sigma_\chi[\frac{\text{l}}{\text{s}}]$	σ_z[m]	$t_{\text{conv},\chi}$[s]	$t_{\text{conv},z}$[s]	t_{exec}[s]
Dynamic Observer (ABSO)	$\mathbf{0.003}$	0.75	0.003	$\mathbf{20.38}$	$\mathbf{24.45}$	$\mathbf{142.21}$	$\mathbf{35.69}$
Algebraic Observer (MFM-based)	0.13	$\mathbf{0.35}$	$\mathbf{0.002}$	24.43	77.13	195.41	135.57

Table 4.4.: KPIs of the dynamic and the algebraic observer in the low noise scenario.

while the algebraic observer gives a smaller deviation regarding the leak localization. The standard deviations of both estimates are smaller than 0.25 % of the mean values of the estimates, such that reliable estimates are provided once the observers have converged. This desirable convergence behaviour is also illustrated graphically by Figure 4.7 where the estimates stay inside the error tolerance bound and show oscillations of smaller than 0.2 % once the observers have converged. A significant difference between both observers is identified w.r.t. the convergence speed. The ABSO needs about 50 s less to provide estimates of the leak size and the leak localization which differ less than 5 % from the real value. Furthermore, both observers are real-time capable, whereby the implementation of the ABSO requires significantly less runtime.

KPI / Observer	$\Delta\chi$[%]	Δz^*[%]	$\sigma_\chi[\frac{\text{l}}{\text{s}}]$	σ_z[m]	$t_{\text{conv},\chi}$[s]	$t_{\text{conv},z}$[s]	t_{exec}[s]
Dynamic Observer (ABSO)	$\mathbf{0.009}$	0.79	0.006	$\mathbf{37.92}$	$\mathbf{24.44}$	$\mathbf{144.01}$	$\mathbf{33.12}$
Algebraic Observer (MFM-based)	0.13	$\mathbf{0.36}$	$\mathbf{0.004}$	46.50	77.08	195.25	145.81

Table 4.5.: KPIs of the dynamic and the algebraic observer in the medium noise scenario.

Finally, the high noise scenario is investigated. In this scenario, the standard deviation of the white noise added to the flow rate measurements represents 20 % of the leak size, leading to an SNR of 13.9 dB, while the standard deviation of the white noise added to the pressure measurements is in the range of 35 % of the pressure change caused by the leak. These numbers stress the severe measurement conditions under which the observers have to detect and localize the leak in the high noise scenario.

Nevertheless, concerning the mean errors of the leak size and leak position estimates, the observers still perform well and fulfill the predefined objectives by providing estimates with a mean error significantly smaller than 1 %. However, it is seen that the noise causes a drastic increase in the standard deviations of the estimates. The standard deviations indicate that the algebraic observer filters better the noise w.r.t. the leak size estimation, while the ABSO gives a less oscillating estimate of the leak position. As Figure 4.8 illustrates graphically, in particular the estimates of

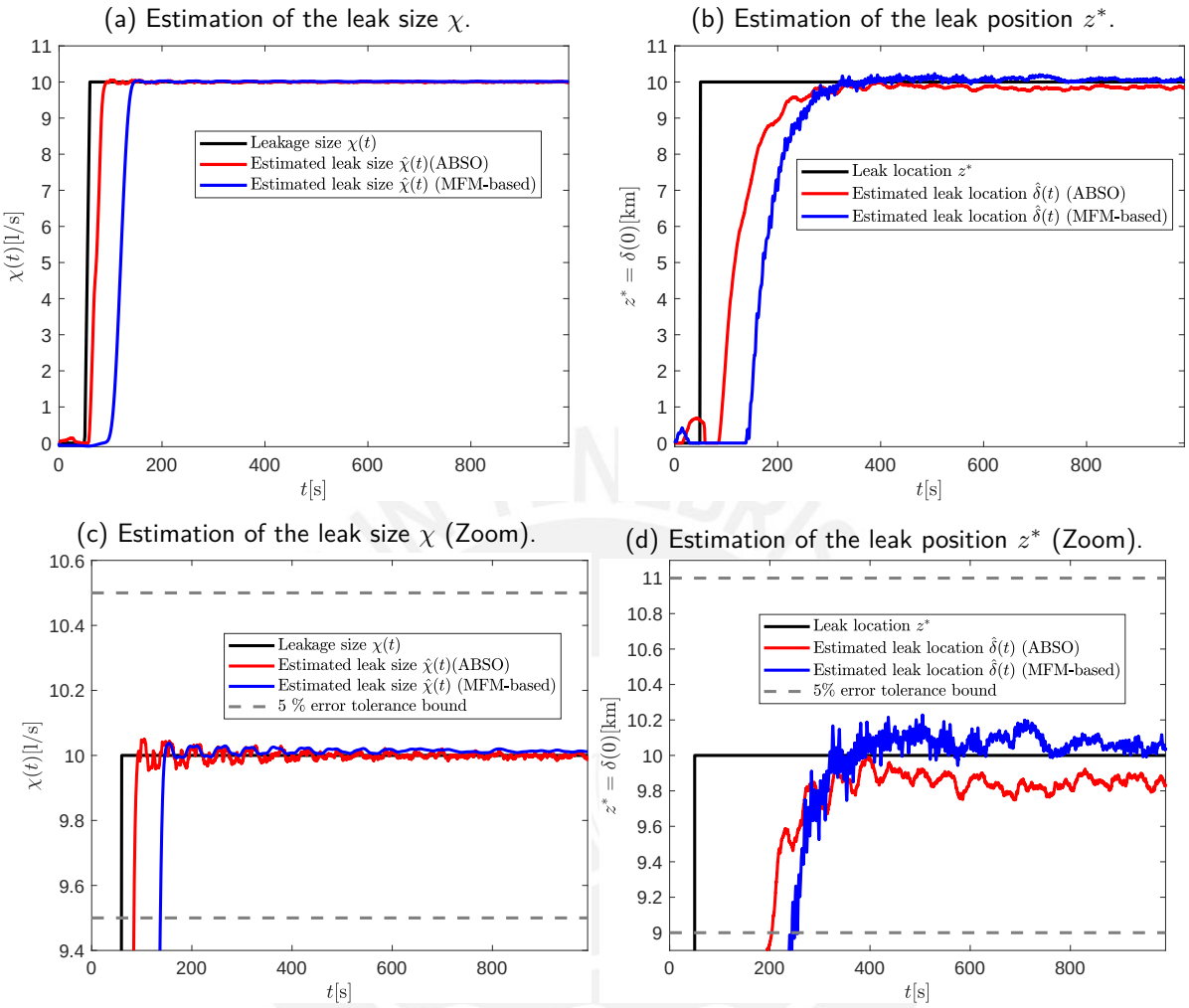

Figure 4.7.: Estimation of the leak size (left) and leak localization (right) for the simulation plant in the medium noise case.

the leak position oscillate strongly such that the estimated leak positions need over 11 min to stay inside the predefined error tolerance bounds. Therefore, it is recommended to filter the leak position estimates in the high noise scenario. To this end, the estimates are passed by a moving average filter with a length of $T = 40$ s. By applying this additional filter, it is achieved, that the standard deviation of the leak position estimates significantly reduces such that the filtered estimates stay inside the predefined error tolerance bounds once the error is smaller than 5 % w.r.t. the total pipe length. Thereby, a more reliable estimation of the leak position is provided to the user.

Altogether, the analysis of the performance of both observers under different measurement noise scenario demonstrates that the ABSO and the algebraic, MFM-based observer, fulfill the predefined objectives by providing accurate estimates of the leak size and leak position. Both observers are

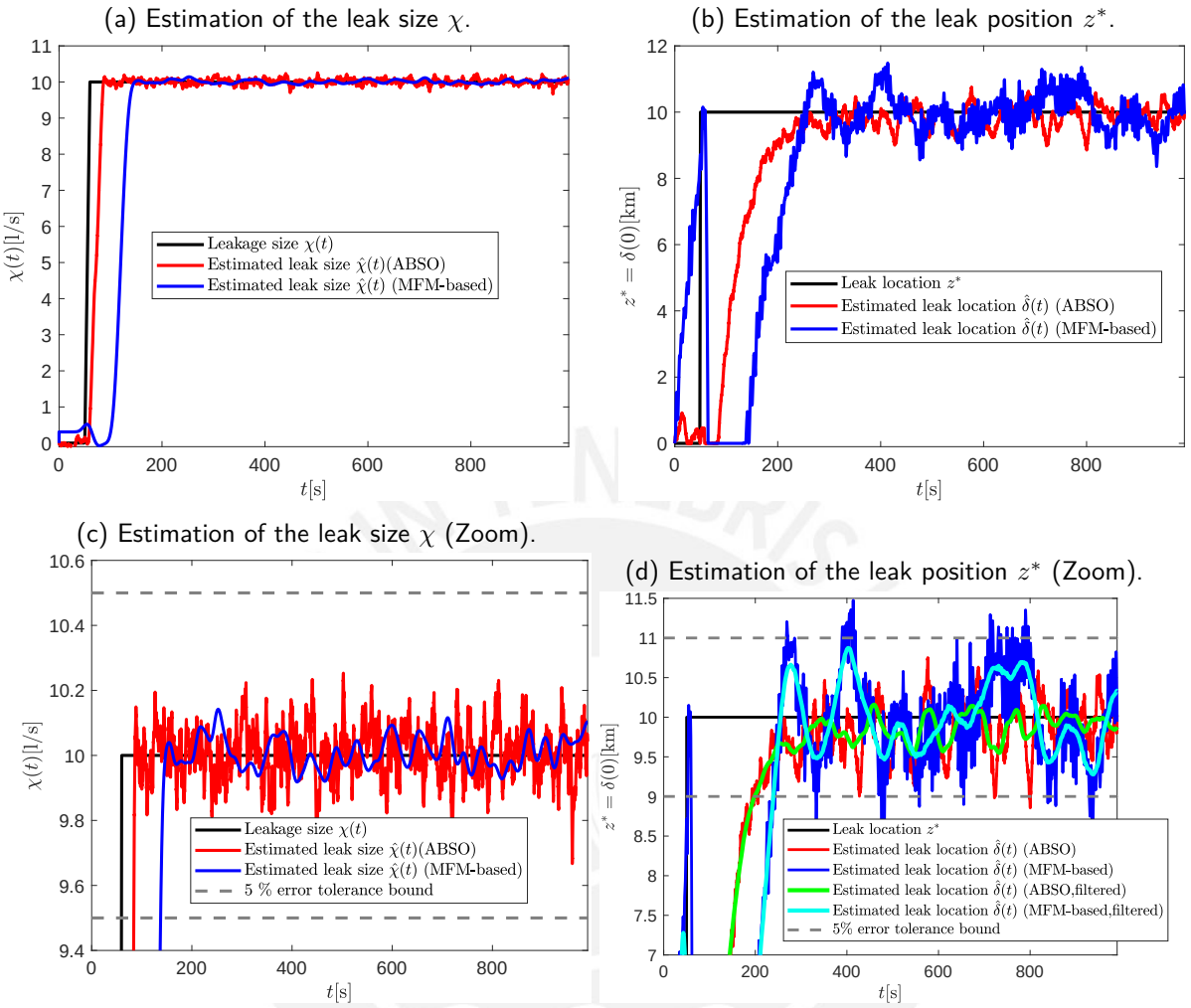

Figure 4.8.: Estimation of the leak size (left) and leak localization (right) for the simulation plant in the high noise case.

KPI / Observer	$\Delta\chi$[%]	Δz^*[%]	$\sigma_\chi[\frac{\text{l}}{\text{s}}]$	σ_z[m]	$t_{\text{conv},\chi}$[s]	$t_{\text{conv},z}$[s]	t_{exec}[s]
Dynamic Observer (ABSO)	**0.11**	0.55	0.08	**330.58**	**24.09**	**740.98**	**31.37**
Algebraic Observer (MFM-based)	0.14	**0.13**	**0.03**	533.33	77.25	878.37	160.17

Table 4.6.: KPIs of the dynamic and the algebraic observer in the high noise scenario.

real-time capable and show a certain robustness to measurement noise. For noise levels comparable to industrial flow rate and pressure sensors, both observers reach the predefined accuracy objectives and provide estimates with mean errors significantly smaller than $1\ \%$. It is noticed, that for both

observers, the leak size can be estimated with a higher accuracy. Moreover, the results of the high noise scenario illustrate that especially the estimation of the leak position is affected significantly by the measurement noise. The standard deviation of the estimates increases drastically, such that the estimated leak position does not stay in between the error tolerance bounds. Nevertheless, an additional filtering of the estimated leak position estimates by a moving average filter improves the results visibly such that reliable estimates with oscillations significantly smaller than the error tolerance bounds are achieved.

Additionally, significant differences in the performance of both observers are noticed regarding the convergence time and the runtime. The ABSO has speed advantages over the algebraic observer and leads to lower runtimes that are needed to execute the MATLAB code. Moreover, the estimates need a shorter convergence time to reach the predefined error tolerance bounds.

The following sections, that analyze the impact of the leak size, the leak localization, the boundary conditions and of model uncertainties, will apply the medium noise level scenario and, if not otherwise stated, the same parametrization of the observers as in this Section 4.2.1.

4.2.2. Simulation-based Leak Observer Results under Variation of the Leak Size

This section analyzes the performance of the dynamic and the algebraic observer under variations of the leak size. In real water pipelines, leaks with different magnitudes do appear, depending on whether the leak is a small background leak or caused by an entire pipe burst. For example, the case study of a real water distribution network presented in [91], distinguishes leak scenarios that range from leak magnitudes smaller than $1\ \%$ w.r.t. the nominal flow up to leak sizes of almost $50\ \%$. Keeping this wide range of possible leak sizes in mind, it is of great practical importance to verify in simulation that both observers are capable to detect and localize relatively small leakages as well as leakages with a large magnitude. Therefore, this section aims at verifying that both observers detect and localize larger as well as smaller leakages in an accurate and reliable way. In this context, the identification of the minimal leak size that can be detected and localized is of special interest.

Firstly, the performance of both observers for a leak of large magnitude is examined. To this end, the simulation plant according to Table 4.1 is regarded in the reference scenario including measurement noise as in the medium noise case. The appearance of a single one-point leak after $t = 60$ s at $z^* = \frac{\ell}{2} = 10$ km with a leak magnitude of $\chi = 0.2\ \frac{\mathrm{m}^3}{\mathrm{s}}$, that represents $20\ \%$ of the nominal flow, is simulated. According to Remark 5, the convergence speed depends linearly on the leak size χ. As a consequence, the amplification of measurement noise in the leak localization observer (3.19) also rises if the leak size χ augments. To take this into account, the leak localization observer gain γ is lowered to $\gamma = 0.02$, for the ABSO as well as for the algebraic, MFM-based

observer.

The Figure 4.9 compares the results graphically, while Table 4.7 compares the resulting KPIs of both observers for the scenario of a large leak. It is observed, that the convergence time to estimate the leak size is comparable to previous cases (see e.g. Table 4.5) while the leak position can be estimated around $30\ \%$ much faster. Moreover, it is still noticed that the ABSO needs a shorter convergence time to provide accurate results of the leak size and position. Furthermore, for both observers, the mean error of the leak localization reduces to about $0.1\ \%$ while the standard deviations of the leak position estimates stay in the same range as in the case of a smaller leak of $1\ \%$ of the nominal flow (see Table 4.5).

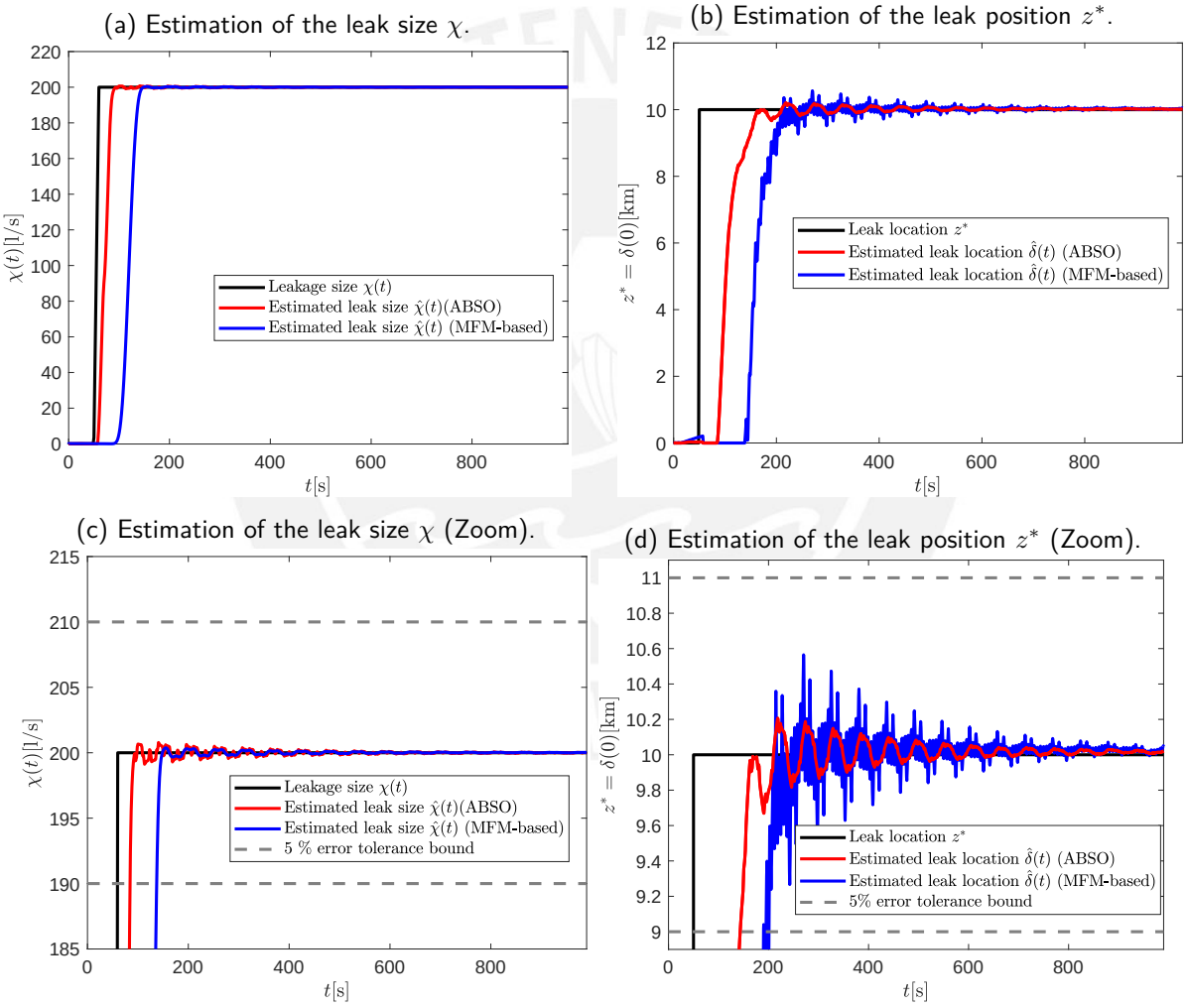

Figure 4.9.: Estimation of the leak size (left) and leak localization (right) for the simulation plant for a large leak of $20\ \%$ of the nominal flow.

This analysis of the leak observer performance in the case of a bigger leak confirms the intuitive

Observer \ KPI	$\Delta\chi$[%]	Δz^*[%]	$\sigma_\chi[\frac{\text{l}}{\text{s}}]$	σ_z[m]	$t_{\text{conv},\chi}$[s]	$t_{\text{conv},z}$[s]	t_{exec}[s]
Dynamic Observer (ABSO)	$\mathbf{6 \cdot 10^{-4}}$	$\mathbf{0.09}$	0.05	$\mathbf{19.45}$	$\mathbf{24.43}$	$\mathbf{83.25}$	$\mathbf{31.85}$
Algebraic Observer (MFM-based)	0.006	0.13	$\mathbf{0.03}$	38.10	77.25	140.91	163.36

Table 4.7.: KPIs of the dynamic and the algebraic observer for a big leak (20 % of the nominal flow).

assumption that leaks with larger magnitudes can be localized more rapidly and more accurate due to its stronger impact on the changes of the fluid dynamics.

In the following, the case of a leak smaller than 1 % of the nominal flow is investigated. Thereby, we aim at validating the ability of both observers to identify small leaks like they do appear, e.g., because of a leaking joint part or due to intentional provoked leaks. In these scenarios, the leak detection and localization problem becomes an even more challenging problem due to the small effects of the leak on the fluid dynamics and due to resolution limits caused by the measurement noise. The following Figure 4.10 and Table 4.8 contrast the performance of both observers for a leak size of $\chi = 10^{-3}\ \frac{\text{m}^3}{s}$ that represents 0.1 % of the nominal flow. Due to the small leak and the thereby provoked smaller convergence rate (see Remark 5), the observer gain for leak localization is changed to $\gamma = 0.6$. The standard deviations of the measurement noise are chosen as in the medium noise scenario defined in Table 4.3. Consequently, the noise causes an SNR of 20 dB between leak size and flow rate measurement noise, and an SNR of -7.3 dB between total pressure change caused by the leak and pressure measurement noise. The results for this case of a small leak illustrate that the algebraic, MFM-based outperforms the ABSO visibly w.r.t. the accuracy of the leak position estimation. While the ABSO is not able to reach the predefined error bound and shows deviations after convergence of about 2 km from the real leak position, the algebraic observer provides an accurate and reliable estimated leak position. The mean error and the standard deviation of the estimate is higher than in the reference case of a leak of 1 % of the nominal flow (see Table 4.5), but still lies clearly inside the predefined error bounds. Furthermore, it is noticed that the smaller leak size causes a slower convergence of the leak localization estimation. A simple increase in the observer gain γ is not recommended since it would lead to a stronger amplification of the measurement noise. Besides, both observers fulfill the predefined accuracy objective regarding the leak size estimation clearly, whereby the ABSO provides an estimate with a significantly smaller mean error.

To improve the accuracy of the ABSO regarding the leak localization, the only remaining tuning parameter is the number of spatial discretization nodes n. In this scenario, a number of $n = 1200$ spatial discretization nodes is needed to reach predefined accuracy goals. As Figure 4.10 illustrates,

the larger number of nodes allows the ABSO to estimate the leak position with the desired accuracy, although the accuracy of the ABSO is still less than the one by the algebraic observer. Moreover, the higher number causes also higher computational, emerging by a runtime of $t_{\text{exec}} = 333.10$ s.

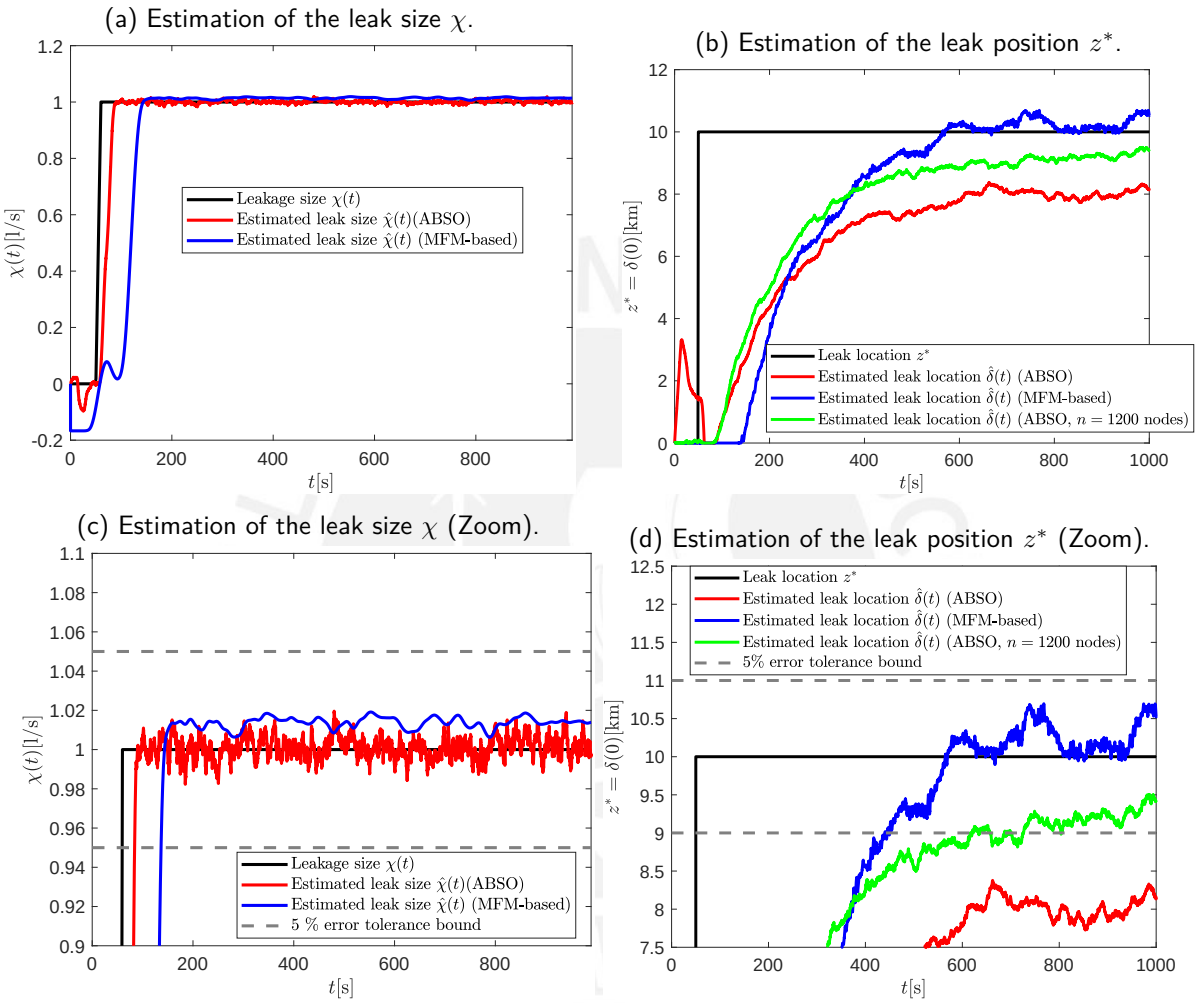

Figure 4.10.: Estimation of the leak size (left) and leak localization (right) for the simulation plant for a small leak of 0.1 % of the nominal flow.

As a concluding statement, this section demonstrates that both observers perform with the desired accuracy concerning leak size and leak localization if leaks with a magnitude greater than 1 % are regarded. In this context, a larger leak magnitude can be localized more accurate and faster by both observers due to the stronger impacts on the fluid dynamics regarding the pressure and the flow rate drop. Concerning a small leak of 0.1 % of the nominal flow, it is shown that the algebraic observer performs significantly better than the ABSO w.r.t. the estimation of the leak

KPI / Observer	$\Delta\chi$[%]	Δz^*[%]	$\sigma_\chi[\frac{\text{l}}{\text{s}}]$	σ_z[m]	$t_{\text{conv},\chi}$[s]	$t_{\text{conv},z}$[s]	t_{exec}[s]
Dynamic Observer (ABSO)	**0.09**	10.33	0.005	226.19	**24.13**	–	**33.72**
Algebraic Observer (MFM-based)	1.40	**1.66**	**0.003**	**202.25**	76.63	**390.20**	147.87

Table 4.8.: KPIs of the dynamic and the algebraic observer for a small leak (0.1 % of the nominal flow).

position. The only way to reach the same accuracy range for the ABSO is increasing the number of spatial discretization nodes, what implies at the same time higher computational costs.

4.2.3. Simulation-based Leak Observer Results under Variation of the Leak Localization and Distribution

Besides the leak magnitude, the leak position and the shape of the leak distribution function is another important part of the leak characteristics whose impact on the observer performance has to be evaluated. In previous works that investigated on the design of a KF for the leak detection and localization problem, it has turned out that the accuracy of the leak position estimated by the KF got significantly worse if the leak appears near to the inlet or the outlet of the pipe [40]. To figure out, whether this problem also arises for the here concerned late-lumped, dynamic and algebraic observer, the reference scenario will be regarded with a leak near to the inlet and near to the outlet of the pipe. Furthermore, the previous Sections 4.2.1 and 4.2.2 examined only the case of one-point leakages where the leak distribution function is assumed as a Dirac impulse. This assumption might be reasonable if intentionally caused leaks or leaking joints are concerned. For an entire pipe burst, that is caused, e.g., by ground movement, where the leakage appears distributed over a wider range of the entire pipe, the assumption of a one-point leak does not seem to be adequate. Therefore, the section addresses this case by assuming the leak distribution function as rectangular and by evaluating the resulting observer performance.

Firstly, the case of leakages near to the inlet and near to the outlet is examined. To this end, the reference scenario of the simulation plant with medium measurement noise level is regarded for the case that a one-point leak with a leak size of 1 % of the nominal flow appears at $z^* = 2$ km and $z^* = 18$ km. For the first case, an observer gain of $\gamma = 0.1$ and for the second case of $\gamma =$ was chosen. The Figures 4.11 and 4.12 show the results graphically, while the Tables 4.9 and 4.10 contrast the resulting KPIs of both observers. It is noticed that in both cases, the accuracy of the leak size estimation and leak localization is in the same range as for the case that the leak appears in the middle of the pipe (see Table 4.5). The desired accuracy is clearly achieved, and

a reliable estimate is provided by both observers. Again, it is observed that the ABSO performs better w.r.t. the convergence speed, the runtime, and the accuracy of the leak size estimation while the algebraic observer achieves a higher accuracy of the estimated leak position.

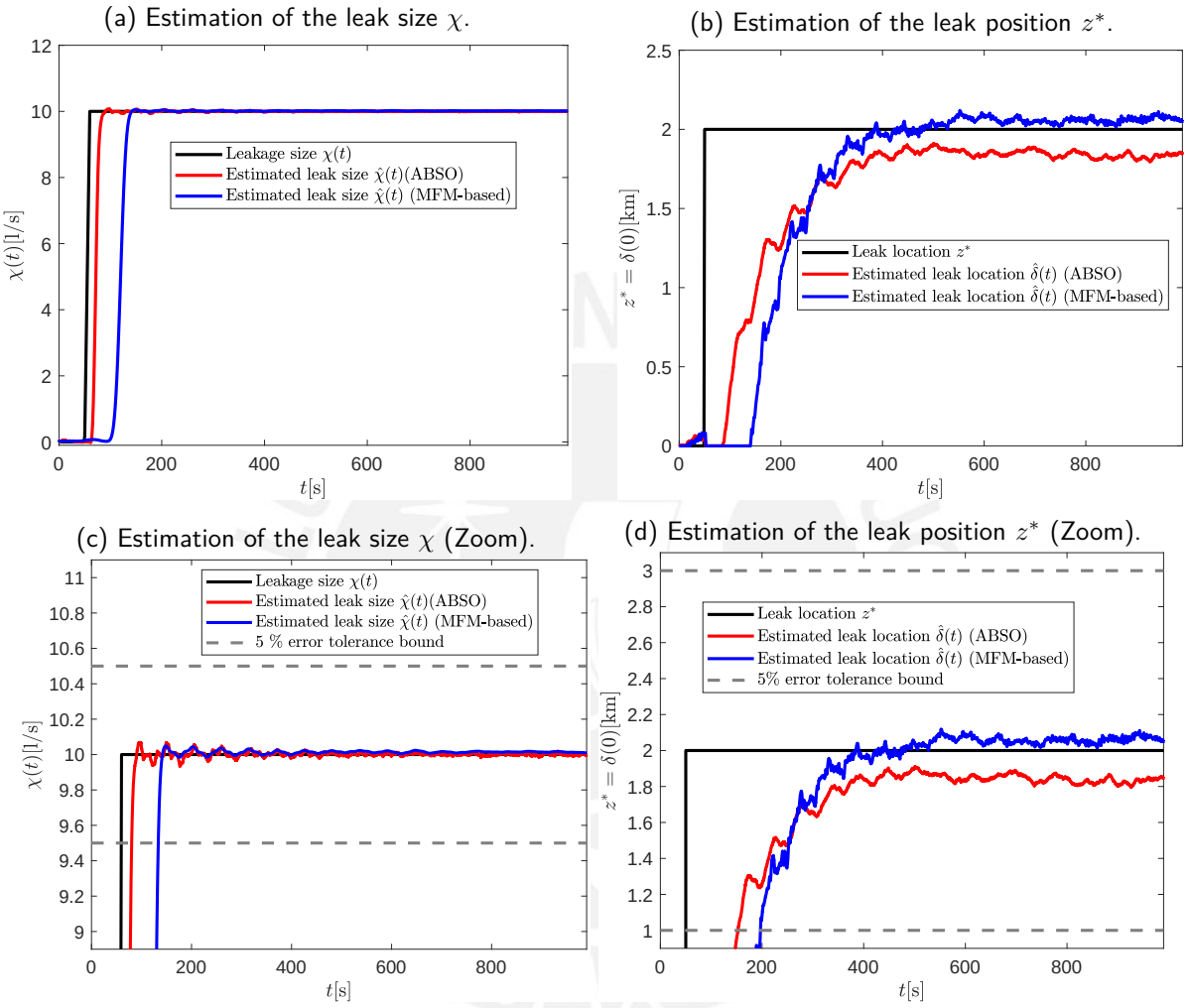

Figure 4.11.: Estimation of the leak size (left) and leak localization (right) for the simulation plant for a leak of 1 % of the nominal flow appearing at $z^* = 2$ km.

Finally, the case of a pipe burst distributed over a wider range of the pipe is examined. To this end, the leakage is assumed to be modelled by a rectangular shape leak distribution function that is centred at $z^* = 10$ km and that has a width of 500 m in each direction. As derived in A.1, the relationship $\delta(z = 0) = z^*$ also holds true for a rectangular-shaped leak distribution function. The Figure 4.13 and the Table 4.11 compare the performance of the dynamic and the algebraic observer for the case of a rectangular-shaped leakage of 1 % of the nominal flow. The accuracy of the leak position is indicated w.r.t. the centre of the rectangular leak distribution function. It is

Observer \ KPI	$\Delta\chi$[%]	Δz^*[%]	$\sigma_\chi[\frac{\text{l}}{\text{s}}]$	σ_z[m]	$t_{\text{conv},\chi}$[s]	$t_{\text{conv},z}$[s]	t_{exec}[s]
Dynamic Observer (ABSO)	**0.01**	0.79	0.007	20.84	**20.29**	**90.01**	**49.29**
Algebraic Observer (MFM-based)	0.14	**0.29**	**0.004**	**19.84**	73.50	140.90	147.34

Table 4.9.: KPIs of the dynamic and the algebraic observer for a leak of $1\ \%$ of the nominal flow appearing at $z^* = 2$ km.

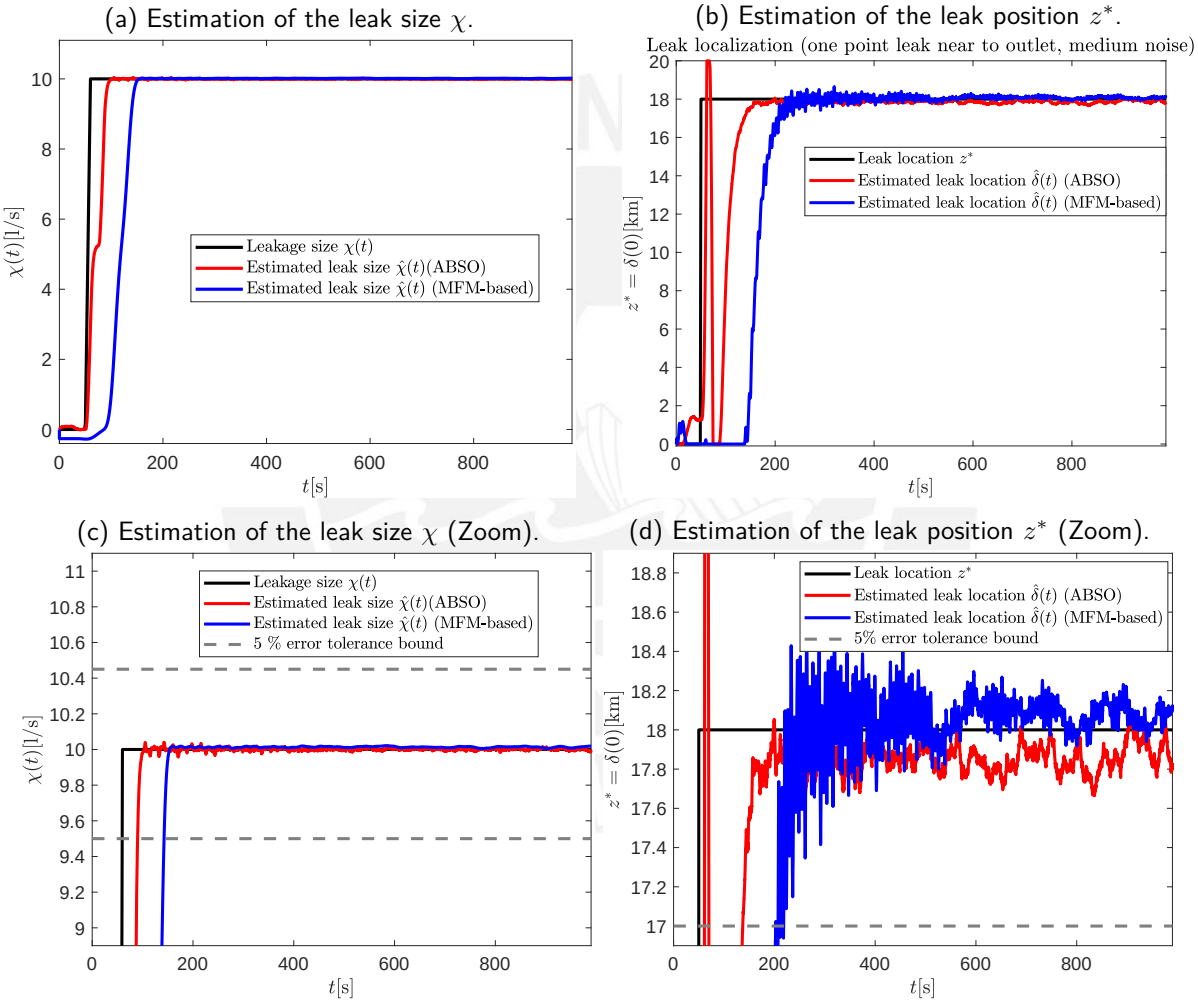

Figure 4.12.: Estimation of the leak size (left) and leak localization (right) for the simulation plant for a leak of $1\ \%$ of the nominal flow appearing at $z^* = 18$ km.

seen that the accuracy of the leak size estimation and the leak localization is in the same range as for a one-point leak (see Table 4.5). The algebraic observer outperforms the ABSO in the accuracy

Observer \ KPI	$\Delta\chi$[%]	Δz^*[%]	$\sigma_\chi[\frac{\text{l}}{\text{s}}]$	σ_z[m]	$t_{\text{conv},\chi}$[s]	$t_{\text{conv},z}$[s]	t_{exec}[s]
Dynamic Observer (ABSO)	$\mathbf{0.006}$	0.73	0.005	$\mathbf{72.56}$	$\mathbf{30.04}$	$\mathbf{77.3}$	$\mathbf{35.38}$
Algebraic Observer (MFM-based)	0.14	$\mathbf{0.07}$	$\mathbf{0.004}$	96.12	82.58	140.29	145.76

Table 4.10.: KPIs of the dynamic and the algebraic observer for a leak of $1\ \%$ of the nominal flow appearing at $z^* = 18$ km.

of the leak localization. On the contrary, the ABSO provides a faster convergence speed as well as a more accurate leak size estimation and needs less runtime. Thereby, it is shown that the desired accuracy objectives are also achieved for leakages that appear over a wider range of the pipe.

Observer \ KPI	$\Delta\chi$[%]	Δz^*[%]	$\sigma_\chi[\frac{\text{l}}{\text{s}}]$	σ_z[m]	$t_{\text{conv},\chi}$[s]	$t_{\text{conv},z}$[s]	t_{exec}[s]
Dynamic Observer (ABSO)	$\mathbf{0.010}$	1.03	0.006	$\mathbf{41.67}$	$\mathbf{24.38}$	$\mathbf{144.70}$	$\mathbf{34.29}$
Algebraic Observer (MFM-based)	0.14	$\mathbf{0.05}$	$\mathbf{0.003}$	42.86	77.13	196.22	175.18

Table 4.11.: KPIs of the dynamic and the algebraic observer for a leak of $1\ \%$ of the nominal flow appearing at $z^* = 10$ km and over a width of 500 m.

In summary, this section has demonstrated two important performance characteristics of both observers. Firstly, both observers perform well and with a comparable accuracy regardless where the leak occurs. Observations, that the leak localization gets worse for leaks near to the inlet or near to the outlet, as it is the case for the KF [40], were not made. Moreover, the performance of both observers is maintained if an entire pipe burst over a wider range of the pipe modelled by a rectangular-shaped leak distribution function is concerned instead of a one-point leak. Consequently, and in conjunction with the investigations on the leak size presented in Section 4.2.2, the ability of both observers to detect and localize accurately leaks of various characteristics is shown.

4.2.4. Simulation-based Leak Observer Results under Variation of the Operating Point

In this section, the performance of both observers under variation of the operating point is examined. Like already discussed in Section 2.1.1, the linear pipe model (2.4) is only valid to an operating point where the flow rate stays approximately constant. Furthermore, Section 4.1 pointed out that the leak localization accuracy provided by the algebraic observer is highly sensitive w.r.t. the choice

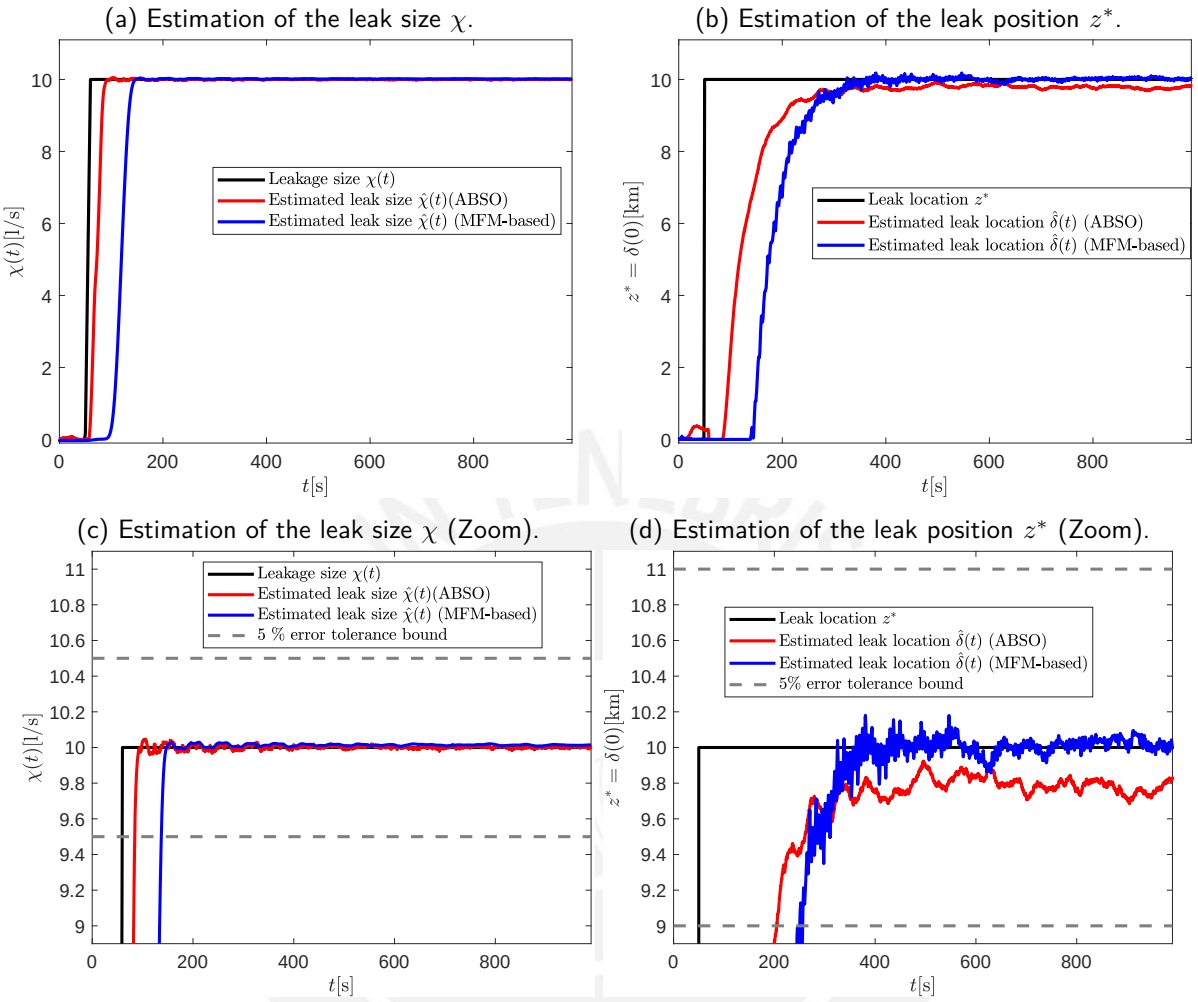

Figure 4.13.: Estimation of the leak size (left) and leak localization (right) for the simulation plant for a leak of 1 % of the nominal flow appearing at $z^* = 10$ km and over a width of 500 m.

of the tuning parameters. Considering these two aspects, it is of great interest to verify that the algebraic observer also performs well if another operating point is regarded. To this end, this section investigates two different scenarios: the first scenario is similar to the reference scenario according to Table 4.1 with a different constant inlet flow rate $q_0(t)$ while the second case considers sinusoidal oscillations in the inlet flow rate $q_0(t)$ and the outlet pressure $p_\ell(t)$, e.g., to model changes in the supply at the inlet or in the demand at the outlet.

The first scenario is defined as given by the reference scenario in Table 4.1, but with a different inlet flow rate of $q_0(t) = 1.5\ \frac{\mathrm{m}^3}{s}$. Analogue to the reference scenario, the friction factor F is calculated again for this nominal flow $q_0(t)$ using the Haaland Equation (2.9) what results in

$F = 13.02\ \frac{\text{kg}}{\text{m}^3 \cdot \text{s}}$. In light of the changed operating conditions, the lengths T_χ and T_δ of the moving time windows of the algebraic observer were readjusted. The tuning process, similar to Section 4.1, resulted in lengths of $T_\chi = 180$ s and $T_\delta = 100$ s for the leak size estimation and leak localization, respectively. Further parameters of the algebraic observer remain unchanged in comparison to Section 4.1 as well as the parametrization of the ABSO.

In Figure 4.14, the resulting leak size and leak position estimates of the ABSO and the algebraic observer are displayed graphically. It is observed, that both observers detect well the leak and estimate the leak size with deviations significantly below $0.1\ \%$. However, the accuracy of the leak localization differs visibly between the two observers. This impression is confirmed numerically by the respective KPIs that are listed in Table 4.12. While the mean error of the leak position estimate provided by the ABSO reaches more rapidly the error tolerance bound and shows deviations of about 250 m from the real the leak position, the algebraic observer needs over 5 min to provide a leak position estimate with deviations of under $5\ \%$ w.r.t. to the total length of the pipe. Moreover, the deviations of the estimated leak position from the real leak position remain in the range of 800 m signifying a notably less accuracy than the ABSO.

KPI / Observer	$\Delta\chi$[%]	Δz^*[%]	$\sigma_\chi[\frac{\text{l}}{\text{s}}]$	σ_z[m]	$t_{\text{conv},\chi}$[s]	$t_{\text{conv},z}$[s]	t_{exec}[s]
Dynamic Observer (ABSO)	0.02	$\mathbf{1.23}$	0.006	$\mathbf{26.74}$	$\mathbf{24.39}$	$\mathbf{82.02}$	$\mathbf{36.53}$
Algebraic Observer (MFM-based)	$\mathbf{0.008}$	$\mathbf{4.54}$	$\mathbf{0.003}$	36.95	100.34	323.19	155.23

Table 4.12.: KPIs of the dynamic and the algebraic observer for a leak of $1\ \%$ of the nominal flow $q_0(t) = 1.5\ \frac{\text{m}^3}{s}$ appearing at $z^* = 10$ km.

Furthermore, it is commented that the accuracy of the leak localization estimation of the ABSO could be further improved by introducing more spatial nodes, while there was not found any parametrization of the algebraic observer that would improve the leak localization accuracy in this case. This observation underlines the high sensitivity of the algebraic observer w.r.t. the tuning parameters and the challenging problem of parametrizing well the algebraic observer.

In the second scenario, that will be discussed in this section, the inlet flow $q_0(t)$ and the outlet pressure $p_\ell(t)$ are chosen to oscillate sinusoidally about a mean value. The interest in these boundary conditions is twofold. Firstly, the previous analysis has shown the tuning parameters of the algebraic observer have to be adjusted if the operating point changes. Therefore, it is worthwhile to subject the algebraic observer to a stress test if the operating conditions are not constant. Secondly, the case of slowly varying operating conditions represents an interesting use case of the pipe, e.g, to model variations in the demand at the end of the pipe or in the delivery rate at the inlet of the pipe between day and night.

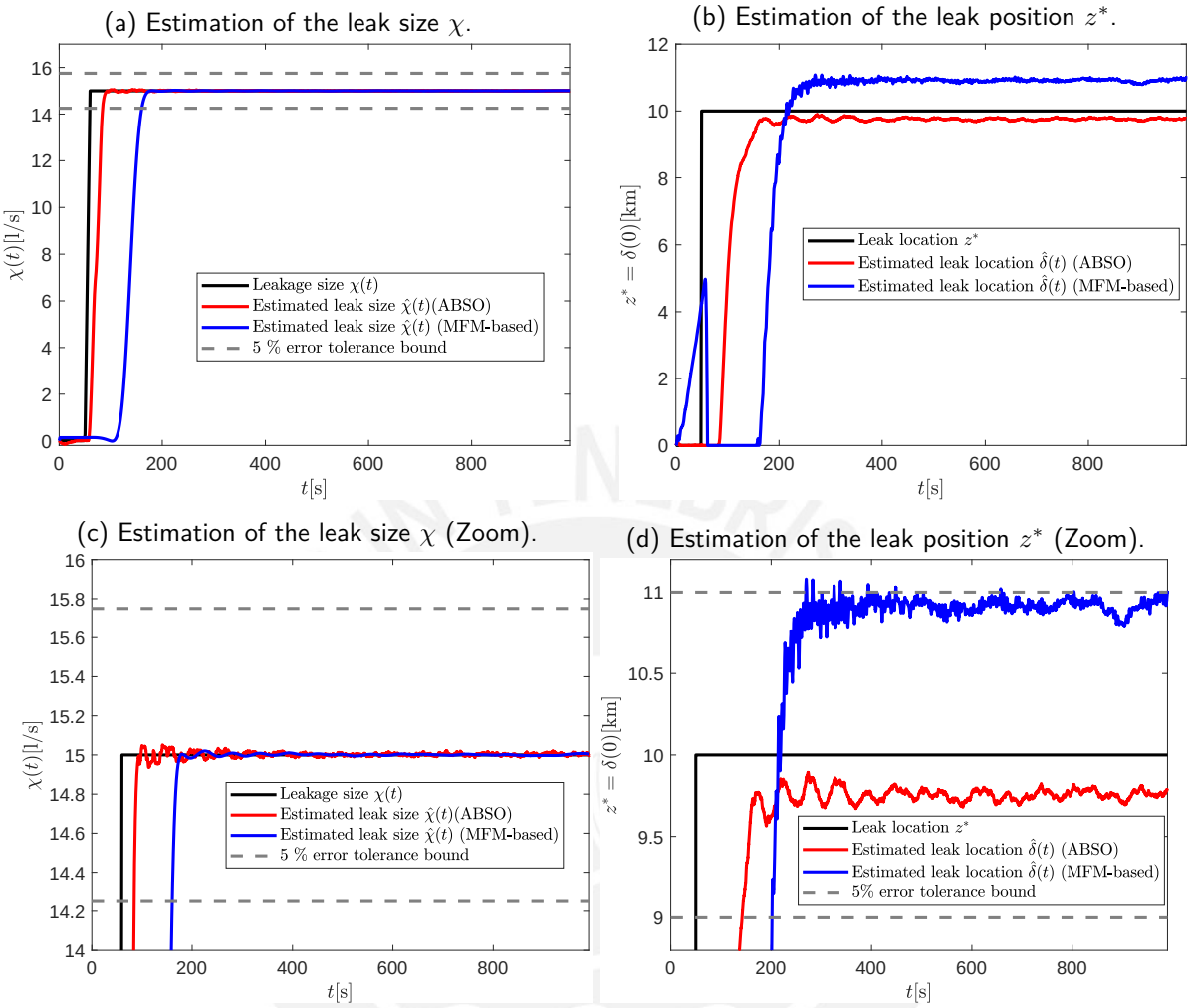

Figure 4.14.: Estimation of the leak size (left) and leak localization (right) for the simulation plant for a leak of $1\ \%$ of the nominal flow $q_0(t) = 1.5\ \frac{\mathrm{m}^3}{s}$ appearing at $z^* = 10$ km.

The Figure 4.15 and the Table 4.13 present the results of the leak size estimation and localization for the case of boundary conditions $q_0(t)$ and $p_\ell(t)$ that oscillate sinusoidally around the mean values utilized in the reference scenario of Table 4.1, i.e. $q_0(t) = (1\ +\ 10^{-2} \cdot \sin(\frac{2\pi}{100}t))\ \frac{\mathrm{m}^3}{s}$ and $p_\ell(t) = (1.1 \cdot 10^5\ +\ 10^3 \cdot \sin(\frac{2\pi}{100}t))$ Pa. In comparison to the parametrization of the algebraic observer presented in Section 4.1, only the length T_δ of the moving time window for the state estimation was readjusted to $T_\delta = 100$ s. The other tuning parameters of the algebraic observer and the ABSO are given as described in Section 4.2.1. Regarding the like size estimation, it is seen that both observers reach the same accuracy as in the case of constant boundary conditions (see Table 4.5) and estimate the leak size with deviations of under $0.15\ \%$ from the leak size. To highlight the significance of this performance under the chosen boundary conditions, Figure 4.15a

shows additionally the flow difference $q_0(t) - q_\ell(t)$ between the inlet flow $q_0(t)$ and the outlet flow $q_\ell(t)$. Since the inlet flow varies over time, the leak size χ is not equal to the flow difference between inlet and outlet. Consequently, the two leak observers presented in this work, the ABSO and the algebraic observer, provide a clearly more accurate and reliable leak detection and leak size estimation than a simple comparison between inlet flow and outlet flow of the pipe would do. While the flow difference $q_0(t) - q_\ell(t)$ oscillates between 4 and 16 $\frac{\text{l}}{\text{s}}$ and does not allow a reasonable conclusion whether a leak has occurred or not, the leak size estimated either by the ABSO or the algebraic observer converges to the real, constant leak size and allows for a reliable leak detection. Moreover, both observers estimate accurately the position of the leak. In the zoomed view shown in Figure 4.15d, sinuslike oscillations are observed in the leak position estimates. Nonetheless, the amplitudes of these oscillations have amplitudes less than 300 m, what represents about 1.5 % of the total length of the pipe, such that the estimates stay inside the 5 % error tolerance bound and the mean errors of the leak position estimation lie under 1 %.

KPI / Observer	$\Delta\chi$[%]	Δz^*[%]	$\sigma_\chi[\frac{\text{l}}{\text{s}}]$	σ_z[m]	$t_{\text{conv},\chi}$[s]	$t_{\text{conv},z}$[s]	t_{exec}[s]
Dynamic Observer (ABSO)	**0.01**	0.76	0.01	**86.13**	**24.25**	**135.77**	**38.31**
Algebraic Observer (MFM-based)	0.14	**0.38**	**0.007**	139.94	76.99	195.26	116.12

Table 4.13.: KPIs of the dynamic and the algebraic observer for a leak of 1 % of the nominal flow $q_0(t) = 1$ $\frac{\text{m}^3}{s}$ appearing at $z^* = 10$ km, sinusoidally varying boundary conditions $q_0(t)$ and $p_\ell(t)$.

This investigation of the observer performance under time-varying boundary conditions highlights a main advantage of the observers developed in the present work. Since the ABSO, as well as the algebraic observer, are derived and designed based on a physical pipe model, the flow dynamics are considered in the observer design independently of the boundary conditions. Hence, the presented observers go beyond less sophisticated leak detection methods, which would simply evaluate the flow difference between inlet and outlet without taking the flow dynamics into account. Furthermore, the investigations discussed in this section point out, that the algebraic observer requires an appropriate fine-tuning of the remaining design parameters for every operating condition to achieve the desired accuracy goals regarding the leak size estimation localization. While the ABSO only requires an adjustment of the number n of spatial discretization nodes used for the MOL, the tuning process of the algebraic observer is more complicated and time-consuming. The auxiliary problems (3.31) as well as (3.69) and (3.70) to obtain the needed MFs have to be simulated offline again, varying the lengths T_χ and T_δ of the moving time windows until a parametrization is found that leads to an accurate estimation of the leak size and leak position. This procedure is less intuitive than the

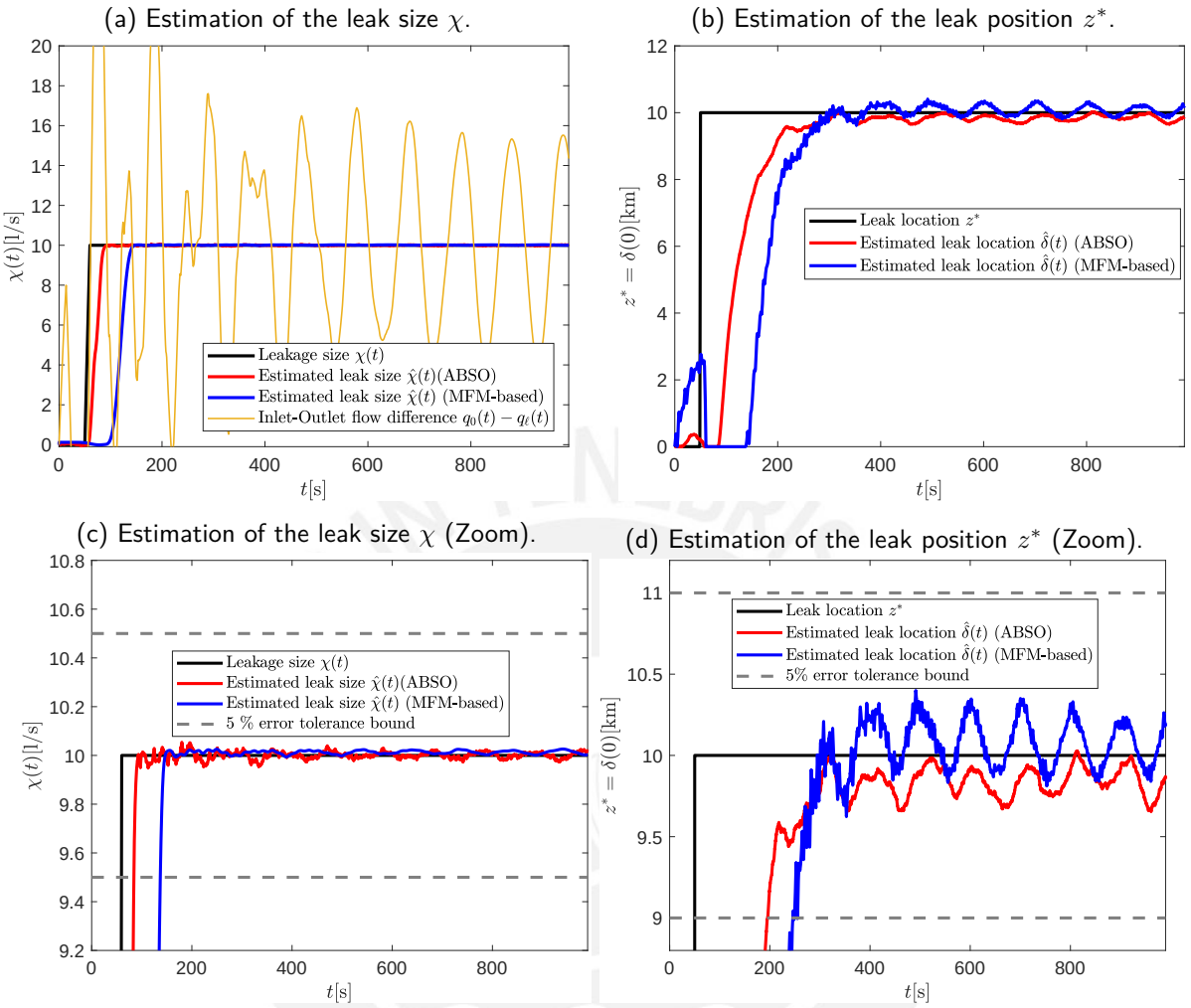

Figure 4.15.: Estimation of the leak size (left) and leak localization (right) for the simulation plant for a leak of 1 % of the nominal flow $q_0(t) = 1\ \frac{\mathrm{m}^3}{s}$ appearing at $z^* = 10$ km, sinusoidally varying boundary conditions $q_0(t)$ and $p_\ell(t)$.

tuning of the ABSO and does not guarantee that the algebraic observer reaches the same accuracy regarding the leak localization as the ABSO, as the first scenario for a higher constant inlet flow rate has demonstrated.

4.2.5. Simulation-based Leak Observer Results under Model Uncertainty

This final section is dedicated to the evaluation of the observer performance under model uncertainties. As discussed in Section 2.1.1, the main uncertainty w.r.t. to the pipe model (2.2) consists in the modeling of the friction losses. An essential assumption for the design of both observers

presented in Chapter 3 is that the friction losses depend linearly on the flow rate, such that they can be parametrized by a constant friction factor F. However, this assumption is a simplification of the fluid dynamics in two respects. Firstly, the friction losses depend strongly on the pipe geometry and material such that the friction factor F may vary over the pipe length, e.g., due to joints and elbow segments that cause additional friction losses or due to variations in the roughness of the inside pipe wall. Secondly, the assumption of linear friction losses is only valid near to an operating point where the flow rate stays approximately constant. If larger flow rate ranges are considered or if the flow rate differs significantly between the inlet and the outlet, e.g. because of a large leak, the nonlinear pipe model (2.10) that involves friction losses depending quadratically on the flow rate, is supposed to be more accurate [63].

In view of these limitations of the utilized linear pipe model (2.4), it is indispensable to validate the robustness of both observers w.r.t. model uncertainties. To this end, two different scenarios will be examined. The first scenario analyzes the case where the measurement data is generated by the linear pipe model (2.4) assuming a nominal linear friction factor F, but the dynamic and the algebraic observer are designed with a linear friction factor F that differs by up to $\pm 0.45\ \%$ from the nominal one. In the second scenario, the nonlinear pipe model (2.10) is utilized to generate the required measurement data of the flow rate and the pressure at the inlet and the outlet of the pipe for the case of a large leak of $10\ \%$ of the nominal flow. This measurement data, that differs significantly from the case where a linear friction factor would have been considered, is fed to both observers and the performance is evaluated. Thereby, the robustness of both observers w.r.t numerical and structural model uncertainties is examined.

The following Figure 4.16 and Table 4.14 present the first case where numerical model uncertainty in the linear friction factor F is regarded. Both observers are designed based on the reference scenario 4.1 while the required measurement data of the pressure and the flow rate at the inlet and the outlet is generated from the linear pipe model (2.4) with a different linear friction factor $F = 8.85\ \frac{\mathsf{kg}}{\mathsf{m}^3 \cdot \mathsf{s}}$, i.e., an uncertainty of $0.23\ \%$ w.r.t. the nominal case $F = 8.83\ \frac{\mathsf{kg}}{\mathsf{m}^3 \cdot \mathsf{s}}$ is regarded. A leak appears after $t = 60$ s in the center of the pipe at $z^* = 10$ km in form of a one-point leak with a magnitude of $1\ \%$ of the nominal flow and the noise level is chosen as in the medium measurement noise scenario.

The results indicate that both observers are able to detect and estimate the leak size correctly and with the same accuracy as in the nominal case (see Table 4.5). On the contrary, it is observed that the accuracy of the leak localization is affected strongly by the model uncertainty, such that the desired accuracy is not achieved. The estimated leak positions differ by about $20\ \%$ from the real leak position, whereby the algebraic observer performs slightly better.

If a higher model uncertainty of $\Delta F = 0.45\ \%$ w.r.t. to the friction factor is concerned, the accuracy of the leak localization gets worse for both observers, as Figure 4.17 and Table 4.15

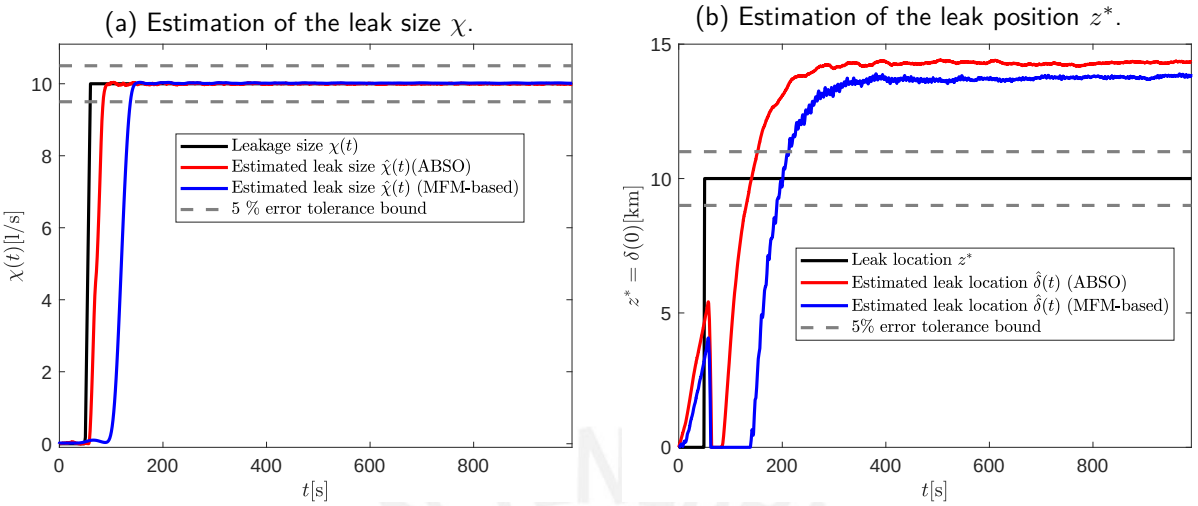

Figure 4.16.: Estimation of the leak size (left) and leak localization (right) for the simulation plant for a leak of 1 % of the nominal flow appearing at $z^* = 10$ km with an uncertainty of $\Delta F = 0.23$ % in the friction factor F.

KPI / Observer	$\Delta\chi$[%]	Δz^*[%]	$\sigma_\chi[\frac{\text{l}}{\text{s}}]$	σ_z[m]	$t_{\text{conv},\chi}$[s]	$t_{\text{conv},z}$[s]	t_{exec}[s]
Dynamic Observer (ABSO)	**0.002**	21.50	0.006	**47.76**	**24.44**	–	**38.54**
Algebraic Observer (MFM-based)	0.18	**18.70**	**0.003**	58.83	77.11	–	143.71

Table 4.14.: KPIs of the dynamic and the algebraic observer for a leak of 1 % of the nominal flow appearing at $z^* = 10$ km with an uncertainty of $\Delta F = 0.23$ % in the friction factor F.

demonstrate. The leak size can still be estimated accurately, but the estimated leak positions show mean errors of over 40 % such that the desired accuracy goals are clearly violated if uncertainty in the friction factor F is concerned.

KPI / Observer	$\Delta\chi$[%]	Δz^*[%]	$\sigma_\chi[\frac{\text{l}}{\text{s}}]$	σ_z[m]	$t_{\text{conv},\chi}$[s]	$t_{\text{conv},z}$[s]	t_{exec}[s]
Dynamic Observer (ABSO)	**0.003**	44.08	0.006	**30.64**	**24.44**	–	**32.65**
Algebraic Observer (MFM-based)	0.20	**41.31**	**0.003**	44.65	77.08	–	149.88

Table 4.15.: KPIs of the dynamic and the algebraic observer for a leak of 1 % of the nominal flow appearing at $z^* = 10$ km with an uncertainty of $\Delta F = 0.45$ % in the friction factor F.

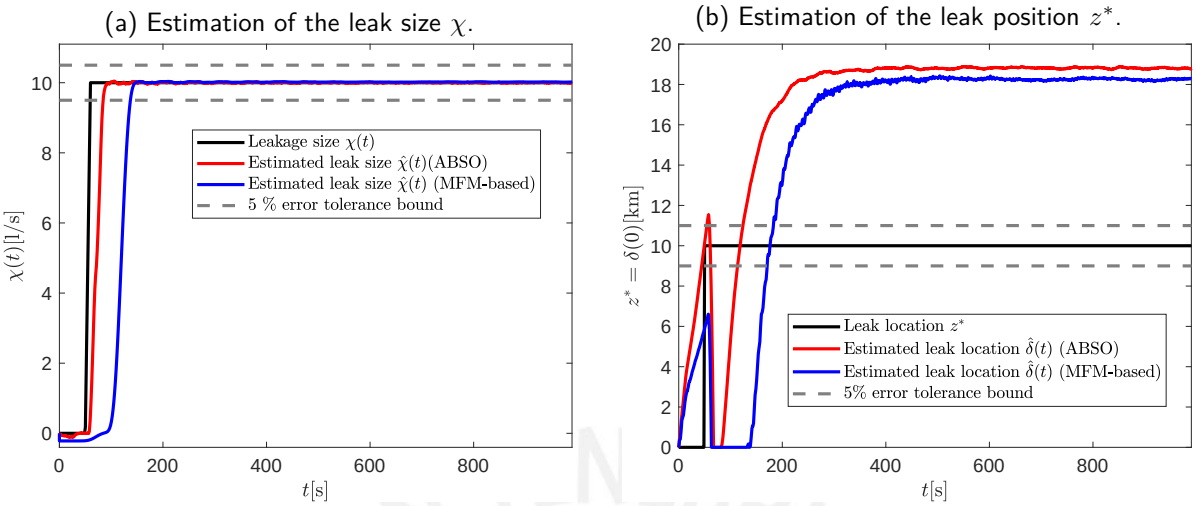

Figure 4.17.: Estimation of the leak size (left) and leak localization (right) for the simulation plant for a leak of $1\ \%$ of the nominal flow appearing at $z^* = 10$ km with an uncertainty of $\Delta F = 0.45\ \%$ in the friction factor F.

The leak localization scheme of both observers relies strongly on the transformation (3.2) of the linear pipe model (2.4) to decouple the unknown leak size from the leak distribution. If there is model uncertainty, e.g., in the friction factor F, the linear pipe model (2.4) and the transformed model (3.3) are not related by the transformation (3.2). As a consequence, the states $u(x,t)$ and $v(x,t)$ estimated either by the ABSO or the algebraic observer differ from the nominal case. Since the leak localization of both observers bases on the inverse state transformation (3.4) and applies Equation (3.19) where the estimates are multiplied with the factor $\frac{\sqrt{\beta\rho}}{A} \sim 10^7$, small errors in the estimation of the transformed states are amplified strongly and deteriorate finally the accuracy of the leak localization.

As a last investigation of this section, the performance of both observers is evaluated if the required measurement data of the pressure and the flow rate at the inlet and the outlet is not generated by the linear pipe model (2.4) but by the nonlinear model (2.10). The nonlinear friction coefficient f_d is chosen such that in the steady state case without leak, the pressure, and the flow rate of the linear and the nonlinear model coincide, i.e. that $F = f_d \cdot \frac{\rho\, q_0}{2 \cdot d \cdot A}$. In the following, constant boundary conditions according to the reference scenario described in Table 4.1 are concerned and a leak with a size of $10\ \%$ of the nominal flow rate occurs after $t = 60$ s. Furthermore, two different leak positions are regarded.

In the first case, the leak occurs near to the outlet at $z^* = 19$ km. The change of the utilized model to generate the measurement data mainly affects the pressure drop from the inlet to the outlet and the value of the inlet pressure $p_0(t)$ as Figure 4.18 illustrates.[2] Due to the leak, the flow

[2]The boundary conditions $p(\ell,t) = p_\ell(t)$ and $q(0,t) = q_0(t)$ are unchanged and the flow rate at the outlet in steady

rate is smaller in the pipe segment behind the leak such that the friction loss reduces in comparison to the linear model and the pressure decreases.

(a) Inlet pressure $p_0(t)$ in steady state for leakage case.

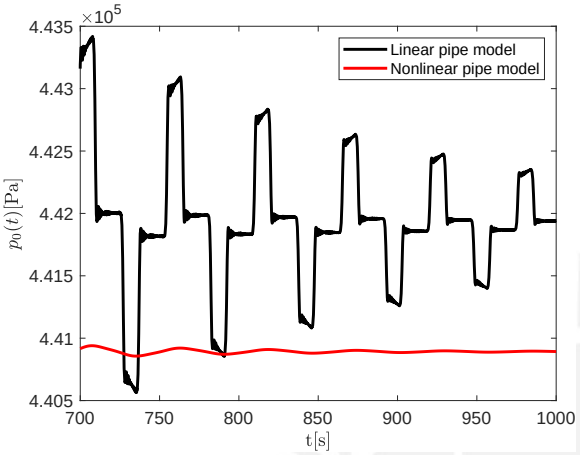

(b) Pressure drop in steady state for leakage case.

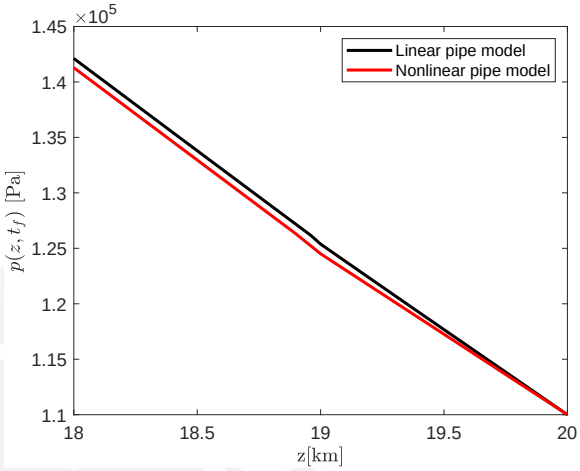

Figure 4.18.: Inlet pressure $p_0(t)$ (left) and pressure drop (right) for a leakage of $10\ \%$ of the nominal flow at $z^* = 19$ km, linear and nonlinear pipe model.

As the Figure 4.19 and the Table 4.10 indicate, the change of the utilized model to generate the measurement data for the observers has a significant impact on the accuracy of both observers regarding the leak localization. While the leak size is estimated with an accuracy that lies in the same range as in the reference scenario (see Table 4.5), the accuracy of the estimated leak position reduces, and both observers show a mean error of almost $5\ \%$.

KPI / Observer	$\Delta\chi$[%]	Δz^*[%]	$\sigma_\chi[\frac{l}{s}]$	σ_z[m]	$t_{\text{conv},\chi}$[s]	$t_{\text{conv},z}$[s]	t_{exec}[s]
Dynamic Observer (ABSO)	$\mathbf{6 \cdot 10^{-6}}$	4.47	0.007	**16.68**	**30.77**	264.77	**33.71**
Algebraic Observer (MFM-based)	0.01	**4.36**	**0.004**	19.14	83.47	**259.4**	147.83

Table 4.16.: KPIs of the dynamic and the algebraic observer for a leak of $10\ \%$ of the nominal flow appearing at $z^* = 19$ km, measurement data generated by the nonlinear pipe model (2.10).

In the second case, the leak occurs in the center of the pipe at $z^* = 10$ km. Consequently, the second half of the pipe works in a lower flow rate regime, such that in this pipe segment the friction losses according to the nonlinear pipe model (2.10) are smaller than the friction losses calculated

state is given directly from the mass balance as $q(\ell, t) = q_0(t) - \chi$.

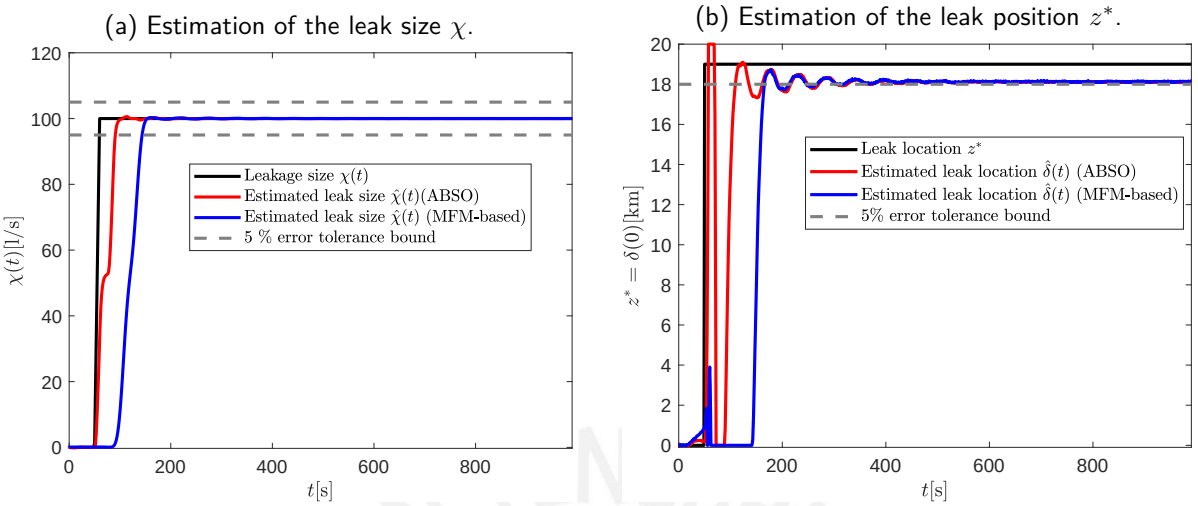

Figure 4.19.: Estimation of the leak size (left) and leak localization (right) for the simulation plant for a leak of 10 % appearing at $z^* = 19$ km, measurement data generated by the nonlinear pipe model (2.10).

by the linear pipe model (2.4). Hence, the inlet pressure and the pressure drop simulated by both models differ more than in the previous case, as Figure 4.20 illustrates.

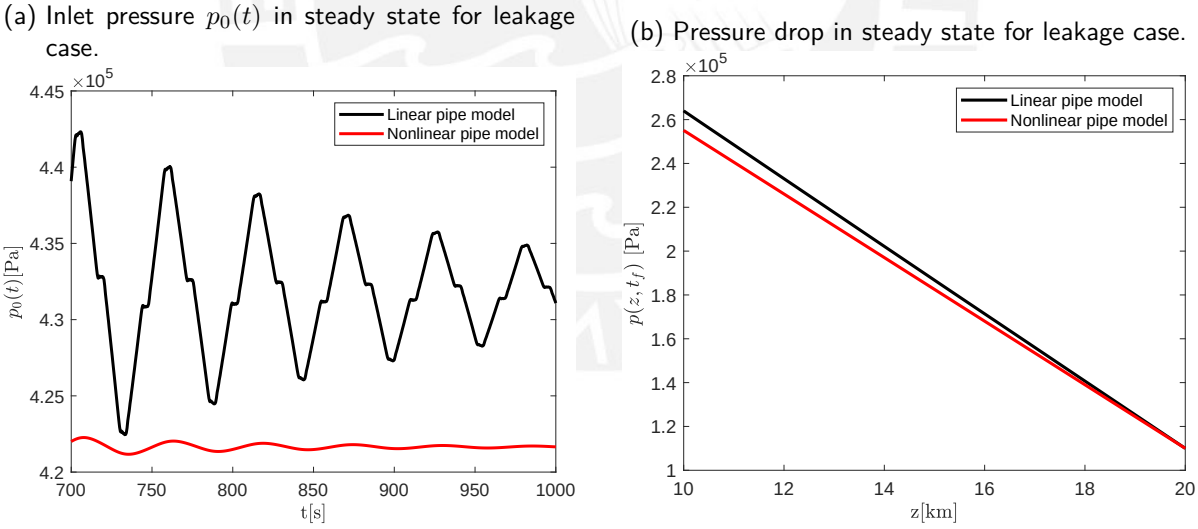

Figure 4.20.: Inlet pressure $p_0(t)$ (left) and pressure drop (right) for a leakage of 10 % of the nominal flow at $z^* = 10$ km, linear and nonlinear pipe model.

As Figure 4.21 and Table 4.17 depict illustratively and numerically, both observers achieve the desired accuracy w.r.t. the leak size estimation with deviations that are in the same range as in the nominal case (see Table 4.5). In contrast, neither the ABSO nor the algebraic observer provide

an accurate estimate of the leak position. Since the inlet pressure $p_0(t)$ that is obtained from the nonlinear pip model (2.10) is significantly smaller than the inlet pressure that would have been expected using the linear pipe model (2.4), the leak localization observer part according to Equation (3.19) underestimates the leak position drastically with deviations of almost $45\ \%$.

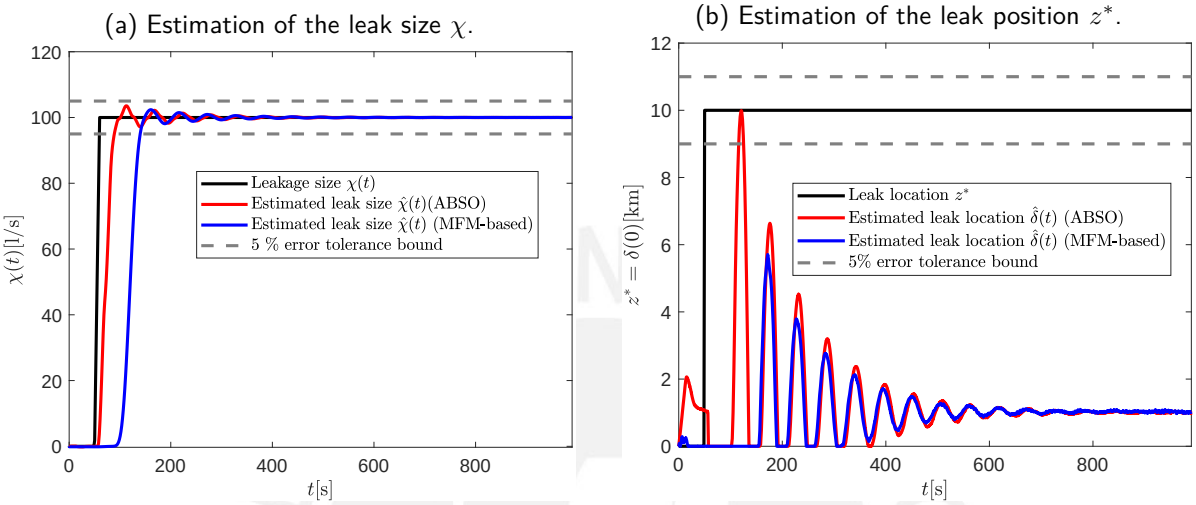

Figure 4.21.: Estimation of the leak size (left) and leak localization (right) for the simulation plant for a leak of $10\ \%$, measurement data generated by the nonlinear pipe model (2.10).

Observer \ KPI	$\Delta\chi$[%]	Δz^*[%]	$\sigma_\chi[\frac{\text{l}}{\text{s}}]$	σ_z[m]	$t_{\text{conv},\chi}$[s]	$t_{\text{conv},z}$[s]	t_{exec}[s]
Dynamic Observer (ABSO)	**0.001**	44.93	0.03	94.04	**28.87**	–	**37.95**
Algebraic Observer (MFM-based)	0.01	**44.83**	**0.03**	**69.80**	79.82	–	138.37

Table 4.17.: KPIs of the dynamic and the algebraic observer for a leak of $10\ \%$ of the nominal flow appearing at $z^* = 10$ km, measurement data generated by the nonlinear pipe model (2.10).

In summary, this section has figured out the main drawback of the two presented observer designs. While the leak size is estimated with the desired accuracy even in the case of model uncertainties, the accuracy of the leak localization shows a low robustness to uncertainties in the parametrization of the friction factor F and to the utilized friction loss model. In general, RTTM approaches require an accurate parametrization of the friction losses because uncertainties in the friction loss model have an effect, similar to a leakage, on the characteristics of the resulting pressure drop from the inlet to the outlet. Since these measurements of the inlet and outlet pressure are the base for the leak localization, the accuracy of the leak localization decreases significantly

if uncertainty in the friction loss model is considered. Similar observations regarding the low robustness to uncertainties in the friction model were also found for KF-based leak detection and localization observers [63]. To overcome this drawback, future works could include the dynamical observer design based on the nonlinear model as presented in [64] and dynamic online-estimation of the friction factor [20, 92] to register changes in the friction characteristics and adapt the ABSO rapidly. To improve the application of the algebraic observer and to adapt the observer design if the flow rates change continuously over a wide range between inlet and outlet, the nonlinear pipe model (2.10) could be considered for the derivation of the MFs and the corresponding auxiliary problem, taking the approach presented in [93] for nonlinear PDEs as a starting point.

As a concluding statement for this chapter, it is reminded that the goal of a high-accurate, real-time capable and fast leak detection and localization that is robust to measurement noise and model uncertainties is a multi-criterial problem that does not have a singular and objective one fits all solution rather than a parametrization of the observers that fulfills all objectives in a well-balanced manner is part of the tuning process and subject to the operating conditions of the examined pipe and the practical requirements. In this sense, the chosen parametrization of the ABSO and the algebraic, MFM-based observer are interpreted to be a possible configuration of the observer such that the multi-criterial goals are combined in a balanced way. Naturally, this configuration is not unique. Exemplarily, the accuracy of the ABSO relies heavily on the number of nodes that is chosen to apply the MOL. As Figure 4.22 indicates for the case of a single one-point leak with a size of $1\ \%$ that occurs at $z^* = \frac{\ell}{2}$, the mean error of the estimates of the ABSO decreases significantly, especially w.r.t. the leak localization if more nodes are utilized up to a critical number of $n \approx 500$ nodes. For further increasing number of nodes, the accuracy of the

(a) Accuracy of the estimation of the leak size χ vs. the number of the nodes for the ABSO.

(b) Accuracy of the estimation of the leak localization z^* vs. the number of the nodes for the ABSO.

(c) Runtime vs. number of nodes for the ABSO.

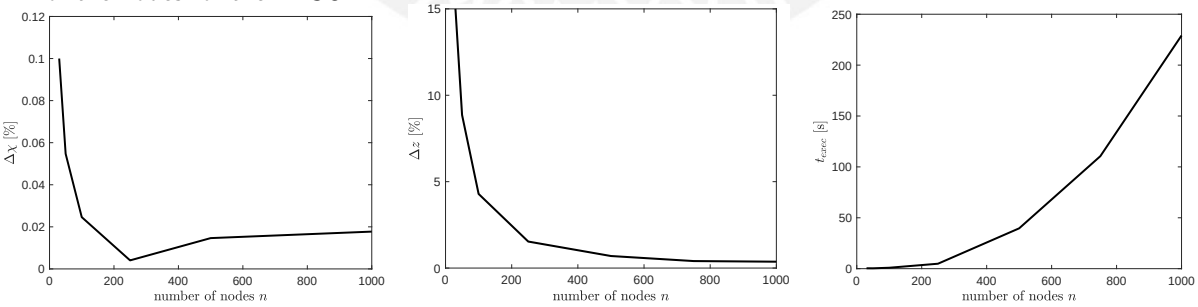

Figure 4.22.: Accuracy of the leak size estimation and leak localization (left) and needed runtime (right) vs. number of spatial discretization nodes n of the ABSO.

leak localization estimation does not improve significantly, and the curve flattens. Moreover, at

the same time, the required runtime increases exponentially to up to 230 s. In the context of this work, model reduction algorithms were examined to reduce the order of the resulting ODE system and to lower the computational costs. The application of a well-established and popular model reduction algorithm, the balanced truncation method [88], reduced indeed the required runtime but also introduces a noticeable, physically senseless undershoot in the leak size estimation since the classical balanced truncation method does not include the effect of the initial conditions of the considered ODE system into the model order reduction. Further investigations could address this topic by using balance truncation approaches like [94] that include the initial conditions. Another model reduction approach, that bases directly on the undiscretized observer PDE-system (3.9) can be found in [95]. Further trade-offs appear, e.g., in the parameterization of the observer gains L and γ of the ABSO between convergence speed and noise robustness or in the parameterization of the length of the moving time horizons of the algebraic observers between accuracy, noise robustness and convergence speed.

5. Experimental-Based Results

In this chapter, the presented dynamic and algebraic observer are used to detect and localize leakages in the pilot fluid transport plant installed in the laboratory of Advanced Control Engineering at the PUCP. The goal is to verify and validate the simulation-based results in a test environment with experimental data to examine the accuracy and performance of the designed observers for a real pipe system and to identify possible limitations in a real application environment.

The instrumentation and initial operation of the pilot plant at PUCP was realized in [54] and is subsequently briefly described. The dimensions of the plant are summarized in Table 5.1. The pilot plant consists of a steel pipe with a length of $\ell = 94.56$ m and a diameter of $d = 52.5$ mm and is arranged in the form of a circuit, as illustrated in the photo and the P & I diagram of the plant in Figure 5.1. For reasons of space constraints, the pipe has 14 horizontal sections and is bent at the end of these sections with an angle of $\pm 90^\circ$ such that a height difference of 0.85 m results. This inclination will be considered in the pipe model (2.4) by the inclination angle θ, as shown in Figure 5.2. The pilot plant operates with water that is provided by a water tank and fed back at the end of the pipe. To transport the water through the pipe, two centrifugal electrical pumps of the type MULTI-H404 by Salmson [96] supply the required flow rate. The rotational speed of the pump motors is controlled by a variable-frequency drive such that the pump motor velocity can be changed to set a desired flow rate at the inlet of the pipe. It is important to notice that the valves between the water tank and the pumps are configured such that the two pumps work in parallel. Thereby, the pipe can operate with one pump over a flow range of $q_0 \in [0, 2.5] \cdot 10^{-3} \ \frac{\mathrm{m}^3}{s}$ and with two pumps over a flow range of $q_0 \in [0, 5] \cdot 10^{-3} \ \frac{\mathrm{m}^3}{s}$.

Furthermore, four flow sensors (FT1, FT2, FT3, FT4) and four pressure sensors (PT1, PT2, PT3, PT4) are installed over the whole pipe length. The flow rate is measured with magnetic flow meters of the model AXW050 of Yokogawa [97], while the pressure is measured with differential pressure transmitters of the model EJA530E by Yokogawa [98]. Regarding the pipe model (2.4), the flow sensors (FT1, FT4) and the pressure sensors (PT1, PT4) are used as the required inlet and outlet flow and pressure measurements. The flow sensors (FT2, FT3), installed at $z = 28.1$ m and $z = 53.15$ m respectively, as well as the pressure sensors (PT2, PT2) installed at $z = 28.4$ m and $z = 53.45$ m are used to validate the pipe model (2.4). Furthermore, these additional sensors (FT2, FT3) and (PT3, PT4) allow to analyze partial segments of the pipe, by using e.g. (FT2)

(a) Photo of the pilot plant.

(b) Schematic P & I Diagram of the pilot plant, based on [54, Figure 2.13].

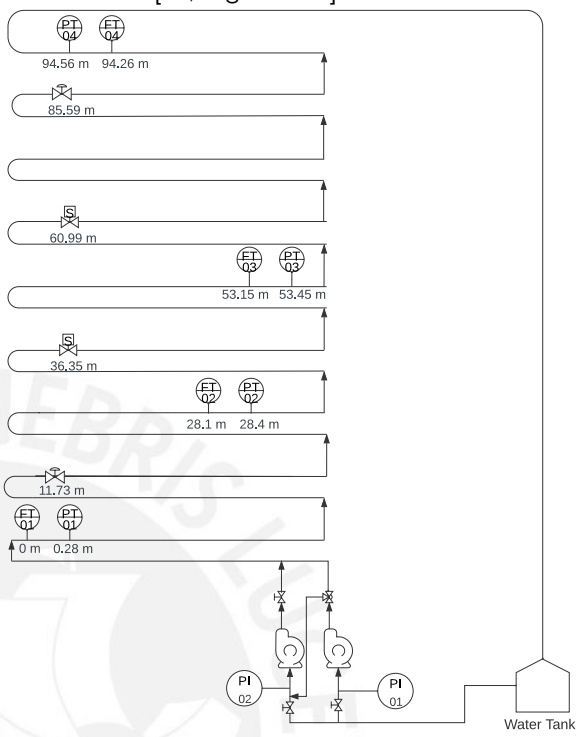

Figure 5.1.: Pilot Plant at PUCP.

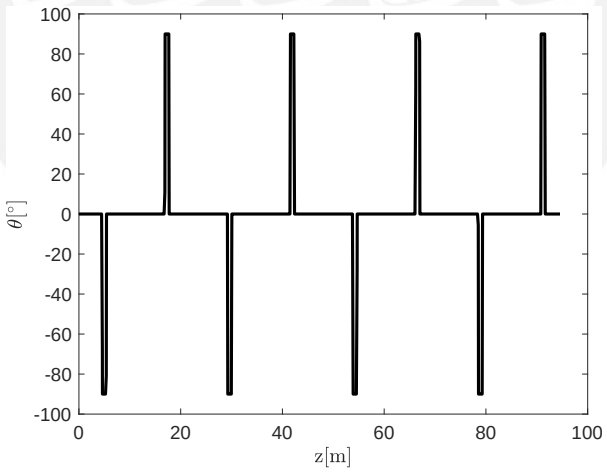

Figure 5.2.: Inclination angle of the pilot plant at PUCP.

and (PT2) as inlet flow and pressure and (FT4) and (PT4) as outlet flow and pressure. For the following investigations, the resulting measurement data of the flow sensors and pressure sensors is logged and fed to the dynamic and algebraic observer with the aim to validate the linear pipe

model (2.4) and to estimate the leak size and the leak position.

The process instrumentation of the pilot plant is completed by two solenoid valves (SV1, SV2) that are installed at $z = 36.35$ m and $z = 60.99$ m and two proportional valves (PV1, PV2) installed at $z = 11.73$ m and $z = 85.59$ m, i.e. the valves are each placed between two flow rate sensors. By opening one or several of these valves, the case of leakage in the pipe can be examined. It is important to point out that the current measurement equipment does not allow to measure the leak size, i.e. the flow rate that escapes through the solenoid or proportional valves, directly. Thus, the measurements in the leakage case will be only taken when the system is in steady state, i.e. a constant inlet flow rate $q_0(t)$ is set. Thereby, the leak size can be inferred from the difference in the flow rate measurements of the sensors in front of and behind the leak. The following Section

Parameter	Value	Unit	
Length ℓ	94.56	m	Pipe geometry
Diameter d	52.5	mm	
Position (FT1)	0	m	Flow sensors
Position (FT2)	28.1	m	
Position (FT3)	53.15	m	
Position (FT4)	94.86	m	
Position (PT1)	0.28	m	Pressure sensors
Position (PT2)	28.4	m	
Position (PT3)	53.45	m	
Position (PT4)	94.56	m	
Position (PV1)	11.73	m	Leakage valves
Position (SV1)	36.35	m	
Position (SV2)	60.99	m	
Position (PV2)	85.59	m	

Table 5.1.: Dimensions of the pilot plant installed at PUCP.

5.1 deals with the identification of the remaining unknown of the pipe parametrization, the friction factor F. Subsequently, in Section 5.2, the resulting linear pipe model according to (2.4) is validated and compared to the nonlinear pipe model (2.10). The underlying model assumptions presented in Chapter 2 are verified and the limitations of the linear pipe model are discussed. Finally, in Section 5.3, the presented dynamic and algebraic observer schemes are used to estimate the leak size and to localize the leak, based on measurement data from the pilot plant in the case of leakage.

5.1. Friction Identification of the Pilot Plant

This section deals with the identification of the linear friction factor F to complete the parametrization of the linear pipe model (2.4). Furthermore, the Darcy-Weisbach friction coefficient f_d of the

nonlinear model (2.10) is estimated from the measurement data to enable the verification and validation of the linear pipe model (2.4) against the nonlinear model (2.10).

The identification of the linear friction factor F and the nonlinear friction coefficient f_d is performed by analysing the general pipe model (2.1) in steady state for constant boundary conditions without leakage. In steady state, the partial derivatives $\frac{\partial p}{\partial t}(z,t)$ and $\frac{\partial q}{\partial t}(z,t)$ vanish such that we obtain

$$\begin{cases} 0 &= -\frac{\beta}{A}\frac{\partial q}{\partial z}(z,t) \\ 0 &= -\frac{A}{\rho}\frac{\partial p}{\partial z}(z,t) \; - A\; g\; \sin(\theta(z)) \\ & \quad -A\; J(q(z,t)) \end{cases} \tag{5.1}$$

$$\Rightarrow \begin{cases} q(z,t) &= const. = q(0,t) \\ \frac{\partial p}{\partial z}(z,t) &= -\rho g\; \sin(\theta(z)) - \rho\; J(q(0,t)) \end{cases} . \tag{5.2}$$

Furthermore, the inlet flow rate $q_0(t)$ and the outlet pressure $p_\ell(t)$ are assumed to be constant. Inserting the boundary conditions $q_0(t) = q(0,t) = q_{0,\infty}$ and $p_\ell(t) = p(\ell,t) = p_{\ell,\infty}$ leads to

$$\begin{cases} q(z,t) & = q_{0,\infty} \\ \int_z^\ell \frac{\partial p}{\partial \bar{z}}(\bar{z},t)\mathrm{d}\bar{z} & = p_{\ell,\infty} - p(z,t) \\ & = -\rho g \int_z^\ell \sin(\theta(\bar{z}))\mathrm{d}\bar{z} - \rho\; J(q_{0,\infty})\; (\ell - z) \\ \Rightarrow p(z,t) & = p(z) = p_{\ell,\infty} + \rho g \int_z^\ell \sin(\theta(\bar{z}))\mathrm{d}\bar{z} + \rho\; J(q_{0,\infty})\; (\ell - z) \end{cases} . \tag{5.3}$$

The Equation (5.3) reveals that in steady state, the flow rate $q(\cdot,\cdot)$ is constant over the whole pipe and corresponds to the inlet flow rate $q_{0,\infty}$. In contrary, the friction term $J(q(\cdot,\cdot))$ leads to a pressure drop from the inlet of the pipe to the outlet and contributes a term that is linear in the position z. Moreover, the inclination of the pipe affects the pressure by adding the geodetic pressure term $\rho g \int_z^\ell \sin(\theta(\bar{z}))\mathrm{d}\bar{z}$ such that the pressure drop is nonlinear if the inclination angle $\theta(\cdot)$ is non-constant. Rearranging (5.3) and inserting the linear friction model (2.3) or the nonlinear friction model (2.6) allows to resolve for the unknown linear friction factor F or the nonlinear friction coefficient f_d:

$$F = \frac{A}{q_{0,\infty}\; (\ell - z)} \cdot \left(p(z) - p_{\ell,\infty} - \rho g \int_z^\ell \sin(\theta(\bar{z}))\mathrm{d}\bar{z} \right) \tag{5.4}$$

$$f_d = \frac{2dA^2}{\rho |q_{0,\infty}| q_{0,\infty}\; (\ell - z)} \left(p(z) - p_{\ell,\infty} - \rho g \int_z^\ell \sin(\theta(\bar{z}))\mathrm{d}\bar{z} \right) . \tag{5.5}$$

In the following, this friction identification approach is applied to the pilot plant. Therefore, the power of the centrifugal pump is varied in steps of $10\ \%$ to establish different flow rate levels in the

pipe. Once the flow rate and the pressure reach steady state, the Equations (5.4) and (5.5) are evaluated. To address possible variations of the friction over the pipe length (e.g. due to different roughness of the pipe interior), the friction identification is performed for each segment separately by using the values of the corresponding flow rate (FT1, FT2, FT3, FT4) and pressure sensors (PT1, PT2, PT3, PT4). Additionally, an overall linear friction factor F and an overall nonlinear friction coefficient f_d for the whole pipe is calculated based on the values of the flow rate sensor FT1 and the pressure sensors (PT1, PT4).

In Figure 5.3, the flow rate and pressure trajectories at the four measurement points are illustrated for changes in the pump power in steps of $10\ \%$. It is observed, that, in accordance with Equation (5.3), the flow rate reaches a constant value at all four measurement points with deviations smaller than $1.4\ \%$ that mainly appear for flow rates higher than $2.5\ \frac{\mathrm{m}^3}{s}$ where both pumps are actuated. In these scenarios, the system is virtually working in steady state, but the flow measurements are not constant. The variation of the flow rate was already observed in other publications [99] and originates from variations in the pump power due to the control by variable-frequency drives that cause disturbances in the pipe. In contrast, the pressure reaches a constant value at each measurement point but drops monotonously from the first to the last measurement point due to the friction. Moreover, in Figure 5.4, the corresponding linear friction factor F and the nonlinear

(a) Flow rate measurement. (b) Pressure measurement.

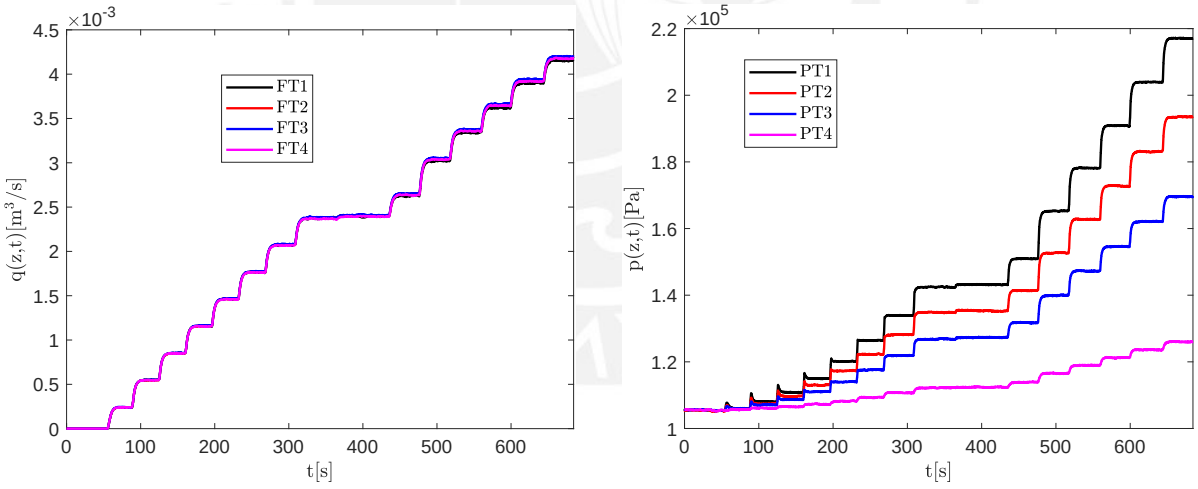

Figure 5.3.: Flow rate and pressure measurement of pilot plant for stepwise increasing pump power.

friction coefficient f_d that result from Equation (5.4) and Equation (5.5) are displayed with their corresponding uncertainties. It is noted that the estimated linear friction factor F increases for all segments significantly if the flow rate rises. The approximation by a straight line shows that this relationship is approximately linear with a Normalized Root Mean Square Error (NRMSE) less than 0.051. Besides, the friction factor F increases by more than $1\ \%$ per $1\ \%$ increase in the flow

rate. This observation can be explained by the fluid flow characteristics in the pipe. For the whole examined flow rate range $q_0 \in [1.5, 4.2] \cdot 10^{-3}\ \frac{\mathrm{m}^3}{s}$, the Reynolds number is greater than 10^4 such that the flow is assumed to be mainly turbulent [59]. Therefore, the assumption of one constant linear friction factor F for the whole flow rate range is not valid.

Contrary to that, the nonlinear friction factor f_d stays almost constant for all segments over the whole flow rate range with variations smaller than $6\ \%$, as shown in Figure 5.4.

Furthermore, the comparison of the identified linear friction factor F between the different segments shows that the friction factor varies with differences up to $26\ \%$ between the different segments, although the flow rate is the same. The same observation holds true for the nonlinear friction coefficient f_d where differences of up to $25\ \%$ between the segments can be noticed. In particular, the identified friction parameters for the first segment differ significantly from the other segments and the overall friction parameters. Since the error bars overlap partially, these differences in the friction parameters can be explained in some part by the uncertainties in the pipe geometry and in the measurements. Moreover, it is argued that the relatively complex geometry of the pipe over a relatively short length causes different friction characteristics in each segment. First, at the U-shaped parts of the pipe that are located at one end of the horizontal parts of the pipe, the direction of the horizontal flow changes by $180°$. As a wide range of investigations [100, 101, 102, 103, 104] on the friction losses in curved or bent pipes indicates, pipe turns imply higher pressure losses than in the horizontal parts. The curved part of the pipe causes that the velocity profile is not symmetric to the axis of the pipe, as it is the case for the horizontal parts of the pipe. Because of the change of the direction of the flow, centrifugal force occurs and provokes that the highest velocity is not located at the center of the pipe section but is displaced towards the pipe wall. This distortion of the velocity profile results, together with other effects of the centrifugal force like a presence of local high and low pressures, eddy zones and streamlines that form in a helix, in higher friction losses [100, 104]. Likewise, the elbow joints at the other end of the horizontal parts of the pipe and the thereby resulting change of the fluid flow direction from a horizontal flow to a vertical flow cause additional friction losses in comparison to a horizontal flow. This spatial variation of the friction losses between the horizontal parts, U-shaped parts and elbow joints is not considered by the friction models (2.3) and (2.6) which assume a horizontal flow direction and a global and constant friction parameter. The additional friction losses can differ from segment to segment, depending on the number of U-shaped pipe turns and elbow joints in each segment, and result in different friction factors F and friction coefficients f_d for every segment.

In short, the analysis of the identified friction parameter reveals that the assumption of a friction factor that stays constant over all segments and over the whole flow rate range is an idealized model assumption that does not reflect the identified behavior of the friction losses in the pilot plant. It is concluded that the assumption of a nonlinear friction model according to Equation (2.6) is more accurate to describe the friction losses in the pipe if the whole flow rate range of the pilot plant is

(a) Identification of friction factor F.

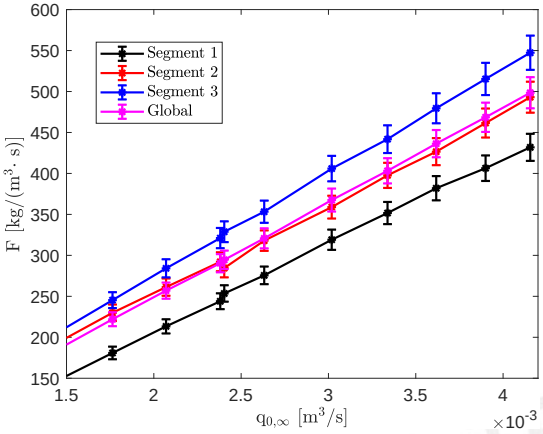

(b) Identification of friction coefficient f_d.

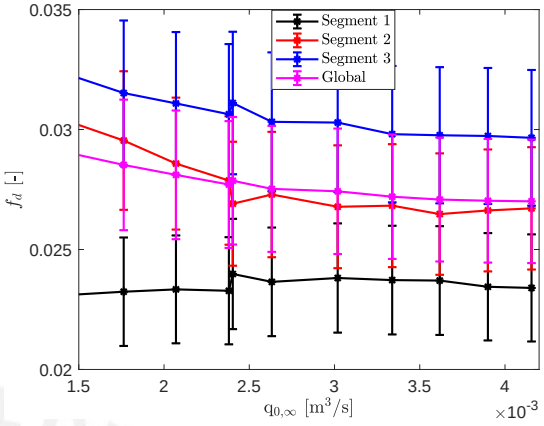

(c) Reynolds number.

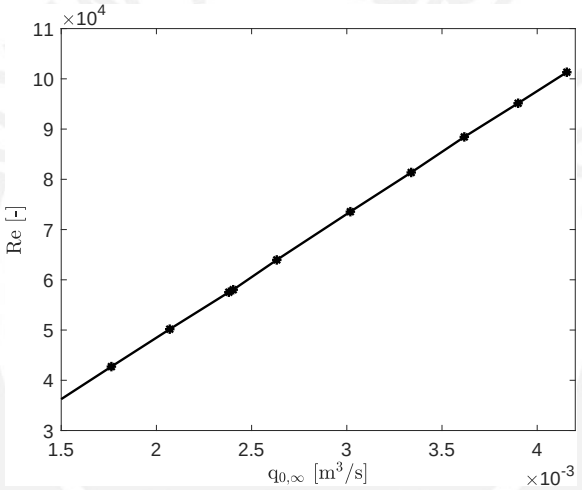

Figure 5.4.: Identification of the linear friction factor F (above, left), the nonlinear friction coefficient f_d (above, right) and the Reynolds number Re (below).

regarded. However, the following Section 5.2 examines whether the assumption of a linear friction factor F is valid at least for small changes in the flow rate, like it is the case when a leak appears.

5.2. Validation of the Pipe Model

Throughout this section, the linear pipe model (2.4) is verified and validated against the nonlinear pipe model (2.10) for small changes in the inlet flow rate. Firstly, the model verification and validation is performed in Section 5.2.1 for the case without leakage. Therefore, small variations in the pump power with steps smaller than $5\ \%$ are applied to the pilot plant and the accuracy of

both models regarding the flow rate and the pressure at the four measurement points is evaluated. Subsequently, the accuracy of both models is compared in Section 5.2.2 for the leakage case. Moreover, this section discusses the model assumptions made in Chapter 2 regarding the leak characteristics. In the following, the model verification and validation without and with leakage is realized for an operating point where both pumps work at $60\ \%$ of their maximum power leading to an inlet flow rate of $q_0(t) \approx 3.1 \cdot 10^{-3}\ \frac{\mathrm{m}^3}{\mathrm{s}}$.

5.2.1. Model Verification and Validation without Leakage

Since the previous Section 5.1 has pointed out that the identified friction factor F differs from pipe segment to pipe segment, the model verification and validation is split up into two parts.

Firstly, only the last segment between the pressure sensor (PT3) and (PT4), that is with a length of $\ell = 41.11$ m the largest segment of the pilot plant, is regarded, i.e. the flow measurement of sensor (FT3) and the pressure measurement of sensor (PT4) are taken as inlet flow rate and outlet pressure. The operating point where both pumps work at $60\ \%$ of their maximum power leading to an inlet flow rate of $q_0(t) = 3.1 \cdot 10^{-3}\ \frac{\mathrm{m}^3}{\mathrm{s}}$ is set. For this operating point, a linear friction factor of $F = 409\ \frac{\mathrm{kg}}{\mathrm{m}^3\mathrm{s}}$ and a nonlinear friction coefficient of $f_d = 0.0299$ are identified. After $t = 30$ s, the power of the first pump is increased to $65\ \%$ resulting in an increase of about $3.3\ \%$ of the inlet flow rate that enters the pipe segment. The Figure 5.5 presents the resulting flow rate measured by the sensor (FT3) and the pressure measured by the sensor (PT4). These measurements are

(a) Inlet flow rate at (FT3). (b) Outlet pressure at (PT4).

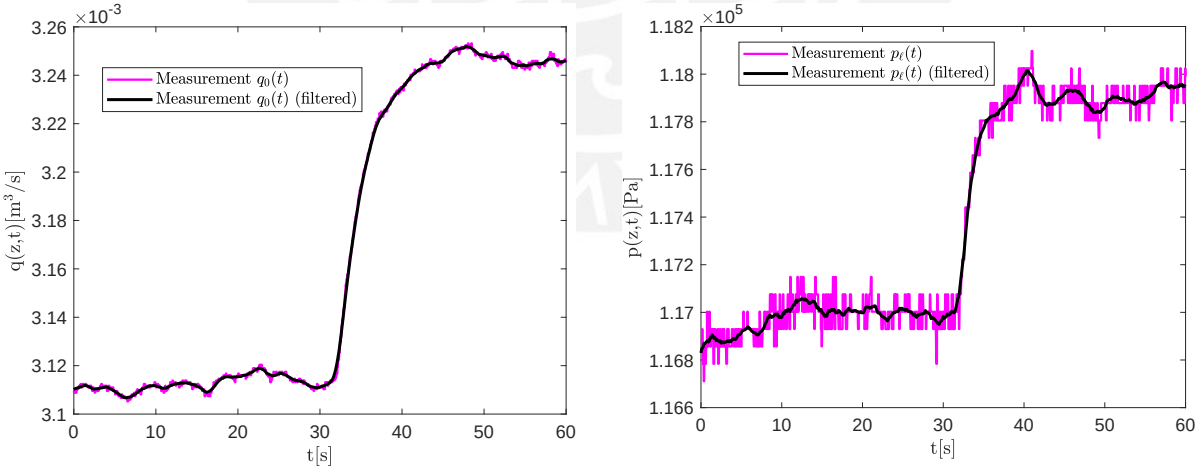

Figure 5.5.: Inlet flow rate at sensor (FT3) (left) and outlet pressure $p_\ell(t)$ at sensor (PT4) (right) of last pipe segment for operating point $q_0(t) \approx 3.1 \cdot 10^{-3}\ \frac{\mathrm{m}^3}{\mathrm{s}}$ and step-like increase of $5\ \%$ in power of first pump.

filtered by a moving average filter with a window length of $T = 7$ s and fed as boundary conditions $q(0,t) = q_0(t),\ p(\ell,t) = p_\ell(t)$ to the linear pipe model (2.4) and the nonlinear pipe model (2.10). Thereby, the outlet flow rate $q_\ell(t)$ and the inlet pressure $p_0(t)$ are obtained by simulating both models via the MOL with $n = 20$ spatial nodes and are compared to the measurement of the sensors (FT4) and (PT3), respectively. As the Figures 5.6a and 5.6c illustrate, both models reflect well the dynamics of the outlet flow rate. The differences between the inlet flow rate simulated by the linear pipe model (2.4) and the nonlinear pipe model (2.10) as well as the difference between the simulated flow rates and the filtered measured flow rate are negligible. The high accuracy of both models w.r.t. the flow rate is also expressed numerically by a NRMSE less than $7 \cdot 10^{-4}$ for both models. However, the comparison of the simulated pressure at the inlet of the segment displayed in Figure 5.6b reveals clearly visible differences in the accuracy of both models. On the one hand, the nonlinear pipe model (2.4) reflects well the pressure change due to the increased inlet flow rate. The dynamics as well as the value in the stationary case are reproduced accurately, leading to an NRMSE less than $2 \cdot 10^{-3}$. In contrast, the linear pipe model (2.4) shows deviations of about $25\ \%$ in steady state. According to the analysis of the friction losses performed in Section 5.1, the friction factor F increases approximately linear with the flow rate. Therefore, the friction factor of $F = 409\ \frac{\mathrm{kg}}{\mathrm{m^3 s}}$ identified for the operating point $q_0(t) = 3.1 \cdot 10^{-3}\ \frac{\mathrm{m}^3}{s}$ is significantly smaller than the friction factor of $F = 430\ \frac{\mathrm{kg}}{\mathrm{m^3 s}}$ that is identified for the flow rate that establishes in the stationary case after the increase in the pump power. Consequently, the friction losses and the pressure drop from the inlet to the outlet are underestimated by the friction factor identified for the first operating point, such that the simulated increase in the inlet pressure is significantly smaller than the measured pressure increase. An ansatz to overcome this drawback of the linear pipe model (2.4) would be to approximate the linear relationship between the friction factor F over the inlet flow rate to perform gain scheduling. The friction factor F in the linear pipe model (2.4) would be permanently updated according to the current inlet flow rate. As Figure 5.6b demonstrates, this adaptation of the linear pipe model (2.4) approximates significantly better the pressure dynamics and leads to the same accuracy as the nonlinear pipe model (2.10).

To broad the model verification and validation, a sequence of rectangular pulses is applied to the power of the first pump such that the power varies between $58\ \%$ and $62\ \%$. Figure 5.7 shows the resulting flow rate at the inlet to the last segment, i.e. at the flow rate sensor (FT3), and the outlet pressure $p_\ell(t)$ at the sensor (PT4). Analogue to the previous analysis, this measurement data is smoothed by a moving average filter and applied to the linear pipe model (2.4) and the nonlinear pipe model (2.10). In Figure 5.6, the simulated and measured flow rate at the outlet as well as the pressure at the inlet are compared. As in the previous case where only one step-like change in the pump power was considered, the dynamics of the flow rate at the outlet are reflected well by both models and an NRMSE less than $7 \cdot 10^{-4}$ is obtained. On the contrary, the linear pipe model (2.4) does not reproduce accurately the changes in the pressure at the inlet. Visible

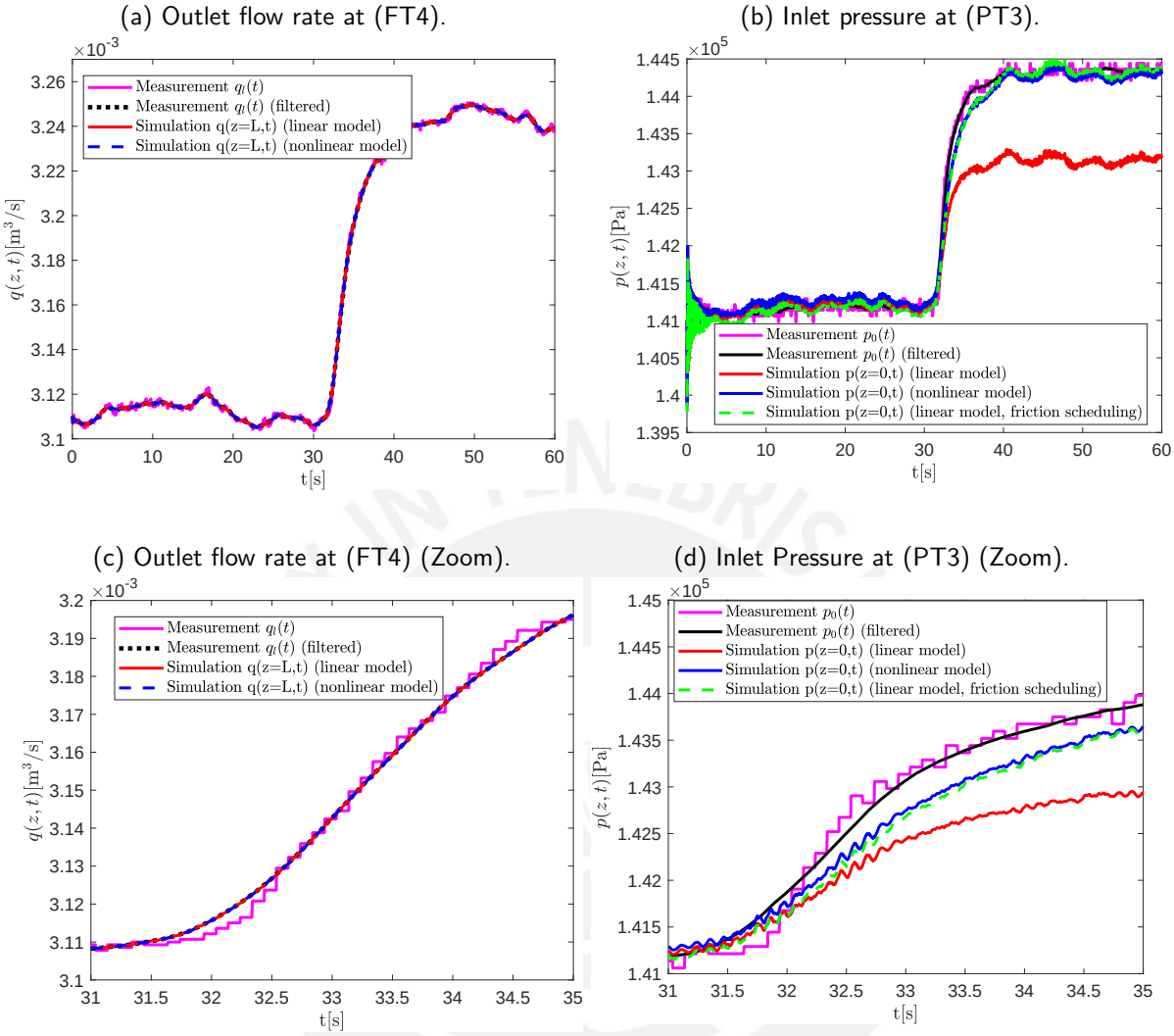

Figure 5.6.: Comparison of the measured and simulated outlet flow rate (left) and inlet pressure (right) for the last pipe segment, and an increase in the pump power of $5\ \%$. Simulation with linear pipe model (2.4) and nonlinear pipe model (2.10).

deviations between the measured pressure and the pressure simulated by the linear pipe model (2.4) show up since the friction factor F is assumed to be constant, while the previous Section 5.1 pointed out that the friction factor F depends on the flow rate. Consequently, the dynamics of the pressure are better represented by the nonlinear pipe model (2.10) that takes the quadratic increase in the friction losses into account and leads to an NRMSE smaller than 0.14. The second part of this section considers not only the last segment but the whole pipe of a length of $\ell = 94.56$ m. The linear pipe model (2.4) and the nonlinear model (2.10) are parametrized with the friction

(a) Inlet flow rate at (FT3). (b) Outlet pressure $p_\ell(t)$ at (PT4).

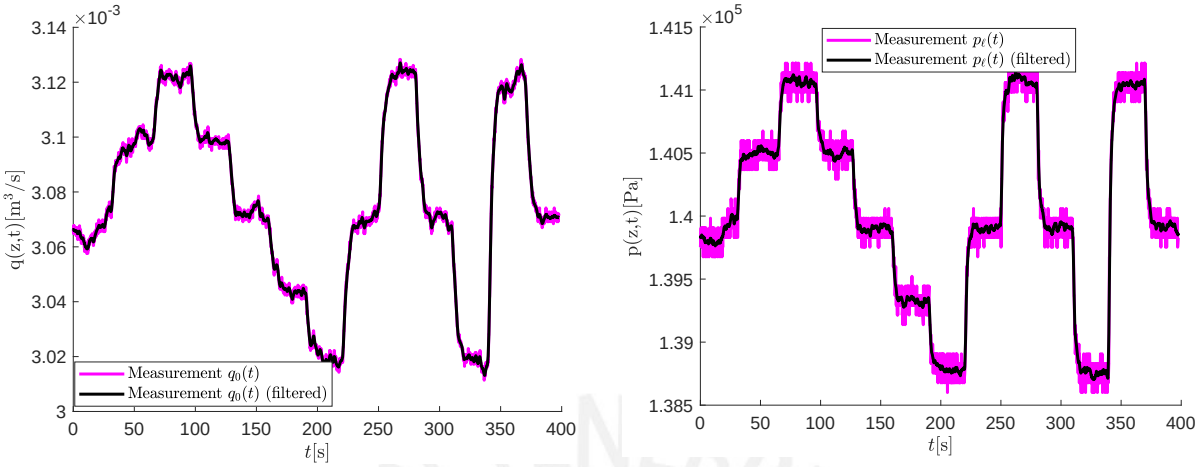

Figure 5.7.: Inlet flow rate at sensor (FT3) (left) and outlet pressure $p_\ell(t)$ at sensor (PT4) (right) of last pipe segment for operating point $q_0(t) \approx 3.1 \cdot 10^{-3}\ \frac{\mathrm{m}^3}{\mathrm{s}}$ and rectangular steps of the power of the first pump.

(a) Outlet flow rate at (FT4). (b) Inlet pressure at (PT3).

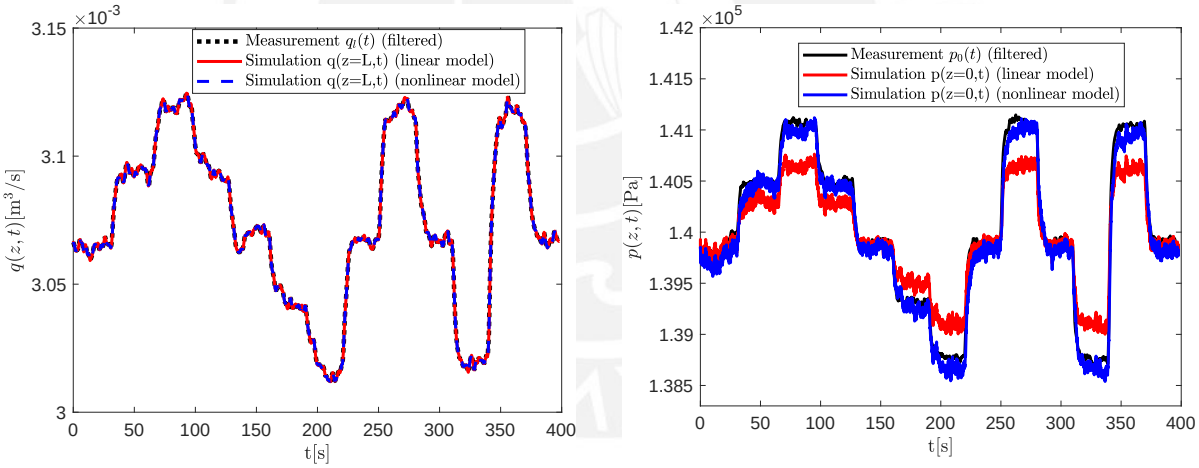

Figure 5.8.: Comparison of the measured and simulated outlet flow rate (left) and inlet pressure (right) for the last pipe segment, and rectangular steps of the power of the first pump. Simulation with linear pipe model (2.4) and nonlinear pipe model (2.10).

factor F and the friction coefficient f_d identified according to the previous Section 5.1 and both models are regarded for the same variations of the pump power as in the previous paragraph, a step-like increase and a sequence of alternating rectangular impulses around the operating point of $q_0(t) \approx 3.1 \cdot 10^{-3}\ \frac{\mathrm{m}^3}{s}$. For this operating point and considering the whole length $\ell = 94.56$ m,

a friction factor of $F = 372.5\ \frac{\text{kg}}{\text{m}^3\text{s}}$ and a friction coefficient of $f_d = 0.0272$ were identified. The measured inlet flow rate $q_0(t)$ at the sensor point (FT1) and the outlet pressure $p_\ell(t)$ at the sensor point (PT4) are logged and filtered to simulate both models. The measured flow rates at the sensor points (FT2), (FT3) and (FT4) as well as the measured pressure at the sensor points (PT1), (PT2), (PT3) are compared with the results of the simulation and the validity of both models is evaluated.

In Figure 5.9, the inlet flow rate $q_0(t)$ at sensor (FT1) and the outlet pressure at sensor (PT4) are shown for a step-like increase in the power of the first pump from $60\ \%$ to $65\ \%$ while the second pump operates constantly at $60\ \%$. This measurement data is utilized as the boundary conditions of the linear pipe model (2.4) and the nonlinear pipe model (2.10) resulting in the flow rate and pressure curves depicted in Figure 5.10 and Figure 5.11. The comparison of the flow rates

(a) Inlet flow rate $q_0(t)$ at (FT1). (b) Outlet pressure at (PT4).

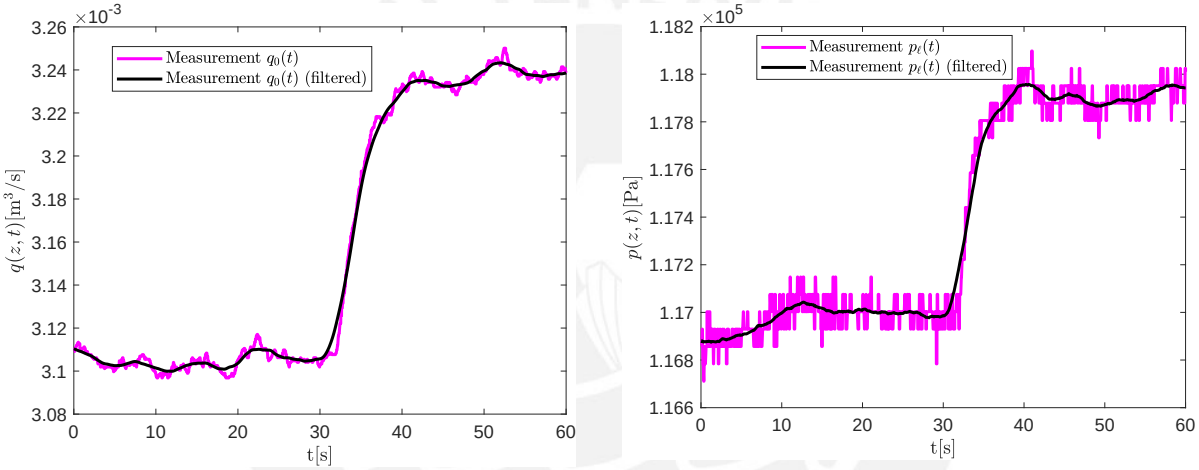

Figure 5.9.: Inlet flow rate $q_0(t)$ at sensor (FT1) (left) and outlet pressure $p_\ell(t)$ at sensor (PT4) (right) for operating point $q_0(t) = 3.1 \cdot 10^{-3}\ \frac{\text{m}^3}{\text{s}}$ and step-like increase in the power of the first pump.

in Figure 5.10 shows that the simulated flow rate corresponds well with the measured flow rate at each measurement point, both for the linear pipe model (2.4) and the nonlinear pipe model (2.10). The dynamic behavior and the stationary values are reproduced accurately with an NRMSE smaller than $0.19\ \%$. Contrary to that, the comparison of the measured and simulated pressure reveals that both models are less accurate than in the previous case, where only the last segment was considered. Like the analysis of the friction losses performed in Section 5.1 demonstrated, the friction factor F and the friction coefficient f_d differ from pipe segment to pipe segment. Since the linear pipe model (2.4) and the nonlinear pipe model (2.10) are parametrized with an overall friction factor F and friction coefficient f_d, that are assumed to be constant over the whole pipe length, only the inlet pressure at the sensor point (PT1) is simulated with an accuracy similar to the previously

(a) Flow rate at (FT2).

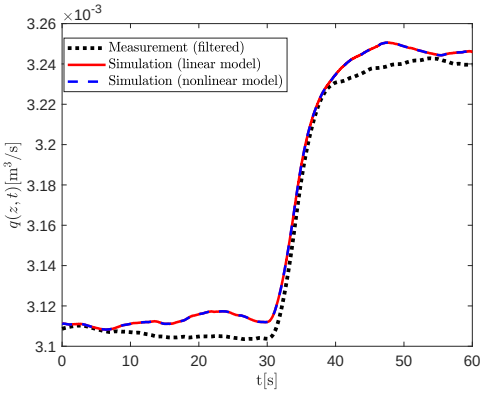

(b) Flow rate at (FT3).

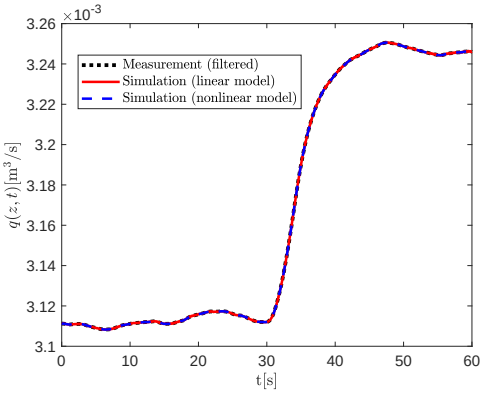

(c) Flow rate at (FT4).

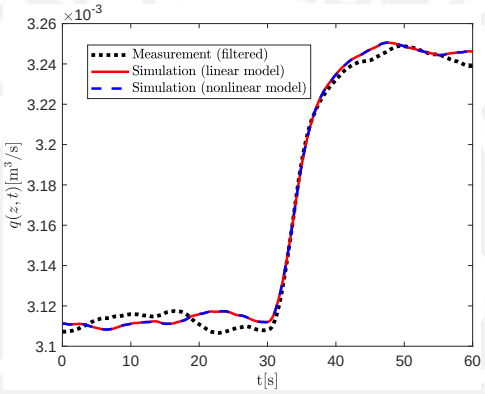

Figure 5.10.: Comparison of the measured and simulated flow rates at (FT2), (FT3) and (FT4) for step-like increase in the power of the first pump. Simulation with linear pipe model (2.4) and nonlinear pipe model (2.10).

regarded case. The nonlinear pipe model (2.10) reflects well the dynamics and the stationary values of the pressure while the linear pipe model (2.4) does not take the linear relationship between the friction factor F and the flow rate into account, such that the amplitude of the pressure change due to the increased inlet flow rate is underestimated. At the following two pressure sensor points (PT2) and (PT3), both the linear pipe model (2.4) and the nonlinear pipe model (2.10) deviate visibly from the measurement data. The linear pipe model (2.4) reproduces neither the values in the stationary case nor the amplitude of the pressure changes, while the nonlinear pipe model (2.10) leads at least to a pressure increase similar to the pressure change in the measurement data. Since both models use a global value for the friction factor F or the friction coefficient f_d to parametrize the friction losses, but the identification of these parameters for each segment separately leads to deviations of up to $11\ \%$ from the globally identified parameter, the pressure drop from the inlet

(a) Pressure at (PT1).

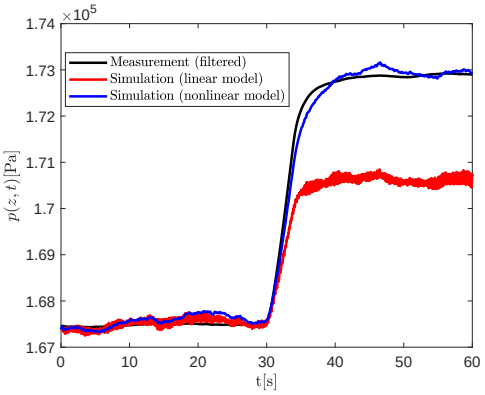

(b) Pressure at (PT2).

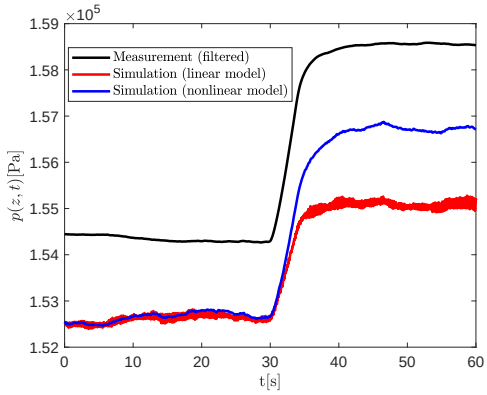

(c) Pressure at (PT3).

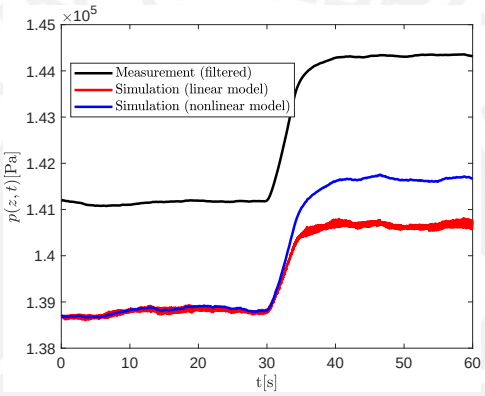

Figure 5.11.: Comparison of the measured and simulated pressure at (PT1), (PT2) and (PT3) for step-like increase in the power of the first pump. Simulation with linear pipe model (2.4) and nonlinear pipe model (2.10).

to the outlet of the pipe according to Equation (5.3) has a slope that differs from segment to segment. Consequently, the simulated pressure at the points that were not used to identify the global friction parameters, i.e. at the sensor points (PT2) and (PT3), do not coincide with the measurement data. To consider the variation of the friction factor F and the friction coefficient f_d in the parametrization of the models (2.4) and (2.10), respectively, one ansatz could be to define both parameters as spatially varying, i.e. $F = F(z)$ $f_d = f_d(z)$, and to set a different friction parameter for each segment. In Figure 5.12, the simulated pressure resulting from this ansatz is illustrated. It is observed that this model leads to a higher accuracy at the sensor points (PT2) and (PT3). The flow rate and pressure curves shown in Figure 5.14 and Figure 5.15 that result from a sequence of rectangular shaped changes of the power of the first pump between $58\ \%$ and $62\ \%$ and lead to the inlet flow rate $q_0(t)$ and the outlet pressure shown in Figure 5.13, strengthen

(a) Pressure at (PT1).

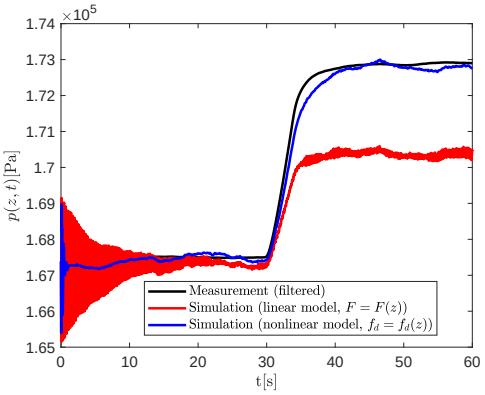

(b) Pressure at (PT2).

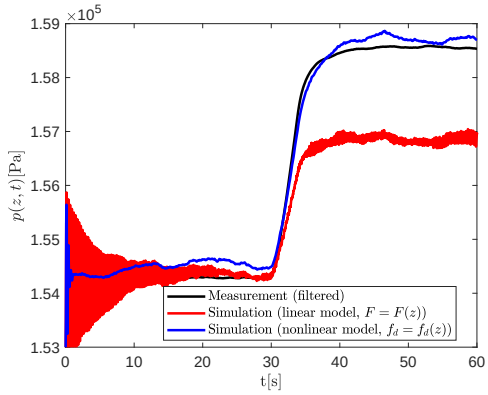

(c) Pressure at (PT3).

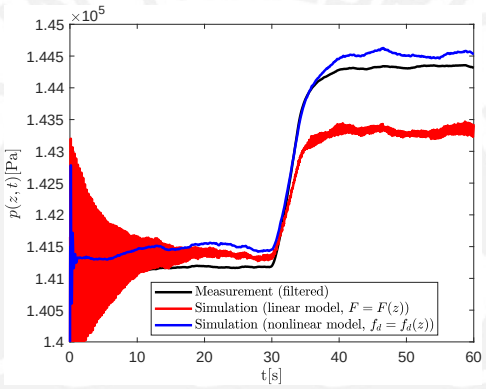

Figure 5.12.: Comparison of the measured and simulated pressure at (PT1), (PT2) and (PT3) for step-like increase in the power of the first pump. Simulation with linear pipe model (2.4) and nonlinear pipe model (2.10) parametrized with spatially varying friction parameters $F = F(z),\ f_d = f_d(z)$.

the previous drawn conclusions. While the flow rate dynamics are reproduced accurately by both models with an NRMSE lower than $0.13\ \%$, the simulated pressure, especially at the sensor points (PT2) and (PT3), shows severe deviations from the measured pressure. De novo, it is observed that the nonlinear pipe model reproduces approximately the pressure change between the stationary establishing values, but the stationary values of the pressure itself differ by up to 30 mbar. On the contrary, the linear pipe model (2.4) reproduces neither the stationary values of the pressure nor the magnitude of the pressure changes.

In summary, the model verification and validation in the non-leakage case has pointed out several limitations of the linear pipe model (2.4) as well as of the nonlinear pipe model (2.10). It has become clear that both models reflect well the dynamics of the flow rate under step-like

(a) Inlet flow rate $q_0(t)$ at (FT1). (b) Outlet pressure at (PT4).

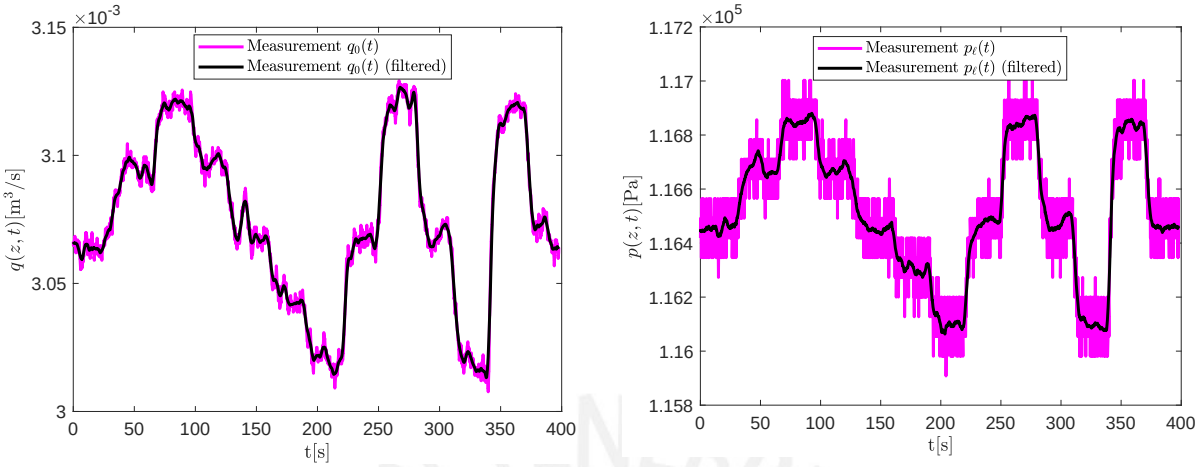

Figure 5.13.: Inlet flow rate $q_0(t)$ at sensor (FT1) (left) and outlet pressure $p_\ell(t)$ at sensor (PT4) (right) for operating point $q_0(t) \approx 3.1 \cdot 10^{-3}\ \frac{\mathrm{m}^3}{\mathrm{s}}$ and rectangular steps of the power of the first pump.

variations of the inlet flow rate $q_0(t)$. However, the linear pipe model (2.4) results in a simulated pressure change that is smaller than the pressure change observed in the measurement data since the model uses a constant friction factor F such that the higher friction losses for increasing flow rates are not considered. Consequently, the magnitude of the pressure drop is not reproduced accurately and the pressure at the inlet differs between simulation and measurement. This limitation could be overcome by applying a gain scheduling of the friction factor F over the flow rate, leading to a more complex system structure similar to the nonlinear pipe model (2.10). Moreover, the analysis of the simulations where the whole pipe is regarded and the friction parameters F and f_d are set as globally constant over the pipe length, pointed out that both models do not reflect well the pressure at the sensor points that are not used to identify the global friction parameters, i.e. at the sensor points (PT2) and (PT3). Like the identification of the friction losses performed in Section 5.1 has shown, the identified friction parameters F and f_d vary from segment to segment, e.g., because of the elbows that change the flow direction. Consequently, the slope of the pressure drop is not constant, but varies from segment to segment. To overcome this limitation, an ansatz that models the friction parameters as spatially variant was applied successfully. However, this ansatz leads to a more complex structure of the pipe model and according to the current literature, there is still no late lumping RTTM approach that detects and localizes leakage based on such a model with spatially varying friction parameters. Furthermore, it has to be born in mind that the pilot plant has a relatively short length of under 100 m and, at the same time, a relative complex geometric structure including bent and inclined parts. Therefore, the variations in the friction parameters appear particularly more noticeable than it would be the case for a longer pipe.

(a) Flow rate at (FT2).

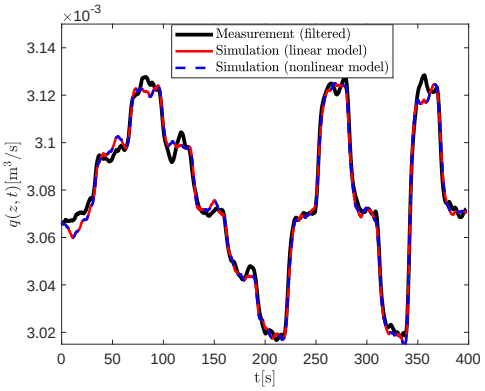

(b) Flow rate at (FT3).

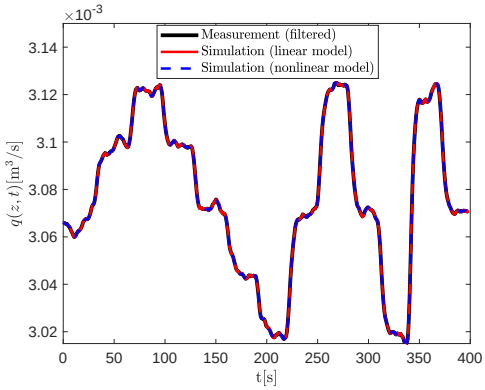

(c) Flow rate at (FT4).

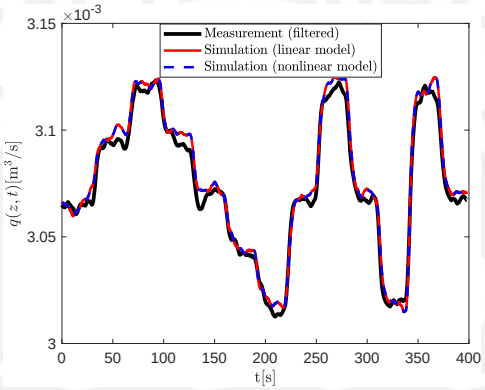

Figure 5.14.: Comparison of the measured and simulated flow rates at (FT2), (FT3) and (FT4) for rectangular steps of the power of the first pump. Simulation with linear pipe model (2.4) and nonlinear pipe model (2.10).

Before the measurement data is applied to detect and localize leaks in the pilot plant with the presented dynamic and algebraic observer structures, the following Section 5.2.2 extends the model validation to the case with leakage in the pipe. A further focus lies on the verification of the assumptions regarding the leak characteristics that were drawn in Chapter 2.

5.2.2. Model Verification and Validation in the Leakage Case

This section deals with the model verification and validation in the case that a leak occurs at one of the solenoid or proportional valves of the pilot plant. The accuracy of the linear pipe model (2.4) and the nonlinear pipe model (2.10) is examined under variation of the leak size and the leak position.

(a) Pressure at (PT1).

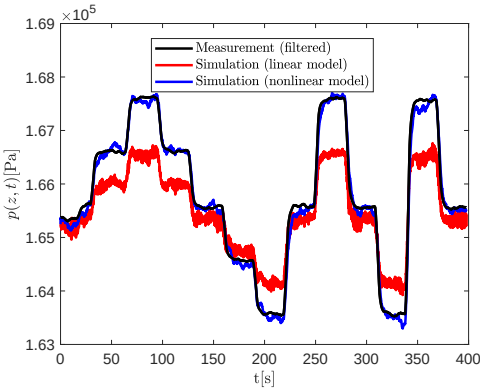

(b) Pressure at (PT2).

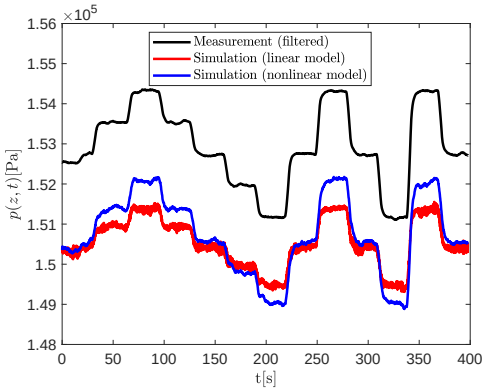

(c) Pressure at (PT3).

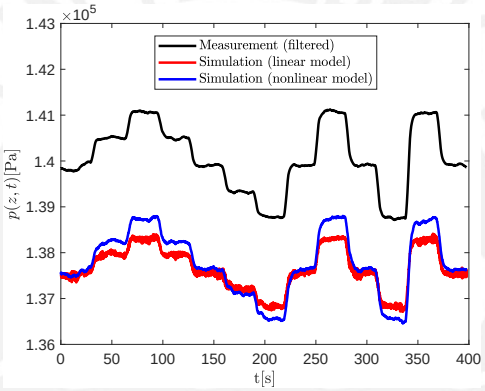

Figure 5.15.: Comparison of the measured and simulated pressure at (PT1), (PT2) and (PT3) for rectangular steps of the power of the first pump. Simulation with linear pipe model (2.4) and nonlinear pipe model (2.10).

Firstly, the case of a relatively small leak near to the end of the pipe is investigated. To this end, both pumps operate at $60\ \%$ of their maximum power leading to an inlet flow of $q_0(t) \approx 3.1 \cdot 10^{-3}\ \frac{\mathrm{m}^3}{s}$. After $t = 30$ s, the proportional valve installed at $z = 85.59$ m is opened partially, which results in a leak size χ that represents about $3\ \%$ of the nominal inlet flow. After $t = 180$ s, the proportional valve is closed. The leak size is inferred from the flow measurements in front of and behind the leak position, i.e. as the difference in the flow rate between the sensor point (FT3) and the sensor point (FT4). In Figure 5.16, the measured inlet flow, the measured outlet pressure and the inferred leak size are depicted. It is observed that the leak size is not constant, but varies around a mean value of approximately $\chi = 8 \cdot 10^{-5}\ \frac{\mathrm{m}^3}{s}$. The amplitude of the variation of the leak size is in the range of the variations of the flow rates for the case without leakage, such that they can be explained by the measurement noise and the oscillations in the inlet flow due to the

variable-frequency drive that controls the pump power. Moreover, it is noticed that the leak size needs about 10 s after opening the valve to reach its mean value. Consequently, the assumption 9 of a constant leak size, that was drawn in Chapter 2, is valid if the pipe operates in steady state, i.e. that the flow rate at the inlet and the outlet have stabilized. To simulate the linear pipe model

(a) Inlet flow rate $q_0(t)$ at (FT1).

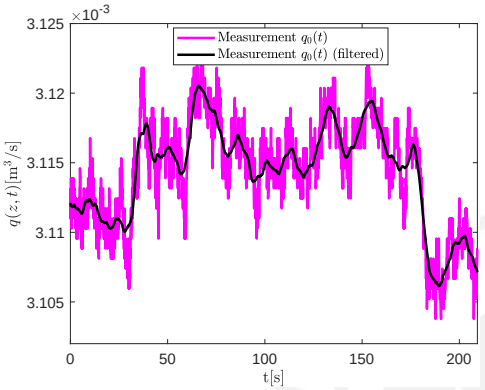

(b) Outlet pressure at (PT4).

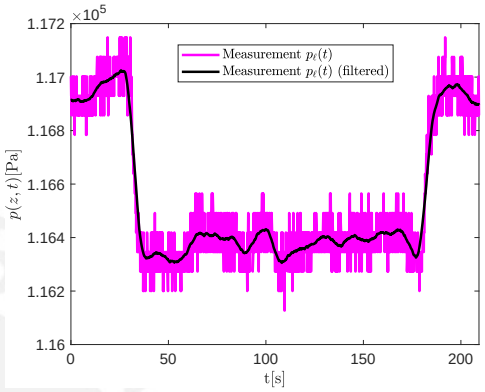

(c) Leak size χ.

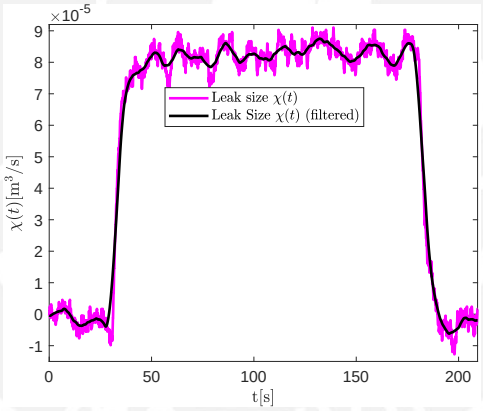

Figure 5.16.: Inlet flow rate $q_0(t)$ at sensor (FT1) (left), outlet pressure $p_\ell(t)$ at sensor (PT4) (middle) and leak size $\chi(t)$ (right) inferred from flow rate measurements (FT3) and (FT4), operating point $q_0(t) \approx 3.1 \cdot 10^{-3}\ \frac{\mathrm{m}^3}{\mathrm{s}}$, small leak occurring after $t = 30$ s at $z^* = 85.59$ m.

(2.4) and the nonlinear pipe model (2.10), this measurement data is filtered by a moving average filter and fed to the models that are discretized via the MOL. The friction factor F and the friction coefficient f_d are identified according to Section 5.1 at the operating point before the leak occurs and considering the whole pipe length. The identified parameters for the considered operating point $q_0(t) \approx 3.1 \cdot 10^{-3}\ \frac{\mathrm{m}^3}{s}$ are $F = 371\ \frac{\mathrm{kg}}{\mathrm{m}^3\mathrm{s}}$ and $f_d = 0.0271$. The leak distribution is modelled by a Dirac impulse, i.e., a point leak is assumed. In Figure 5.17 and Figure 5.18, the resulting simulated

flow rate and pressure are compared to the measurement data. Similar to the previous investigated cases without leakage, the flow rate is reproduced with a high accuracy and maximal deviations of under 0.5 %. Regarding the pressure at the three sensor points, it is observed again that the simulated pressure at the sensor points (PT2) and (PT3) differs significantly by about 20 mbar from the measurement data due to the different friction loss characteristics of each segment. Contrary to that, the pressure at the inlet, i.e. at the pressure sensor (PT1), is reproduced accurately by both models with deviations lying in the range of the measurement noise of about 2 mbar. In

(a) Flow rate at (FT2).

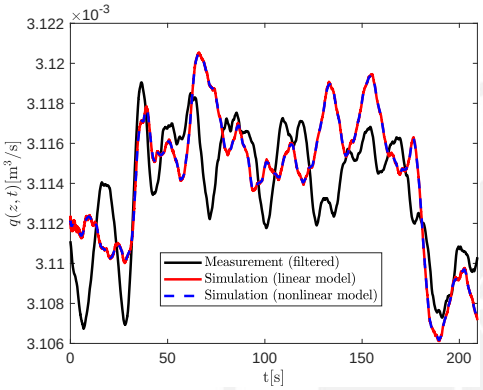

(b) Flow rate at (FT3).

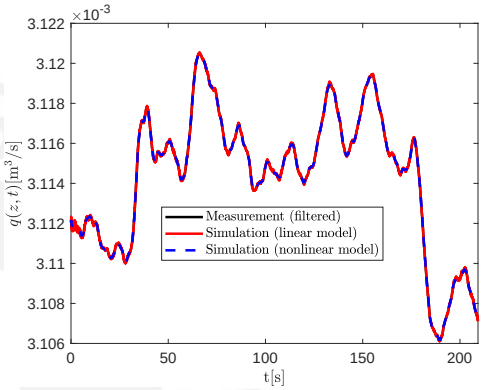

(c) Flow rate at (FT4).

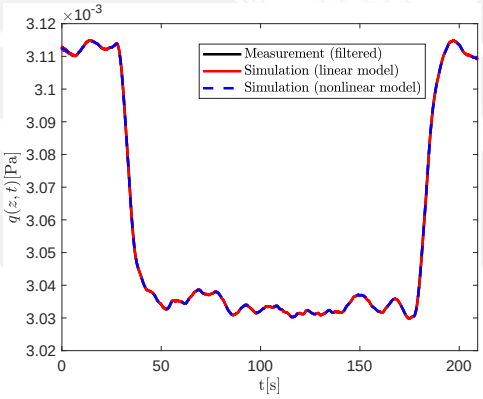

Figure 5.17.: Comparison of the measured and simulated flow rates at (FT2), (FT3) and (FT4), operating point $q_0(t) \approx 3.1{\cdot}10^{-3}\ \frac{\mathrm{m}^3}{\mathrm{s}}$, small leak occurring after $t = 30$ s at $z^* = 85.59$ m. Simulation with linear pipe model (2.4) and nonlinear pipe model (2.10).

the second scenario, the leak that occurs at the same position $z^* = 85.59$ m, but has a bigger size of about 16 % of the nominal flow. The Figure 5.19 presents the inlet flow, the outlet pressure and the inferred leak size that result from this leak. It is observed, that the flow rate at the inlet increases by about 1 %, as well as at the other flow sensors (FT2) and (FT3) in front of the leak,

(a) Pressure at (PT1).

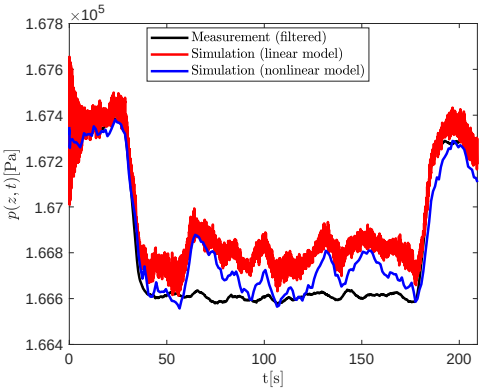

(b) Pressure at (PT2).

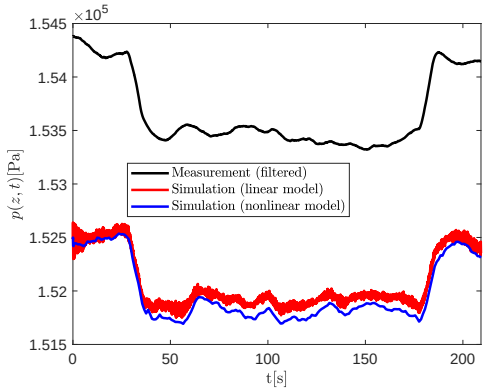

(c) Pressure at (PT3).

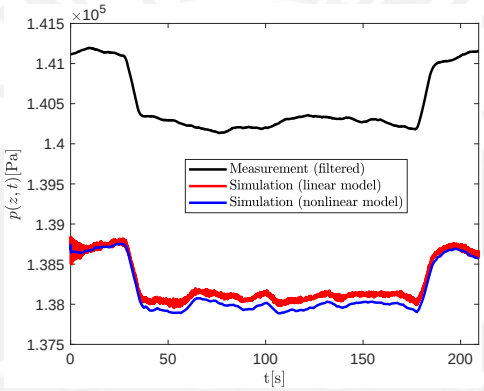

Figure 5.18.: Comparison of the measured and simulated pressure at (PT1), (PT2) and (PT3), operating point $q_0(t) \approx 3.1{\cdot}10^{-3}\ \frac{\mathrm{m}^3}{\mathrm{s}}$, small leak occurring after $t = 30$ s at $z^* = 85.59$ m. Simulation with linear pipe model (2.4) and nonlinear pipe model (2.10).

after the leak has occurred. This effect has already been noticed in other publications [63] and is explained by the dynamic behavior of the pumps which produce for the same rotational velocity a higher inlet flow rate if the pressure at the inlet, e.g. due to a leak, decreases. In Figure 5.20 and 5.21, the simulated flow rate and pressure curves are compared to the measurement data. Besides the high accuracy of both models regarding the flow rate and the deviations in the pressure at the sensor points (PT2) and (PT3), it is noticed that also at the inlet, the simulated pressure differs visibly by about 100 mbar from the measured pressure. Since the occurred leak is relatively big with about $16\ \%$ of the nominal flow, the segment of the pipe behind the leak position operates in a significantly lower flow rate regime. Consequently, the friction losses are smaller than it would be expected by the friction parameters F and f_d that were identified for the whole pipe at a operating point with a higher flow rate of $q_0(t) \approx 3.1 \cdot 10^{-3}\ \frac{\mathrm{m}^3}{\mathrm{s}}$. An ansatz to overcome this drawback and

(a) Inlet flow rate $q_0(t)$ rate at (FT1).

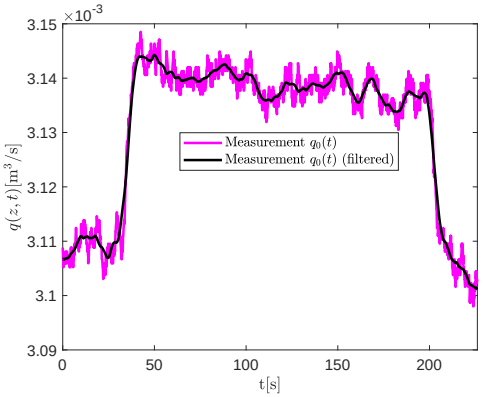

(b) Outlet pressure at (PT4).

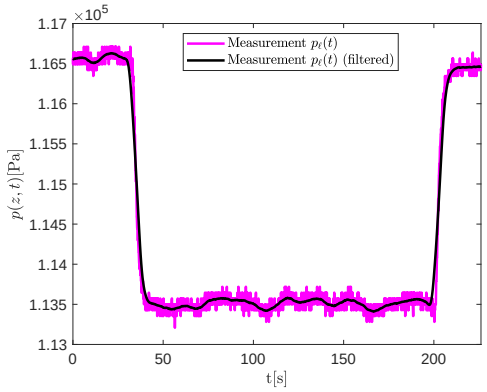

(c) Leak size χ.

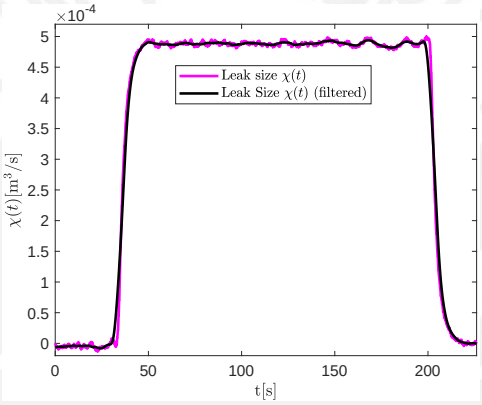

Figure 5.19.: Inlet flow rate $q_0(t)$ at sensor (FT1) (left), outlet pressure $p_\ell(t)$ at sensor (PT4) (middle) and leak size $\chi(t)$ inferred from flow rate measurements (FT3) and (FT4), operating point $q_0(t) \approx 3.1 \cdot 10^{-3}\ \frac{\mathrm{m}^3}{\mathrm{s}}$, big leak occurring after $t = 30$ s at $z^* = 85.59$ m.

to improve the accuracy of the simulated pressure, would be to define the friction parameters as function of the flow rate, i.e. $F = F(q(z,t)),\ f_d = f_d(q(z,t))$. In Figure 5.21a, this approach is implemented exemplarily for the nonlinear model (2.10). The friction coefficient for the segment behind the leak is calculated to be about $1.1\ \%$ smaller than the global friction coefficient such that the simulated pressure at the inlet corresponds visibly better to the measurement data.

Finally, the model accuracy is examined under variation of the leak position. To this end, the proportional valve installed at $z = 11.73$ m is opened partially after $t = 30$ s leading to a relatively small leak of about $4.8\ \%$ of the nominal flow. The Figure 5.22 presents the inlet flow $q_0(t)$, the outlet pressure $p_\ell(t)$ and the leak size χ inferred from the measurements of the flow rate sensors (FT1) and (FT2). In Figure 5.23 and Figure 5.24, the simulated flow rate and pressure curves are

(a) Flow rate at (FT2).

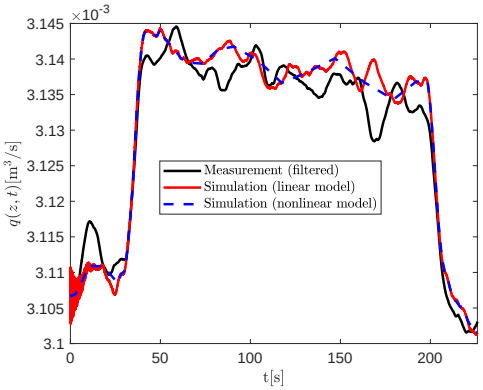

(b) Flow rate at (FT3).

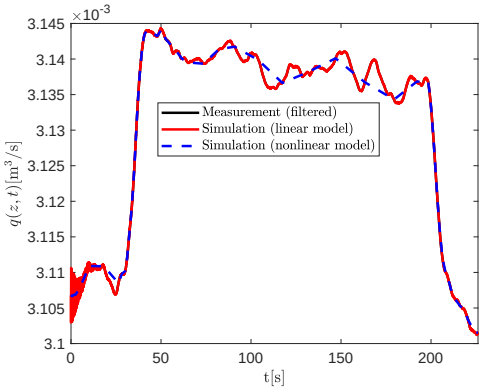

(c) Flow rate at (FT4).

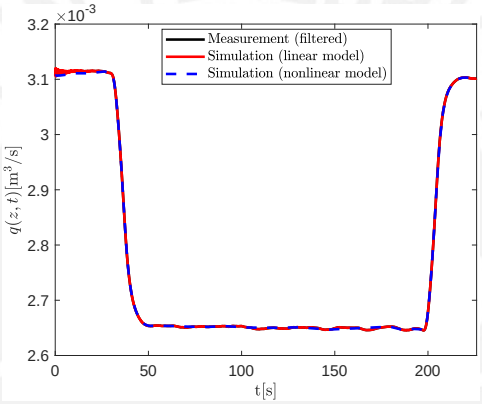

Figure 5.20.: Comparison of the measured and simulated flow rates at (FT2), (FT3) and (FT4), operating point $q_0(t) \approx 3.1 \cdot 10^{-3}\ \frac{\mathrm{m}^3}{\mathrm{s}}$, big leak occurring after $t = 30$ s at $z^* = 85.59$ m. Simulation with linear pipe model (2.4) and nonlinear pipe model (2.10).

compared against the measurement data. The comparison of the pressure simulated by the linear pipe model (2.4) and the nonlinear pipe model (2.10) at the sensor point (PT1) reveals, that the nonlinear pipe model (2.10) reproduces more accurately the value of the pressure in steady state. While the linear pipe model (2.4) leads to deviations of over 15 mbar, the nonlinear model (2.10) results in deviations of under 5 mbar. For the sensor points (PT2) and (PT3) it is noticed, that the linear pipe model (2.4) reproduces better the absolute value of the pressure, but the nonlinear pipe model (2.10) shows a higher accuracy considering the amplitude of the pressure decrease caused by the leak. This observation can be explained by the Figure 5.4 that illustrates the friction factor F over the flow rate $q_0(t)$. The curve in Figurew 5.4 reveals that the friction factor F depends strongly on the flow rate regime and changes by more than $1\ \%$ per a flow rate change of $1\ \%$. Since the leak occurs relatively close to the inlet, a large part of the pipe operates in a lower flow

(a) Pressure at (PT1).

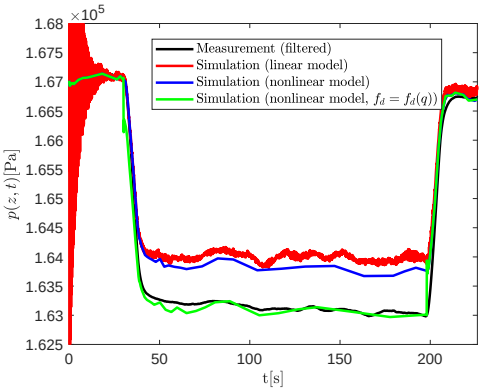

(b) Pressure at (PT2).

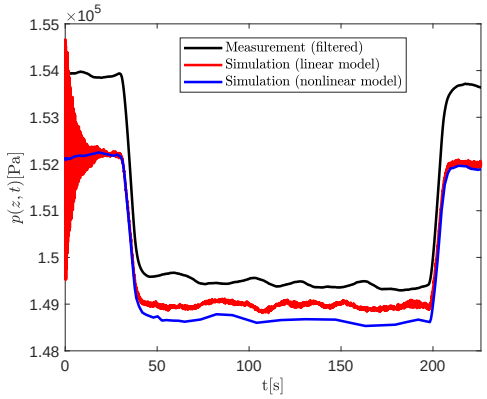

(c) Pressure at (PT3).

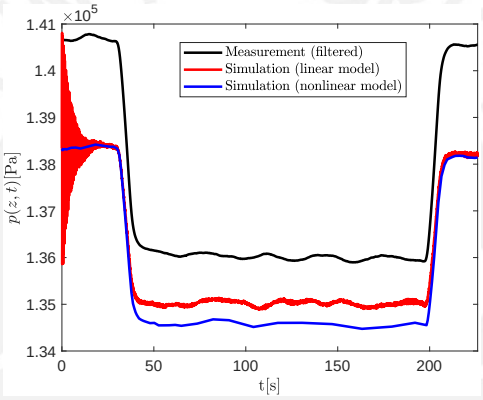

Figure 5.21.: Comparison of the measured and simulated pressure at (PT1), (PT2) and (PT3), operating point $q_0(t) \approx 3.1 \cdot 10^{-3}\ \frac{\mathrm{m}^3}{\mathrm{s}}$, big leak occurring after $t = 30$ s at $z^* = 85.59$ m. Simulation with linear pipe model (2.4) and nonlinear pipe model (2.10).

rate regime after the leak has occurred. Consequently, the friction factor F identified for the higher operating point $\approx 3.1 \cdot 10^{-3}\ \frac{\mathrm{m}^3}{\mathrm{s}}$ does not reflect well the friction losses in the leakage case. Since the pressure drop according to Equation (5.3) depends linearly on the friction factor F and due to the high sensitivity of the friction factor F regarding the flow rate, the pressure simulated by the linear pipe model (2.4) shows visible deviations from the measurement data. In contrast, the nonlinear pipe model (2.10) assumes friction losses that depend quadratically on the flow rate, such that the linear relationship between the friction factor F and the flow rate is reflected in the model. Consequently, the nonlinear pipe model (2.10) leads to a higher model accuracy regarding the pressure if a small leak further away from the outlet occurs.

In sum, this section has shown that both models, the linear pipe model (2.4) and the nonlinear pipe model (2.10) have several limitations concerning the accuracy of the pressure model if a

(a) Inlet flow rate $q_0(t)$ rate at (FT1).

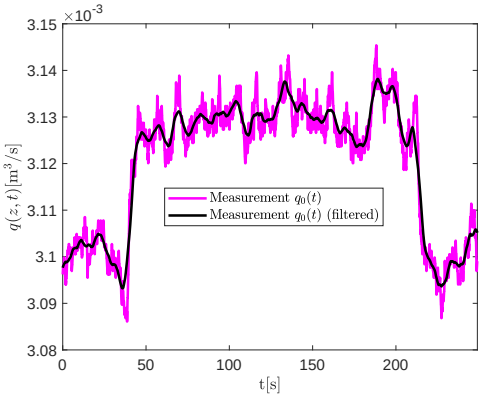

(b) Outlet pressure at (PT4).

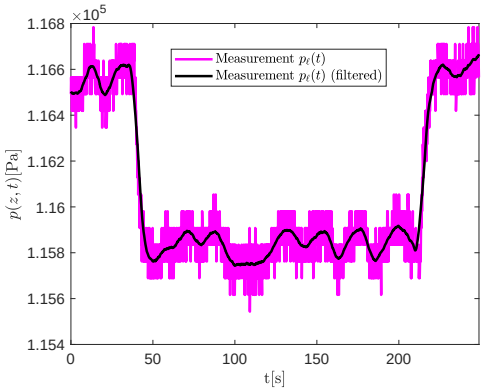

(c) Leak size χ.

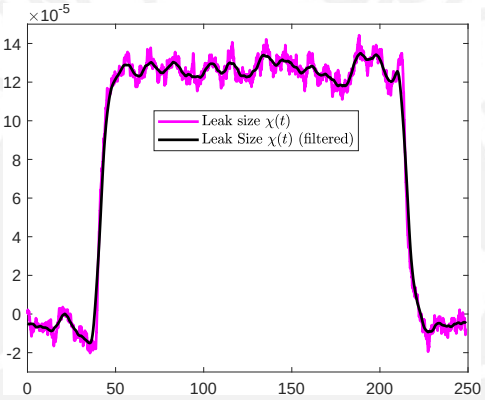

Figure 5.22.: Inlet flow rate $q_0(t)$ at sensor (FT1) (left), outlet pressure $p_\ell(t)$ at sensor (PT4) (middle) and leak size $\chi(t)$ inferred from flow rate measurements (FT3) and (FT4), operating point $q_0(t) \approx 3.1{\cdot}10^{-3}\ \frac{\mathrm{m}^3}{\mathrm{s}}$, small leak occurring after $t = 30$ s at $z^* = 11.73$ m.

leakage occurs. While the flow rate is reproduced in the simulations with a high accuracy, the pressure shows visible deviations if leaks of a larger size are considered. Thereby, this section has pointed out, that the friction parameters F and f_d not only depend on the position z, as shown in the previous Section 5.2.1, but also on the flow rate $q(z,t)$. Furthermore, it has become clear that the linear pipe model (2.4) underestimates the amplitude of the pressure change if a leakage occurs further away from the outlet. In these scenarios, a large part of the pipe operates in a lower flow regime such that the friction factor F, that was previously identified for a higher flow regime, does not fit well the pressure drop in steady state with leakage. These limitations and inaccuracies of the linear pipe model (2.4) have to be considered as a constraining framework in the following section, where the performance of the dynamic and the algebraic observer is evaluated utilizing

(a) Flow rate at (FT2).

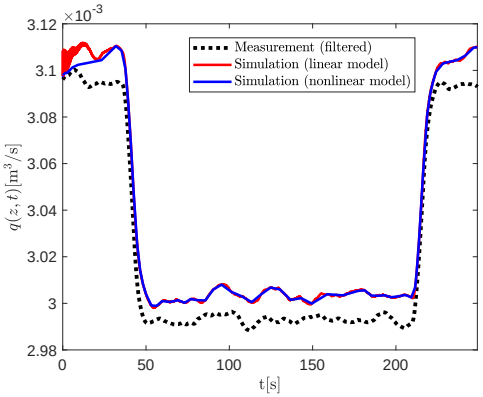

(b) Flow rate at (FT3).

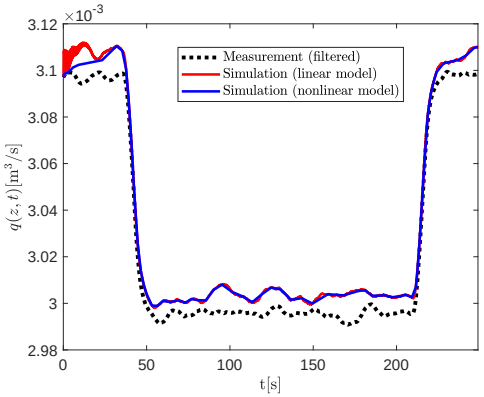

(c) Flow rate at (FT4).

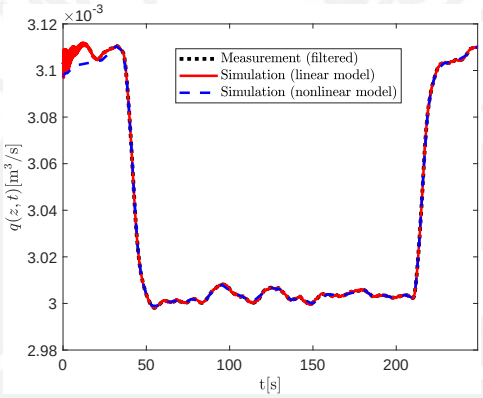

Figure 5.23.: Comparison of the measured and simulated flow rates at (FT2), (FT3) and (FT4), operating point $q_0(t) \approx 3.1 \cdot 10^{-3} \ \frac{\mathrm{m}^3}{\mathrm{s}}$, small leak occurring after $t = 30$ s at $z^* = 11.73$ m. Simulation with linear pipe model (2.4) and nonlinear pipe model (2.10).

measurement data from the pilot plant.

5.3. KPI-based Evaluation of the Leak Observer Results for the Pilot Plant

This section presents the highlight of the chapter, the evaluation of the performance of both observers, the ABSO and the algebraic observer, w.r.t. to the leak detection, size estimation and localization by utilizing measurement data obtained from the pilot plant in the leakage case. The previous Sections 5.1 and 5.2 form the basis for this analysis by identifying the unknown

(a) Pressure at (PT1).

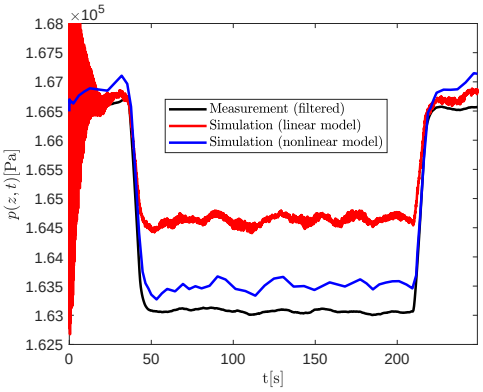

(b) Pressure at (PT2).

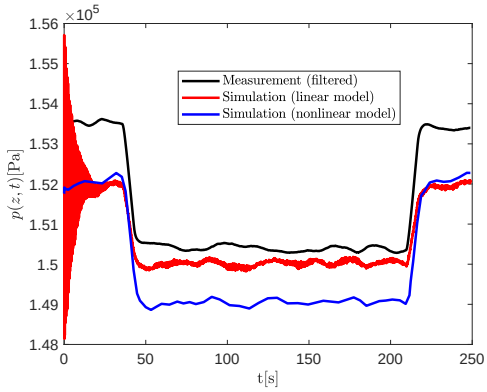

(c) Pressure at (PT3).

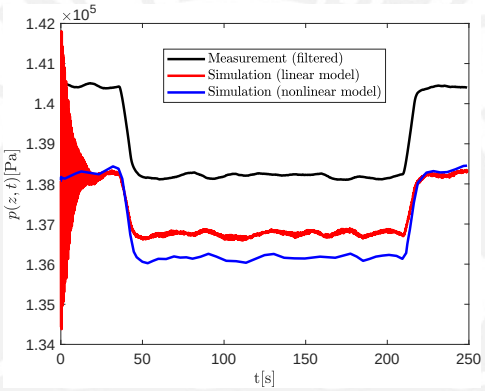

Figure 5.24.: Comparison of the measured and simulated pressure at (PT1), (PT2) and (PT3), operating point $q_0(t) \approx 3.1{\cdot}10^{-3}\ \frac{\mathrm{m}^3}{\mathrm{s}}$, small leak occurring after $t = 30$ s at $z^* = 11.73$ m. Simulation with linear pipe model (2.4) and nonlinear pipe model (2.10).

model parameters and by providing a constraining framework, revealing the differences between the model assumptions drawn in Chapter 2 and the dynamic behavior of the pilot plant. To compare the performance of both observers in a fair and generic way, the KPIs defined in Chapter 4 and summarized in Table 4.2 are reutilized, i.e., the accuracy, the standard deviation and the convergence speed of the leak size and leak position estimates provided by both observers are contrasted. Since Section 5.2.2 has revealed that the leak size χ is not exactly constant in the measurements, the evaluation of the standard deviation of the leak size estimate is omitted. Furthermore, the real-time capability of the ABSO and the algebraic observer is verified by comparing the required runtime. Moreover, the impact of the operating conditions and the leak characteristics on the KPIs is analyzed. To this end, the pilot plant is regarded for different leak sizes, leak positions and inlet flows. It is reminded that the real leak size escaping through one of the solenoid valves (SV1, SV2)

or one of the proportional valves (PV1, PV2) can only be inferred from the flow rate measurements (FT1) and (FT4) at the inlet and the outlet, but cannot be directly measured. Therefore, the performance of both observers will only be analyzed for the steady state case, i.e., the pump power is held constant to keep the inlet flow rate approximately constant.

In the first scenario, that will form the reference scenario for the following investigations, the pumps of the pilot plant work both at $60\ \%$ of their maximum power, leading to an inlet flow of $q_0(t) \approx 3.1 \cdot 10^{-3}\ \frac{\mathrm{m}^3}{s}$. After $t = 30$ s, the proportional valve (PV2), that is located near to the outlet of the pipe at $z = 85.59$ m, is opened partially, leading to a leak size that represents in steady state about $2.55\ \%$ of the inlet flow rate. At $t = 180$ s, the proportional valve (PV2) is closed. The inlet and outlet flow rate and pressure data measured by the sensors (FT1, FT4) and (PT1, PT4), respectively, is logged. Hereinafter, this measurement data is filtered by a moving average filter with a time window of length $T = 5$ s.[1]. Finally, this filtered measurement data is fed to the ABSO and the algebraic observer.

In Figure 5.25, the measured pressure and flow rate at the inlet and outlet are shown together with the filtered data. The linear friction factor F is identified according to Equation (5.3) from the flow and pressure measurements before the leakage occurs, resulting in $F = 371\ \frac{\mathrm{kg}}{\mathrm{m}^3\mathrm{s}}$. The tuning of the ABSO is done according to the tuning guidelines presented in Section 3.2 and led to an observer gain for the leak size of $L = -100$, an observer gain $\gamma = 0.005$ for the leak localization[2] and a spatial discretization with $n = 90$ nodes. On the other hand, the design of the algebraic observer is realized following the indications described in Section 4.1. The adjustment process of the design parameters resulted in moving time windows of length $T_\chi = 1$ s and $T_\delta = 3.9$ s for the leak size estimation and the state estimation and an approximation order of $N = 1$ for the function expansion (3.67). Since the pilot plant is much shorter than the pipe considered in Chapter 4, the wave velocity $\epsilon = \frac{1}{L}\sqrt{\frac{\beta}{\rho}}$ increases. As Theorem 3.3.5 indicates, the wave velocity ϵ determines the required time t_F to control the auxiliary problems (3.69) and (3.70). The greater ϵ, the smaller the required time t_F. Moreover, the small approximation order of $N = 1$ also originates from the short length of the pilot plant in comparison to the pipe examined in Chapter 4. Since the length ℓ is relatively small, the term $e^{\pm\frac{\ell F}{2\sqrt{\beta\rho}}x}$ in the state transformation (3.2) varies by about less than $1.2\ \%$ over the domain of the spatial variable x. Consequently, the relationship between the states $u(\cdot,\cdot),\ v(\cdot,\cdot)$ and the spatial variable x is approximately linear, such that it is reasonable to also take a linear approximation for the function expansion (3.67). Besides, a relatively short time window T_δ for the leak size estimation is chosen to capture well the variations of the inferred

[1] Since the main focus lies on the comparison of both observers and the required computational costs for their implementation, the filtering process is not considered in the indicated runtimes.

[2] According to Remark 5, the convergence, speed of the leak localization depends linearly on the friction factor F. Since the friction factor F identified for the pilot plant is about two dimensions greater than the friction factor F assigned to the simulation plant examined in Chapter 4, the observer gain γ is significantly smaller than for the simulation plant.

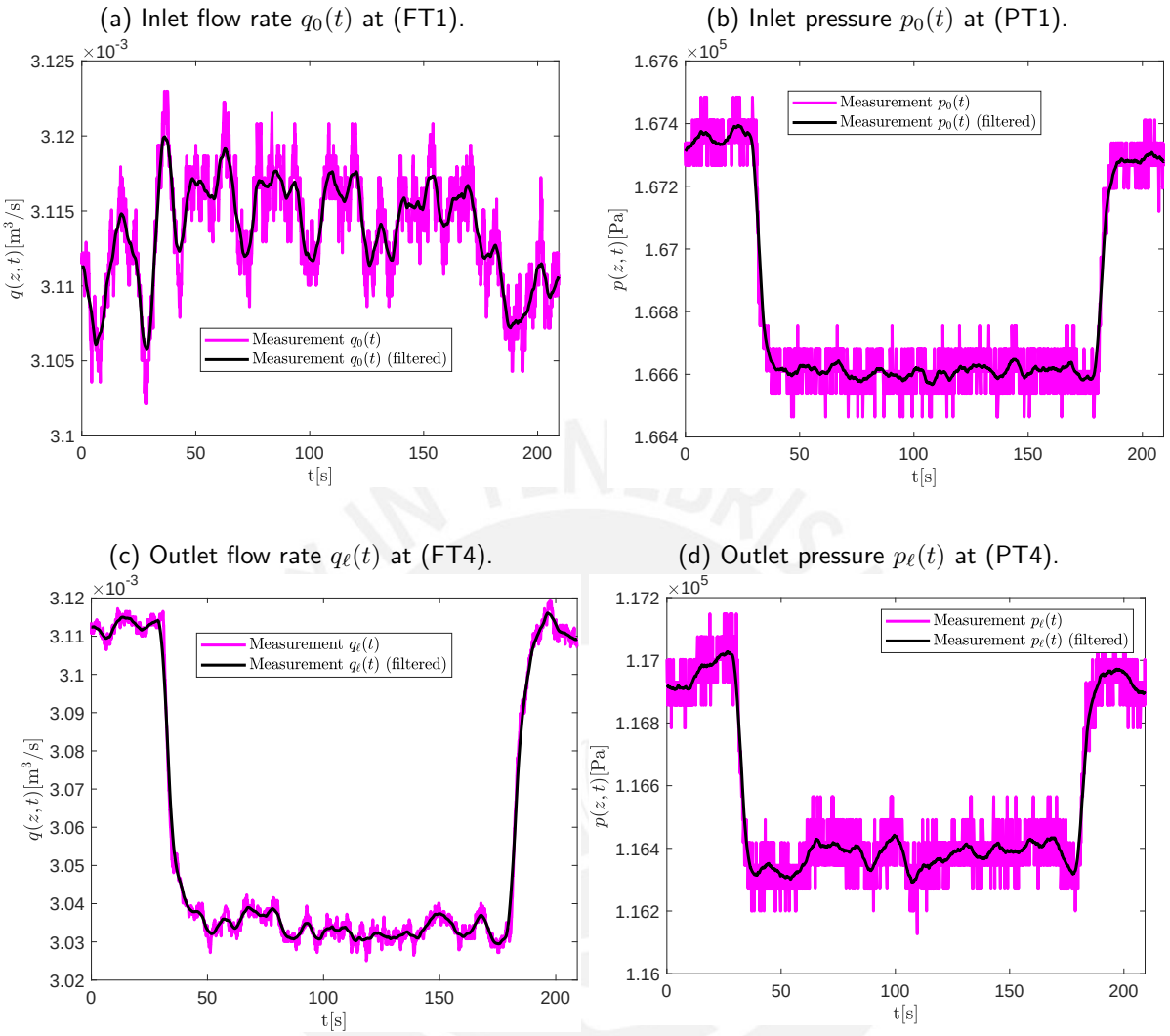

Figure 5.25.: Flow rate (left) and pressure (right) at inlet (above) and outlet (below) of pilot plant at PUCP, operating point $q_0(t) \approx 3.1 \cdot 10^{-3}\ \frac{\mathrm{m}^3}{\mathrm{s}}$, small leak occurring after $t = 30$ s at $z^* = 85.59$ m.

leak size χ due to fluctuations in the inlet flow. Furthermore, an observer gain of $\gamma = 0.003$ is chosen. It is commented that for higher observer gains γ, the estimate of the leak position oscillates strongly with amplitudes of up to 20 m such that a reasonable leak localization was not possible. Furthermore, a longer time window T_δ has not led to a better noise suppression. Finally, both observers work with a sample time of $T_s = 1$ ms and the leak estimation is initialized with $\hat{\chi}(0) = 0,\ \hat{\delta}(t = 0) = \frac{\ell}{2}$.

In Figure 5.26 and Table 5.2, the leak size and leak position estimates are compared graphically

as well as numerically. For reasons of better visibility, the leak size χ is displayed in $\frac{\text{l}}{\text{s}}$. It is clearly noticed that both observers estimate accurately and rapidly the current leak size. Although the leak size is relatively small with under $2.5\ \%$ of the nominal flow, both observers provide a leak size estimate with deviations of significantly under $0.1\ \%$ from the real leak size within a time period of under 0.5 s. The analysis of the KPIs summarized in Table 5.2 shows that the ABSO provides a more rapid and slightly more accurate estimate of the leak size. However, the more noticeable differences between both observers are regarded considering the estimation of the leak position. Firstly, it is highlighted that both observers fulfill the predefined accuracy goal of a leak localization with an error less than $5\ \%$ w.r.t. the length of the pipe. While the ABSO needs less than 1 min to provide an accurate estimate of the leak position that stays inside the desired error tolerance bounds, the algebraic observer needs about 30 s more to reach the same accuracy. On the other side, it is seen that the algebraic observer provides a more accurate estimate of the leak position with a mean deviation of under $1\ \%$ once the estimate has converged. Furthermore, the comparison of the runtime points out that the implementation ABSO is noticeably faster than the implementation of the algebraic observer. Nonetheless, it is underlined that the runtime of both observers is significantly smaller than the considered time horizon, such that an implementation in real time is enabled.

(a) Estimation of the leak size χ.

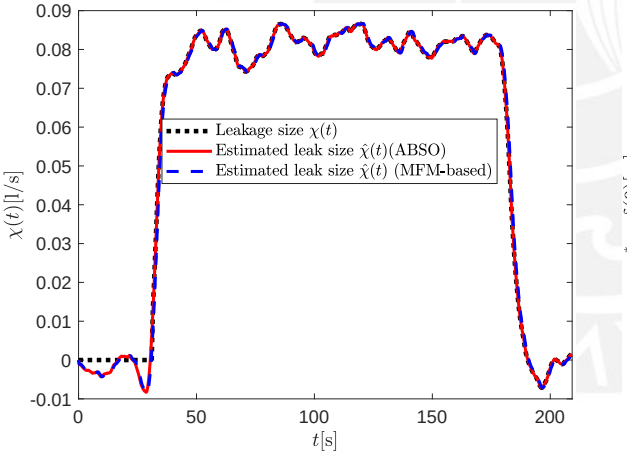

(b) Estimation of the leak position z^*.

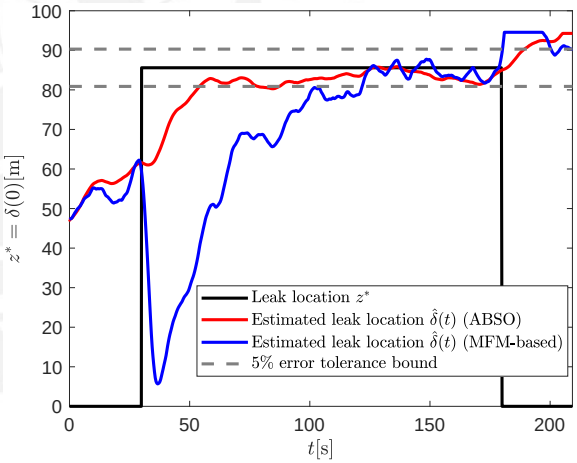

Figure 5.26.: Estimation of the leak size χ and the leak position z^* for the pilot plant at PUCP, operating point $q_0(t) \approx 3.1{\cdot}10^{-3}\ \frac{\text{m}^3}{\text{s}}$, small leak occurring after $t = 30$ s at $z^* = 85.59$ m.

The following Sections 5.3.1 through 5.3.3 extend the validation and comparison of the leak estimation performance by considering different leak sizes and positions at the pilot plant, as well as different inlet flow rates.

Observer \ KPI	$\Delta\chi$[%]	Δz^*[%]	σ_z[m]	$t_{\text{conv},\chi}$[s]	$t_{\text{conv},z}$[s]	t_{exec}[s]
Dynamic Observer (ABSO)	$\mathbf{0.0001}$	2.59	$\mathbf{1.31}$	$\mathbf{0.07}$	$\mathbf{56.07}$	$\mathbf{2.16}$
Algebraic Observer (MFM-based)	0.004	$\mathbf{0.85}$	1.53	0.47	90.51	89.78

Table 5.2.: KPIs of the dynamic and the algebraic observer for a small leak of $2.5\ \%$ of the nominal flow $q_0(t) \approx 3.1 \cdot 10^{-3}\ \frac{\text{m}^3}{\text{s}}$ appearing at $z^* = 85.59$ m.

5.3.1. Experimental-based Leak Observer Results under Variation of the Leak Size

In this section, the performance of both observers is examined for a smaller and a higher leak size than in the reference scenario. The goal is to validate that both observers perform well leaks of different size to ensure that in a real application environment small background leaks as well as larger leaks that could be caused, e.g., by a pipe burst, are detected and localized accurately. The operating point and the leak position are the same as in the reference scenario, and only the aperture of the proportional valve (PV2) is varied.

In the first case, the proportional valve (PV2) is opened wider than in the reference scenario, leading to a flow rate through the leak that represents about $15.66\ \%$ of the nominal inlet flow rate. The resulting leak size and position estimates provided by both observers are shown graphically and numerically in Figure 5.27 and Table 5.3. Firstly, it is clearly noticed that both observers estimate accurately the current leak size with negligible deviations. Moreover, the ABSO detects the leak size within one sample period while the algebraic observer has a delay of under 0.5 s due to the moving time window T_χ that incorporates the past measurements of the flow rate and the pressure. On the other hand, the leak localization is less accurate than in the reference scenario and the mean value of the estimates of both observers are almost violating the $5\ \%$ error tolerance bound. Furthermore, the estimates of the leak position do not stay inside the desired error tolerance bounds. Since the leak is relatively large with over $15\ \%$ of the nominal inlet flow, the segment of the pipe behind the leak operates in a significantly smaller flow rate regime. Consequently, the friction losses and the friction factor F in this part of the pipe are smaller than it is described by the friction factor $F = 371\ \frac{\text{kg}}{\text{m}^3\text{s}}$. Therefore, both observers underestimate the real leak position. These results agree with the model validation performed in Section 5.2.2 that has revealed that the linear pipe model (2.4) is less accurate for larger leaks. Besides, it is observed, that although the leak localization estimates do not stay inside the desired error tolerance bound, they converge faster than in the reference scenario. The ABSO needs about 5 s and the algebraic observer about 30 s to reach the range of their final values what represents a reduction of $90\ \%$ and $65\ \%$, respectively, in

comparison to the reference scenario (see Table 5.2). The faster convergence speed agrees with the results presented in Section 4.2.2 (see Table 4.7) and is explained by Remark 5.

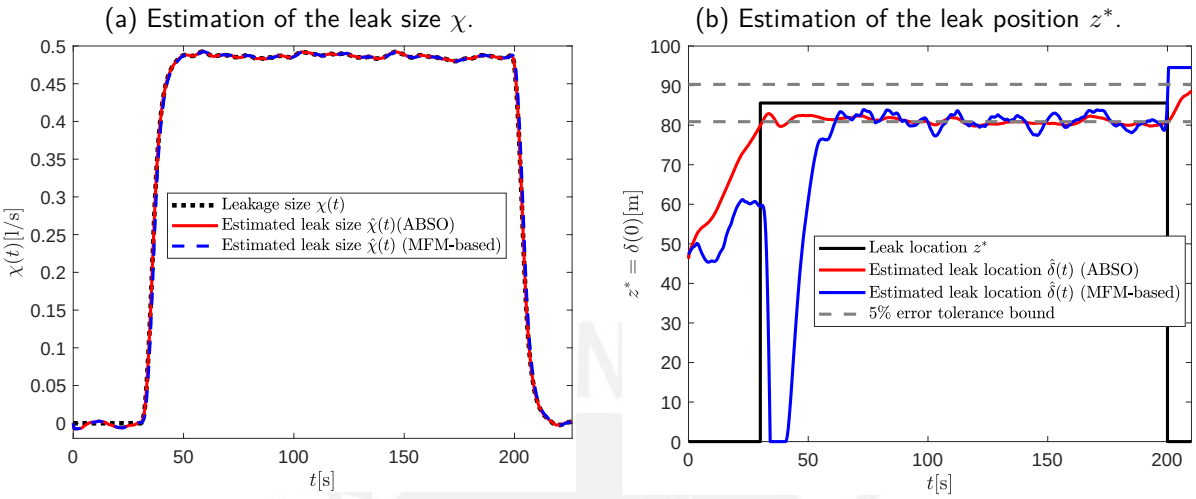

Figure 5.27.: Estimation of the leak size χ and the leak position z^* for the pilot plant at PUCP, operating point $q_0(t) \approx 3.1 \cdot 10^{-3}$ $\frac{\text{m}^3}{\text{s}}$, large leak occurring after $t = 30$ s at $z^* = 85.59$ m.

Observer \ KPI	$\Delta\chi$[%]	Δz^*[%]	σ_z[m]	$t_{\text{conv},\chi}$[s]	$t_{\text{conv},z}$[s]	t_{exec}[s]
Dynamic Observer (ABSO)	**0.001**	4.98	**0.58**	**0.001**	–	**2.00**
Algebraic Observer (MFM-based)	0.006	**4.72**	1.63	0.43	–	88.02

Table 5.3.: KPIs of the dynamic and the algebraic observer for a large leak of 15.66 % of the nominal flow $q_0(t) \approx 3.1 \cdot 10^{-3}$ $\frac{\text{m}^3}{\text{s}}$ appearing at $z^* = 85.59$ m.

The second part of this section examines a small leak that represents less than 1.4 % of the nominal inlet flow. In this case, the variation of the pressure $p_\ell(t)$ that is measured at the outlet due to the leak is in the range of the measurement noise and results in an SNR of 8 dB between pressure variation at the outlet and measurement noise of the flow rate measurements and an SNR of about 24 dB between leak size and measurement noise of the flow rate measurements. Nonetheless, both observers estimate well the leak size with deviations of clearly under 0.1 % as Figure 5.28 illustrates. Besides, it is noticed that the leak size inferred from the measurements at the inlet and the outlet shows fluctuations of about 20 % around the mean value $\bar{\chi} = 0.05$ $\frac{\text{l}}{\text{s}}$. These fluctuations also affect the estimation of the leak position, such that the estimates triple their standard deviation w.r.t. the reference scenario (see Table 5.2). It is seen that both observers provide a leak position

estimate that roughly reflects the real leak position. However, the fluctuations in the inferred leak size effect that the estimates do not stay inside the predefined error bounds. In particular, the algebraic observer that converges slower, shows oscillations with amplitudes of about 10 m such that the desired accuracy goal of a mean error of under 5 % is not reached. On the other hand, the leak localization provided by the ABSO oscillates less and leads to a mean error of about 1 %.

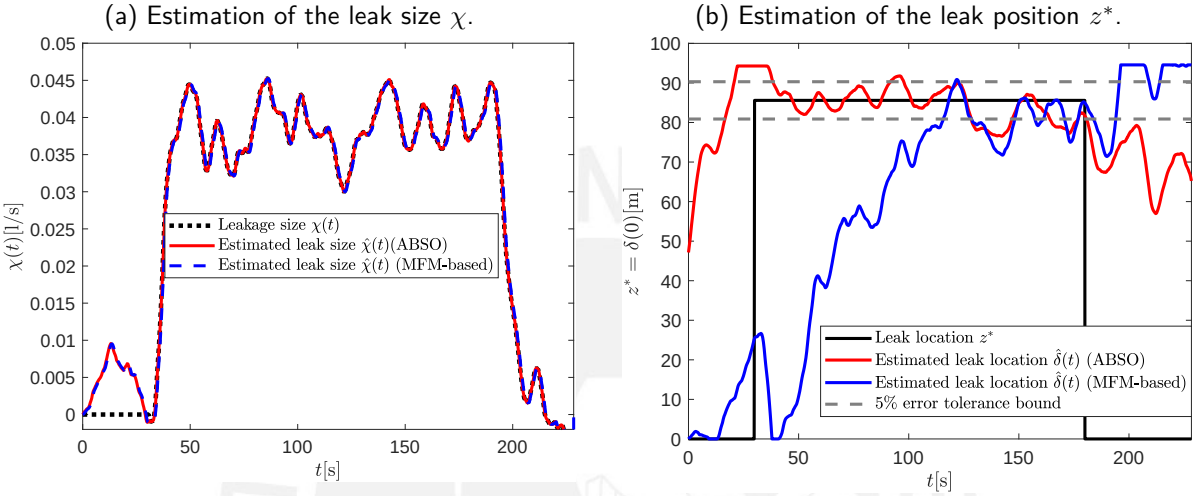

Figure 5.28.: Estimation of the leak size χ and the leak position z^* for the pilot plant at PUCP, operating point $q_0(t) \approx 3.1{\cdot}10^{-3}\ \frac{\text{m}^3}{\text{s}}$, small leak occurring after $t = 30$ s at $z^* = 85.59$ m.

KPI / Observer	$\Delta\chi$[%]	Δz^*[%]	σ_z[m]	$t_{\text{conv},\chi}$[s]	$t_{\text{conv},z}$[s]	t_{exec}[s]
Dynamic Observer (ABSO)	**0.008**	**1.08**	**3.47**	**0.01**	–	**2.22**
Algebraic Observer (MFM-based)	0.07	5.75	4.28	0.54	–	81.21

Table 5.4.: KPIs of the dynamic and the algebraic observer for a small leak of 1.4 % of the nominal flow $q_0(t) \approx 3.1 \cdot 10^{-3}\ \frac{\text{m}^3}{\text{s}}$ appearing at $z^* = 85.59$ m.

In summary, this section has pointed out that both observers estimate accurately the leak size for different magnitudes of the leakage. Thereby, a reasonable and valid leak detection is enabled. Moreover, it turns out that the size of the leakage is crucial for the accuracy of the leak localization. For a leak size of about 2.5 %, both observers provide an accurate estimate of the leak position with deviations clearly under 5 %. In this reference scenario, the algebraic observer estimates less

rapid but more accurate the leak position. If a very large leak of over $15\ \%$ of the nominal flow is considered, the accuracy of the linear pipe model (2.4) decreases as Section 5.2.2 revealed. Since both models base on this model and on the assumption of a constant linear friction factor F, the leak localization becomes less accurate with deviations of up to $5\ \%$ from the real leak position. Moreover, the performance of the observer was analyzed for a small leak whose characteristics w.r.t. to its size and to the caused pressure change are near to the resolution limits of the measurement equipment. It has been shown that the leak position can be estimated roughly by both observers, but that the impact of the fluctuations in the inlet flow and the leak size disturb the leak localization such that the estimates do not stay inside the desired error tolerance bounds. In this scenario, the ABSO provides a more accurate leak position estimate with a mean error of about $1\ \%$ while the algebraic observer does not reach the desired accuracy. In the following section, the impact of another leak characteristic, the leak position, on the observer accuracy is examined.

5.3.2. Experimental-based Leak Observer Results under Variation of the Leak Position

This section analyzes the performance of both observers if the leak occurs not near to the outlet, as in the previous scenarios discussed above, but nearer to the inlet. The further operating conditions (inlet flow rate, leak size) are not changed.

In the first scenario, the solenoid valve (SV2) is opened partially after $t = 60$ s and closed at $t = 250$ s, i.e. the leak occurs at $z = 60.99$ m. The leak has a magnitude of about $2.5\ \%$ of the inlet flow. In Figure 5.29 and Table 5.5 the leak size and leak position estimates provided by both observers are compared graphically and numerically. Firstly, it is seen that both observers estimate well the current leak size with deviations clearly under $0.1\ \%$. Thereby, a valid and reasonable leak detection is performed. However, the accuracy of the leak localization decreases drastically and mean errors of over $20\ \%$ are obtained. The mean error of the algebraic observer is about $1\ \%$ than the mean error of the ABSO, but in total, both observers fail clearly to fulfill the desired accuracy goal. Since the leak occurs nearer to the inlet, a significant pipe segment

KPI / Observer	$\Delta\chi$[%]	Δz^*[%]	σ_z[m]	$t_{\text{conv},\chi}$[s]	$t_{\text{conv},z}$[s]	t_{exec}[s]
Dynamic Observer (ABSO)	0.08	24.81	$\mathbf{0.43}$	$\mathbf{0.03}$	$-$	$\mathbf{3.27}$
Algebraic Observer (MFM-based)	$\mathbf{0.07}$	$\mathbf{23.28}$	3.99	0.41	$-$	106.75

Table 5.5.: KPIs of the dynamic and the algebraic observer for a small leak of $2.5\ \%$ of the nominal flow $q_0(t) \approx 3.1 \cdot 10^{-3}\ \frac{\text{m}^3}{\text{s}}$ appearing at $z^* = 60.99$ m.

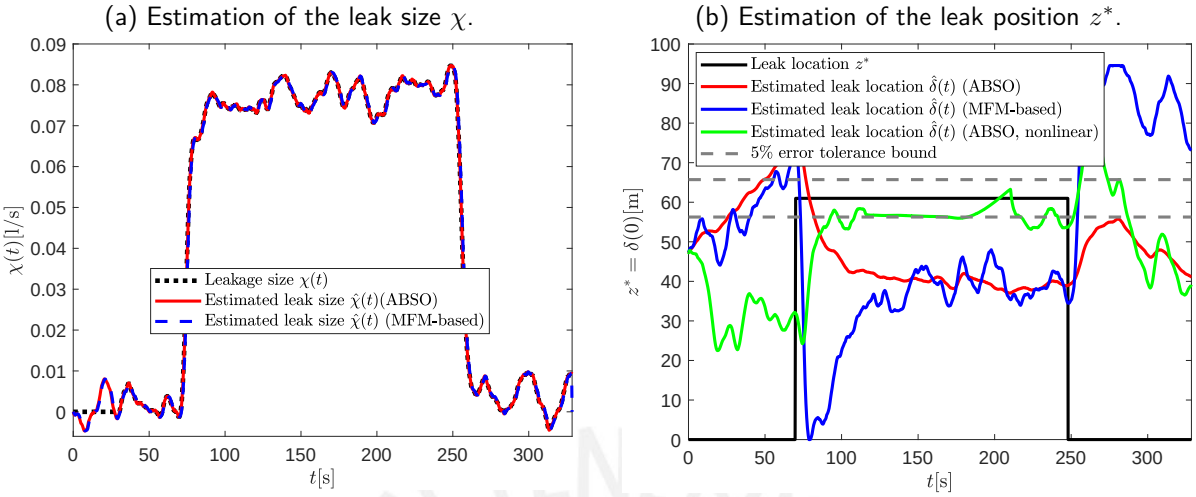

Figure 5.29.: Estimation of the leak size χ and the leak position z^* for the pilot plant at PUCP, operating point $q_0(t) \approx 3.1{\cdot}10^{-3}\ \frac{\mathrm{m}^3}{\mathrm{s}}$, small leak occurring after $t = 60$ s at $z^* = 60.99$ m.

with a length of over 30 m operates in a lower flow regime than the pipe segment in front of the leak. Therefore, the friction losses in the pipe segment behind the leak are smaller than it is assumed according to the friction factor F identified for the nominal inlet flow. Consequently, both observers visibly underestimate the leak position.To overcome this drawback, the extension of the ABSO to the nonlinear pipe model (2.10) is implemented based on the instructions in [64]. The friction coefficient f_d is identified as $f_d = 0.027$ from the measurements in steady state without leakage. It is observed that this nonlinear ABSO provides a more accurate leak position estimate with a mean error of under $4.3\ \%$ while the runtime increases to about $t_{\text{exec}} = 45.6$ s.

In the second scenario, the proportional valve installed at $z = 11.73$ m is opened partially after $t = 30$ s, resulting in a leak size that represents about $4\ \%$ of the nominal inlet flow. The Figure 5.30 and the Table 5.6 present the leak size and leak position estimates for both observers. The results strengthen the conclusion drawn from the previous scenario. While the leak size is estimated accurately with deviations of under $0.1\ \%$, both observers fail to estimate accurately the leak position. The estimates of the leak position stay constantly in $z = 0$ m once they have converged, leading to deviations of over $10\ \%$ from the real leak position. The linear pipe model (2.4) that is the base for the design of both observers does not reflect well the friction losses, since the segment in front of and the segment behind the leak operate in different flow rate regimes, such that the friction factor of the first segment is greater than the friction factor of the second segment. Consequently, the friction factor F identified for the nominal inlet flow rate is too high and the pressure $\hat{p}_0(t)$ at the inlet estimated by the leak localization observer (3.19) is higher than

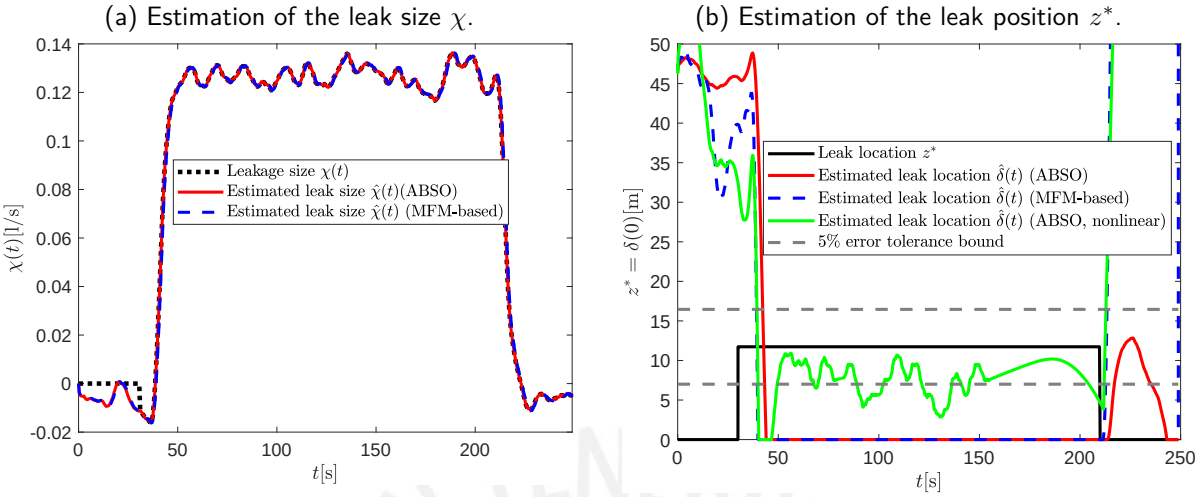

Figure 5.30.: Estimation of the leak size χ and the leak position z^* for the pilot plant at PUCP, operating point $q_0(t) \approx 3.1{\cdot}10^{-3}\ \frac{\mathrm{m}^3}{\mathrm{s}}$, small leak occurring after $t = 30$ s at $z^* = 11.73$ m.

Observer \ KPI	$\Delta\chi$[%]	Δz^*[%]	σ_z[m]	$t_{\mathrm{conv},\chi}$[s]	$t_{\mathrm{conv},z}$[s]	t_{exec}[s]
Dynamic Observer (ABSO)	**0.002**	12.44	0	**0.002**	–	**2.37**
Algebraic Observer (MFM-based)	0.004	12.44	0	0.42	–	82.16

Table 5.6.: KPIs of the dynamic and the algebraic observer for a small leak of $4\ \%$ of the nominal flow $q_0(t) \approx 3.1 \cdot 10^{-3}\ \frac{\mathrm{m}^3}{\mathrm{s}}$ appearing at $z^* = 11.73$ m.

the measured pressure $p_0(t)$. Hence, the estimated leak position is visibly smaller than the real leak position and the accuracy goal is not reached. On the contrary, the nonlinear ABSO based on [64] leads to a mean error of under $4.1\ \%$ and fulfills thereby the desired accuracy goal.

Overall, this section has revealed one of the major drawbacks of both observers, namely the localization of leaks that are located further away from the outlet of the pipe. The design of the ABSO and the algebraic observer is based on a model that assumes friction losses that are linear to flow rate and are parametrized by a constant friction factor F. However, the system identification of the friction parameters in Section 5.1 has demonstrated that the friction losses rather depend quadratically on the flow rate and the friction factor F is not constant. Therefore, as the model validation in Section 5.2.2 has pointed out, a nonlinear pipe model represents better the flow dynamics. If a leak occurs, that is not near to the outlet of the pipe, a significant part of the pipe operates in a lower flow regime than the flow regime concerned for the identification

of the friction factor F and thereby, for the design of the algebraic and the dynamic observer. Consequently, the linear pipe model (2.4) parametrized for the higher flow regime does not reflect well the flow dynamics in the pipe segment behind the leak. Since both observers show low robustness to uncertainties in the friction modeling, as Section 4.2.5 has revealed, the accuracy of the leak localization decreases significantly if the leak is not near to the outlet. For the case of a leak near to the inlet, both observers fail to localize the leak and show deviations of over $50\ \%$ w.r.t. to the total length of the pipe. However, it has to be noticed, that the resolution limits of the measurement equipment and the dead zone of the solenoid and proportional valves have not permitted to provoke leaks smaller than $2\ \%$ of the nominal inlet flow. Furthermore, the relative short length of the pilot plant of the pipe of under 100 m has to be born in mind. Therefore, it would be interesting to validate the observer performance for a longer pipe where smaller leaks can be provoked, It is expected that a smaller leak changes less the parametrization of the friction losses such that a higher accuracy for leaks that are located further away from the outlet is obtained. Furthermore, the extension of the ABSO based on [64] has improved significantly the accuracy of the leak localization. However, the stability performed in [64] analysis of this nonlinear observer similar to Theorem 3.2.2 and Theorem 3.2.3 is still part of current research. Beyond that, an extension of the algebraic observer to the nonlinear pipe model (2.10), e.g., based on the ansatz presented in [93], is not realized yet, but part of current investigations in the research group at PUCP. The following section complements the analysis of the performance of both observers with real measurement data by examining the impact of the inlet flow rate.

5.3.3. Experimental-based Leak Observer Results under Variation of the Inlet Flow Rate

This final section of the chapter validates the performance of both observers for a further operating point. To this end, the second pump is turned off and the power of the first pump is increased to $80\ \%$, resulting in an inlet flow of $q_0(t) \approx 2.4 \cdot 10^{-3}\ \frac{\mathrm{m}^3}{s}$. After $t = 30$ s, the proportional valve (PV2) is opened partially, leading to a flow rate that escapes through the valve of approximately $\chi = 0.08 \cdot 10^{-3}\ \frac{\mathrm{m}^3}{s}$, i.e. less than $3\ \%$ of the nominal flow. In Figure 5.31, the measurements of the flow rate and the pressure at the inlet and the outlet are illustrated. For the operating point $q_0(t) \approx 2.4 \cdot 10^{-3}\ \frac{\mathrm{m}^3}{s}$, a linear friction factor $F = 289.5\ \frac{\mathrm{kg}}{\mathrm{m}^3\mathrm{s}}$ is identified. For the following analysis of the observer performance, the design parameters of the ABSO were not changed in comparison to the reference scenario considered in Table 5.2. The auxiliary problems (3.31) as well as (3.69) and (3.70) were solved with the same lengths $T_\chi =$ and $T_\delta =$ of the moving time windows, considering the new friction factor F.

In Figure 5.32 and Table 5.7, the performance of both observers is contrasted graphically and

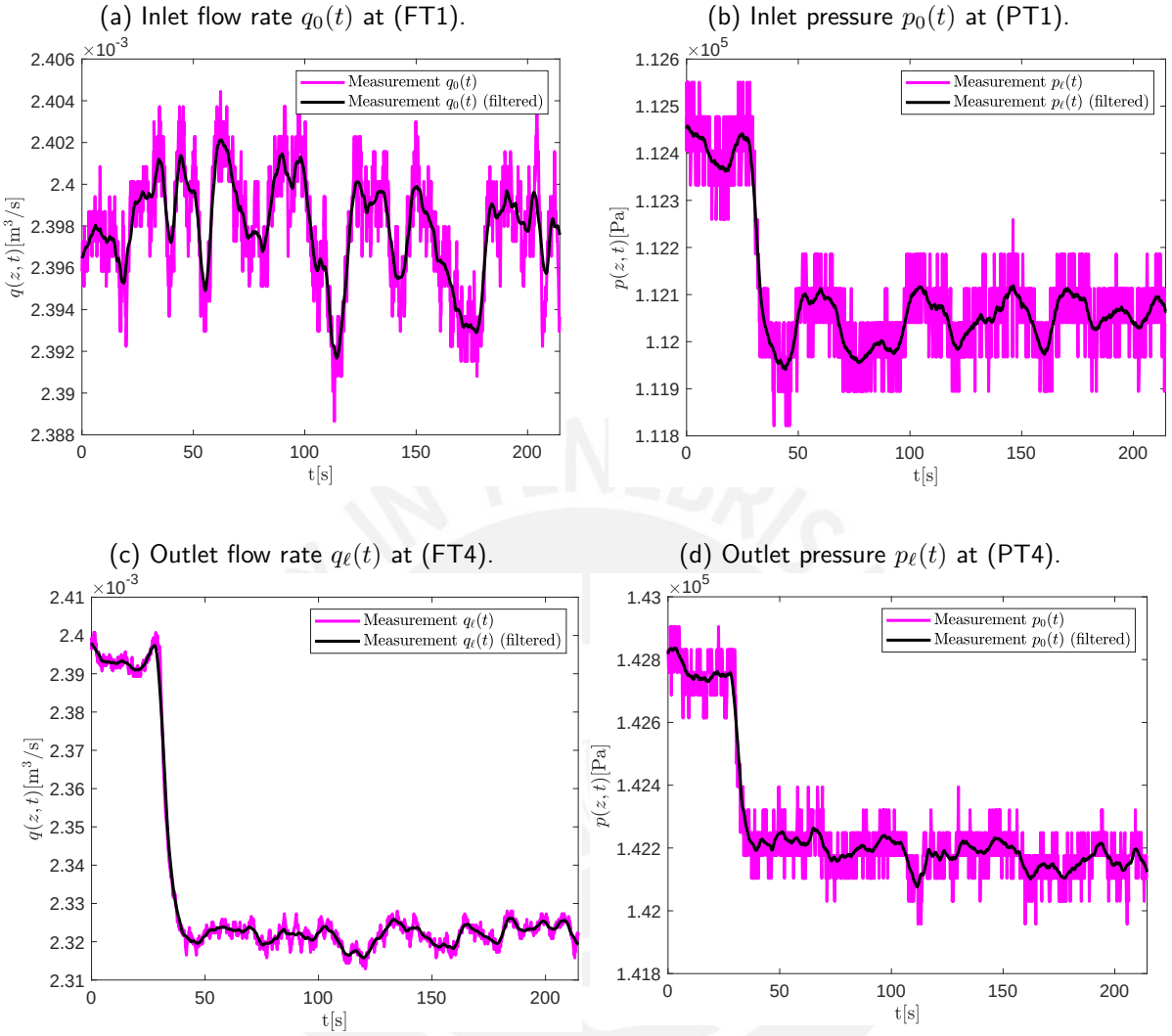

Figure 5.31.: Flow rate (left) and pressure (right) at inlet (above) and outlet (below) of pilot plant at PUCP, operating point $q_0(t) \approx 2.4 \cdot 10^{-3}\ \frac{\mathrm{m}^3}{\mathrm{s}}$, small leak occurring after $t = 30$ s at $z^* = 85.59$ m.

numerically. The mean error of the leak size estimation is in the same range as in the previous investigated cases throughout this chapter, and lies clearly under $0.01\ \%$. Once again, it is noticed that the ABSO detects more rapidly and slightly more accurate the leak size. Regarding the estimation of the leak position, it is seen that both observer fulfill the desired accuracy goal and provide a leak localization estimate with a mean error of clearly under $5\ \%$. It is noticed that the mean error of the algebraic observer is about $1\ \%$ smaller in comparison to the ABSO. However, the leak position estimate of the ABSO converges faster into the range of the real leak position and

shows fewer fluctuations, as the comparison of the standard deviations σ_z demonstrates numerically. Furthermore, it is observed that the leak position estimates do not stay inside the $5\ \%$ error tolerance bound once they have converged. However, the maximal deviations are in the range of under $6\ \%$ such that the accuracy and reliability of the leak localization affected strongly.

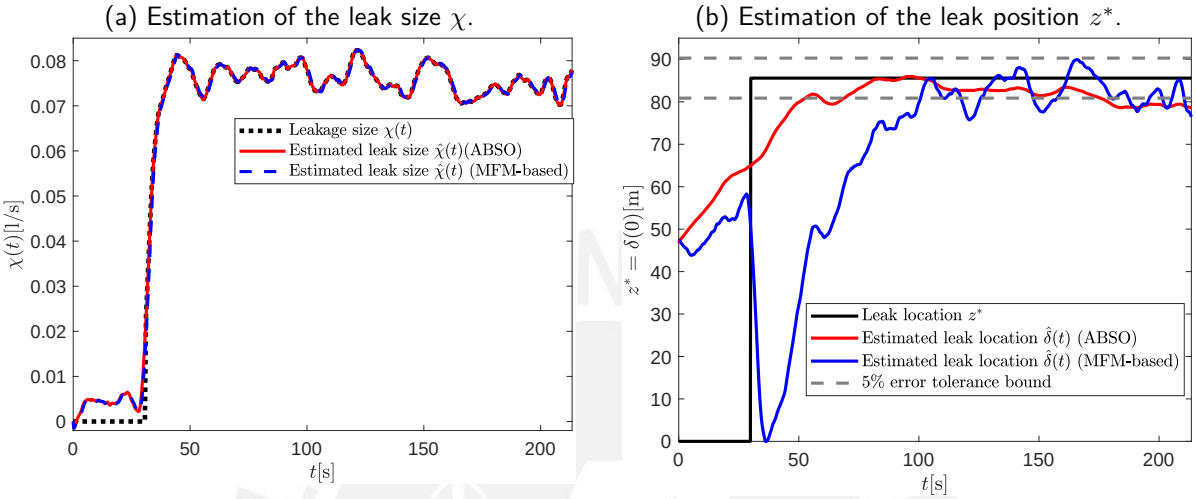

Figure 5.32.: Estimation of the leak size χ and the leak position z^* for the pilot plant at PUCP, operating point $q_0(t) \approx 2.4{\cdot}10^{-3}\ \frac{\mathrm{m}^3}{\mathrm{s}}$, small leak occurring after $t = 30$ s at $z^* = 85.59$ m.

Observer \ KPI	$\Delta\chi$[%]	Δz^*[%]	σ_z[m]	$t_{\mathrm{conv},\chi}$[s]	$t_{\mathrm{conv},z}$[s]	t_{exec}[s]
Dynamic Observer (ABSO)	**0.0002**	2.26	**0.59**	**0.06**	–	**1.65**
Algebraic Observer (MFM-based)	0.004	**1.17**	3.79	0.45	–	95.94

Table 5.7.: KPIs of the dynamic and the algebraic observer for a small leak of under $3.0\ \%$ of the nominal flow $q_0(t) \approx 2.4 \cdot 10^{-3}\ \frac{\mathrm{m}^3}{\mathrm{s}}$ appearing at $z^* = 85.59$ m.

To sum up the results of this section, it is verified that both observers perform well, complying with the desired accuracy goals w.r.t. the leak localization and leak size estimation if another operating point of the pilot plant is considered. Since the leak size cannot be measured directly, but only inferred from the flow rate measurements at the inlet and the outlet, a validation of the observer performance under time-varying boundary conditions similar to the case investigated in Table 4.13 is omitted.

6. Conclusion and Outlook

The main goal of this work, as formulated in Section 1.2.1, is to derive, implement and validate a dynamic and an algebraic observer to detect in real-time leaks smaller than $1\ \%$ of the nominal flow rate, estimate its size and localize its position with deviations under $5\ \%$ regarding the real leak size and the total length of the pipe. This final chapter summarizes the main results of this work and points out whether this general objective is achieved and where are the limitations of the two presented leak observers. Furthermore, an outlook is given how future work could face these limitations to further improve the performance of the two presented leak observers.

Since both observers are model-based, Chapter 2 presents the modeling of the fluid dynamics in the water pipe by two coupled linear hyperbolic PDEs of first order. The main difference in comparison to other literature [56] is the assumption of a constant leak size and of friction losses that depend linearly on the flow rate.

The theoretical core of this work lies in Chapter 3 where the model-based design of the dynamic and the algebraic observer is derived. It is strongly emphasized that both observers are late lumped, and in contrast to other model-based leak observer (e.g., KF-type leakage observers [56]), the observer design bases directly on the PDE model of the pipe and no spatial discretization is needed to derive the observer. While the design of the dynamic observer is extracted from [27], the algebraic observer presents a novel approach for a model-based late lumped leak observer and addresses thereby a current research gap. The MFM is applied to transform the pipe model into the auxiliary PDE problems $\Sigma_{\text{aux},\chi}$ and $\Sigma_{\text{aux},u}$, $\Sigma_{\text{aux},u}$ and the algebraic IO equations (3.30) and (3.68). It is shown mathematically that a direct estimation of the leak position by applying the MFM to the pipe model is not possible. Instead, the leak position is estimated, similar to the scheme of the dynamic observer, via a (MFM-based) state estimation.

A remaining issue for future work is the proof of the convergence of the power series ansatz (3.43) to solve the transition problem formulated by the auxiliary problem $\Sigma_{\text{aux},\chi}$ based on Gevrey functions. Alternatively, one could try to solve the auxiliary problem $\Sigma_{\text{aux},\chi}$ by utilizing the backstepping control law (3.76) and subdividing the time horizon into two parts. During the first part $t \in [0, \frac{T_\chi}{2}]$ of the time horizon, the state $\varphi(x,\tau)$ of the auxiliary problem would be steered from $\varphi(x,0) = 0$ to an (arbitrary) final state $\varphi(x, \frac{T_\chi}{2}) = \varphi_0^* \neq 0$ taking the approach from Theorem 3.3.5. During the second part $t \in (\frac{T_\chi}{2}, T_\chi]$ of the time horizon, the auxiliary problem $\Sigma_{\text{aux},\chi}$ would be stabilized,

applying the backstepping control law (3.76), to finally complete the state transition $\varphi(x,0) = 0 \rightsquigarrow \varphi(x,T_\chi) = 0$. Once the MF $\varphi(\cdot,\cdot)$ is obtained by joining the two subtrajectories, one has to verify that the condition $\int_{t-T_\chi}^{t} \varphi_1(0,\tau - t + T_\chi)\mathrm{d}\tau \neq 0$ of Theorem 3.3.2 is fulfilled.

Moreover, the backstepping control law (3.76) that is used to solve the auxiliary problems $\Sigma_{\text{aux},u}$, $\Sigma_{\text{aux},v}$ does not have any tuning parameters, but the time horizon for stabilizing the auxiliary problems depends only on the physical parameterization of the pipe. Future work could examine if and how additional tuning parameters can be introduced into the backstepping control law (3.76), such that the transition error could be minimized not only by augmenting the time horizon T_δ, but by adjusting the introduced tuning parameters.

The comprehensive simulation studies performed in Chapter 4 show that the initially defined objective is achieved by both observers if the linear pipe model (2.4) is concerned without any model uncertainty. A leak size that represents $1\ \%$ of the nominal flow is estimated with mean deviations of about $0.1\ \%$ and the leak position is localized with a mean deviation of under $1\ \%$ under various operating conditions regarding the measurement noise and the leak position. It is observed that both observers are real-time capable and that the algebraic observer achieves a higher accuracy of the leak localization, while the dynamic observer estimates more accurate the leak size. For a small leak size of $0.1\ \%$ of the nominal flow, the algebraic observer clearly outperforms the dynamic observer regarding the accuracy of the leak localization, as shown in Section 4.2.2.

However, the algebraic observer has several drawbacks in comparison to the dynamic observer. First, the convergence time that the algebraic observer needs to detect and to localize the leak accurately is significantly higher than for the dynamic observer. Since the lengths T_χ and T_δ of the moving time windows for the leak size and state estimation have to be chosen relatively large to ensure an accurate solution of the auxiliary problems, the algebraic observer needs more time to detect and to localize the leak. Furthermore, the large time windows increase the computational costs of the implementation of the algebraic observer as the comparison with the run time of the dynamic observer indicates. Future work could investigate on whether alternative ways to solve the auxiliary problem $\Sigma_{\text{aux},\chi}$, e.g., like described above, would reduce the convergence time. Furthermore, a main drawback of the algebraic observer is the time-consuming tuning of the design parameters. While the tuning of the ABSO is relatively straightforward (number of spatial nodes n to adjust the desired leak localization accuracy, observer gains L and γ to balance convergence speed and robustness to measurement noise), the tuning of the algebraic observer is more challenging. As discussed in Section 4.1, the accuracy of the leak localization reveals a strong sensitivity w.r.t. the choice of the length T_δ of the moving time window for the state estimation and the approximation order N of the function expansion (3.67). Small variations in these parameters or in the operating point, as shown in Section 4.2.4, can deteriorate the accuracy of the leak localization strongly. Therefore, it is recommended to research in the future on approaches to improve the accuracy of the solution of the auxiliary problems $\Sigma_{\text{aux},u}, \Sigma_{\text{aux},v}$ in particular at the boundary $x = 0$, e.g., by

integrating the homogenization ansatz from [90].

Besides, both observers have a low robustness of the accuracy of the leak localization regarding uncertainties in the friction loss model. Small variations of the friction factor F of under $0.5\ \%$ deteriorate visibly the leak localization and lead to deviations of up to over $40\ \%$ from the real leak position. Hence, the robustification of both observers against model uncertainties, e.g., by estimating the friction factor F via a dynamic update law similar to [20, 92], is an important issue to improve the observer performance in real applications where the friction parameters may be uncertain or vary in time and space.

Finally, the evaluation of the measurement data from the pilot fluid transport plant installed in the laboratory of Advanced Control Engineering at the PUCP reveals that the friction losses are not linear in the flow rate, contrastingly to the linear pipe model (2.4) that is utilized for the design of both observers. Even in the case of small step-line changes in the inlet flow with an amplitude of about $3\ \%$ of the inlet flow, the linear pipe model 2.4 does not reflect accurately the pressure change at the inlet. In contrast, the nonlinear pipe model (2.10) reproduces significantly more accurate the pressure change due to variations in the inlet flow. Moreover, it is observed that the friction parameters vary from pipe segment to pipe segment such that at the intermediate pressure sensors, the pressure simulated by the linear as well as the nonlinear pipe model differ significantly from the measured pressure. To overcome this limitation and to improve the model accuracy, spatially varying friction parameters $F = F(z),\ f_d = f_d(z)$ can be introduced. However, it remains an open question how the state transformation (3.2) and the observer design have to be adjusted for this case of a more complex model structure.

The discrepancies between the model assumption of linear friction losses and the friction loss behavior observed at the pilot plant leads to one of the major drawbacks of both observers, the localization of leaks that do not occur near to the outlet. For a leak that occurs near to the outlet of the pipe, both observers estimate the leak position with an acceptable accuracy, whereby the dynamic observer outperforms the algebraic observer in particular for smaller leak sizes (see Table 5.4). In this case, only a short segment of the pipe is affected by the variation of the friction losses due to the lower flow rate. By contrast, leaks that do not occur near to the outlet cannot be localized accurately, neither by the dynamic nor by the algebraic observer. In these scenarios, the friction factor, F that is assumed to be constant, varies in time and in space. After the leak has occurred, the segment behind the leak operates in a lower flow regime as before, such that the friction factor F between the segment in front of and behind the leak differs significantly. Consequently, and in accordance with the low robustness of the observers against model uncertainties in the friction model, the leak position is not estimated accurately and deviations of up to over $20\ \%$ from the real leak position are recognized. Hence, it is strongly recommended to extend the design of the dynamic and the algebraic observer based on the nonlinear pipe model (2.10) to achieve an accurate leak localization in real application cases. It is demonstrated that the nonlinear dynamic

observer according to [64] clearly improves the leak localization and reaches the desired accuracy independently of the leak position. The concise stability proof for this nonlinear observer remains as an open issue for future work. Similarly, the current observations motivate to deal with the further development of the algebraic observer by applying the MFM to the nonlinear pipe model (2.10). Since the ansatz of the MFM is strongly related to linear systems, the extension for nonlinear systems is a challenging and ongoing research topic. An inspiring starting point to deal with nonlinearities inside the MFM framework can be found in [93].

Finally, it is reminded that the present work only regards the case of water pipes. It remains as an open issue for the future how the results of the present work can be transferred to the application case of oil pipelines, where temperature effects have to be considered such that the mathematical model becomes more complex.

7. Bibliography

[1] H. Lu, Z.-D. Xu, T. Iseley, H. Peng, and L. Fu, *Pipeline Inspection and Health Monitoring Technology: The Key to Integrity Management*. Springer, 2023.

[2] Global Infrastructure Hub, "Global infrastructure hub - pipe access," 2023. Available at `https://pipeline.gihub.org/` Accessed: March 13, 2023.

[3] GlobalData Plc, "New build trunk/transmission pipelines projects analytics and forecast by project type, regions, countries, development stage, and cost 2022-2026- product image new build trunk/transmission pipelines projects analytics and forecast by project type, regions, countries, development stage, and cost 2022-2026," tech. rep., 2023.

[4] European Gas Pipeline Incident Data Group, "Gas pipeline incidents 10th report of the european gas pipeline incident data group (period 1970 – 2016)," tech. rep., European Gas Pipeline Incident Data Group, Groningen (Netherlands), March 2018.

[5] M. Farley, *Leakage Management and Control : a best practice training manual*. Geneva, Switzerland: WHO, 2001. Available at `https://apps.who.int/iris/bitstream/handle/10665/66893/WHO_SDE_WSH_01.1_eng.pdf?sequence=1&isAllowed=y` Accessed: June 30, 2023.

[6] OECD, *Water Governance in Cities (OECD Studies on Water)*. Paris: OECD Publishing, 2016. Available at `https://www.pseau.org/outils/ouvrages/ocde_water_governance_in_cities_2016.pdf` Accessed: June 30, 2023.

[7] R. Liemberger and A. Wyatt, "Quantifying the global non-revenue water problem," *Water Science and Technology: Water Supply*, vol. 19, pp. 831–837, July 2018.

[8] Petróleos del Perú, "Petroperú contuvo fuga de crudo en ramal norte del oleoducto norperuano," September 11, 2022. Available at `https://www.petroperu.com.pe/Storage/modsnw/image/3282-e3If3Os8Zy5Al3I.jpg` Accessed: June 16, 2023.

[9] Petróleos del Perú, "Fuga de crudo que llegó a río cuninico fue provocada por corte al oleoducto norperuano," September 17, 2022. Available at `https://www.petroperu.com.pe/Storage/modsnw/image/3302-m9Tw3Cq7Tc5Bn1F.jpg` Accessed: June 16, 2023.

[10] Gestión, "Loreto: Alrededor de 150 turistas han sido retenidos por comuneros de cuninico," November 03, 2022. Available at `https://gestion.pe/peru/loreto-alrededor-de-150-turistas-han-sido-retenidos-por-comuneros-de-cuninico-rmmn-noticia/` Accessed: June 16, 2023.

[11] Steffelbauer, D., *Model-Based Leak Localization in Water Distribution Systems*. PhD thesis, Graz University of Technology, 2018.

[12] P.-S. Murvay and I. Silea, "A survey on gas leak detection and localization techniques," *Journal of Loss Prevention in the Process Industries*, vol. 25, no. 6, pp. 966–973, 2012.

[13] G. Geiger, T. Werner, and D. Matko, "Leak detection and locating - a survey," in *35th Annual PSIG Meeting*, pp. 1–20, October 2003.

[14] Y. Bai and Q. Bai, "Leak detection systems," in *Subsea Pipeline Integrity and Risk Management* (Y. Bai and Q. Bai, eds.), ch. 6, pp. 125–143, Boston: Gulf Professional Publishing, 2014.

[15] M. Henrie, P. Carpenter, and R. Nicholas, *Pipeline Leak Detection Handbook*. Elsevier Science, July 2016.

[16] I. F. Tello, A. Wouwer, and D. Coutinho, "A concise review of state estimation techniques for partial differential equation systems," *Mathematics*, vol. 9, December 2021. 3180.

[17] R. Tetzner, "Model-based Pipeline Leak Detection And Localization," *Fachberichte 3R international*, pp. 454–460, July 2003.

[18] G. Geiger, "State-of-the-art in leak detection and localization," in *Pipeline Technology Conference 2006*, pp. 193–198, April 2006.

[19] J. Sowinski and M. Dziubinski, "Analysis of the impact of pump system control on pressure gradients during emergency leaks in pipelines," in *E3S Web of Conferences*, vol. 44, January 2018. 00166.

[20] O. Aamo, J. Salvesen, and B. Foss, "Observer design using boundary injections for pipeline monitoring and leak detection," in *6th IFAC Symposium on Advanced Control of Chemical Processes*, pp. 53–58, 2006.

[21] C. Verde, "Minimal order nonlinear observer for leak detection," *Journal of Dynamic Systems Measurement and Control*, vol. 126, pp. 467–472, September 2004.

[22] L. Torres, G. Besançon, and D. Georges, "A collocation model for water-hammer dynamics with application to leak detection," in *CDC 2008 - 47th IEEE Conference on Decision and Control*, pp. 3890–3894, December 2008.

[23] B. Arifin, Z. Li, and S. Shah, "Pipeline Leak Detection Using Particle Filters," in *9th IFAC Symposium on Advanced Control of Chemical Processes ADCHEM 2015*, vol. 48, pp. 76–81, June 2015.

[24] G. Besançon, "Observer tools for pipeline monitoring," in *Modeling and Monitoring of Pipelines and Networks* (C. Verde and L. Torres, eds.), vol. 7, ch. 5, pp. 83–97, Cham (Switzerland): Springer Nature, 1 ed., May 2017.

[25] L. Torres, J. Jiménez-Cabas, O. Gonzalez, and F.-R. López-Estrada, "Kalman filters for leak diagnosis in pipelines: Brief history and future research," *Journal of Marine Science and Engineering*, vol. 8, March 2020. 173.

[26] O. Aamo, "Disturbance rejection in 2 x 2 linear hyperbolic systems," *IEEE Transactions on Automatic Control*, vol. 58, no. 5, pp. 1095–1106, 2013.

[27] O. Aamo, "Leak detection, size estimation and localization in pipe flows," *IEEE Transactions on Automatic Control*, vol. 61, no. 1, pp. 246–251, 2016.

[28] A. Navarro, O. Begovich, J. Sanchez-Torres, G. Besançon, and J. Murillo, "Leak detection and isolation using an observer based on robust sliding mode differentiators," in *World Automation Congress 2012*, pp. 1–6, 2012.

[29] W. Rahiman and Z. Ding, "Leak detection in pipeline via sliding motion," in *2017 17th International Conference on Control, Automation and Systems (ICCAS)*, pp. 749–754, 2017.

[30] T. Digernes, "Real-Time Failure-Detection and Identification Applied to Supervision of Oil Transport in Pipelines," *Modeling, Identification and Control*, vol. 1, pp. 39–49, January 1980.

[31] C. Verde, "Multi-leak detection and isolation in fluid pipelines," *Control Engineering Practice*, vol. 9, pp. 673–682, June 2001.

[32] A. Navarro-Díaz, J. Delgado-Aguiñaga, I. Santos-Ruiz, and V. Puig, "Real-time leak diagnosis in water distribution systems based on a bank of observers and a genetic algorithm," *Water*, vol. 14, no. 20, 2022. 3289.

[33] G. Geiger, "Principles of leak detection," Reken, 2005. KROHNE Oil and Gas.

[34] A. Benkherouf and A. Allidina, "Leak detection and location in gas pipelines," in *IEE Proceedings (Control Theory and Applications)*, vol. 135, pp. 142–148, March 1988.

[35] G. Besançon, D. Georges, O. Begovich, C. Verde, and C. Aldana, "Direct observer design for leak detection and estimation in pipelines," in *2007 European Control Conference (ECC)*, pp. 5666–5670, July 2007.

[36] A. Navarro, O. Begovich, G. Besançon, and J. Dulhoste, "Real-time leak isolation based on state estimation in a plastic pipeline," in *2011 IEEE International Conference on Control Applications (CCA)*, pp. 953–957, September 2011.

[37] C. Verde, L. Torres, and O. Gonzalez, "Decentralized Scheme for Leaks' Location in a Branched Pipeline," *Journal of Loss Prevention in the Process Industries*, vol. 43, pp. 18–28, April 2016.

[38] J. Delgado-Aguiñaga and G. Besançon, "EKF-based leak diagnosis schemes for pipeline networks," in *10th IFAC Symposium on Fault Detection, Supervision and Safety for Technical Processes SAFEPROCESS 2018*, pp. 723–729, August 2018.

[39] P. Liu, S. Li, and Z. Wang, "Multi-leak diagnosis and isolation in oil pipelines based on Unscented Kalman filter," in *2018 Chinese Control And Decision Conference (CCDC)*, pp. 2222–2227, June 2018.

[40] F. Salas Camacho, "Desarrollo de un sistema de detección y localización de fugas basado en filtro de kalman extendido para sistemas de transporte de petróleo crudo aplicado al tramo I del oleoducto norperuano," Master's thesis, Pontificia Universidad Católica del Perú, 2022.

[41] J. Jouffroy and J. Reger, "Finite-time simultaneous parameter and state estimation using modulating functions," in *Proceedings of IEEE International Conference on Control Applications*, pp. 394 – 399, September 2015.

[42] F. Fischer, J. Deutscher, and T. Laleg-Kirati, "Source estimation for first order time-varying hyperbolic systems," in *Proceedings of 23rd International Symposium on Mathematical Theory of Networks and Systems*, pp. 78–84, July 2018.

[43] L. Ghaffour, M. Noack, J. Reger, and T. Laleg-Kirati, "Non-asymptotic state estimation of linear reaction diffusion equation using modulating functions," in *IFAC World Congress*, pp. 4262–4267, July 2020.

[44] O. Egeland and J. Gravdahl, *Modeling and Simulation for Automatic Control*. Trondheim (Norway): Marine Cybernetics AS, 2 ed., January 2003.

[45] W. Schiesser, *The Numerical Method of Lines: Integration of Partial Differential Equations*. Elsevier Science, 1991.

[46] H. Anfinsen and O. Aamo, "Leak detection, size estimation and localization in branched pipe flows," *Automatica*, vol. 140, March 2022. 110213.

[47] M. Shinbrot, "On the analysis of linear and nonlinear dynamical systems from transient-response data," technical note, National Advisory Commitee for Aeronautics NACA, December 1954.

[48] S. Asiri, S. Elmetennani, and T. Laleg-Kirati, "Moving-Horizon Modulating Functions-Based Algorithm for Online Source Estimation in a First-Order Hyperbolic Partial Differential Equation," *Journal of Solar Energy Engineering*, vol. 139, September 2017. 061007.

[49] F. Fischer and J. Deutscher, "Algebraic fault detection and isolation for parabolic distributed–parameter systems using modulation functions," in *2nd IFAC Workshop on Control of Systems Governed by Partial Differential Equations*, pp. 162–167, June 2016.

[50] M. Noack, J. Rueda-Escobedo, J. Reger, and J. Moreno, "Fixed-time parameter estimation in polynomial systems through modulating functions," in *Proceedings of IEEE 55th Conference on Decision and Control (CDC)*, pp. 2067–2072, December 2016.

[51] D. Pumaricra Rojas, M. Noack, J. Reger, and G. Pérez-Zúñiga, "State Estimation for Coupled Reaction-Diffusion PDE Systems Using Modulating Functions," *Sensors*, vol. 22, July 2022. 5008.

[52] M. Gevrey, "Sur la nature analytique des solutions des équations aux dérivées partielles. premier mémoire," *Annales Scientifiques de l' École Normale Supérieure*, vol. 35, pp. 129–190, 1918.

[53] R. Vazquez, M. Krstic, and J.-M. Coron, "Backstepping boundary stabilization and state estimation of a 2×2 linear hyperbolic system," in *2011 50th IEEE Conference on Decision and Control and European Control Conference*, pp. 4937–4942, December 2011.

[54] E. Córdova Avila, "Desarrollo e implementación de un sistema de supervisión para una planta piloto de transporte de fluidos," Master's thesis, Pontificia Universidad Católica del Perú, 2022.

[55] G. Banse, *Technik - Technologie - Technikwissenschaften. Beiträge zur Technikphilosophie*, ch. Nicht so exakt wie möglich, sondern so genau wie nötig! Das Einfachheitsprinzip in den Technikwissenschaften. trafo Wissenschaftsverlag, 2021.

[56] J.-F. Dulhoste, M. Guillén, G. Besançon, and R. Santos, "One-dimensional modeling of pipeline transients," in *Modeling and Monitoring of Pipelines and Networks* (C. Verde and L. Torres, eds.), vol. 7, ch. 4, pp. 63–81, Cham (Switzerland): Springer Nature, 1 ed., May 2017.

[57] M. Andreev, U. Grätz, and A. Lamparter, "Pipeline simulation by the method of characteristics for calculating the pressure pulsation of a high-pressure water plunger pump," in *Proceedings of 11th International Fluid Power Conference*, pp. 155–165, March 2018.

[58] R. A. Bajura, "A Model for Flow Distribution in Manifolds," *Journal of Engineering for Power*, vol. 93, pp. 7–12, January 1971.

[59] H. Oertel jr, "Dynamik zäher Flüssigkeiten," in *Prandtl - Führer durch die Strömungslehre: Grundlagen und Phänomene* (H. Oertel jr, ed.), ch. 3, pp. 119–186, Wiesbaden: Springer Vieweg, 14 ed., 2017.

[60] C. F. Colebrook, "Turbulent flow in pipes, with particular reference to the transition region between the smooth and rough pipe laws.," *Journal of the Institution of Civil Engineers*, vol. 11, no. 4, pp. 133–156, 1939.

[61] D. Brkić, "Review of explicit approximations to the colebrook relation for flow friction," *Journal of Petroleum Science and Engineering*, vol. 77, pp. 34–48, September 2011.

[62] S. E. Haaland, "Simple and explicit formulas for the friction factor in turbulent pipe flow," *Journal of Fluids Engineering*, vol. 105, pp. 89–90, March 1983.

[63] J.-F. Dulhoste, G. Besançon, L. Torres, O. Begovich, and A. Navarro, "About friction modeling for observer-based leak estimation in pipelines," in *2011 50th IEEE Conference on Decision and Control and European Control Conference*, pp. 4413–4418, December 2011.

[64] N. Wilhelmsen and O. Aamo, "Distributed observer-based leak detection in pipe flow with nonlinear friction." unpublished, Extended Abstract for the 2nd IFAC Workshop on Control Methods for Water Resource Systems, 2022.

[65] D. Simon, *Optimal State Estimation: Kalman, H_∞, and Nonlinear Approaches*. Hoboken (New Jersey): John Wiley & Sons, INC, 1 ed., January 2006.

[66] M. Shinbrot, "On the Analysis of Linear and Nonlinear Systems," *Transactions of the American Society of Mechanical Engineers*, vol. 79, pp. 547–551, April 1957.

[67] T. Co, "Dynamic modeling of nonlinear systems using modulating functions methods," in *13th World Congress of IFAC, 1996, San Francisco USA, 30 June - 5 July*, pp. 4363–4367, July 1996.

[68] S. Ungarala and T. Co, "Time-varying system identification using modulating functions and spline models with application to bio-processes," *Computers & Chemical Engineering*, vol. 24, pp. 2739–2753, December 2000.

[69] W. Byrski, M. Drapała, and J. Byrski, "An Adaptive Identification Method Based on the Modulating Functions Technique and Exact State Observers for Modeling and Simulation of a Nonlinear Miso Glass Melting Process," *International Journal of Applied Mathematics and Computer Science*, vol. 29, pp. 739–757, December 2019.

[70] A. Ionesi, H. Ramezani, and J. Jouffroy, "On-line parameter and state estimation of an air handling unit model: experimental results using the modulating function method," *Modeling, Identification and Control: A Norwegian Research Bulletin*, vol. 40, pp. 161–176, July 2019.

[71] I. Aranda-Cetraro, G. Pérez-Zúñiga, R. Rivas-Pérez, and J. Sotomayor-Moriano, "Nonlinear robust control by a modulating-function-based backstepping super-twisting controller for a quadruple tank system," *Sensors*, vol. 23, May 2023. 5222.

[72] B. Laroche, P. Martin, and P. Rouchon, "Motion planning for the heat equation," *International Journal of Robust and Nonlinear Control*, vol. 10, p. 629–643, July 2000.

[73] A. F. Lynch and J. Rudolph, "Flatness-based boundary control of a class of quasilinear parabolic distributed parameter systems," *International Journal of Control*, vol. 75, pp. 1219–1230, October 2002.

[74] F. Woittennek, "Flatness based feedback design for hyperbolic distributed parameter systems with spatially varying coefficients," in *1st IFAC Workshop on Control of Systems Governed by Partial Differential Equations*, vol. 1, pp. 37–42, September 2013.

[75] J. Rudolph, J. Winkler, and F. Woittennek, *Flatness based control of distributed parameter systems: Examples and computer exercises from various technological domains*. Shaker Verlag, January 2003.

[76] Servais, É., *Trajectory planning and control of collaborative systems : Application to trirotor UAVS*. PhD thesis, Université Paris Sud - Paris XI, September 2015.

[77] T. Meurer, "Flatness–based motion planning and tracking," in *55th IEEE Conference on Decision and Control*, December 2016. Lecture Notes for the Workshop "New Trends in Control of Distributed Parameter Systems", Available at `https://www.control.tf.uni-kiel.de/en/teaching/cdc-workshop-2016/fileadmin/tmeurer_cdc2016_lecture_notes` Accessed: July 26, 2023.

[78] H. Amann and J. Escher, *Analysis I*. Grundstudium Mathematik, Basel: Birkhäuser, 3 ed., 2006.

[79] Zweckverband Bodensee-Wasserversorgung, "Weg des Wassers - Verteilung." Available at `https://www.bodensee-wasserversorgung.de/trinkwasser/weg-des-wassers.html` Accessed: June 29, 2023.

[80] Stadtwerke Bochum Holding GmbH, "Wasser-Hausanschluss und Bauwasser." Available at `https://www.stadtwerke-bochum.de/privatkunden/produkte/wasser/wasser-fuer-den-hausbau` Accessed: June 29, 2023.

[81] Wesernetz Bremen GmbH, "Informationen zum trinkwassernetz in bremen." Available at `https://www.wesernetz.de/fuer-die-region/wesernetz/netzbeschreibung/trinkwassernetz` Accessed: June 29, 2023.

[82] M. Tukker, K. Kooij, and I. Pothof, *Hydraulic design and management of wastewater transport systems*. Delft: IWA (International Water Association), 2016.

[83] J. Taler and P. Duda, "Solution of non-linear inverse heat conduction problems using the method of lines," *Heat and Mass Transfer*, vol. 37, pp. 147–155, April 2001.

[84] H. Lee, C. Matthews, R. Braddock, G. Sander, and F. Gandola, "A MATLAB method of lines template for transport equations," *Environmental Modelling & Software*, vol. 20, pp. 603–614, June 2004.

[85] F. Shakeri and M. Dehghan, "The method of lines for solution of the one-dimensional wave equation subject to an integral conservation condition," *Computers & Mathematics with Applications*, vol. 56, pp. 2175–2188, November 2008.

[86] G. Meyer, "The Method of Lines (MOL) for the Diffusion Equation," in *The Time-Discrete Method of Lines for Options and Bonds- A PDE Approach*, ch. 2, pp. 57–74, World Scientific Publishing Co. Pte. Ltd., 2015.

[87] P. Joshi and M. Pathak, "Numerical solution of acoustic wave equation using method of lines," *World Journal of Modelling and Simulation*, vol. 14, pp. 243–256, July 2018.

[88] A. Antoulas, "Approximation of large-scale dynamical systems: An overview," in *10th IFAC/IFORS/IMACS/IFIP Symposium on Large Scale Systems 2004: Theory and Applications, Osaka, Japan, 26-28 July, 2004*, pp. 19–28, July 2004.

[89] S. Asiri and T.-M. Laleg-Kirati, "Modulating functions-based method for parameters and source estimation in one-dimensional partial differential equations," *Inverse Problems in Science and Engineering*, vol. 25, pp. 1191–1215, October 2016.

[90] F. Friedrich, "MF-based State Estimation with homogenization (Research Notes)." unpublished, 2023.

[91] M. Capelo, B. Brentan, L. Monteiro, and D. Covas, "Near–real time burst location and sizing in water distribution systems using artificial neural networks," *Water*, vol. 13, July 2021. 1841.

[92] E. Hauge, "Advanced leak detection in oil and gas pipelines using a nonlinear observer and OLGA models," Master's thesis, Norwegian University of Science and Technology (NTNU), 2007.

[93] N. Fokken, "Zustandsschätzung eindimensionaler reaktionsdiffusionssysteme mit nichtlinearen reaktionstermen auf basis der modulationsfunktionsmethode," Master's thesis, TU Ilmenau, 2021.

[94] M. Heinkenschloss, T. Reis, and A. Antoulas, "Balanced truncation model reduction for systems with inhomogeneous initial conditions," *Automatica*, vol. 47, no. 3, pp. 559–564, 2011.

[95] H. Anfinsen and O. Aamo, "A model reduction algorithm for irrational transfer functions with application to leak detection in pipelines," in *2015 American Control Conference (ACC)*, pp. 3298–3303, July 2015.

[96] Salmson, *MULTI-H Installation and Starting Instructions*, June 2016. Available at `http://www.salmson.com/fileadmin/user_upload/UPLOAD/product/notice_mise_en_service/MULTI-H-NMS.pdf` Accessed: June 7, 2023.

[97] Yokogawa Electric Corporation, *User's Manual ADMAG TI Series AXG###, AXW###, AXG4A, AXW4A, AXG1A Magnetic Flowmeter Read Me First (Optional Code EC)*, April 2022. Available at `https://web-material3.yokogawa.com/IM01E21A11-01EN.pdf?_ga=2.246858756.1864378261.1686155232-256640030.1686155231`, Accessed: June 7, 2023.

[98] Yokogawa Electric Corporation, *User's Manual EJX and EJA-E Series Differential Pressure and Pressure Transmitters Installation Manual*, January 2023. Available at `https://web-material3.yokogawa.com/IM01C25A01-01EN.pdf?_ga=2.153026617.1864378261.1686155232-256640030.1686155231`, Accessed: June 7, 2023.

[99] R. Carrera and C. Verde, "LabVIEW-Based SCADA System for Sequential Leaks' Diagnosis in Pipelines," in *Fault Diagnosis and Tolerant Control: Applications* (C. Verde, ed.), ch. 7, pp. 149–173, Mexico City: Instituto de Ingeniería UNAM, 1 ed., March 2023. Available at `https://comite-editorial.iingen.unam.mx/omp-new/index.php/sii/catalog/book/15` Accessed: July 1, 2023.

[100] G. Keulegan and K. Beij, "Pressure losses for fluid flow in curved pipes," *National Bureau of Standards*, vol. 18, pp. 89–114, January 1937.

[101] Itō, H., "Friction factors for turbulent flow in curved pipes," *Journal of Basic Engineering*, vol. 81, pp. 123–132, June 1959.

[102] H. Hassoon, "Pressure drop in 180° pipe bends," *Building Services Engineering Research and Technology*, vol. 3, no. 2, pp. 70–74, 1982.

[103] N. Crawford, *Pressure Losses at Bends and Junctions*. PhD thesis, Queen's University Belfast, 2005.

[104] I. Idelchik and M. Steinberg, *Handbook of Hydraulic Resistance*. Begell House, 3 ed., 1996.

List of Figures

1. Distribution of leak causes (2007-2016, EGIG) [4] 2

1.1. Overview of leak detection techniques, based on [12]. 3

2.1. Schematic illustration of the pipe system 14

3.1. Schematic illustration of the general structure of the proposed algebraic and dynamic leak detection and localization observers. 18
3.2. Schematic illustration of the structure of the ABSO according to Equation (3.9) and Equation (3.19) based on the linear pipe model (2.4). 28
3.3. Bump Function of Gevrey order $\alpha = 1 + 1/\sigma$ for $T = 1$ varying the slope σ. . . . 37
3.4. Schematic illustration of the structure of the algebraic observer. 46

4.1. Comparison and error norm $||e_\varphi(\tau)||^2$ of the MFs for the leak size estimation obtained by the power series approach (3.43) and the MOL-based solution for the pipe in the reference scenario according to Table 4.1. 50
4.2. Leak size estimation for the pipe in the noise free reference scenario defined in Table 4.1 with leakage of $1\ \%$ of the nominal flow occurring after $t = 60$ s. 51
4.3. Error $e(x, T_\delta) = \begin{bmatrix} e_1(x, T_\delta) & e_2(x, T_\delta) \end{bmatrix}^\top$ in state transition of the auxiliary problems (3.69) and (3.70) for $N = 0$, pipe parametrization according to the reference scenario in Table 4.1. 52
4.4. Estimated states $u(x, t_f)$ (left) and $v(x, t_f)$ (right) at end time $t_f = 1000$ s of simulation under variation of the approximation order N and the length T_δ of the moving time window, pipe parametrization according to the reference scenario in Table 4.1 with leak of $1\ \%$ of the nominal flow occurring at $z^* = 10$ km. 53
4.5. Leak size localization for the pipe in the noise free reference scenario defined in Table 4.1 with leakage of $1\ \%$ of the nominal flow occurring after $t = 60$ s, variation of approximation order N and length T_δ of the moving time window of the algebraic observer, $\gamma = 0.2$. 54
4.6. Estimation of the leak size (left) and leak localization (right) for the simulation plant in the low noise case. 57

4.7. Estimation of the leak size (left) and leak localization (right) for the simulation plant in the medium noise case. 59
4.8. Estimation of the leak size (left) and leak localization (right) for the simulation plant in the high noise case. 60
4.9. Estimation of the leak size (left) and leak localization (right) for the simulation plant for a large leak of $20\ \%$ of the nominal flow. 62
4.10. Estimation of the leak size (left) and leak localization (right) for the simulation plant for a small leak of $0.1\ \%$ of the nominal flow. 64
4.11. Estimation of the leak size (left) and leak localization (right) for the simulation plant for a leak of $1\ \%$ of the nominal flow appearing at $z^* = 2$ km. 66
4.12. Estimation of the leak size (left) and leak localization (right) for the simulation plant for a leak of $1\ \%$ of the nominal flow appearing at $z^* = 18$ km. 67
4.13. Estimation of the leak size (left) and leak localization (right) for the simulation plant for a leak of $1\ \%$ of the nominal flow appearing at $z^* = 10$ km and over a width of 500 m. 69
4.14. Estimation of the leak size (left) and leak localization (right) for the simulation plant for a leak of $1\ \%$ of the nominal flow $q_0(t) = 1.5\ \frac{\mathrm{m}^3}{s}$ appearing at $z^* = 10$ km. 71
4.15. Estimation of the leak size (left) and leak localization (right) for the simulation plant for a leak of $1\ \%$ of the nominal flow $q_0(t) = 1\ \frac{\mathrm{m}^3}{s}$ appearing at $z^* = 10$ km, sinusoidally varying boundary conditions $q_0(t)$ and $p_\ell(t)$. 73
4.16. Estimation of the leak size (left) and leak localization (right) for the simulation plant for a leak of $1\ \%$ of the nominal flow appearing at $z^* = 10$ km with an uncertainty of $\Delta F = 0.23\ \%$ in the friction factor F. 75
4.17. Estimation of the leak size (left) and leak localization (right) for the simulation plant for a leak of $1\ \%$ of the nominal flow appearing at $z^* = 10$ km with an uncertainty of $\Delta F = 0.45\ \%$ in the friction factor F. 76
4.18. Inlet pressure $p_0(t)$ (left) and pressure drop (right) for a leakage of $10\ \%$ of the nominal flow at $z^* = 19$ km, linear and nonlinear pipe model. 77
4.19. Estimation of the leak size (left) and leak localization (right) for the simulation plant for a leak of $10\ \%$ appearing at $z^* = 19$ km, measurement data generated by the nonlinear pipe model (2.10). 78
4.20. Inlet pressure $p_0(t)$ (left) and pressure drop (right) for a leakage of $10\ \%$ of the nominal flow at $z^* = 10$ km, linear and nonlinear pipe model. 78
4.21. Estimation of the leak size (left) and leak localization (right) for the simulation plant for a leak of $10\ \%$, measurement data generated by the nonlinear pipe model (2.10). 79

4.22. Accuracy of the leak size estimation and leak localization (left) and needed runtime (right) vs. number of spatial discretization nodes n of the ABSO. 80

5.1. Pilot Plant at PUCP. 83
5.2. Inclination angle of the pilot plant at PUCP. 83
5.3. Flow rate and pressure measurement of pilot plant for stepwise increasing pump power. 86
5.4. Identification of the linear friction factor F (above, left), the nonlinear friction coefficient f_d (above, right) and the Reynolds number Re (below). 88
5.5. Inlet flow rate at sensor (FT3) (left) and outlet pressure $p_\ell(t)$ at sensor (PT4) (right) of last pipe segment for operating point $q_0(t) \approx 3.1 \cdot 10^{-3}\ \frac{\mathrm{m}^3}{\mathrm{s}}$ and step-like increase of $5\ \%$ in power of first pump. 89
5.6. Comparison of the measured and simulated outlet flow rate (left) and inlet pressure (right) for the last pipe segment, and an increase in the pump power of $5\ \%$. Simulation with linear pipe model (2.4) and nonlinear pipe model (2.10). 91
5.7. Inlet flow rate at sensor (FT3) (left) and outlet pressure $p_\ell(t)$ at sensor (PT4) (right) of last pipe segment for operating point $q_0(t) \approx 3.1 \cdot 10^{-3}\ \frac{\mathrm{m}^3}{\mathrm{s}}$ and rectangular steps of the power of the first pump. 92
5.8. Comparison of the measured and simulated outlet flow rate (left) and inlet pressure (right) for the last pipe segment, and rectangular steps of the power of the first pump. Simulation with linear pipe model (2.4) and nonlinear pipe model (2.10). . 92
5.9. Inlet flow rate $q_0(t)$ at sensor (FT1) (left) and outlet pressure $p_\ell(t)$ at sensor (PT4) (right) for operating point $q_0(t) = 3.1 \cdot 10^{-3}\ \frac{\mathrm{m}^3}{\mathrm{s}}$ and step-like increase in the power of the first pump. 93
5.10. Comparison of the measured and simulated flow rates at (FT2), (FT3) and (FT4) for step-like increase in the power of the first pump. Simulation with linear pipe model (2.4) and nonlinear pipe model (2.10). 94
5.11. Comparison of the measured and simulated pressure at (PT1), (PT2) and (PT3) for step-like increase in the power of the first pump. Simulation with linear pipe model (2.4) and nonlinear pipe model (2.10). 95
5.12. Comparison of the measured and simulated pressure at (PT1), (PT2) and (PT3) for step-like increase in the power of the first pump. Simulation with linear pipe model (2.4) and nonlinear pipe model (2.10) parametrized with spatially varying friction parameters $F = F(z),\ f_d = f_d(z)$. 96
5.13. Inlet flow rate $q_0(t)$ at sensor (FT1) (left) and outlet pressure $p_\ell(t)$ at sensor (PT4) (right) for operating point $q_0(t) \approx 3.1 \cdot 10^{-3}\ \frac{\mathrm{m}^3}{\mathrm{s}}$ and rectangular steps of the power of the first pump. 97

5.14. Comparison of the measured and simulated flow rates at (FT2), (FT3) and (FT4) for rectangular steps of the power of the first pump. Simulation with linear pipe model (2.4) and nonlinear pipe model (2.10). 98
5.15. Comparison of the measured and simulated pressure at (PT1), (PT2) and (PT3) for rectangular steps of the power of the first pump. Simulation with linear pipe model (2.4) and nonlinear pipe model (2.10). 99
5.16. Inlet flow rate $q_0(t)$ at sensor (FT1) (left), outlet pressure $p_\ell(t)$ at sensor (PT4) (middle) and leak size $\chi(t)$ (right) inferred from flow rate measurements (FT3) and (FT4), operating point $q_0(t) \approx 3.1 \cdot 10^{-3}\ \frac{\mathrm{m}^3}{\mathrm{s}}$, small leak occurring after $t = 30$ s at $z^* = 85.59$ m. 100
5.17. Comparison of the measured and simulated flow rates at (FT2), (FT3) and (FT4), operating point $q_0(t) \approx 3.1 \cdot 10^{-3}\ \frac{\mathrm{m}^3}{\mathrm{s}}$, small leak occurring after $t = 30$ s at $z^* = 85.59$ m. Simulation with linear pipe model (2.4) and nonlinear pipe model (2.10). 101
5.18. Comparison of the measured and simulated pressure at (PT1), (PT2) and (PT3), operating point $q_0(t) \approx 3.1 \cdot 10^{-3}\ \frac{\mathrm{m}^3}{\mathrm{s}}$, small leak occurring after $t = 30$ s at $z^* = 85.59$ m. Simulation with linear pipe model (2.4) and nonlinear pipe model (2.10). 102
5.19. Inlet flow rate $q_0(t)$ at sensor (FT1) (left), outlet pressure $p_\ell(t)$ at sensor (PT4) (middle) and leak size $\chi(t)$ inferred from flow rate measurements (FT3) and (FT4), operating point $q_0(t) \approx 3.1 \cdot 10^{-3}\ \frac{\mathrm{m}^3}{\mathrm{s}}$, big leak occurring after $t = 30$ s at $z^* = 85.59$ m. 103
5.20. Comparison of the measured and simulated flow rates at (FT2), (FT3) and (FT4), operating point $q_0(t) \approx 3.1 \cdot 10^{-3}\ \frac{\mathrm{m}^3}{\mathrm{s}}$, big leak occurring after $t = 30$ s at $z^* = 85.59$ m. Simulation with linear pipe model (2.4) and nonlinear pipe model (2.10). . . . 104
5.21. Comparison of the measured and simulated pressure at (PT1), (PT2) and (PT3), operating point $q_0(t) \approx 3.1 \cdot 10^{-3}\ \frac{\mathrm{m}^3}{\mathrm{s}}$, big leak occurring after $t = 30$ s at $z^* = 85.59$ m. Simulation with linear pipe model (2.4) and nonlinear pipe model (2.10). . . . 105
5.22. Inlet flow rate $q_0(t)$ at sensor (FT1) (left), outlet pressure $p_\ell(t)$ at sensor (PT4) (middle) and leak size $\chi(t)$ inferred from flow rate measurements (FT3) and (FT4), operating point $q_0(t) \approx 3.1 \cdot 10^{-3}\ \frac{\mathrm{m}^3}{\mathrm{s}}$, small leak occurring after $t = 30$ s at $z^* = 11.73$ m. 106
5.23. Comparison of the measured and simulated flow rates at (FT2), (FT3) and (FT4), operating point $q_0(t) \approx 3.1 \cdot 10^{-3}\ \frac{\mathrm{m}^3}{\mathrm{s}}$, small leak occurring after $t = 30$ s at $z^* = 11.73$ m. Simulation with linear pipe model (2.4) and nonlinear pipe model (2.10). 107

5.24. Comparison of the measured and simulated pressure at (PT1), (PT2) and (PT3), operating point $q_0(t) \approx 3.1 \cdot 10^{-3}\ \frac{\mathrm{m}^3}{\mathrm{s}}$, small leak occurring after $t = 30$ s at $z^* = 11.73$ m. Simulation with linear pipe model (2.4) and nonlinear pipe model (2.10). 108
5.25. Flow rate (left) and pressure (right) at inlet (above) and outlet (below) of pilot plant at PUCP, operating point $q_0(t) \approx 3.1 \cdot 10^{-3}\ \frac{\mathrm{m}^3}{\mathrm{s}}$, small leak occurring after $t = 30$ s at $z^* = 85.59$ m. 110
5.26. Estimation of the leak size χ and the leak position z^* for the pilot plant at PUCP, operating point $q_0(t) \approx 3.1 \cdot 10^{-3}\ \frac{\mathrm{m}^3}{\mathrm{s}}$, small leak occurring after $t = 30$ s at $z^* = 85.59$ m. 111
5.27. Estimation of the leak size χ and the leak position z^* for the pilot plant at PUCP, operating point $q_0(t) \approx 3.1 \cdot 10^{-3}\ \frac{\mathrm{m}^3}{\mathrm{s}}$, large leak occurring after $t = 30$ s at $z^* = 85.59$ m. 113
5.28. Estimation of the leak size χ and the leak position z^* for the pilot plant at PUCP, operating point $q_0(t) \approx 3.1 \cdot 10^{-3}\ \frac{\mathrm{m}^3}{\mathrm{s}}$, small leak occurring after $t = 30$ s at $z^* = 85.59$ m. 114
5.29. Estimation of the leak size χ and the leak position z^* for the pilot plant at PUCP, operating point $q_0(t) \approx 3.1 \cdot 10^{-3}\ \frac{\mathrm{m}^3}{\mathrm{s}}$, small leak occurring after $t = 60$ s at $z^* = 60.99$ m. 116
5.30. Estimation of the leak size χ and the leak position z^* for the pilot plant at PUCP, operating point $q_0(t) \approx 3.1 \cdot 10^{-3}\ \frac{\mathrm{m}^3}{\mathrm{s}}$, small leak occurring after $t = 30$ s at $z^* = 11.73$ m. 117
5.31. Flow rate (left) and pressure (right) at inlet (above) and outlet (below) of pilot plant at PUCP, operating point $q_0(t) \approx 2.4 \cdot 10^{-3}\ \frac{\mathrm{m}^3}{\mathrm{s}}$, small leak occurring after $t = 30$ s at $z^* = 85.59$ m. 119
5.32. Estimation of the leak size χ and the leak position z^* for the pilot plant at PUCP, operating point $q_0(t) \approx 2.4 \cdot 10^{-3}\ \frac{\mathrm{m}^3}{\mathrm{s}}$, small leak occurring after $t = 30$ s at $z^* = 85.59$ m. 120

List of Tables

1.1. Overview of RTTM approaches. 5

4.1. Parametrization of the pipe model $\Sigma_{\mathsf{WH}_{\mathsf{lin}},\mathsf{leak}}$ in the reference scenario. 48
4.2. KPIs for the evaluation of the simulation-based leak size estimation and localization results. 55
4.3. Definition of the standard deviations of the additive white Gaussian noise in the three noise scenarios. 56
4.4. KPIs of the dynamic and the algebraic observer in the low noise scenario. 58
4.5. KPIs of the dynamic and the algebraic observer in the medium noise scenario. . . . 58
4.6. KPIs of the dynamic and the algebraic observer in the high noise scenario. 60
4.7. KPIs of the dynamic and the algebraic observer for a big leak ($20\ \%$ of the nominal flow). 63
4.8. KPIs of the dynamic and the algebraic observer for a small leak ($0.1\ \%$ of the nominal flow). 65
4.9. KPIs of the dynamic and the algebraic observer for a leak of $1\ \%$ of the nominal flow appearing at $z^* = 2$ km. 67
4.10. KPIs of the dynamic and the algebraic observer for a leak of $1\ \%$ of the nominal flow appearing at $z^* = 18$ km. 68
4.11. KPIs of the dynamic and the algebraic observer for a leak of $1\ \%$ of the nominal flow appearing at $z^* = 10$ km and over a width of 500 m. 68
4.12. KPIs of the dynamic and the algebraic observer for a leak of $1\ \%$ of the nominal flow $q_0(t) = 1.5\ \frac{\mathrm{m}^3}{s}$ appearing at $z^* = 10$ km. 70
4.13. KPIs of the dynamic and the algebraic observer for a leak of $1\ \%$ of the nominal flow $q_0(t) = 1\ \frac{\mathrm{m}^3}{s}$ appearing at $z^* = 10$ km, sinusoidally varying boundary conditions $q_0(t)$ and $p_\ell(t)$. 72
4.14. KPIs of the dynamic and the algebraic observer for a leak of $1\ \%$ of the nominal flow appearing at $z^* = 10$ km with an uncertainty of $\Delta F = 0.23\ \%$ in the friction factor F. 75

4.15. KPIs of the dynamic and the algebraic observer for a leak of $1\ \%$ of the nominal flow appearing at $z^* = 10$ km with an uncertainty of $\Delta F = 0.45\ \%$ in the friction factor F. 75
4.16. KPIs of the dynamic and the algebraic observer for a leak of $10\ \%$ of the nominal flow appearing at $z^* = 19$ km, measurement data generated by the nonlinear pipe model (2.10). 77
4.17. KPIs of the dynamic and the algebraic observer for a leak of $10\ \%$ of the nominal flow appearing at $z^* = 10$ km, measurement data generated by the nonlinear pipe model (2.10). 79

5.1. Dimensions of the pilot plant installed at PUCP. 84
5.2. KPIs of the dynamic and the algebraic observer for a small leak of $2.5\ \%$ of the nominal flow $q_0(t) \approx 3.1 \cdot 10^{-3}\ \frac{\mathrm{m}^3}{\mathrm{s}}$ appearing at $z^* = 85.59$ m. 112
5.3. KPIs of the dynamic and the algebraic observer for a large leak of $15.66\ \%$ of the nominal flow $q_0(t) \approx 3.1 \cdot 10^{-3}\ \frac{\mathrm{m}^3}{\mathrm{s}}$ appearing at $z^* = 85.59$ m. 113
5.4. KPIs of the dynamic and the algebraic observer for a small leak of $1.4\ \%$ of the nominal flow $q_0(t) \approx 3.1 \cdot 10^{-3}\ \frac{\mathrm{m}^3}{\mathrm{s}}$ appearing at $z^* = 85.59$ m. 114
5.5. KPIs of the dynamic and the algebraic observer for a small leak of $2.5\ \%$ of the nominal flow $q_0(t) \approx 3.1 \cdot 10^{-3}\ \frac{\mathrm{m}^3}{\mathrm{s}}$ appearing at $z^* = 60.99$ m. 115
5.6. KPIs of the dynamic and the algebraic observer for a small leak of $4\ \%$ of the nominal flow $q_0(t) \approx 3.1 \cdot 10^{-3}\ \frac{\mathrm{m}^3}{\mathrm{s}}$ appearing at $z^* = 11.73$ m. 117
5.7. KPIs of the dynamic and the algebraic observer for a small leak of under $3.0\ \%$ of the nominal flow $q_0(t) \approx 2.4 \cdot 10^{-3}\ \frac{\mathrm{m}^3}{\mathrm{s}}$ appearing at $z^* = 85.59$ m. 120

Appendix

A. Appendix

A.1. Leak Localization with ABSO for different Leak Distribution Functions

This section of the appendix examines the leak localization by means of Theorem 3.2.3 for different modelling of the leak distribution. Therefore, the value of the auxiliary variable $\delta(z) = \ell - z - \int_z^\ell \int_0^\eta d(\gamma)\mathrm{d}\gamma\mathrm{d}\eta$ for different shapes of the leak distribution function $d(z)$.

Corollary A.1.0.1. *(i) Assume that the leak distribution function is given by* $d(z) = \frac{1}{M}\mathit{rect}(\frac{z-z^*}{M})$*, i.e. the leak is modelled by a rectangular distribution of length* M*. Then,* $\delta(0) = z^*$

Proof. (i) The integral $\int_0^\eta d(\gamma)\mathrm{d}\gamma$ is split into 3 parts:

$$\begin{aligned}
\forall \eta \in [0, z^* - \frac{M}{2}] : \int_0^\eta d(\gamma)\mathrm{d}\gamma = 0 \\
\forall \eta \in (z^* - \frac{M}{2}, z^* + \frac{M}{2}) : \int_0^\eta d(\gamma)\mathrm{d}\gamma = \frac{1}{M}\left(\eta - (z^* - \frac{M}{2})\right) \\
\forall \eta \in [z^* + \frac{M}{2}, \ell] : \int_0^\eta d(\gamma)\mathrm{d}\gamma = 1
\end{aligned}$$

Therefore, the value $\delta(0)$ is given by

$$\begin{aligned}
\delta(0) &= \ell - 0 - \int_0^{z^* - \frac{M}{2}} 0\mathrm{d}\eta - \int_{z^* - \frac{M}{2}}^{z^* + \frac{M}{2}} \frac{1}{M}\left(\eta - (z^* - \frac{M}{2})\right)\mathrm{d}\eta - \int_{z^* + \frac{M}{2}}^{\ell} 1\mathrm{d}\eta \\
&= \ell - \frac{1}{M}\left(\left(z^* + \frac{M}{2}\right)^2 - \left(z^* - \frac{M}{2}\right)^2 - M(z^* - \frac{M}{2})\right) - \ell + z^* + \frac{M}{2} \\
&= z^*
\end{aligned}$$

□

A.2. FIR Filter Realization of the Algebraic Leak Size Estimation Equation

To implement the leak size estimation equation

$$\hat{\chi} = \frac{1}{\langle \varphi_1(0) \rangle_I} \left(\langle \varphi_1(0), q_0 - q_{in} \rangle_I - \langle \varphi_1(1), Y \rangle_I + \langle \varphi_2(1), U \rangle_I \right) \tag{A.1}$$

via a FIR filter, firstly, the involved integrals are approximated by

$$\begin{aligned}
\int_{t-T}^{t} \varphi_1(0, \tau - t + T) \mathrm{d}\tau &\approx T_s \sum_{m=0}^{M} W_m \varphi_1(0, mT_s) \\
\int_{t-T}^{t} \varphi_1(0, \tau - t + T) \left(q_0(\tau - q_{in}) \, \mathrm{d}\tau \right. &\approx T_s \sum_{m=0}^{M} W_m \varphi_1(0, mT_s) \left(q_0((l - M + m)T_s) - q_{in} \right) \\
\int_{t-T}^{t} \varphi_2(1, \tau - t + T) U(\tau) \mathrm{d}\tau &\approx T_s \sum_{m=0}^{M} W_m \varphi_1(0, mT_s) U((l - M + m)T_s) \\
\int_{t-T}^{t} \varphi_2(1, \tau - t + T) Y(\tau) \mathrm{d}\tau &\approx T_s \sum_{m=0}^{M} W_m \varphi_1(0, mT_s) Y((l - M + m)T_s)
\end{aligned} \tag{A.2}$$

where $T_s := \frac{T}{M}$ is the sampling time and the approximation coefficients W_m are given dependingly on the selected integration method by

$$W_0 = \begin{cases} 1 & : \text{forward} \\ 0 & : \text{backward} \\ \frac{1}{2} & : \text{trapedoizal} \end{cases} ; \forall m = 1, \ldots, M-1 : W_m = \begin{cases} 1 & : \text{forward} \\ 1 & : \text{backward} \\ 1 & : \text{trapedoizal} \end{cases} ; W_M = \begin{cases} 0 & : \text{forward} \\ 1 & : \text{backward} \\ \frac{1}{2} & : \text{trapedoizal} \end{cases} \tag{A.3}$$

to shift the available measurements in time, the following discrete system is defined

$$z(l+1) = \underbrace{\left[\begin{array}{ccc} \begin{bmatrix} 0 & 1 & & \\ & \ddots & \ddots & \\ & & \ddots & 1 \\ & & & 0 \end{bmatrix} & \mathbf{0} & \mathbf{0} \\ \mathbf{0} & \begin{bmatrix} 0 & 1 & & \\ & \ddots & \ddots & \\ & & \ddots & 1 \\ & & & 0 \end{bmatrix} & \mathbf{0} \\ \mathbf{0} & \mathbf{0} & \begin{bmatrix} 0 & 1 & & \\ & \ddots & \ddots & \\ & & \ddots & 1 \\ & & & 0 \end{bmatrix} \end{array}\right]}_{:=A_\chi} z(l) + \underbrace{\left[\begin{array}{ccc} \begin{bmatrix} 0 \\ \vdots \\ 1 \end{bmatrix} & \mathbf{0} & \mathbf{0} \\ \mathbf{0} & \begin{bmatrix} 0 \\ \vdots \\ 1 \end{bmatrix} & \mathbf{0} \\ \mathbf{0} & \mathbf{0} & \begin{bmatrix} 0 \\ \vdots \\ 1 \end{bmatrix} \end{array}\right]}_{:=B_\chi} \underbrace{\begin{bmatrix} q_0(l) \\ U(l) \\ Y(l) \end{bmatrix}}_{:=y(l)} \tag{A.4}$$

Furthermore, the filter coefficients K^q, K^U, K^Y are defined as

$$\begin{aligned} \forall m = 1, \dots, M : K^q &= T_s W_m \varphi_1(0, mT_s) \\ \forall m = 1, \dots, M : K^U &= T_s W_m \varphi_2(1, mT_s) \\ \forall m = 1, \dots, M : K^Y &= -T_s W_m \varphi_1(1, mT_s) \end{aligned} \tag{A.5}$$

Thus, the estimated leak size $\hat{\chi}$ is given by the output of the following time discrete system

$$\begin{aligned} z(l+1) &= A_\chi z(l) + B_\chi y(l) \\ \hat{\chi}(l) &= \frac{1}{\sum_{m=0}^{M} K^q(mT_s)} \left[K^q(0) \dots K^q((M-1)T_s) K^U(0) \dots K_U^q((M-1)T_s) K^Y(0) \dots K^Y((M-1)T_s) \right] z(l) \\ &\quad + \frac{1}{\sum_{m=0}^{M} K^q(mT_s)} \left[K^q(MT_s) K^U(MT_s) K^Y(MT_s) \right] y(l) \end{aligned} \tag{A.6}$$

where $l \in \mathbb{N}$ indicates the discrete time index with $t = lT_s$.

A.3. Spatial Discretization of the Pipe Model

To reduce the infinite-dimensional pipe model, we apply the MOL by introducing n spatial nodes and the spatial discretization step size $\Delta z := \frac{\ell}{n}$. Then, the spatial derivatives $\frac{\partial}{\partial z}p(z,t)$ and $\frac{\partial}{\partial z}q(z,t)$ are approximated by means of forward and backward finite differences, respectively:

$$\begin{aligned}\frac{\partial}{\partial z}p(z,t) &\approx \frac{p(z+\Delta z,t)-p(z,t)}{\Delta z}\\ \frac{\partial}{\partial z}q(z,t) &\approx \frac{q(z,t)-q(z-\Delta z,t)}{\Delta z}\end{aligned} \tag{A.7}$$

Furthermore, we introduce the state vectors $p_d(t),\ q_d(t)$ containing the states at the discrete nodes:

$$\begin{aligned}p_d(t) &= \begin{bmatrix} p_{d,1}(t) \\ \vdots \\ p_{d,n}(t) \end{bmatrix} := \begin{bmatrix} p(0,t) \\ \vdots \\ p(\frac{n-1}{n}\ell,t) \end{bmatrix}\\ q_d(t) &= \begin{bmatrix} q_{d,1}(t) \\ \vdots \\ q_{d,n}(t) \end{bmatrix} := \begin{bmatrix} q(\frac{\ell}{n},t) \\ \vdots \\ q(\ell,t) \end{bmatrix}\end{aligned} \tag{A.8}$$

Replacing the spatial derivatives in the pipe model (2.4) by the finite differences (A.7) gives:

$$\begin{aligned}
\dot{p}_{d,1}(t) &= -\frac{\beta}{A}\frac{\partial}{\partial z}q(0,t) - \frac{\beta}{A}d(0)\chi \\
&\approx -\frac{\beta}{A\Delta z}\left(q(\Delta z,t) - q(0,t)\right) - \frac{\beta}{A}d(0)\chi \\
&= -\frac{\beta}{A\Delta z}\left(q_{d,1}(t) - q_0(t)\right) - \frac{\beta}{A}d(0)\chi \\
\forall i \in \{2,\dots,n\} : \dot{p}_{d,i}(t) &\approx -\frac{\beta}{A\Delta z}\left(q_{d,i}(t) - q_{d,i-1}(t)\right) - \frac{\beta}{A}d(\frac{i-1}{n}\ell)\chi \\
\dot{q}_{d,1}(t) &= -\frac{A}{\rho}\frac{\partial}{\partial z}p(\Delta z,t) - \frac{F}{\rho}q(\Delta z,t) - Ag\sin(\theta(\Delta z)) - \frac{\eta}{A}d(\Delta z)\chi \\
&\approx -\frac{A}{\rho\Delta z}\left(p(_{d,2}(t) - p_{d,1}(t)\right) - \frac{F}{\rho}q_{d,1}(t) - Ag\sin(\theta(\Delta z)) - \frac{\eta}{A}d(\Delta z)\chi \\
\forall i \in \{2,\dots,n-1\} : \dot{q}_{d,i}(t) &\approx -\frac{A}{\rho\Delta z}\left(p(_{d,i+1}(t) - p_{d,i}(t)\right) - \frac{F}{\rho}q_{d,i}(t) - Ag\sin(\theta(i\Delta z)) - \frac{\eta}{A}d(i\Delta z)\chi \\
\dot{q}_{d,n}(t) &= -\frac{A}{\rho\Delta z}\left(p(_{\ell}(t) - p_{d,n}(t)\right) - \frac{F}{\rho}q_{d,n}(t) - Ag\sin(\theta(n\Delta z)) - \frac{\eta}{A}d(n\Delta z)\chi
\end{aligned} \tag{A.9}$$

Finally, summarizing the equations (A.9) in matrix-vector-notation leads to the following set of $2n$ linear ODE's:

$$\begin{bmatrix} \dot{p}_{d,1}(t) \\ \vdots \\ \dot{p}_{d,n}(t) \\ \hline \dot{q}_{d,1}(t) \\ \vdots \\ \dot{q}_{d,n}(t) \end{bmatrix} = \left[\begin{array}{cccc|cccc} & & & & -\frac{\beta}{A\Delta z} & \frac{\beta}{A\Delta z} & & \\ & & & & & \ddots & \ddots & \\ & \mathbf{0} & & & & & \ddots & \frac{\beta}{A\Delta z} \\ & & & & & & & -\frac{\beta}{A\Delta z} \\ \hline \frac{A}{\rho\Delta z} & -\frac{A}{\rho\Delta z} & & & -\frac{F}{\rho} & & & \\ & \ddots & \ddots & & & \ddots & & \\ & & \ddots & -\frac{A}{\rho\Delta z} & & & \ddots & \\ & & & \frac{A}{\rho\Delta z} & & & & -\frac{F}{\rho} \end{array}\right] \begin{bmatrix} p_{d,1}(t) \\ \vdots \\ p_{d,n}(t) \\ \hline q_{d,1}(t) \\ \vdots \\ q_{d,n}(t) \end{bmatrix}$$

$$+ \left[\begin{array}{ccc} 0 & \frac{\beta}{A\Delta z} & -\frac{\beta}{A\Delta z}d(0) \\ 0 & 0 & -\frac{\beta}{A\Delta z}d(0) \\ \vdots & \vdots & \vdots \\ 0 & 0 & -\frac{\beta}{A\Delta z}d(\frac{n-1}{n}\ell) \\ \hline 0 & 0 & -\frac{\eta}{A}d(\Delta z) \\ 0 & 0 & -\frac{\eta}{A}d(2\Delta z) \\ \vdots & \vdots & \vdots \\ -\frac{A}{\rho\Delta z} & 0 & -\frac{\eta}{A}d(\ell) \end{array}\right] \begin{bmatrix} p_\ell(t) \\ q_0(t) \\ \chi \end{bmatrix} + \left[\begin{array}{c} 0 \\ \vdots \\ 0 \\ \hline -Ag\sin(\theta(\Delta z)) \\ \vdots \\ -Ag\sin(\theta(\ell)) \end{array}\right] \tag{A.10}$$